

A Thesis Submitted for the Degree of PhD at the University of Warwick

Permanent WRAP URL:

<http://wrap.warwick.ac.uk/108359>

Copyright and reuse:

This thesis is made available online and is protected by original copyright.

Please scroll down to view the document itself.

Please refer to the repository record for this item for information to help you to cite it.

Our policy information is available from the repository home page.

For more information, please contact the WRAP Team at: wrap@warwick.ac.uk

Synthesis and Application of Novel Colloidal Material

By

Robert A. Young

A thesis submitted in fulfilment of the requirements for the
Degree of Doctor of Philosophy

University of Warwick, Department of Chemistry

September 2016

Contents

1	Chapter 1 – The Use of UCST to Generate Thermochromic Materials	vi
1.1	Abstract.....	1
1.2	Introduction	2
1.2.1	Type I	3
1.2.2	Type II	15
1.2.3	Polymer Solution Phase Separation.....	31
1.2.4	Polymers Exhibiting UCST	40
1.2.5	Encapsulation	47
1.3	Results and Discussion	50
1.3.1	Measuring the Phase Change	51
1.3.2	Copolymers.....	61
1.3.3	Labels.....	110
1.3.4	Encapsulation - Capsules.....	114
1.3.5	Encapsulation - Fibres.....	120
1.4	Conclusion	126
1.5	Experimental	127
1.5.1	General Characterisation Techniques	127
1.5.2	Photographic Phase Change Technique	128
1.5.3	Materials	129
1.5.4	Polymer Synthesis.....	130

1.5.5	Capsule Synthesis.....	132
1.5.6	Fibre Synthesis.....	133
1.6	References	134
2	Chapter 2: Hollow Silica Shells for Opacity Modifiers and Ultrasound Contrast Agents.....	148
2.1	Abstract.....	148
2.2	Introduction	149
2.2.1	Introduction to coatings	150
2.2.2	TiO ₂ and replacement opacifiers for coatings.....	156
2.2.3	Sacrificial Templating.....	166
2.2.4	Microbubbles as Ultrasound Contrast Agents.....	172
2.3	Results and Discussion	177
2.3.1	Characterisation of calcium carbonate particles	177
2.3.2	Encapsulation of SOCAL <i>via</i> Stöber method	183
2.3.3	Etching interior core and characterisation of nanoparticles	200
2.3.4	Dynamic Vapour Sorption.....	212
2.3.5	Ultrasound Contrast Agent.....	216
2.3.6	Light Scattering	222
2.4	Conclusion	230
2.5	Experimental	231
2.5.1	Materials	231

2.5.2	Characterisation Techniques.....	231
2.5.3	Typical synthesis of hollow SiO ₂ particles <i>via</i> templating onto SOCAL P3.....	233
2.5.4	Typical DVS Method.....	234
2.5.5	Typical Ultrasound Measurement	234
2.5.6	Typical Formulations for the etch tests.....	235
2.5.7	Opacifier Test Formulations	235
2.6	References	237
3	Chapter 3: Effect of Hollow Silica Particles on PMMA's Mechanical Properties.....	242
3.1	Abstract.....	242
3.2	Introduction	243
3.2.1	Polymeric Composites.....	243
3.2.2	Carbon based Nanocomposite.....	246
3.2.3	Inorganic Based Nanocomposites.....	249
3.3	Results and Discussion	252
3.3.1	Thermal Properties	254
3.3.2	Optical Properties	262
3.3.3	Tensile Testing	264
3.4	Conclusion	279
3.5	Experimental	280

3.5.1	Materials	280
3.5.2	Equipment and Measurements.....	280
3.6	References	282
4	Chapter 4: Tagging Poly(styrene) with Fluorescent Dyes	286
4.1	Abstract.....	286
4.2	Introduction	287
4.3	Results and Discussion	292
4.3.1	Polymer Synthesis.....	292
4.3.2	Phase Change Response.....	295
4.4	Conclusion	299
4.5	Experimental	300
4.5.1	Materials	300
4.5.2	General Characterisation Techniques	300
4.5.3	Synthesis of TPE-MA.....	300
4.5.4	Hostasol Methacrylate Synthesis	301
4.5.5	Polymer Synthesis.....	302
4.6	References	303
5	Conclusion and Outlook	305
6	Appendix I – Characterisation Techniques	307
6.1	Scanning electron microscopy (SEM)	307

6.2	Transmission electron microscopy (TEM).....	308
6.3	Energy Dispersive X-ray Spectroscopy (EDX)	309
6.4	Mie Scattering.....	309
6.5	References	312
7	Appendix II – Supporting info for Chapter 1	313

Figures

Figure 1-1. Crystal violet lactone (CVL) reversible switching from the non-planar leuco form to the planar coloured form triggered by the pH of the system.	4
Figure 1-2. Thermochromic fibres with central black core containing 40 wt% cholesteryl oleyl carbonate, 40 wt% cholesteryl nonanoate and 20 wt% cholesteryl 2,4-dichlorobenzoate. The reflected wavelength shifts depending on temperature shown above. ⁵²	8
Figure 1-3. Poly(styrene)- <i>block</i> -poly(4-vinyl pyridine) (PS- <i>b</i> -P4VP) quaternised with methanesulfonic acid. Below 125 °C, 3- <i>n</i> -pentadecylphneol (PDP) associates with the P4VP section swelling it (c) and exhibiting a strong green colour (b). Upon heating above 125 °C, hydrogen bonding is interrupted and the PDP distributes evenly throughout the system (g) and causes a loss of colour (f). ⁸⁵	14
Figure 1-4. a) Diffraction from the PNIPAM sphere CCA at 10 °C and 40 °C. Insert represents the switching between swollen spherical arrays below phase transition and identical though compacted array above transitional temperature. b) Diffraction from 125 µm CCA film of PS spheres embedded within a PNIPAM gel. The shift in peak is caused by temperature induced volume changes altering the lattice spacing. Inset top left represents the change in lattice spacing between high and low temperatures. Inset top right shows the temperature dependence of the diffracted wavelength from the CCA. ¹⁰⁵	18

Figure 1-5. a) Photographs of porous PNIPAM inverse CCAs with differing cross-linker concentrations at 27.6 °C. Top left [NIPAM]:[MBAA] = 20:1, top right [NIPAM]:[MBAA] = 30:1, bottom left [NIPAM]:[MBAA] = 60:1, and bottom right [NIPAM]:[MBAA] = 100:1. b) reflection spectra of the PNIPAM porous hydrogel ([NIPAM]:[MBAA] = 30:1) at varying temperatures. ¹²¹	21
Figure 1-6. a) Reflection spectra of the interconnected gel particle array in water. An increase in temperature shows a blue shift in colour. b) Reflection spectra of swellable particles in PS inverse opal. An increase in temperature shows a decrease in the ability to reflected light. ¹²³	23
Figure 1-7. Left) depiction of protonated PNIPAM- <i>c</i> -PTMPAM chains with water molecules hydrogen bonded to it. Middle) colour change upon heating aqueous PNIPAM- <i>c</i> -PTMPAM with phenolphthalein indicator present. At low temperatures the system is basic and phenolphthalein shows a strong fuchsia colour. Upon loss of hydration shell from PNIPAM- <i>c</i> -PTMPAM at high temperature, the solution becomes acidic causing colour to be lost. Right) depiction of deprotonated PNIPAM- <i>c</i> -PTMPAM chains leading to a lowering in pH. ¹⁶⁶	27
Figure 1-8. Phase transition curves of (left to right) P(DEVP _{0.51} - <i>c</i> -DPVP _{0.49}), P(DEVP _{0.69} - <i>c</i> -DPVP _{0.31}), P(DEVP _{0.89} - <i>c</i> -DPVP _{0.11}), P(DMVP _{0.22} - <i>c</i> -DEVP _{0.78}), P(DMVP _{0.4} - <i>c</i> -DEVP _{0.6}), and P(DMVP _{0.59} - <i>c</i> -DEVP _{0.41}). Photograph of turbidity difference between homogeneous and heterogeneous phases with chemical structure of the polymers synthesised. ¹⁷⁵	29
Figure 1-9. Phase diagram of a polymer solution containing both an LCST and an UCST. — is the coexistence/binodal curve and — is the spinodal curve.	38
Figure 1-10. Chemical structures of (left) SPE and (right) SPP.	42
Figure 1-11. Effect of M_w of PS in methyl acetate (■), cyclohexane (●), methyl cyclohexane (▲), and acetone (▼). Data taken from references. ^{198,199,207,210-220}	44
Figure 1-12. Example of coacervation forming particles within an aqueous solution involving i) oil emulsification within the solution, ii) polymer coacervation formed upon changes in pH, iii) deposition of particles onto the surface of the oil, and iv) hardening of the wall to form a barrier. ● is the oil, ● is the polymer coacervate, and ● the aqueous phase.	48
Figure 1-13. Chemical structure of dioctyl phthalate.	50

Figure 1-14. UV/Vis spectra of light absorbed by a 3.5 cm ³ sample of 10 wt% PS in DOP cooled from 10 °C to 1 °C and held at that temperature. Symbols represent wavelengths of ▲ - 400 nm ● - 500 nm ■ - 600 nm. Measurements were taken every 5 minutes.	52
Figure 1-15. Phase transition curve of 10 wt% PS in DOP recorded <i>via</i> UV/Vis spectrometry. ▲ - 400 nm, ● - 500 nm, and ■ - 600 nm wavelength absorbance values. The samples were left 60 minutes before each spectra was recorded. Insets are the cuvette filled with 10 wt% PS in DOP (left) immediately after it was cooled to – 5 °C and (right) after it was left at ambient conditions for 5 minutes.	53
Figure 1-16. Phase curve of 10 wt% PSDOP solution held at 10 °C for 5 minutes before cooling to -2.4 °C. Recorded using the new photographic technique. Images were taken every minute before processing. ● - the grey value measured and ■ - the temperature recorded at each point.	58
Figure 1-17. Phase change curve of 10 wt% of PS in DOP measured using ▲ – UV-Vis at 500 nm and ◆ – photographic technique.....	60
Figure 1-18. UCST curves of PS in DOP. ■ - measured using the photographic technique, ▲ - measured by Ver Strate, ²²⁵ and ● - measured by Rangel – Nafaile. ¹⁹⁶	61
Figure 1-19. Schematic of a) Mayo and b) Flory proposed reaction mechanism for thermal self-initiation of styrene at high temperatures. ²⁵³	62
Figure 1-20. Offset SEC traces of the polymers synthesised from the polymerisation of different concentrations of styrene and MMA after 1 hour at 140 °C. The traces are — PSMMA 1, — PSMMA 2, — PSMMA 3, -- PSMMA 4, -- PSMMA 5, and -- PSMMA 6.	64
Figure 1-21. NMR spectrum of (—) PSMMA 1, (—) PSMMA 2, (—) PSMMA 3, (—) PSMMA 4, (—) PSMMA 5, and (—) PSMMA 6 in CDCl ₃	65
Figure 1-22. Phase diagrams of PSMMA 1 (■), PSMMA 2 (●), PSMMA 3 (▲), PSMMA 4 (▣), PSMMA 5 (⦿), and PSMMA 6 (▲) in DOP.....	71
Figure 1-23. Offset SEC traces of the polymers synthesised from the polymerisation of different concentrations of styrene and EMA after 1 hour at 140 °C. The traces are — PSEMA 1, — PSEMA 2, — PSEMA 3, -- PSEMA 4, -- PSEMA 5, and -- PSEMA 6.....	74

Figure 1-24. NMR spectrum of (—) PSEMA 1, (—) PSEMA 2, (—) PSEMA 3, (—) PSEMA4, (—) PSEMA 5, and (—) PSEMA 6 in CDCl ₃ .	75
Figure 1-25. Phase diagrams of PSEMA 1 (■), PSEMA 2 (●), PSEMA 3 (▲), PSEMA 4 (▣), and PSEMA 5 (●) in DOP.	78
Figure 1-26. Offset SEC traces of the polymers synthesised from the polymerisation of different concentrations of styrene and EA after 1 hour at 140 °C. The traces are — PSEA 1, — PSEA 2, — PSEA 3, -- PSEA 4, -- PSEA 5, and -- PSEA 6.	80
Figure 1-27. NMR spectrum of (—) PSEA 1, (—) PSEA 2, (—) PSEA 3, (—) PSEA4, (—) PSEA 5, and (—) PSEA 6 in CDCl ₃ .	81
Figure 1-28. Phase diagram of PSEA 1 (■), PSEA 2 (●), PSEA 3 (▲), PSEA 4 (▣), PSEA 5 (●), and PSEA 6 (▲) in DOP.	83
Figure 1-29. Offset SEC traces of the polymers synthesised from the polymerisation of different concentrations of styrene and 2-EHA after 1 hour at 140 °C. The traces are — PS2EHA 1, — PS2EHA 2, — PS2EHA 3, -- PS2EHA 4, -- PS2EHA 5, and -- PS2EHA 6.	87
Figure 1-30. NMR spectrum of (—) PS2EHA 1, (—) PS2EHA 2, (—) PS2EHA 3, (—) PS2EHA4, (—) PS2EHA 5, and (—) PS2EHA 6 in CDCl ₃ .	88
Figure 1-31. Phase diagram of PS2EHA 1 (■), PS2EHA 2 (●), and PS2EHA 3 (▲) in DOP.	91
Figure 1-32. Offset SEC traces of the polymers synthesised from the polymerisation of different concentrations of styrene and LA after 1 hour at 140 °C. The traces are — PSLA 1, — PSLA 2, — PSLA 3, -- PSLA 4, -- PSLA 5, and -- PSLA 6.	94
Figure 1-33. NMR spectrum of (—) PSLA 1, (—) PSLA 2, (—) PSLA 3, (—) PSLA 4, (—) PSLA 5, and (—) PSLA 6 in CDCl ₃ .	95
Figure 1-34. UCST curve of PSLA 1 (■), PSLA 2 (●), PSLA 3 (▲), and PSLA 4 (▣) in DOP.	98
Figure 1-35. Offset SEC traces of the polymers synthesised from the polymerisation of different concentrations of styrene and NIPAM after 1 hour at 140 °C. The traces are — PSNIPAM 1, — PSNIPAM 2, — PSNIPAM 3, -- PSNIPAM 4, -- PSNIPAM 5, and -- PSNIPAM 6.	100
Figure 1-36. NMR spectrum of (—) PSNIPAM 1, (—)PSNIPAM 2, (—)PSNIPAM 3, (—)PSNIPAM 4, (—)PSNIPAM 5, and (—)PSNIPAM 6 in CDCl ₃ .	101

Figure 1-37. UCST curve of PSNIPAM 1 (■), PSNIPAM 2 (●), PSNIPAM 3 (▲), PSNIPAM 4 (▣), PSNIPAM 5 (⦿), and PSNIPAM 6 (▲) in DOP.	104
Figure 1-38. Experimental Mayo-Lewis plot of monomer feed versus end polymer composition of comonomer for the (■) PSMMA, (●) PSEMA, (▲) PSEA, (▼) PS2EHA, (◆) PS LA, and (◄) PSNIPAM series after 1 hours at 140 °C resulting in roughly 30% conversion. The diagonal (—) indicates an azeotropic polymerisation where mol% of monomer in feed and end polymer are equal.	106
Figure 1-39. Normalised phase transition curves of 10 wt% polymer in DOP solutions of pure PS (■), 75 : 25 weight ratio of PS : PS LA 4 (●), 50 : 50 weight ratio of pure PS :PS LA 4 (▲), 25 : 75 weight ratio of PS : PS LA 4 (▣), and PS LA 4 (⦿).....	109
Figure 1-40. Liquid crystal thermometer schematic. Copyright Hallcrest © 2016. ³	111
Figure 1-41. Prototype thermochromic strip using 10 wt% PS in DOP when a) cooled below phase transition point, b) warmed above phase transition point, and c) cooled below the phase transition point again. Dyes used were oil blue, rose bengal, and 4-phenylazopheonl.	112
Figure 1-42. Prototype thermochromic label comprised of three different polymeric solutions: 10 wt% of PS, PS LA 2, and PSEMA 5 in DOP. The labels were held at a) – 18 °C, b) – 12 °C, c) – 6 °C, and d) 3 °C. The temperature was held for 15 minutes before each photo was acquired.	113
Figure 1-43. Particle size distribution of PS in DOP capsules of (—) unfiltered and (—) filtered samples.	116
Figure 1-44. Micrograph of the lemon shaped gelatin coated PS in DOP capsules at a) – 5 °C, b) 5 °C, and c) - 5 °C. Scale bar is 250 µm.	117
Figure 1-45. Images of a PS/BA/AA latex binder containing 25 wt% PS in DOP capsules a) immediately after cooling to - 15 °C and b) after being left at 20 °C for 2 minute. Scale bar represents 10 mm.	118
Figure 1-46. Schematic for the formation of PS in DOP oil droplets within an alginate fibre <i>via</i> microfluidic manufacturing.	121

Figure 1-47. Both a) light and b) dark field micrographs of alginate fibres encapsulating PS in DOP oil droplets. Scale bars in ai and bi represent 800 μm whilst in aii and bii they represent 200 μm .	123
Figure 1-48. Images cross linked alginate fibre containing droplets of 10 wt% PS in DOP within a saturated salt solution at a) ambient temperature and b) -2°C where phase change occurs. Scale bar = 3300 μm	124
Figure 2-1. Film formation process schematic. i) application of the waterborne system, ii) concentration <i>via</i> evaporation of water, iii) hexagonal array formed by deformation of spherical latex and temperature exceeding the MFFT, iv) polymer chain interdiffusion and coalescence forming a homogenous film.	153
Figure 2-2. Schematic particles (circles) scattering light (arrows) within a film where a) the particles have low RI and b) the particles have high RI. Due to the light being fully scattered before contacting the substrate, (b) would be considered fully opaque and (a) only partially.	157
Figure 2-3. a) <i>Pieris rapae</i> butterfly, b) overlapping scales on the wings of the <i>P. rapae</i> (scalebar = 50 μm). c-f) SEM micrographs of a dorsal wing scale after immersion in a 1% ammonium hydroxide solution. c) an untreated scale, d) 10 second exposure, e) 30 second exposure, and f) 1 minute exposure. (c-f scale bars 1 μm). ³⁹	162
Figure 2-4. A) An optical micrograph showing the arrangement of the scales of the <i>Cyphochilus</i> beetle (scale bar 1.0 mm). B) SEM image of a fractured edge of one of the scales showing a disordered internal structure (scale bar 3.0 μm) and C) TEM images of a section of the scale (scale bar 3.0 μm). ⁴¹	163
Figure 2-5. Image of hollow ROPAQUE [™] freeze fractured particles. The hollow particles have an interior space of $\sim 1\ \mu\text{m}$ and a shell wall of $\sim 200\ \text{nm}$. ⁴⁴	165
Figure 2-6. Schematic for sacrificial templating where i) the formation of the shell material by layer by layer, precipitation, or polymerisation occurs, ii) removal of core material via a selective process to obtain a hollow particle.	167

Figure 2-7. SEM images of Cu ₂ O nanocrystals of a) truncated cubic, b) cuboctahedral, c) truncated octahedral, and d) octahedral. Insets show an enlarged view of individual nanocrystals with a scale bar of 100 nm. ⁴⁹	168
Figure 2-8. Hydrolysis and subsequent condensation of TEOS in the presence of water and ammonium hydroxide to form a silica network.	170
Figure 2-9. TEM images of a) hematite (α -Fe ₂ O ₃) cubes, b) hematite cubes coated in amorphous silica, c) silica hollow cubes after acid etching of hematite. Scale bars are 1 μ m. ⁵⁷	171
Figure 2-10. Schematic for how ultrasound contrast agents interact with ultrasound waves.	173
Figure 2-11. a) SEM image of 2089 \pm 150 nm, b) TEM images indicating polystyrene core coated in silica, c) TEM images of etched particles with some breakages in the silica shell, d and e) SEM and TEM of OTES – TSPA - TEOS hollow silica particles collapsing under high vacuum, f) SEM (insert) and TEM images of TSPA – TEOS composite with little collapse. Scale bars are all 1 μ m. ⁷³	175
Figure 2-12. a) SEM micrographs of the SOCAL template with scale bar of 200 μ m, and TEM micrograph of the SOCAL template with scale bar 200 nm.....	178
Figure 2-13. a) EDX spectrum of SOCAL indicating only the presence of Ca, O, and C and b) XRD of spectrum of SOCAL (—). (■) represent peaks corresponding to calcite, demonstrating that SOCAL is calcite.....	179
Figure 2-14. Nitrogen adsorption isotherm of SOCAL ; it has a type II isotherm, indicating that SOCAL P3 is essentially non-porous.	181
Figure 2-15. BET transform plot of SOCAL obtained by nitrogen porosimetry; quantity of gas adsorbed as a function of relative pressure. SOCAL P3 has a BET surface area of 7.96 \pm 0.05 m ² g ⁻¹ and a C value of 45.	182
Figure 2-16. Chemical structure of TEOS (left) and BTEOSO (right).	184
Figure 2-17. Particle size analysis by laser diffraction of CaCO ₃ template (SOCAL) (—), SOCAL coated in silica (SOCAL@TBT 1) (—), SOCAL@TBT 2 (—), and SOCAL@TBT 3 (—).....	186

Figure 2-18. SEM micrographs of a) SOCAL@TBT 1 and b) SOCAL@TBT 3. Scale bars represent 1 μm .	188
Figure 2-19. Nitrogen adsorption isotherm of nanocomposite SOCAL@TBT 1 (—), SOCAL@TBT 2 (—), and SOCAL@TBT 3 (—). The lower curve represents the adsorption portion of the isotherm, whereas the higher curve represents the desorption branch.	190
Figure 2-20. BET transform plot of TBT 1 (■), TBT 2 (●), and TBT 3 (▲) obtained by nitrogen porosimetry; quantity of gas adsorbed as a function of relative pressure. TBT 1 has a BET surface area of $68.86 \pm 0.05 \text{ m}^2 \text{ g}^{-1}$ and a C value of 190, TBT 2 has a surface area of $80.09 \pm 0.06 \text{ m}^2 \text{ g}^{-1}$ and a I value of 108, and TBT 3 has surface area of $104.65 \pm 1.02 \text{ m}^2 \text{ g}^{-1}$ with a C value of 236.	191
Figure 2-21. $V_A - t$ plot for TBT 1 (■), TBT 2 (●), and TBT 3 (▲) required for the calculation of micropore area, external surface area, and micropore volume.	192
Figure 2-22. a) EDX spectra and b) XRD spectra of i) SOCAL and nanocomposites ii) SOCAL@TBT 1, iii) SOCAL@TBT 2, and iv) SOCAL@TBT 3. The ■ indicators in (bi) represent the standard crystal pattern expected for a calcite crystal.	195
Figure 2-23. Schematic of electron microscopy showing that the electron excited x-rays used in EDX are generated within the sample in a tear drop shape, leading to a large internal area investigated.	196
Figure 2-24. TGA of SOCAL (—), SOCAL@TBT 1 (—), SOCAL@TBT 2 (—), and SOCAL@TBT 3 (—) nanocomposites from 25 – 1000 $^{\circ}\text{C}$. A heating rate of 10 $^{\circ}\text{C min}^{-1}$ was used under a N_2 atmosphere.	198
Figure 2-25. TEM micrographs of etched silica shells A) TBT 1, B) TBT 2, and c) TBT 3. Scale bars are 250 nm. SEM micrographs of etched silica shells ii) TBT 1 and ii) TBT 2, and iii) TBT 3 silica shells after interior core was acid etched.	202
Figure 2-26. a) EDX spectra and b) XRD spectra of silica shells remaining after etching out the CaCO_3 leaving the shell of i) TBT 1 and ii) TBT 3 showing a loss of both the $\text{Ca } \alpha$ and $\text{Ca } \beta$ in the EDX and the crystalline peaks in the XRD.	204

Figure 2-27. Cross polarised ^{29}Si Solid state NMR (SSNMR) of silica shells post etching. TBT 1, TBT 2, and TBT 3 correspond to the etched SOCAL@TBT 1, SOCAL@TBT 2, and SOCAL@TBT 3 nanocomposites respectively.	212
Figure 2-28. DVS isotherms of silica shells TBT 1 (—), TBT 2(—), and TBT 3 (—) in octane. Absorption curve (◆) and desorption curve (◀). The data was standardised to a constant volume to ensure an equal comparison between all samples.....	213
Figure 2-29. DVS isotherms of silica shells TBT 1(—), TBT 2(—), and TBT 3 (—) in water. Absorption curve (◆) and desorption curve (◀).....	215
Figure 2-30. Ultrasound measurements at low concentration ($0.025\text{ cm}^3\cdot\text{L}^{-1}$) of a) TBT 1, b) TBT 2, and c) TBT 3 silica shells at differing mechanical indexes (Top to bottom MI= 0.66 – 0.43).	219
Figure 2-31. Greyscale snapshots of video from ultrasonic imaging of a) pure water and pure water containing b) TBT 1, c) TBT 2, and d) TBT 3 at $0.025\text{ cm}^3\cdot\text{L}^{-1}$ measured at MI 0.66. Lighter grey sections seen in b-d are indicative of low level ultrasound response whilst the white spots seen in c and d indicate a strong response to ultrasound imaging.....	220
Figure 2-32. Ultra sound measurements at high concentration ($0.25\text{ cm}^3\cdot\text{L}^{-1}$) of TBT 1, b) TBT 2, and c) TBT 3 silica shells at differing mechanical indexes (Top to bottom MI = 0.66 – 0.43).	222
Figure 3-1. Schematic of three main types of layered composite arising from interaction between sheets and polymer chains. a) phase separated microcomposite, b) intercalated nanocomposite, and c) exfoliated nanocomposite. ¹³	245
Figure 3-2. Schematic for ASTM D638 V dogbones.....	254
Figure 3-3. TGA of pure PMMA (—), nanocomposite of PMMA/TBT 1 - 1 (—), PMMA/TBT 1 - 2 (—), and PMMA/TBT 1 - 3 (—).....	255
Figure 3-4. TGA of PMMA/TBT 2 - 1 (—), PMMA/TBT 2 - 2 (—), and PMMA/TBT 2 - 3 (—).....	259
Figure 3-5. TGA of PMMA/TBT 3 - 1 (—), PMMA/TBT 3 - 2 (—), and PMMA/TBT 3 - 3 (—).....	261
Figure 3-6. Transmission of UV and visible light recorded using a UV/Vis Spectrometer of a) PMMA dogbone, b) PMMA/TBT 3 1.3 wt% dogbone, c) PMMA/TBT 3 2.2 wt% dogbone, d)	

PMMA/TBT 2 0.9 wt% dogbone, e) PMMA/TBT 2 2 wt% dogbone, and f) remaining PMMA/TBT composites.	263
Figure 3-7. Stress – strain response curves of PMMA (—), PMMA/TBT 1 - 1 (—), PMMA/TBT 1 - 2 (—), and PMMA/TBT 1 - 3 (—) averaged over 5 runs.	266
Figure 3-8. SEM images taken at the fracture points of a) PMMA/TBT 1 4.8 wt%, b) PMMA/TBT 1 2.2 wt%, and c) PMMA/TBT 1 1.6 wt% at i) high magnification and ii) low magnification. The smooth surface present in both ai and ci are indicative of pure PMMA systems with low dispersion of silica particles. Scale bars represent (i) 2 μ m and (ii) 50 μ m.	269
Figure 3-9 Stress – strain response curves of PMMA (—), PMMA/TBT 2 4.83 wt% (—), PMMA/TBT 2 2 wt% (—), and PMMA/TBT 2 0.9 wt% (—) averaged over 5 runs.	271
Figure 3-10. SEM images taken at the fracture points of a) PMMA/TBT 2 4.83 wt%, b) PMMA/TBT 2 2 wt%, and c) PMMA/TBT 2 0.9 wt% at i) high magnification and ii) low magnification. Scale bars represent (i) 2 μ m and (ii) 50 μ m.	273
Figure 3-11. Stress – strain response curves of PMMA (—), PMMA/TBT 3 4.6 wt% (—), PMMA/TBT 3 2.2 wt% and PMMA/TBT 3 1.3 wt% (—) averaged over 5 runs.	275
Figure 3-12. SEM images taken at the fracture points of a) PMMA/TBT 3 4.6 wt%, b) PMMA/TBT 3 2.2 wt%, and c) PMMA/TBT 3 1.3 wt% at i) high magnification and ii) low magnification. Scale bars represent (i) 2 μ m and (ii) 50 μ m.	277
Figure 4-1. Fluorescence intensity of calcein as function of the concentration of calcein present. ⁴	287
Figure 4-2. Silole based AIE dye (1,2,3,4,5-pentaphenylsilole). ⁹ Reducing the free rotation of the aromatic pendant groups leads to emission.	288
Figure 4-3. i) phase change curve of TPE with a) 3 PEO units, b) 4 PEO units, and c) 5 PEO units with ii) corresponding changes in cloud points based on concentration, iii) emission intensity of TPE with 4 PEO units dependant on temperature, and iv) particle size dependent on temperature. ²⁰	290
Figure 4-4. Chemical structure of (left) Hostasol, and (right) 1,1,2,2-tetraphenyl ethylene (TPE).	292

Figure 4-5. Images of DOP solutions containing i)PSHost, ii)PSTPEMA 1, iii)PSTPEMA 2, and iv)PSTPEMA 3 under UV illumination at a) – 20 °C and b) 30 °C.	294
Figure 4-6. Phase change curves of PSHost (■), PSTPE 1 (●), PSTPE 2 (▲), and PSTPE 3 (▣) under visible light illumination.....	295
Figure 4-7. Phase change curves of PSHost (■), PSTPE 1 (●), PSTPE 2 (▲), and PSTPE 3 (▣) under ultra violet light illumination.	297
Figure 6-1. Diagram illustrating different values that can be compared between irregular samples, and b) difference seen between two differently sized samples measured using number, volume and intensity. ²	311
Figure 7-1 Schematic designed for aluminium block used for the photographic phase change measurement technique	313
Figure 7-2. Mayo-Lewis plot of styrene and MMA (▲), BMA (■) (used instead of EMA), EA (▣), 2EHA (●), LMA (⊖) (used in place of LA), and TAA (▲) (used in place of NIPAM). Diagonal is the azeotropic line where $f_1 = F_1$	314
Figure 7-3. Phase change curves of a) PMMA 1, b) PMMA 2, c) PMMA 3, d) PMMA 4, e) PMMA 5, and f) PMMA 6.	315
Figure 7-4. Phase change curves of a) PEMA 1, b) PEMA 2, c) PEMA 3, d) PEMA 4, e) PEMA 5, and f) PEMA 6.	316
Figure 7-5. Phase change curves of a) PEA 1, b) PEA 2, c) PEA 3, d) PEA 4, e) PEA 5, and f) PEA 6.....	317
Figure 7-6 Phase change curves of a) P2EHA 1, b) P2EHA 2, c) P2EHA 3, d) P2EHA 4, e) P2EHA 5, and f) P2EHA 6.	318
Figure 7-7. Phase change curves of a) PLA 1, b) PLA 2, c) PLA 3, d) PLA 4, e) PLA 5, and f) PLA 6.....	319
Figure 7-8. Phase change curves of a) PNIPAM 1, b) PNIPAM 2, c) PNIPAM 3, d) PNIPAM 4, e) PNIPAM 5, and f) PNIPAM 6.....	320
Figure 7-9. PSDOP capsules within a) polysiloxane binder, b) fast curing epoxy binder, c) slow curing epoxy binder, and d) silane binder at i) -5 °C and ii) 20 °C.....	321

Tables

Table 1-1. Tabulated data for MMA containing polymers recorded from NMR, SEC and Equation 1.33.	67
Table 1-2. UCST point data of the PSMMA series from Figure 1-21.	71
Table 1-3. Tabulated data for EMA containing polymers recorded from NMR, SEC, and Equation 1.33.	77
Table 1-4. UCST data for the PSEMA series from Figure 1-25.	78
Table 1-5. Tabulated data for EA containing polymers recorded from NMR, SEC, and Equation 1.33.	82
Table 1-6. UCST data for the PSEA series from Figure 1-25.	84
Table 1-7. Tabulated data for 2EHA containing polymers recorded from NMR, SEC, and Equation 1.33.	90
Table 1-8. UCST data for the PS2EHA series from Figure 1-31.	91
Table 1-9. Tabulated data for LA containing polymers recorded from NMR, SEC, and Equation 1.33.	97
Table 1-10. UCST data for the PSLA series from Figure 1-29.	98
Table 1-11. Tabulated data for NIPAM containing polymers recorded from NMR, SEC, and Equation 1.33.	103
Table 1-12. UCST data of the PSNIPAM series obtained from Figure 1-37.	104
Table 1-13. Mass of DOP, PS in DOP, and encapsulated PS in DOP over time.	120
Table 1-14. Poly(styrene- <i>co</i> -methyl methacrylate) monomer quantities.	130
Table 1-15. Poly(styrene- <i>co</i> -ethyl methacrylate) monomer quantities.	131
Table 1-16. Poly(styrene- <i>co</i> -ethyl acrylate) monomer quantities.	131
Table 1-17. Poly(styrene- <i>co</i> -2ethylhexyl acrylate) monomer quantities.	131
Table 1-18. Poly(styrene- <i>co</i> -lauryl acrylate) monomer quantities.	132
Table 1-19. Poly(styrene- <i>co</i> - <i>n</i> -isopropyl acrylamide) monomer quantities.	132

Table 2-1. Typical formulation for a white decorative coating including the mill base and let down. The mill base is the premixed system with the let down added after full dispersion of the mill base is acquired. Formulations were obtained from Hempel.	151
Table 2-2. Tabulated statistics of laser scattering data plotted in Figure 2-17. The d(0.1), d(0.5), and d(0.9) values refer to the diameter of 10, 50, and 90% of the sample.	187
Table 2-3. Tabulated data obtained from the $V_A - t$ plot show in Figure 2-21.....	193
Table 2-4. Tabulated data extracted from TGA analysis (Figure 2-24).....	199
Table 2-5. Conversion data of silica coating.....	200
Table 2-6. Calculated density of films with both intact and compromised air voids using Equation 2-11 along with the measured specific gravity by hydrostatic weighing.	209
Table 2-7. Skeletal density determined by helium pycnometry for the CaCO_3 template, $\text{CaCO}_3@ \text{SiO}_2$ nanocomposites and the SiO_2 shells.	210
Table 2-8. Average multi angle gloss readings for dry films containing CaCO_3 , TBT 1-3, or no pigmentation.	223
Table 2-9. LAB colour space recording for films containing differing pigments.	225
Table 2-10. Tabulated average hiding power, scattering coefficient, and absorption coefficient calculated using Kubelka – Munk theory (Equation 2-5).....	227
Table 2-11. Typical formulation used in etch test study.	235
Table 2-12. Opacifier test formulation for TBT 1.....	235
Table 2-13. Opacifier test formulation for TBT 2.....	236
Table 2-14. Opacifier test formulation for TBT 3.....	236
Table 3-1. SEC data from both the pure and milled PMMA.	253
Table 3-2. Tabulated TGA data from Figure 3-3.....	257
Table 3-3. Tabulated TGA data from Figure 3-4.....	260
Table 3-4. Tabulated TGA data from Figure 3-5.....	261
Table 3-5. Tensile data of PMMA/TBT 1 composites averaged over 5 runs obtained from Figure 3-7. Errors are reported as 1 standard deviation from the mean.....	267
Table 3-6. Tensile data of PMMA/TBT 2 composites averaged over 5 runs obtained from Figure 3-9. Errors are reported as 1 standard deviation from the mean.....	272

Table 3-7. Tensile data of PMMA/TBT 3 composites averaged over 5 runs obtained from Figure 3-11. Errors are reported as 1 standard deviation from the mean.....	276
Table 4-1. Tabulated data for dye tagged polystyrene samples.....	293

Acknowledgements

I would like to thank the entire Bon Lab group, both past and present whom I have had the great pleasure to work with; namely Brooke, Sam, Pat, Andrea, Andrés, Matt, Melody, and Chris. Special thanks is need to both Corinna and Ross for their help and support they provided in the last couple of months. I would also like to thank the academic staff, support staff, and other PhD students at Warwick who I have worked with along the way.

I would also like to particularly thank my supervisor, Prof. Stefan Bon for his help and support throughout my time at Warwick and the opportunities this afforded me.

Thanks also to Hempel and Crown for the funding of this project. In particular I would like to thank Ian Pickering for this help with the opacity work with the silica particles.

Finally, a most special thanks to my close ones who helped me through this final hurdle. In particular Amilija who had to deal with me day to day with all the mood swings and still stuck it out.

Declaration

I hereby declare that this thesis consists of my own work with the exception of the collaborative work listed below:

- Chapter 1 – some polymer synthesis and optimisation of the photographic technique was performed with Andrés Richards. Ross Jagers performed the microfluidic work to create the alignate fibres.
- Chapter 2 – Ultrasound measurements were acquired under the supervision of Nadia Tsao. DVS was performed by Dr James Bowen whilst at the University of Birmingham. Patrik Olsson assisted with the acquisition of XRD data.
- Chapter 4 – Synthesis of TPMA was undertaken along with Dr Corinna Preuss

All work contained herein was conducted in the Department of Chemistry at the University of Warwick, between October 2012 and October 2016. No material contained in this thesis has been submitted for any other degree, or at any other institution.

Signed _____

Date _____

Robert A Young

Abstract

Within this thesis we explore the synthesis of novel colloidal particles for the use as both a thermochromic indicator and opacifiers. Initially in **Chapter 1** we describe the synthesis of polystyrene copolymers and the effect the comonomers have upon the phase transitional temperature within dioctyl phthalate. Co-polymers containing varying mol% of copolymers led to a decrease in the transitional temperatures for the systems. Following the determination of the phase transitions, we touched upon the potential to encapsulate the oils and use them within both a soft fibre and a waterborne latex binder as a thermochromic pigment. In **Chapter 2** we looked into the synthesis of hollow non-spherical silica particles and their potential use within both ultrasound imaging and films as an opacifying agent. In **Chapter 3** we expand upon the use of the silica shells by dispersing them within a PMMA nanocomposite to determine the effect on the mechanical properties. In **Chapter 4** we explored further into the UCST systems shown in Chapter 1 with the addition of specialised dye tagging of the polystyrene chains to obtain a fluorescent changes upon phase transition.

Abbreviations

BTEOSO	1,8-bis(triethoxy silyl)octane	MMA	Methyl methacrylate
2EHA	2-ethyl hexyl acrylate	NIPAM	<i>N</i> -isopropyl acrylamide
CCA	Colloidal crystal array	T_{onset}	Phase transition onset temp.
CVL	Crystal violet lactone	PMMA	Polymethylmethacrylate
	Differential scanning		
DSC	calorimetry	PS	Polystyrene
DOP	Dioctyl phthalate	SEM	Scanning Electron Microscope
\bar{D}	Dispersity	SSNMR	Solid state NMR
DFT	Dry film thickness	TEOS	Tetraethyl orthosilicate
DVS	Dynamic vapour sorption	TPE	Tetraphenyl ethylene
d_{eff}	Effective particle density	TLC	Thermochromic liquid crystal
EDX	Energy dispersive x-ray	TGA	Thermogravimetric analysis
EA	Ethyl acrylate	TEM	Transmission Electron Microscope
EMA	Ethyl methacrylate	UTS	Ultimate tensile strength
GHMP	Gelatin-hexametaphosphate	UCST	Upper critical solution temperature
T_g	Glass transition temperature	WFT	Wet film thickness
LA	Lauryl acrylate	XRD	X-ray diffraction
M_w	Mass average molar mass		

1 Chapter 1 – The Use of UCST to Generate Thermochromic Materials

1.1 Abstract

We demonstrate the random copolymerisation of styrene and co-monomers *via* free radical polymerisation. With these polymers we demonstrate the effect the co-monomers have upon the phase transition temperature in dioctyl phthalate using a new photographic method for determining the phase transition of the polymer solutions. Our polymerisation strategy relies upon the thermal self-initiation of styrene at elevated temperatures to form an initiation species for the polymerisation. We demonstrate that control of the phase transition of a sample can be easily tuned using different monomer ratios in the reaction mixture. Following the successful synthesis of multiple temperature phase changes, we demonstrate the use of the thermochromic solution within prototype labels. Further to this, we encapsulated PS in DOP solution to form thermochromic pigment for use within a waterborne binder where optical changes dependant on temperature could be observed in multiple binders. Finally we formed a flexible fibre containing phase change droplets.

1.2 Introduction

Colour changing materials are interesting for a wide range of applications as the materials' properties can be changed crucially. One of the major interest in this area lies in thermochromic materials, whose change in colour and thus, optical properties, can be triggered by temperature change.¹ These very versatile materials can be found in a lot of different systems.² A closer look at the origin of the thermochromic behaviour reveals the ability to change colour can be molecular or structural in nature. We will refer to these thermochromic systems as type I and type II respectively (see sections **1.2.1** and **1.2.2**).

The principal idea for the material presented in this chapter is to develop a thermochromic system with a temperature response between – 15 °C to 5 °C from polymer solution phase separations *via* upper critical solution temperature (UCST) changes and to utilise the polymer solutions in the development of pigment capsules to be used in waterborne coatings for temperature responsive road markings, and temperature strips as an alternative to existing liquid crystalline based technology.³ The polymeric material used in our approach is based on polystyrene and its random copolymers, the latter to tailor the temperature range of UCST-type phase separations, by means of free radical copolymerization with a selection of different co-monomers. A concise overview of the physics of UCST phase change behaviour is provided in section **1.2.3**. Afterwards, several examples

for polymer solutions that exhibit UCST changes, which are quite rare, are discussed in section **1.2.4**.

1.2.1 Type I

The colour change of Type I thermochromic materials originates from molecular interactions with light and can be differentiated into four types of materials, that is leuco dyes (**Section 1.2.1.1**), thermochromic liquid crystals (**Section 1.2.1.2**), inorganic thermochromic compounds (**Section 1.2.1.3**), and thermochromic photonic blocks copolymers (**Section 1.2.1.4**).

1.2.1.1 Leuco Dye Thermochromic Systems

Leuco dyes make up one of the most widely known subsections of thermochromism.^{4–8} The leuco dyes itself are halochromic (pH change triggers colour change) dyes and exhibit no thermochromic behaviour on their own.⁹ They exist in either a colourless or white state in their neutral form but become coloured upon protonation.¹⁰ In order to acquire thermochromic responsiveness based on these dyes, a ternary mixture that consists of a *colour former* (leuco dye), a *colour developer* (weak acid / electron acceptor), and a *co-solvent* is required.¹¹

The most common leuco dye is crystal violet lactone (CVL) (**Figure 1-1**).¹² When the lactone ring is closed, the non-planar spiropyran form of the dye exhibits no colour as the corresponding light activated electron transition lies outside the visible spectrum ($\lambda_{max} (\pi \rightarrow \pi^*) = 280 \text{ nm}$).¹³ In the presence of a weak acid or electron acceptor (*colour developer*) the dye is protonated and the lactone ring opens. The new ring opened merocyanine form is highly

conjugated and the transition is shifted into the visible part of the spectrum ($\lambda_{max} (\pi \rightarrow \pi^*) = 620 \text{ nm}$), which can be observed by the change to an intense blue colour.¹³ Long chain acids¹⁴ as well as gallates,^{10,15} phenols,^{6,16,17} and hydroxyl benzoates¹⁸ are common *colour developers*. *Colour developers* require hydrophobic alkyl side chains to increase the solubility in the non-polar *co-solvent*.¹⁹

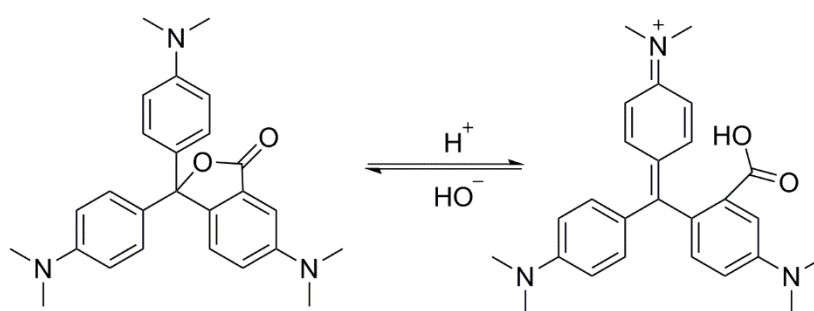


Figure 1-1. Crystal violet lactone (CVL) reversible switching from the non-planar leuco form to the planar coloured form triggered by the pH of the system.

The *co-solvent* is needed to tailor the temperature at which the colour change occurs. Long-chain acids, esters, and alkyl alcohols are the most commonly used due to their high melting points.^{11,17,20–22} Upon heating above the melting point of the *co-solvent*, both *colour former* and *colour developer* become dispersed. The relatively large distance between the molecules stop association and, thus, no colour is observed.¹¹ When the system is cooled below the melting point, phase separation occurs, and both the *colour former* and the *colour developer* are forced into close proximity.^{12,15} Association

occurs between the molecules and the ring opening transpires, which subsequently generates the colour owing to the induced protonation.

An interesting example by Azizian *et al.* shows the synthesis of new fluorans (*colour former*) containing phenolic groups (*colour developer*) by performing a Suzuki coupling of benzofluoran and a variety of phenolic moieties.^{23,24} Due to the presence of the phenolic groups, the addition of *colour developers* to form the coloured compound is not required whilst retaining similar colour changes.

The limitations arising for such leuco dye systems are poor stability with respect to UV light and subjection to elevated temperatures.^{10,25} Exposure to UV light causes degradation of the dye molecule, which reduces the colour in turn.^{25,26} Due to the degradation upon exposure to UV light, these systems cannot be used long term outside. Temperatures exceeding 200 °C causes irreversible damage to leuco dyes system, as the *colour former* and *colour developer* overcome a minimum energy and become closely associated and, hence, re-melting the *co-solvent* will not force a dissociation to occur.^{11,12,15} This leads to a loss of reversibility of the system and upon cooling the decolouration is not feasible and the previous colour remains.

1.2.1.2 Thermochromic Liquid Crystals

Thermochromic liquid crystals (TLCs) form the second subsection of type I thermochromic compounds. TLCs have long been studied due to their tunability, multiple colour transitions and high temperature accuracy.²⁷ They can be found in strip thermometers,^{28,29} mugs,^{30,31} mood rings,³²⁻³⁴ tiles,³⁵ and

fibres.³⁶ TLCs consist of rigid optically active organic compounds that exhibit a chiral molecular structure.³⁷ Traditionally, they were termed cholesteric liquid crystal as they were originally derived from cholesterol, whereas chiral nematic liquid crystals would be the correct term.³⁷ Since their discovery by Reinitzer,³⁸ both cholesterol and non-sterol derived molecules have been found to form chiral nematic liquid crystals.³⁹

Rigid chiral molecules exhibit a rod like shape and can form one of two main phases: smetic and isotropic. A system within the smetic phase self-organises into lamellar structure where the layers align their long axes in parallel and therefore, can slide over each other.⁴⁰ Within the isotropic phase, the molecules lose all long and short range order and transition to a liquid.³⁹ The chiral nematic mesophase which is traversed *via* temperature changes, induces the colour change, exists between the smetic and isotropic phase.³⁷ The molecules self-organise into a lamellar structure, which is similar to the one found in smetic phase, but the layers show a slight rotation on the previous one.⁴¹ This angular offset between layers leads to the formation of a helix.⁴² The helical arrangement of molecules provides the optical properties. The separation of layers with the same orientation within the chiral structure leads to selective reflection of incident light.⁴² This selective light reflection is analogous to Bragg reflection of layered solids.⁴³ Incident light is reflected (λ_{ref}) following the **Equation 1-1**.

$$\lambda_{ref}(T) = p(T)\eta \sin \theta \quad \mathbf{1-1}$$

Where p is the pitch length at the set temperature, θ the angle of incidence, and η the refractive index of the material.

The pitch length is defined as the distance along the helical axis within one 360° rotation and is controlled by the temperature, causing the thermochromic characteristic.^{44,45} With an increase in temperature, the helical structure twists more which causes a shorter pitch length and thus, results in a blue shift of the observed colour.⁴⁴ As the system transitions into the isotropic phase at a high temperature, a loss in structure, and therefore pitch length, occurs and no light is Bragg reflected. When the temperature is decreased, the system undergoes an untwisting of the helical structure. As a result the pitch length increases, which leads to a red shift.^{46,47} Within this phase the pitch is infinitely long and visible light is no longer reflected.⁴⁴ A more rapid transition between colours is seen within the red end of the range due to the non-linearity of the pitch length with temperature.⁴³ dP/dT increases toward the chiral nematic – smectic transition.³⁷

A major advantage of the TLC systems is the relatively short rearrangement time upon temperature changes. For instances, a bulk mixture of cholesteryl nonanoate requires 100 ms and cholesteryl oleyl carbonate requires 200 ms to rearrange.⁴⁸ Furthermore, upon encapsulation, the rearrangement was even decreased to 3 ms, which originates from the new confinement of the system as well as a decrease in overall volume.^{27,49}

TLCs within the chiral nematic mesophase will always reflect light depending on the pitch length and allow the rest to pass through. However, if

an object behind the TLC reflects the wavelengths allowed to pass through, no colour is observed. For optimal visualisation of the thermochromic effect, a black background is required.⁴⁶ This ensures no transmitted light is reflected through the system to disrupt the colour observed.^{50,51} An example by Werff *et al.*, who employed a melt extrusion process to produce fibres containing a black centre and liquid crystals surrounded by an impermeable polypropylene layer (**Figure 1-2**), represents an application where the material already exhibits the required black colour.⁵² Hence the addition of a separate black compound is redundant.

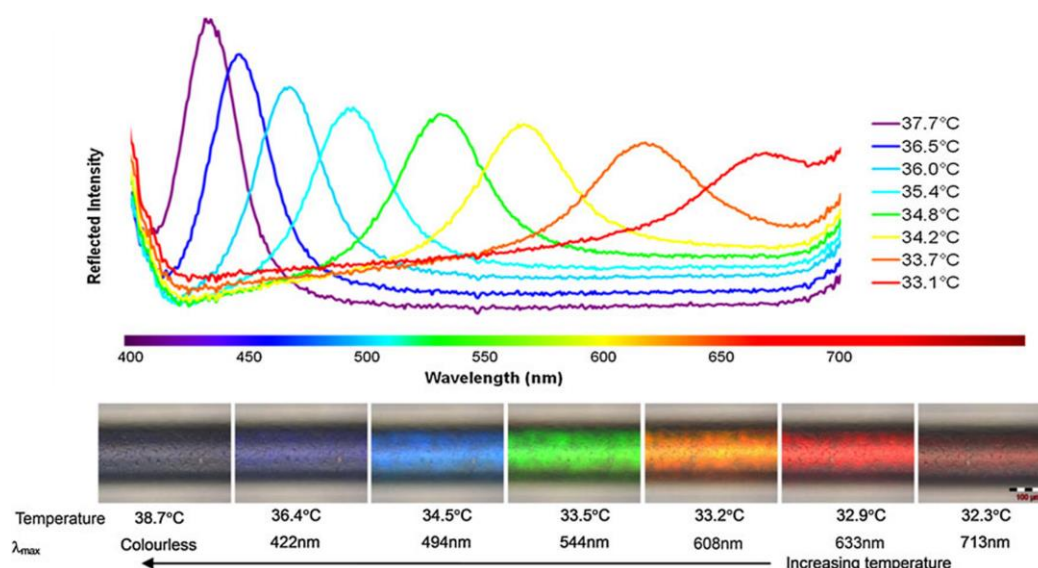


Figure 1-2. Thermochromic fibres with central black core containing 40 wt% cholesteryl oleyl carbonate, 40 wt% cholesteryl nonanoate and 20 wt% cholesteryl 2,4-dichlorobenzoate. The reflected wavelength shifts depending on temperature shown above.⁵²

Similarly to leuco dyes, TLCs are very sensitive toward UV light due to the extended conjugation within the molecules.^{37,50} Colour play range (the

temperature range in which colour can be observed) is another issue.^{46,52} Outside the chiral nematic range, there is no indication of colour in both the smectic-A and isotropic phases meaning that it cannot be specified whether the system is on either end of the chiral nematic range. In order to expand the range of chiral nematic phase small polystyrene (PS) chains (M_n of 490 – 9500 $\text{g}\cdot\text{mol}^{-1}$) have been introduced to stabilise the blue phase to higher temperatures.⁵³ However the isotropic phase is also present in the expanded area and a loss of colour was still observed. TLCs are commercially available, however, the costs for the components are drastically higher than that of leuco dyes.

1.2.1.3 Inorganic Thermochromic Compound

Thermochromic substances made from inorganic compounds, more precisely transition metal complexes, make up the third subsection of type I.⁵⁴ The colour of metallic complexes originates from the different electron distribution in their d -orbital electrons.^{54–56} These metal complexes can be further modified by doping with other metal ions or the introduction of additional ligands, which causes changes in the energy levels and, thus, the colour observed.⁵⁵ In contrast, the term “thermochromic inorganics” implies electrons can be excited to higher energy levels upon heating, which alters the chromic response.² When returning to the lower temperatures, the emissive energy returns to the original levels and a reversible colour change is observed.

Ruby gemstones have long been known to exhibit a thermochromic response upon heating, transitioning the known ruby red colour into a shiny green similar to an emerald and returns to red upon cooling.⁵⁷ This chromic change is due to Cr^{3+} within the structure where increasing the temperature leads to an electron exchange between Cr – Cr neighbours.⁵⁷ An antiferromagnetic compound is formed as a result and the new electron arrangement exhibits a photonic band gap causing a green colour to arise.⁵⁷ Upon cooling this returns to the red coloured complex. The thermochromic temperature change depends solely on the Cr^{3+} content. At 58 atom% (the atom% of Cr^{3+} found within the similar inorganic gemstone, emerald), the change occurs at $-183\text{ }^{\circ}\text{C}$. Upon decreasing to 8 atom% (roughly the atom% found within common rubies), the chromic change occurs at $186\text{ }^{\circ}\text{C}$ with a further increase to $376\text{ }^{\circ}\text{C}$ at 2 atom%.

Another example of a simple complex is vanadium (IV) oxide. A semiconductor to metal transition occurs at $68\text{ }^{\circ}\text{C}$ for a single pure crystal of VO_2 .⁵⁸ Accompanying this transition is structural phase change from a monocyclic crystal structure at low temperature to a rutile, tetragonal-type lattice above $68\text{ }^{\circ}\text{C}$.^{59,60} A large increase in electrical conductivity is met with an increase in infrared reflectivity with slight red visible light reflectivity.⁶¹ Doping of these systems with tungsten and magnesium can alter thermochromic change to be within $30 - 80\text{ }^{\circ}\text{C}$.⁶²

The polymeric iron (II) compound, $[\text{Fe}(\text{4-amino-1,2,4-triazole})_3](\text{NO}_3)_2 \cdot 2\text{H}_2\text{O}$ also shows exceptional thermochromic properties

within an inorganic material.⁶³⁻⁶⁶ The family of thermochromic materials based around Fe(II) with 1,2,4-triazole ligands has been well patented.^{67,68} The colour change within these substances is caused by the thermally induced spin crossover between high and low spin states.⁶⁹ At low temperatures ($< 26\text{ }^{\circ}\text{C}$) the compound is in a high spin state and shows a pink-violet colour. Upon heating ($> 26\text{ }^{\circ}\text{C}$) the transition to low spin state occurs and the colour changes to white. Owing to the hysteresis of the system, relatively large time periods are required for it to return to the original state (~ 5 minutes).^{63,65} This thermochromic process is in seen both aqueous solution and solid phase.^{66,69}

Inorganic compounds that undergo Jahn-Teller (JT) splitting are also prone to exhibit thermochromism.⁷⁰ CuCl_6^{4-} readily undergoes JT splitting, causing a difference in Cu-Cl bond lengths and, thus, changes the energy levels.⁷¹ Above $67\text{ }^{\circ}\text{C}$, the JT splitting leads to a decrease in the crystal field splitting, and hence the $d-d$ transitions, causing a change to the colour red being observed. Upon returning to lower than $67\text{ }^{\circ}\text{C}$, the original non-coloured state is obtained.

Whilst most inorganic systems show thermochromic response in the solid state, high temperatures are often needed for the effect to occur. Furthermore, systems with lower temperature change exhibit large hysteresis.^{57,58,70,72,73} No low temperature ($-10 - +10\text{ }^{\circ}\text{C}$) indicators have yet been found.

1.2.1.4 Thermochromic Photonic Block Copolymers

The final subsection of type I is photonic block copolymers (PBCs). Whilst the colour is formed due to the interaction of light between layers, direct molecular movement is required for the creation of stimuli responsive block copolymers.^{74,75} PBCs consist of a variety of self-assembled phases due to mutually repulsive blocks. Some of the phases formed are lamellar (1D), cylindrical (2D), and gyroid (3D).⁷⁶ To form self-assembled structures, block copolymers often need to be annealed for phase separation of the polymers to occur.^{76,77} Lamellar structured PBCs (1D) are the most commonly found to exhibit thermochromic behaviour as 1D swelling of the copolymers is easier to control.⁷⁶ To achieve 1D PBC, the volume fraction of both polymers needs to be ~ 50 % for the packing parameter to favour lamellar packing.

The distance between the two layers of the same polymer (A and A in an A-B-A structure) is fixed by the thickness of the layer of the other polymer (B layer), PBCs exhibit only one specific colour in their original state.⁷⁸ Most of the polymers used often have similar refractive indexes.^{76,79-81} However, the system can be tweaked by swelling the inner layer (B), which results in a change of colour owing to both the change in refractive index and the lamellar spacing.^{76,79,82} The Bragg reflection caused by this change in refractive index and distance between the layers of polymer A are similar to those found in TLCs.⁷⁷ The light reflected is controlled by the distance between the non-swollen polymer layers (**Equation 1-2**).

$$\lambda_{ref} = 2nd \sin \theta \quad 1-2$$

Where d is the distance between polymer layers, n is the refractive index, and θ is the angle of observation.

To impart thermochromic behaviour into PBCs, the preferential swelling of one region must be controlled thermally.⁷⁹ This is achieved by including an additional molecule that preferentially exists in one region at low temperature but upon heating can migrate into both layers, losing the preferential swelling.^{83,84} Valkama *et al.* demonstrated this using a Poly(styrene)-*b*-poly(4-vinyl pyridine) copolymer quaternised with methane sulfonic acid (**Figure 1-3**).⁸⁵ 3-*n*-pentadecylphenol (PDP) was found to swell the 4-vinyl pyridine block at low temperatures. Upon heating above 125 °C, migration of the PDP molecule into the non-swollen poly(styrene) block occurs until an equilibrium is met and both layers become equal, losing the colour of the system. Different solvents, acids, chromophores, and hydrogen bond donors have been shown to serve as such additional molecules that exhibit this behaviour.^{79,85-91}

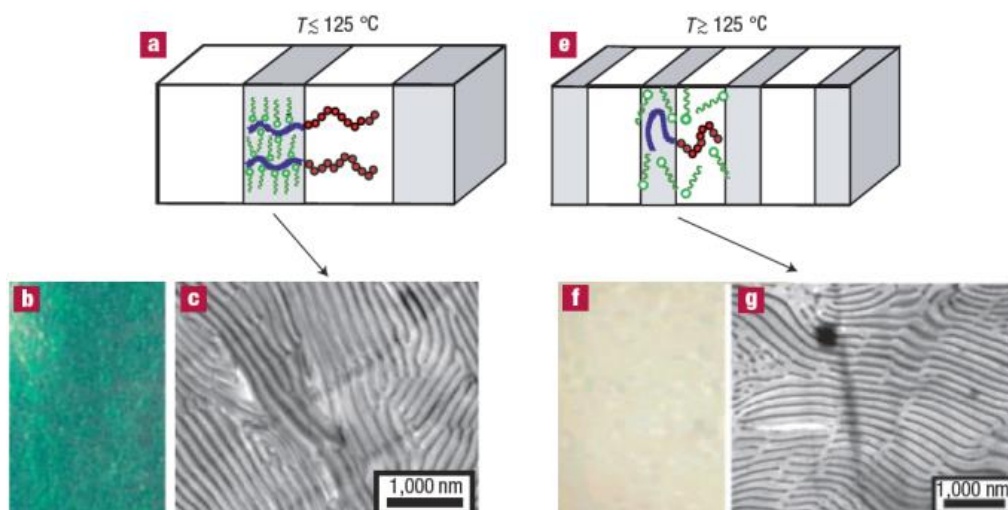


Figure 1-3. Poly(styrene)-*block*-poly(4-vinyl pyridine) (PS-*b*-P4VP) quaternised with methanesulfonic acid. Below 125 °C, 3-*n*-pentadecylphneol (PDP) associates with the P4VP section swelling it (c) and exhibiting a strong green colour (b). Upon heating above 125 °C, hydrogen bonding is interrupted and the PDP distributes evenly throughout the system (g) and causes a loss of colour (f).⁸⁵

Alternatively, thermally controlled refractive index of the B layer has been shown to work with the addition of a liquid crystal.⁹¹ The layers between the polymer is impregnated with a liquid crystal and upon heating, the refractive index of the central LC layer (layer B) between polymer (layers A) changes.⁹¹ The change in refractive index leads to differing distance the light has to travel between the polymeric layers without increasing the distance between the A layers.

Whilst these systems exhibit highly tuneable and multiple colour changes, some major drawbacks for wide scale use occur. Very high M_n polymers ($> 300,000 \text{ g}\cdot\text{mol}^{-1}$) with low \bar{D} (< 1.2) are required to form ordered

structures where the gap between layers is large enough for Bragg reflection of visible light.^{81,92} For solid state polymer systems, high temperatures (> 120 °C) are needed to cause localised swelling between polymeric layers.⁸⁵ Other systems require the addition of polymer specific solvent to cause swelling of one layer only.^{76,82} For efficient thermochromic PBC's, further nanomaterial additives are required to increase the refractive index difference, increasing the overall cost of the system.⁹² Lastly, phase separation of the PBCs is always required for the system to show any chromic abilities which is done *via* annealing at high temperatures (> 100 °C) or casting from a solvent (drop cast or spin coating).^{79,86–88,93} Due to this, encapsulation of the material for pigmentation use becomes impossible. Whilst it does allow for direct application of PBC onto substrate, it cannot currently be done on large scale.

1.2.2 Type II

The optical change of type II thermochromic materials originates from light defraction with colloidal material and can be differentiated into two subsections. These two subsections are colloidal crystal arrays (**Section 1.2.2.1**) and colloids formed by phase separation (**Section 1.2.2.2**).

1.2.2.1 Colloidal Crystal arrays

Colloidal crystal arrays (CCAs) make up the first subsection of type II thermochromic materials. CCAs are colloidal matter which forms a 3D structure by regularly arranging colloidal particles with low dispersity.^{94–96}

The most common colloids geometry used to form the arrays are spherical due to the ease of synthesis. Using spherical particles, both non-close-packed and close-packed CCAs can be formed using either normal evaporation of solvent or a template made *via* lithography.⁹⁷⁻¹⁰⁰ Large scale CCAs are complex to form though an effective method for creating them on a 2 cm by 2 cm scale has been shown.¹⁰¹⁻¹⁰³ It was found that continuous sonication was the key parameter to allow the colloids to be placed within a lattice site where the thermodynamic minimum existed.^{101,103} This periodic arrangement of colloids causes Bragg reflections similar to that shown in PBC and **Equation 1-2**. However, the spacing between planes needs to be redefined due to the 3D network. When combined with Snell's law the reflected wavelength is formulated by **Equation 1-3**.¹⁰⁴

$$m\lambda_{ref} = \sqrt{\frac{8}{3}}D \left(\sum_j n_j^2 V_j - \sin \theta \right) \quad \mathbf{1-3}$$

where m is an integer for the order of diffraction, λ_{ref} is the first order diffracted light, D is the centre-to-centre distance between the colloids, θ angle between incident light and the sample, n_j the refractive index of j , and V_j the volume fraction of j .

Pioneering work undertaken by Asher *et al.* demonstrated two methods to thermally change the colour of a CCA.¹⁰⁵ Firstly, poly(*n*-isopropyl acrylamide) (PNIPAM) colloids were synthesised *via* dispersion polymerisation at 70 °C.^{106,107} The reaction was required to be undertaken at 70 °C to result in collapsed colloidal spheres.¹⁰⁵ A noticeable volume change

was observed with the spherical diameter of ~ 300 nm at 10°C to ~ 100 nm at 40°C . The particles were left in deionised water to form a CCA. At low temperatures ($< 25^\circ\text{C}$) the CCA weakly diffracts light. Upon raising the temperature to 40°C , the swollen colloids expel the water molecules (**Figure 1-4 a**) causing a contraction of the particles and, in turn, changing the sphere scattering cross section of the colloids.¹⁰⁵ As the crystal lattice spacing only alters by 1 nm, this spacing is not the reason for light diffraction. In contrast, light diffraction is caused by the change in refractive index following the expulsion of the water molecules.¹⁰⁵ However, the described method only shows a change in diffraction intensity rather than a change of colour with temperature.¹⁰⁵ Similar results were seen using NIPAM-*co*-acrylic acid (AA) to form charged NIPAM colloids.¹⁰⁸ An issues that arises with this system is the time needed to equilibrate the system into the CCA. Upon heating above 32°C , the CCA becomes disrupted. Upon cooling, it takes ~ 160 minutes to reform the initial CCA.¹⁰⁹

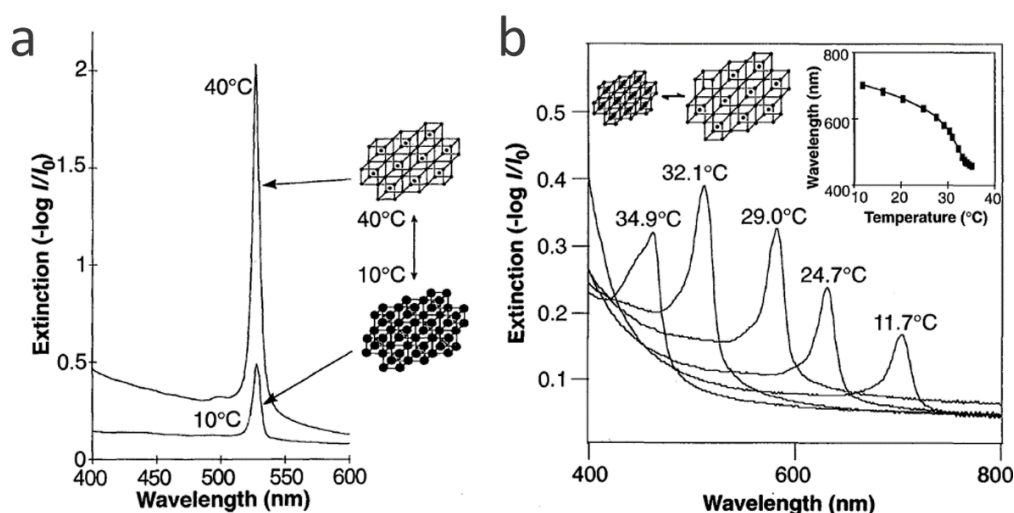


Figure 1-4. a) Diffraction from the PNIPAM sphere CCA at 10 °C and 40 °C. Insert represents the switching between swollen spherical arrays below phase transition and identical though compacted array above transitional temperature. b) Diffraction from 125 μm CCA film of PS spheres embedded within a PNIPAM gel. The shift in peak is caused by temperature induced volume changes altering the lattice spacing. Inset top left represents the change in lattice spacing between high and low temperatures. Inset top right shows the temperature dependence of the diffracted wavelength from the CCA.¹⁰⁵

Asher and co-workers also demonstrated changing the distance between colloids within a polymer matrix.¹⁰⁵ They had previously shown an effective method to prepare a hydrogel matrix around a CCA to help lock the ordering in.^{110,111} This matrix was prepared by dispersing a negatively charged PS latex into an aqueous mixture containing NIPAM, *N,N'*-methylenebisacrylamide (MBAA) as a cross-linker, and 2,2-diethoxyacetophenone as a photoinitiator. In the following photo-induced polymerisation, the resulting NIPAM-based hydrogel contained a CCA film of

PS spheres, referred to as a PS in PNIPAM CCA (**Figure 1-4 b**).¹⁰⁵ By increasing the temperature, water is expelled from the PNIPAM matrix, shrinking the matrix, and forcing the colloids closer together. A reduction in spacing between the colloids leads to a blue shift in the colour observed. Upon cooling, the system swells and is returned to its original state. Changes in spacing between colloids lead to different light being diffracted. Unlike the PNIPAM CCA, the PS in PNIPAM CCA showed continuous colour change over a 25 °C range, which displays a major advantage over the previously described pure PNIPAM CCAs.¹¹² However, an issue in using this system for temperature indicator is the use of water. With a vapour pressure of 3.169 kPa at 25 °C, evaporation of water overtime at ambient conditions occurs which changes the system and its properties.¹¹³

Hu *et al.* expanded on the first system discovered by Asher and co-workers,¹⁰⁹ by preparing two charged copolymers, PNIPAM-co-Poly(2-hydroxyethyl acrylate(PHEA)) and PNIPAM-co-PAA and forming them separately into a CCA *via* electrostatic interactions and steric repulsion.^{105,106} As a cross-linker for the carboxylic acid groups present within the PNIPAM-co-PAA, epichlorohydrin was used, whereas the hydroxyl groups on HEA units were cross-linked divinylsulfone (DVS). In this context, it was important to test whether the DVS would not interrupt LCST behaviour of PNIPAM, which could be confirmed.¹¹⁴ Due to crosslinking, the arrays formed were solid in nature in contrast to the rather liquid systems shown by Asher. At room temperature, these CCAs present an intense green iridescences. Upon heating to 50 °C, the sample exhibits an opaque white colour. After cooling back to

room temperature, the green iridescences is once again obtained.¹⁰⁹ This system takes ~ 1000 times less time to reform the original CCA than the original system reported by Asher and coworkers.^{105,109} However, whilst these cross-linked systems do show quicker response to reduction in temperature, water is still needed in order to instigate the swelling.¹⁰⁴

Inverse CCA have long been known to also show the same Bragg reflection properties as normal opals.^{104,115,116} These can be found in nature within the *Lamprocyphus Augustus* beetle and *Parides Sesostris* butterfly.¹¹⁷⁻¹¹⁹ Inverse CCAs (also referred to as inverse opals) consist of a matrix in which voids are present in the place of colloidal particles.¹²⁰ Synthetic inverse opals are usually prepared using a CCA as the template, which is interpenetrated with a monomeric solution. After the following polymerisation, the colloid template is removed to give an inverse CCA.^{116,120}

Watanabe and Takeoka followed the initial work by Asher *et al.* and investigated the use of inverse CCAs.^{121,122} The thermochromic inverse opal was fabricated using 210 nm closest packed silica colloids as a template, which was later etched out.¹²³ Once the CCA had formed, a solution of NIPAM, MBAA, and benzoylperoxide (BPO) in dioxane was infiltrated into the crystal. After polymerisation, the silica was etched out hydrofluoric (HF) acid solution to give the desired inverse CCA structure whereby the voids left by removal of the SiO₂ spheres acted as the periodic arrangements.¹²² The photonic membrane still showed reversible chromic response with temperature cycles, indicating that the structure had remained intact with the removal of the

template colloids.¹²³ A diverse range of cross-linker concentrations at a constant temperature were tested to determine the effect on the colour (**Figure 1-5 a**). An increase in cross-linker led to lower swelling capabilities of the solution, resulting in a blue shift, whereas lower cross-linker concentrations led to high degrees in swelling of the total array, leading to a red shift in colour.¹²¹⁻¹²³ The array synthesised using [NIPAM]:[MBAA] = 30:1 formed an array that had great chromic responses over a temperature range of 15 °C (**Figure 1-5 b**).

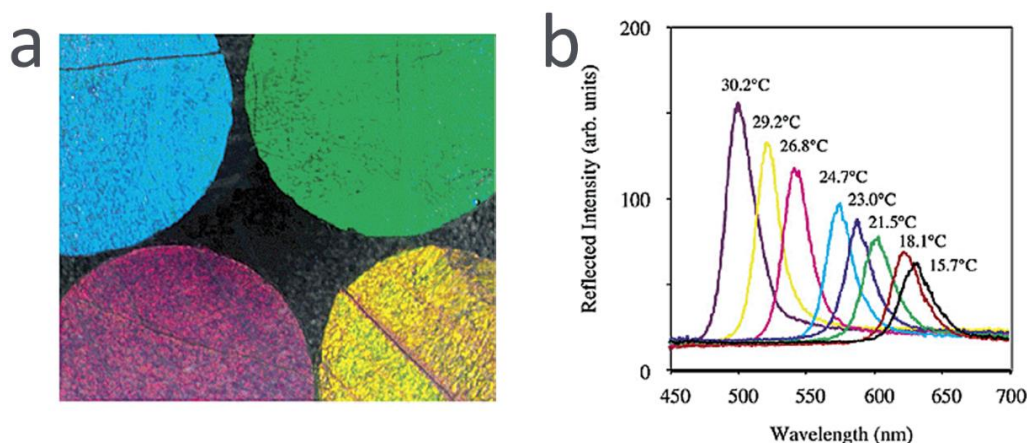


Figure 1-5. a) Photographs of porous PNIPAM inverse CCAs with differing cross-linker concentrations at 27.6 °C. Top left [NIPAM]:[MBAA] = 20:1, top right [NIPAM]:[MBAA] = 30:1, bottom left [NIPAM]:[MBAA] = 60:1, and bottom right [NIPAM]:[MBAA] = 100:1. b) reflection spectra of the PNIPAM porous hydrogel ([NIPAM]:[MBAA] = 30:1) at varying temperatures.¹²¹

Further work by Takeoda *et al.* investigate the effect of using a rigid inverse CCA with swellable particles.¹²³ The inverse CCA was formed using a similar technique as previously mentioned.¹²¹ First, a closest-packing colloidal

crystal of 210 nm silica colloids was formed that was then immersed in an organic mixture of styrene and BPO. After the polymerisation, the silica was removed with HF. The resulting PS inverse CCA was then subject to two different techniques. To start with, the PS frame was submerged into an aqueous solution of NIPAM, MBAA, and BPO and a redox polymerisation was conducted. From this composite, the next steps followed two different approaches. With the first, the PS framework was removed *via* flushing with toluene, ethanol, and water, which resulted in a standalone interconnected PNIPAM CCA. Upon heating in water, the particles decreased in volume, changing the lattice spacing and refractive index. A blue shift was observed in the reflected light (**Figure 1-6 a**). However, only a 6% change in refractive index was achieved, which indicates that the change in lattice parameter was the dominant change. In the second approach, the PS framework was not dissolved. The gel particles were separated by heating to 25 °C and using the collapse transition by effect of cononsolvency.^{124,125} This resulted in “trapped” swellable colloids within the PS framework. Each colloid is able to swell and contract irrespective of the others within the framework. Increasing the temperature showed a decrease in the reflection intensity (**Figure 1-6 b**), the inverse of which was observed within the work of Asher and co-workers.¹⁰⁵ The new proposed theory for the system is that as the particles decreasing in volume, the colloids would stick to the PS framework. Nevertheless, all colloids are independent of each other, each colloid is able to stick to different parts of the framework, forming a disordered array. As no periodic arrangement was present, a decrease in reflective intensity was observed.

Upon cooling, the colloids became swollen and occupied the volume of the pore again and, thus, restoring the order.

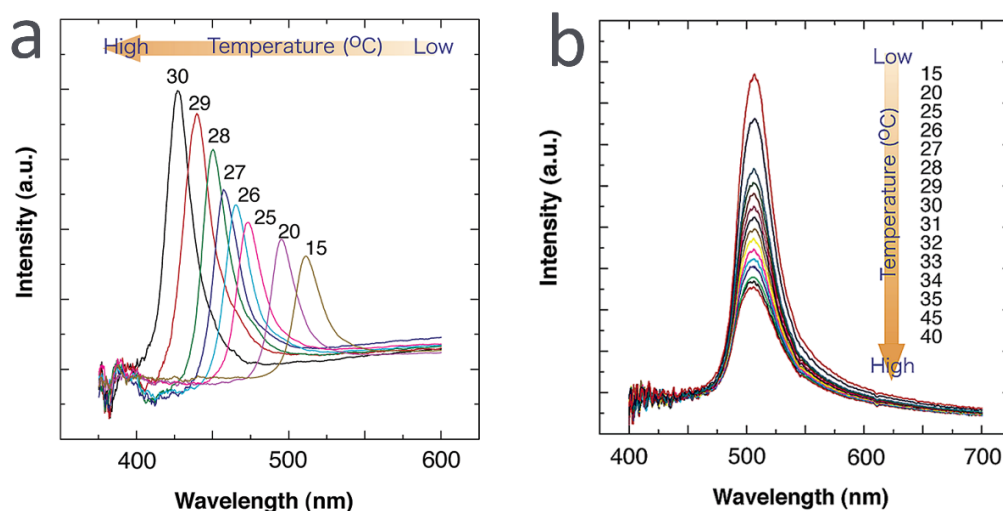


Figure 1-6. a) Reflection spectra of the interconnected gel particle array in water. An increase in temperature shows a blue shift in colour. b) Reflection spectra of swellable particles in PS inverse opal. An increase in temperature shows a decrease in the ability to reflected light.¹²³

Inverse CCA do show a great opportunity for use as a thermochromic temperature indicator. With the removal of the colloidal template, the film becomes more malleable and less susceptible to cracking.^{126,127} The systems show great tunability to temperature and other stimuli such as pH and molecule detection.^{104,128,129} However, an ever present water solvent is needed for the swelling. Easy incorporation into a binder is still impossible due to this issue.

Thermoresponsive CCA (both standard and inverse) show a possibility for thermochromic materials due to similar tunability and multiple colour

changes observed in PBCs. However, use as a temperature indicator becomes difficult. CCAs cannot be incorporated directly into film coatings due to penetration of the film upon drying, removing any change in periodic distance and, thus, the Bragg reflection capability. Encapsulation has been shown to be a possibility with reduction in reflected light intensity and multiple colours were observed due to multi-angle diffraction within the sphere.¹³⁰ The systems always require a constant solvent source. As the solvent (water) has a high vapour pressure, continuous replenishment would be required.

1.2.2.2 Colloids Formed by Phase Separation

Phase separation of solutions form the second subsection of type II thermochromic materials and show a great opportunity as thermochromic temperature indicators.^{131,132} When these systems undergo a phase separation event, a change in turbidity / opacity is induced. The change is caused by a difference in refractive index between the solvent and the precipitated molecules.^{133,134} An explanation for the theory behind phase separation is given in **Section 1.2.3**.

Smart polymers exhibit changes in solution due to external stimuli. These stimuli can be changes in pH,^{135,136} ion concentration,^{137,138} light irradiation,^{139,140} or temperature.¹⁴¹⁻¹⁴⁴ Temperature responsive polymers exhibit a volume transition upon reaching certain temperatures whereby the polymer shrinks in size due to the expulsion of solvent molecules.^{89,145,146} Systems that become homogenous upon heating possess an upper critical solution temperature (UCST),^{147,148} whereas systems that become

heterogeneous upon heating exhibit a lower critical solution temperature (LCST).¹⁴⁹ Some systems even show both types of transition temperatures, LCST and UCST.^{150,151} Certain lipid / water systems, such as phytantriol and glyceryl monooleate, also show a change in turbidity with increasing temperature.^{152–154} These phase transitions of both LCST / UCST polymers and lipid systems have shown potential for temperature dependent drug delivery.^{89,154–156} Phase transitions of polymers in solutions generally depend on the polymers architecture (linear, star, block etc.), polymer concentration, and the polymers molecular weight.^{157–160}

One of the most common polymers to exhibit an LCST in solution is PNIPAM, which has been first report in 1956,^{161,162} and was found to be an effective rodent repellent. Ever since, it has gained popularity due to its phase separation transition occurring around biologically relevant conditions ($\sim 32\text{ }^{\circ}\text{C}$).^{132,137} To dissolve PNIPAM in water, ordering of PNIPAM chains *via* efficient hydrogen bonding to the water molecules is required.^{132,163} As water is already an ordered system it must therefore reorientate around hydrophobic parts of the polymer chain. Upon heating, the hydrogen bonding between water molecules and polymer is disrupted, resulting in intramolecular hydrogen bonding between NIPAM units, loss of hydration shell, and an apparent “hydrophobic” polymer crashing out of solution. The first example published example of PNIPAM exhibiting an LCST transition in water was by Scarpa *et al.* in 1967.¹⁶³

Tagging PNIPAM chains with dye compounds have been shown to exhibit an increase in response upon phase separation.^{131,164,165} Françoise Winnik reported on the hydrophobic nature of PNIPAM above the LCST point by tagging PNIPAM chains with the fluorescent dye, pyrene (Py).¹⁶⁴ These polymers were dissolved in an aqueous solution containing the Py quenchers, nitromethane and ethylpyridinium bromide. At 25 °C, the Py excitation was quenched due to the full solubility of the PNIPAM within water and ease of access to the Py moiety by the quenching molecules. Upon heating above 33 °C, phase separation of the PNIPAM and water occurred causing the emission from Py to increase in the system with nitromethane present and was found to be fully emissive within the ethylpyridinium bromide solution. This increase was due to the hydrophobic Py moiety residing within the hydrophobic PNIPAM phase where the water soluble quenchers could not interact with the Py pendant groups.

Bergbreiter and co-workers used a PNIPAM-*c*-poly(*N*-acryloxy-4-amino-2,2,6,6-tetramethylpiperidine) (PNIPAM-*c*-PTMPAM) copolymer to show thermochromic changes within aqueous solutions *via* pH changes.¹⁶⁶ PNIPAM-*c*-PTMPAM was synthesised by polymerising NIPAM and *N*-acryloxysuccinimide as comonomers and reacting the succinimide group with 4-amino-2,2,6,6-tetramethylpiperidine. The resulting copolymer exhibited strong basic behaviour when dissolved in water. Upon heating above the LCST point, the phases separated and became white as expected.¹⁶⁶ With the addition of phenolphthalein, however, a colour change from pink to clear was observed (**Figure 1-7**). This was due to the fact that at low temperatures, the

homogeneous mixture is basic, indicated by the phenolphthalein fuchsia colour. Upon phase transitioning, the loss of hydration shell around the copolymer lowers the pH and leading to a loss in colour from phenolphthalein.¹⁶⁷ The solution exhibited the turbidity seen without presence of indicator upon heating and lowering the temperature showed the return of the characteristic pink colour.¹⁶⁷

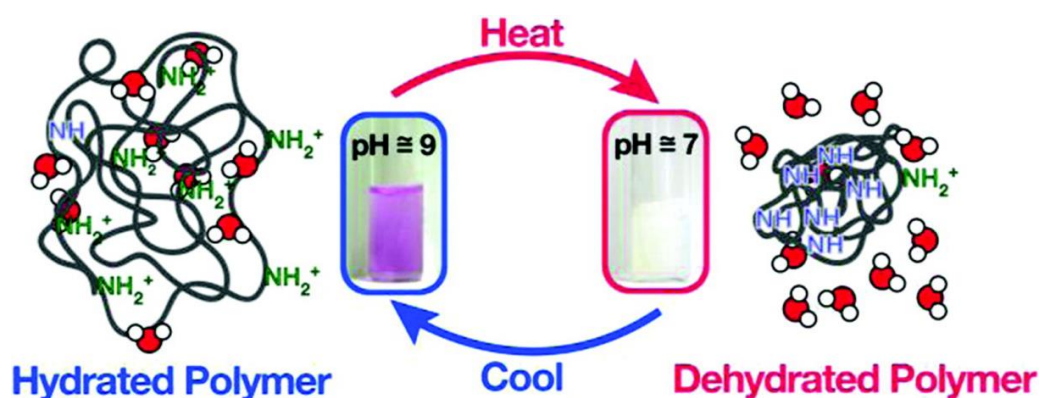


Figure 1-7. Left) depiction of protonated PNIPAM-*c*-PTMPAM chains with water molecules hydrogen bonded to it. Middle) colour change upon heating aqueous PNIPAM-*c*-PTMPAM with phenolphthalein indicator present. At low temperatures the system is basic and phenolphthalein shows a strong fuchsia colour. Upon loss of hydration shell from PNIPAM-*c*-PTMPAM at high temperature, the solution becomes acidic causing colour to be lost. Right) depiction of deprotonated PNIPAM-*c*-PTMPAM chains leading to a lowering in pH.¹⁶⁶

The tuning of phase transition temperatures has further been shown in ethylene glycol based polymers,^{168–170} oxazoline based polymers,^{171,172} NIPAM based polymers,^{173,174} as well as others types of polymers.^{157,158,175} Some

polymers that exhibit UCST-like phase transitions have been shown to switch to LCST-like transitions upon esterification of side groups.¹⁷⁶ Rieger and co-workers investigated the effect on phase transition temperature, and the hysteresis of the system with vinyl phosphate copolymers.¹⁷⁷ Statistical copolymerisation of dimethyl, diethyl and di-*n*-propyl vinyl phosphate (DMVP, DEVP, and DPVP respectively) was undertaken using rare earth metal-mediated group transfer polymerisation.¹⁷⁵ A homopolymer of PDEVP exhibits a phase change at 42 °C. Incorporation of DPVP with increasing concentrations showed a decrease in phase transition temperature, which is caused by the hydrophobic nature of the DPVP's propyl pendant moieties.¹⁷⁵ Incorporation of DMVP increased the phase transition point. The methyl groups in DMVP exhibit a lower hydrophobicity than the ethyl moieties of DEVP, which reduces the hydrophobic interactions within water (**Figure 1-8**). Hysteresis of the system was tested using varying heating and cooling rates. PNIPAM has shown hysteresis in phase transition within aqueous media due to time needed to reorientate water molecules around the uncoiling PNIPAM chain.¹⁷⁸ Inter and intramolecular hydrogen bonding is present within the collapsed state of PNIPAM acting as crosslinking sites. Upon cooling, the chains initially swell with water before becoming fully soluble again. In contrast, PDEVP copolymers form hydrogen bonding with water molecules and cannot form them between chains, which reduces hysteresis.¹⁷⁸ As an example, heating at 40 °C / min showed a hysteresis of only 1.5 °C.

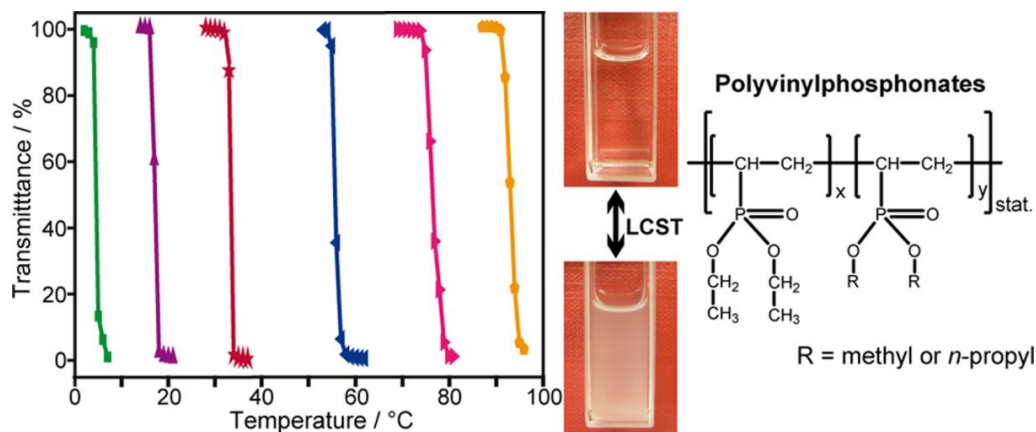


Figure 1-8. Phase transition curves of (left to right) P(DEVP_{0.51}-*c*-DPVP_{0.49}), P(DEVP_{0.69}-*c*-DPVP_{0.31}), P(DEVP_{0.89}-*c*-DPVP_{0.11}), P(DMVP_{0.22}-*c*-DEVP_{0.78}), P(DMVP_{0.4}-*c*-DEVP_{0.6}), and P(DMVP_{0.59}-*c*-DEVP_{0.41}). Photograph of turbidity difference between homogeneous and heterogeneous phases with chemical structure of the polymers synthesised.¹⁷⁵

Certain polymeric solutions exhibit both LCST and UCST transitions with several OH-functional copolymers showing LCST < UCST behaviour depending on compositions.^{179–181} Furthermore, copolymers of zwitterionic sulfopropylbetaine methacrylate exhibit UCST < LCST behaviour.^{182–184} Käfer *et al.* demonstrated a rare case of non-hydroxyl and non-ionic polymers showing both UCST and LCST.¹⁸⁵ Copolymers of poly(ethylene glycol) (PEG) and poly(acrylamide-*c*-acrylonitrile) (PAMcAN) were synthesised randomly *via* free radical polymerisation with a PEG macro-azoinitiator. The homopolymer of PAMcAN exhibits UCST behaviour in water at 56 °C (M_n 37,200 g·mol⁻¹ and \bar{D} 2.92).¹⁸⁶ The addition of a PEG block to the copolymer led to a multiphase system occurring with changes in temperature. Firstly, increasing the PEG chain length showed an increase in water solubility

with M_n 2000 g·mol⁻¹ exhibiting an LCST-like transition at 50 °C and a UCST-like transition at 68 °C. Further increasing the length of PEG chain to 6000 g·mol⁻¹ led to a loss of all transitions occurring due to high hydrophilicity. With an increase in the concentration of AN within the polymer, a raise in both the LCST and UCST type transition temperature occurred. Polymers containing 7 mol% AN exhibited a phase change (LCST-like) at 13 °C with a return to homogeneous state (UCST-like phase change) upon heating to 23 °C. Increasing to 12 mol% AN, the LCST phase change occurred at 50 °C and returned to a single phase at 68 °C. The two-in-one phase transition behaviour was attributed to morphology changes. At low temperatures, micelles were observed which formed aggregates upon heating, whilst further heating led to separation and micelles reforming. An increase in molecular weight may have shown some difference, however not enough results were obtained to show direct correlation between M_n and phase transition temperature.

Polymer solution phase separation offers a great avenue of research towards synthesising thermochromic system. Work undertaken at MIT has even looked into the creation of white, heat reflective tiles triggering upon heating where PNIPAM in water was trapped between acrylic layers.¹⁸⁷ However, much work in the area of LCST and UCST has recently focused on biologically relevant systems (water based) and temperatures (~ 32 °C). The temperature range we are interested in (-10 °C - +10 °C) would not work for

many of these system, especially using water as a solvent due to its melting point (0 °C).

1.2.3 Polymer Solution Phase Separation

In this section, the theory behind the Flory –Huggins lattice model will be explained with regards to binary polymer solutions.¹⁸⁸ Further explanation of binary systems consisting of molecule solutions or polymer blends can be found in chapter 4 of Polymer Physics by Colby and Rubinstein.¹⁸⁹ Binary polymer solutions contain only two components: the polymer and the solvent used to dissolve it. Homogenous systems are where a uniform mixture is obtained with all components intermixed. If one or more phases are present, the system is then referred to as heterogeneous. Entropy and energy changes of mixing determine whether the equilibrium state is homo- or heterogeneous.

1.2.3.1 Binary Mixing – Entropy

When mixing two species, A and B, it is assumed there is no change in volume. In this case, A is a polymer and B is the solvent. If volume of A (V_A) is mixed with a volume of B (V_B) the total volume is therefore $V_A + V_B$. The volume fraction of the two components in a binary mixture is stated in **Equation 1-4**.

$$\phi_A = \frac{V_A}{V_A + V_B} \text{ and } \phi_B = \frac{V_B}{V_A + V_B} = 1 - \phi_A \quad \mathbf{1-4}$$

Where ϕ_A and ϕ_B are the volume fractions of species A and B respectively. For ease of comprehension, ϕ_A shall be referred to as simply ϕ henceforth.

The volume of each lattice site, v_0 , is defined by the smallest unit (in this case B), with large polymer molecules (A) occupying multiple connected lattice sites. A single polymer chain of A has the volume

$$v_A = N_A v_0 \quad 1-5$$

N_A is the number of lattice sites occupied by an A chain.

whilst a molecule of species B has molecule volume of

$$v_B = N_B v_0 = v_0. \quad 1-6$$

N_B is the number of lattice sites occupied by B.

In a regular solution, low molar mass species are present where $N_A = N_B = 1$. In a polymer solution, polymer chains occupy multiple sites ($N_A \gg 1$) whilst the solvent molecule occupies only 1 ($N_B = 1$). The total number of lattice sites (n) occupied upon mixing is therefore defined as

$$n = \frac{V_A + V_B}{v_0} \quad 1-7$$

and a single polymer chain occupies

$$\frac{V_A}{v_0} = n\phi \quad 1-8$$

lattice sites.

Entropy for a system is determined by the natural logarithm of the number of ways the molecules can arrange themselves within the lattice (Ω). The number of arrangements before mixing (Ω_A) is equal to the number of lattice sites occupied upon mixing.

$$\Omega_A = n\phi \quad \mathbf{1-9}$$

Therefore for a single polymer chain, the entropy of mixing is

$$\begin{aligned} \Delta S_A &= k \ln \Omega_{AB} - k \ln \Omega_A = k \ln \left(\frac{\Omega_{AB}}{\Omega_A} \right) \quad \mathbf{1-10} \\ &= k \ln \left(\frac{1}{\phi} \right) = -k \ln \phi . \end{aligned}$$

As the volume fraction is less than 1 ($\phi < 1$), the entropy change post mixing will always be positive. **Equation 1-10** accounts for the entropy of species A with a similar equation for species B. Contributions for each molecule in the system must be summed to calculate the total entropy of mixing.

$$\Delta S_{mix} = n_A \Delta S_A + n_B \Delta S_B = -k[n_A \ln \phi + n_B \ln(1 - \phi)]. \quad \mathbf{1-11}$$

The entropy of mixing per lattice site ($\Delta \bar{S}_{mix}$) is defined as $\Delta S_{mix}/n$. For a polymer solution, this can be stated as

$$\Delta \bar{S}_{mix} = -k \left(\frac{\phi}{N} \ln \phi + [1 - \phi] \ln[1 - \phi] \right). \quad \mathbf{1-12}$$

Using **Equation 1-12** to determine entropy of mixing of both regular solution and polymer solutions shows a large difference. Using $\phi = 0.6$, in a regular solution $\Delta \bar{S}_{mix}/k = 0.67$ as $N = 1$. In comparison, within polymer

solutions N is typically large, negating the first term. Therefore $\Delta\bar{S}_{mix}/k = 0.36$. Entropy of mixing is always positive and, consequently, always promotes mixing.

Ideal mixtures are mixtures where no difference in interaction energy between components is present. Free energy of mixing for an ideal mixture is purely entropic in nature. Due to this, ideal mixtures are consistently homogenous. The free energy of mixing can be stated as

$$\Delta\bar{F}_{mix} = -T\Delta\bar{S}_{mix} = kT \left[\frac{\phi}{N} \ln \phi + (1 - \phi) \ln(1 - \phi) \right]. \quad \mathbf{1-13}$$

In calculating the entropy of a polymer solution, the assumption of no volume change is made. However, many solution containing polymers have an excluded volume that changes the possible conformations of the polymer in solution. As well as this, polymer solutions do have very small volume changes when mixing occurs.

1.2.3.2 Binary Mixing – Energy

Energy of mixing can be either positive (opposing mixing) or negative (promoting mixing). A mean field approach is employed to determine the energy of the system. The energy of mixing can be defined by 3 pairs of interaction; species A with A (u_{AA}), species A with B (u_{AB}), and B with B (u_{BB}). Before mixing, species A and B are in there pure state, allowing only interaction between the same species. The total energy of both species before mixing (U_0) is defined as

$$U_0 = \frac{zn}{2} [u_{AA}\phi + u_{BB}(1 - \phi)] \quad \mathbf{1-14}$$

where z is the coordination number of the lattice.

The total energy of the mixture can be calculated by summing all the interactions between each molecule. As each interaction is a pairwise interaction, the overall energy must be halved. This is due to all molecules being counted twice. The energy of the mixture can be calculated as

$$U = \frac{zn}{2} ([u_{AA}\phi + u_{AB}\{1 - \phi\}]\phi + [u_{AB}\phi + u_{BB}\{1 - \phi\}]\{1 - \phi\})$$

$$U = \frac{zn}{2} (u_{AA}\phi^2 + 2u_{AB}\phi[1 - \phi] + u_{BB}[1 - \phi]^2). \quad \mathbf{1-15}$$

The energy change of the system upon mixing is **Equation 1-14 - Equation 1-15**.

$$U - U_0 = \frac{zn}{2} \phi(1 - \phi)(2u_{AB} - u_{AA} - u_{BB}) \quad \mathbf{1-16}$$

To calculate the energy change per mixing site (\bar{U}_{mix}), **Equation 1-16** is divided by n . Further simplification of **Equation 1-16** can be made with the introduction of the Flory interaction parameter, χ . χ measures the differences in pairwise interaction energy strengths between the species within a mixture.

$$\chi \equiv \frac{z}{2} \frac{(2u_{AB} - u_{AA} - u_{BB})}{kT} \quad 1-17$$

Therefore, the energy of mixing per lattice site can be stated as

$$\Delta \bar{U}_{mix} = \chi \phi (1 - \phi) kT. \quad 1-18$$

Equation 1-18 is therefore the mean-field description of all binary regular mixtures. One main assumption made within this energy calculation is that polymer chains are calculated as segments of the chain rather than the whole.

Combining the energy of mixing per site (**Equation 1-18**) with the entropy of mixing per site of a polymer solution (**Equation 1-13**) leads us to the Flory – Huggins equation for polymer solutions.

$$\begin{aligned} \Delta \bar{F}_{mix} &= \Delta \bar{U}_{mix} - T \Delta \bar{S}_{mix} \\ &= kT \left[\frac{\phi}{N} \ln \phi + (1 - \phi) \ln(1 - \phi) + \chi \phi (1 - \phi) \right] \end{aligned} \quad 1-19$$

The entropic terms within **Equation 1-19** (the first two) always act to promote mixing. Longer polymer chains have larger N values often leading to the first entropic term having little overall impact. The third term is the energetic in origin. Depending on the sign of χ , these can be negative (promote mixing), neutral (ideal mixture) or positive (oppose mixing). If there is a net attraction between polymer and solvent, $\chi < 0$, therefore mixing is favourable. Usually a net repulsion is present as species tend towards

interacting with similar rather than other species. In this case, $\chi > 0$ leads to an unfavourable energy for mixing.

As stated before, the Flory – Huggins theory assumes no volume change occurs upon mixing and both species can fit on sites of the same lattice. In real cases, polymers can often pack closer or further away within a solvent. Due to these volume changes, a temperature independent constant is added to the Flory interaction parameter.

$$\chi(T) \cong A + \frac{B}{T} \quad \mathbf{1-20}$$

The terms A and B within **Equation 1-20** are not to be mistaken as species A and B . A is temperature independent and referred to as the entropic part. B/T is temperature dependent and referred to as the enthalpic part. Any deviation from the lattice model is held within the interaction parameter. χ is able to display convoluted dependencies on temperature, chain length, and composition where large amount of work over the years since its inception has gone into determining A and B values for a wide variety of polymers and polymer/solvents mixtures.¹⁹⁰

1.2.3.3 Phase Separation

Phase diagrams can be constructed to display the behaviour of mixtures as they show the mixtures regions of stability, metastability, and instability.

This can only be done when the temperature dependence of the free energy of mixing is accounted for.

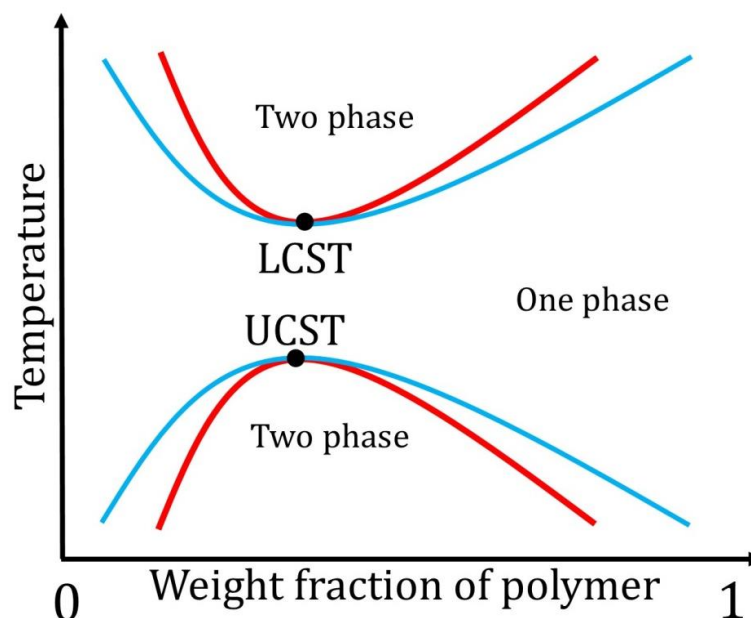


Figure 1-9. Phase diagram of a polymer solution containing both an LCST and an UCST. — is the coexistence/binodal curve and — is the spinodal curve.

Phase diagrams often show two curves within them. These are the binodal (blue in **Figure 1-9**) and spinodal curves (red in **Figure 1-9**). The binodal curve denotes the coexistence curve. Outside of this curve only one phase exists, inside the phases are metastable. Small changes in composition or temperature do not force phase separation to occur. However, the spinodal curve depicts the area in which spontaneous phase separation occurs.

The interaction parameter can be solved for the binodal line to give

$$\chi_b = \frac{1}{2\phi - 1} \left(\frac{\ln \phi}{N} - \ln[1 - \phi] \right) = \frac{\ln \left(\frac{\phi}{(1 - \phi)} \right)}{(2\phi - 1)N}. \quad 1-21$$

Equation 1-21 can then be combined with **Equation 1-20** to determine the binodal curve with regards to temperature and composition (**Figure 1-9**).

$$T_b = \frac{B}{\ln \left[\frac{\phi}{(1 - \phi)} \right] - A} \quad 1-22$$

The spinodal curve can also be defined for a polymer solution by the interaction parameter to give

$$\chi_s = \frac{1}{2} \left(\frac{1}{N\phi} + \frac{1}{1 - \phi} \right). \quad 1-23$$

Similar to χ_b , χ_s can be transformed into a temperature and composition curve by combining with **Equation 1-20**.

$$T_s = \frac{2B}{\left[\frac{1}{N\phi} + \frac{1}{1 - \phi} \right] - A}. \quad 1-24$$

The critical point is where the spinodal and binodal curves meet. The critical interaction parameter (**Equation 1-25**)

$$\chi_c = \frac{1}{2} \frac{(\sqrt{N} + 1)^2}{N} = \frac{1}{2} \left(\frac{1}{\sqrt{N}} + 1 \right)^2. \quad 1-25$$

Using the χ_c , the critical temperature, T_c , can be determined by utilising **Equation 1-20**.

$$T_c = \frac{B}{\chi_c - A} = \frac{2B}{\left(\frac{1}{\sqrt{N}} + 1\right)^2 - A} \quad \mathbf{1-26}$$

Polymer solution phase diagrams are strongly asymmetric due to the size difference between polymer and solvent molecules. When $\chi < \chi_c$, the mixture is homogeneous and stable at all compositions. When χ exceeds χ_c , the mixture is always within the miscibility gap and phase separation will occur.

UCST curves occur when $B > 0$ in **Equation 1-20**. In this case, χ decreases as the temperature is raised. When $T > T_c$, the homogeneous mixture is stable. As T is lowered below T_c , the homogeneous mixture becomes unstable and phase separation occurs. Conversely, if $B < 0$, χ increases as the temperature is raised. This gives rise to LCST curves. If $T > T_c$ the polymer phase separates out. It should be noted that the lattice theory does not take into account interactions such as hydrogen bonding between solvent and polymers and, therefore, some calculations may be imprecise.^{191,192}

1.2.4 Polymers Exhibiting UCST

Polymers exhibiting UCST-like phase transitions have recently garnered less interest than those that exhibit LCST-like behaviour.¹⁹³ It is thought to be

due to the cloud point found in polymers exhibiting LCST-like transitions are less effected by M_w than polymers exhibiting UCST.^{194,195} In all cases where these phase transitions occur, the measuring of cloud points raises a series of difficulties. Various researchers define the cloud point in various ways. Some note the appearance of the first cloudiness,^{179,196} some a drop in transmittance of $\sim 10\%$,¹⁹⁷ others take the cloud point as 50 % of the transition, whilst some use the inflection point of the turbidity curve. Some of the first work used personal optical inspection for the cloud point, leading to varied results being recorded.^{198,199}

In more recent years, many polymers exhibiting UCST like transitions in aqueous media have been reported.^{148,200,201} Whilst many papers show the phase change curves of polymer solutions, often full or partial phase diagrams are not reported and, therefore, neither is the UCST point. Polymers containing zwitterionic betaine moiety are among the most popular for exhibiting UCST in water with 0 – 100 °C range.^{150,184,202–206} Poly(3-dimethyl(methacryloyloxyethyl) ammonium propane sulphate (PSPE)^{202,203} and poly(3-[*N*-(3-methacrylamidopropyl)-*N,N*-dimethyl]ammoniopropane sulfonate (PSPP)²⁰⁴ (**Figure 1-10**) are among the only betaine polymers with full phase diagrams reported.

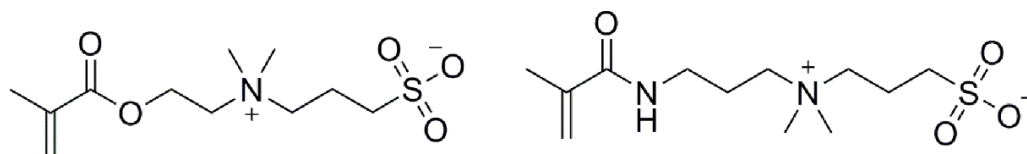


Figure 1-10. Chemical structures of (left) SPE and (right) SPP.

PDMAPS exhibits an unusual dumbbell shaped phase diagram at $436,000 \text{ g}\cdot\text{mol}^{-1}$. At 0.1 wt% a UCST point is seen at 32°C with a decrease to 15°C at 8 wt%. Upon increasing wt%, the phase change temperature once again increase to 25°C at 25 wt%. As expected, an increase in the M_W alters the UCST point. Huglin and Radwan reported M_W of 215,000, 620,000, 1,090,000 1,520,000, and 2,070,000 $\text{g}\cdot\text{mol}^{-1}$ exhibiting UCST at 22, 28, 30, 30.5, and 31.5°C respectively.²⁰³ Roth *et al.* demonstrated a click method to attach sulfobetaine pendant groups to both poly(pentafluorostyrene) and poly(2-vinyl-4,4-dimethylazlactone) main chains.^{150,184} By increasing the sulfobetaine content and reducing the benzylacrylamide content, the phase change curves' temperature could be altered.¹⁵⁰ It was also noted that increasing the salt concentration of the system lowered the phase transition temperature. Addition of salts to the aqueous solutions disturbs the intra and intermolecular interactions, which is done by decreasing the Debye length (Equation 1-27).

$$l_D = \sqrt{4\pi \cdot l_B \cdot c_S} \quad 1-27$$

Where l_B is the Bjerrum length in pure water and c_s is the salt concentration added.

The Debye length is the distance at which the opposite charges “sense” each other. Therefore addition of salt enhances the polymers solubility and lowers the UCST.²⁰³

Whilst certain polymeric chains exhibit UCST behaviour within aqueous conditions, similar to systems exhibiting LCST behaviour, low temperatures cannot be reached due to restrictions imposed by the solvent. Reproduction of the values obtained can also prove difficult due to the strong effect pH and ion concentration within water can have on the UCST point.²⁰⁴

Polystyrene is one of the most widely studied polymers that exhibit UCST in hydrocarbon solvents.^{207–209} Some of the more well studied solvent/PS systems UCST points are shown in **Figure 1-11**. M_w of PS has a large impact on the UCST point in methyl acetate systems.^{198,207,210} The lowest molecule weight report (2,200 g·mol⁻¹) exhibited an UCST point at -59 °C. Increasing the M_w to 37,000 g·mol⁻¹ showed an increase in the UCST to -7 °C. Further increases in M_w to 860,000 g·mol⁻¹ and 2,700,000 g·mol⁻¹ so an increase to 25 °C and 37 °C respectively. This is expected as the polymer chains will occupy more lattice sites within the system (**Equation 1-5**). Saeki *et al.* and Zeman *et al.* both studied a PS M_w 670,000 g·mol⁻¹ in methylacetate. A temperature discrepancy of 5 °C can be seen between the results of both. The difference here could be due to cloud points being optically determined rather than use of additional equipment.

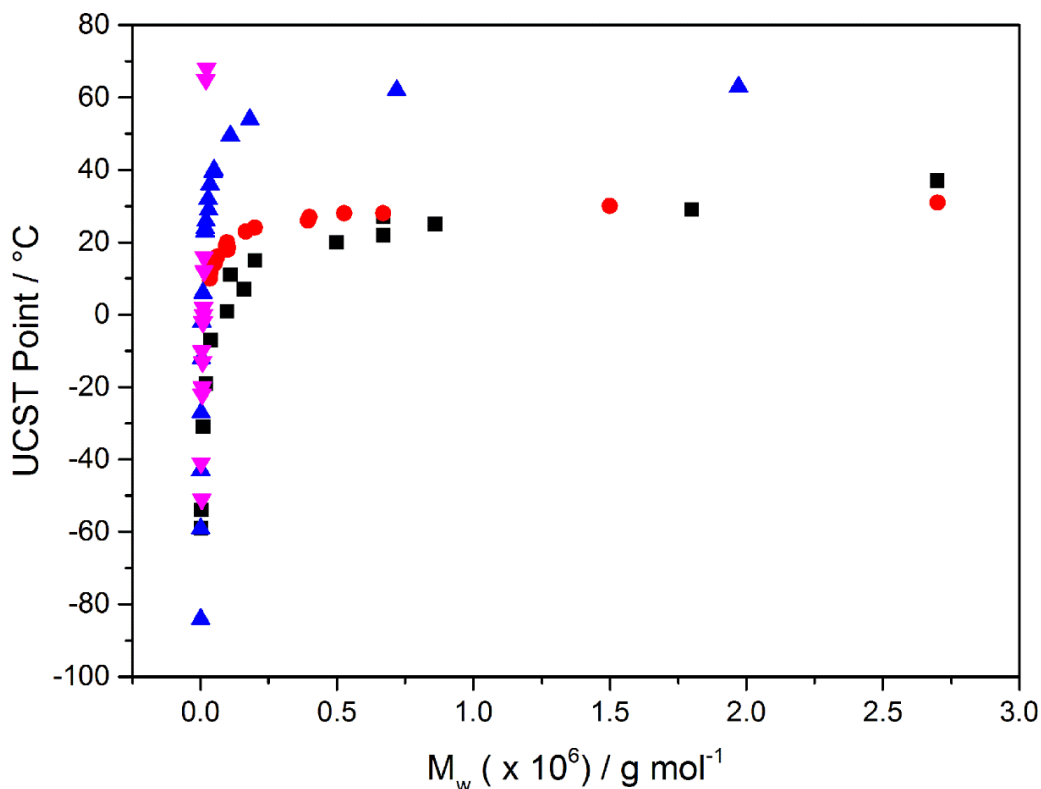


Figure 1-11. Effect of M_w of PS in methyl acetate (■), cyclohexane (●), methyl cyclohexane (▲), and acetone (▼). Data taken from references.^{198,199,207,210-220}

All examples of polystyrene shown in **Figure 1-11** show the trend where slight increases (eg $2000 \text{ g}\cdot\text{mol}^{-1}$) of low molecular weight polymers ($< 200,000 \text{ g}\cdot\text{mol}^{-1}$) resulting in large changes in UCST point of the system. Polystyrene in both acetone and methyl cyclohexane show the greatest changes in UCST point with these small changes. Unlike low molecular weight polymers, further increases in M_w ($>300,000 \text{ g}\cdot\text{mol}^{-1}$) results in the UCST point start to plateau with increasing molecular weight. This change in response can be linked back to **Equation 1.5**. An increase in M_w increases the number of lattice sites a polymer occupies. A low molecular weight polymer doubling

in size increases the number of sites that the polymer occupies within the system drastically. However, when applying to larger molecular weight polymers, increases of double molecular weight take up a much smaller portion of the remaining sites remaining in the system.

A less dramatic change in UCST appears within cyclohexane solutions.²¹¹⁻²¹⁴ A change of only 20 °C is seen from 35,400 g·mol⁻¹ to 2,700,000 g·mol⁻¹ (10 °C and 31 °C respectively). A less pronounced effect is also seen at 1,500,000 g·mol⁻¹ which is only 30 °C, 1 °C less than nearly double its molecular weight. Scholte and co-workers also investigated the effect of dispersity on the UCST point. Three PS samples with M_w 100,000 g·mol⁻¹ were chosen. It was found that dispersity had little effect on the overall UCST point. \bar{D} 1.43, \bar{D} 2.63, and \bar{D} 4.62 had UCST points at 18 °C, 18.5 °C, and 19 °C respectively. Strazielle et al. determined that the deuteration of cyclohexane also had a slight effect on PS's UCST.²²¹ PS of M_w 625,000 g·mol⁻¹ in deuterated cyclohexane had its UCST point at 31 °C and M_w 310,000 g·mol⁻¹ at 29 °C. In comparison to 670,000 g·mol⁻¹ at 28 °C and 394,000 g·mol⁻¹ at 26 °C, there is a clear increase in UCST temperature of ~3 °C.

Work on methylcyclohexane PS systems by Imre and co-workers,²¹⁵ Dobashi and co-workers,^{216,217} and Vanhee and co-workers²²² shows the same trend in increase UCST with M_w . A large difference in UCST between similar M_w PS in cyclohexane and methylcyclohexane was observed. The difference is as large as 30.5 °C between 100,000 g·mol⁻¹ in cyclohexane and 109,000 g·mol⁻¹ in methylcyclohexane.

Lastly, acetone exhibited the same increase in UCST with M_w .^{199,218-220} Surprisingly, a large change in UCST point was seen between 2,510 g·mol⁻¹ and 22,900 g·mol⁻¹. The UCST point changed from - 41 °C to 68 °C. Upon using deuterated acetone, a large change was also observed.^{218,219} UCST PS with M_w 5,770 g·mol⁻¹ in acetone was found to be -22 °C. Changing to deuterated acetone resulted in an increase to - 3 °C. The most dramatic change was observed by Szydlowski et al. 11,500 g·mol⁻¹ PS in acetone exhibited a UCST at 0 °C. The same sample in acetone-d₆ exhibited a UCST at 17 °C. Whilst the deuterated acetone exhibited a more pronounced effect on UCST than cyclohexane, this could stem from difference in M_w . Only large M_w were investigated in cyclohexane whilst acetone systems were < 14,000 g·mol⁻¹.

These systems show a broad range of possible phase change temperatures depending on solvents chosen. M_w plays an important role in the temperature at which phase change occurs which can be related back to **Equation 1-5**. Increasing M_w leads to an increase in lattice sites that the polymer occupies. All solvents shown above possess high vapour pressures leading to high evaporation rates (cyclohexane 13.3 kPa, methylacetate 22 kPa, methyl cyclohexane 4.9 kPa, and acetone 24.5 kPa).¹¹³

In order to obtain a system where the solvent had a low vapour pressure, we looked into using dioctyl phthalate (DOP) as our chosen solvent system. As DOP has both a low vapour pressure (8.6×10^{-4} Pa at 24 °C)²²³ and melting point (- 50 °C)²²⁴ it had the potential to offer us the largest temperature range in which the phase transition could occur. Both Ver Strate

and Philippoff, and Rangel-Nafaile and co-workers independently demonstrated that solutions of PS dissolved in DOP phase separates with temperatures between 6 and 10 °C depending on the M_W of the PS chosen. It was also reported that when the systems were put under shear pressure *via* flowing through small capillaries, and increase in UCST occurred.^{196,225–227}

1.2.5 Encapsulation

Encapsulation is an important step in the creation of a thermochromic particle. Without a protective barrier layer separating the internal oil from the binder system the particles are dispersed within, the oil would simple diffuse through the system and lose any thermochromic behaviour. Multiple methods have been shown to encapsulate oils: spray drying, freeze drying, *in situ* polymerisation, microfluidic droplet formation, and coacervation. This section will focus on the coacervation encapsulation though for a more information on encapsulation techniques please refer to an excellent review by Liang *et al* as well as the text book by Mishra.^{228,229}

Coacervation is one of the oldest and widely used encapsulation techniques (**Figure 1-12**) and has been widely used to encapsulate TLCs,³⁷ e-inks for displays^{230,231}, and many other oils.^{22,232,233} A coacervate is a spherical droplet of assorted organic molecules, held together by hydrophobic interactions. To form a shell out of coacervates, 4 steps are required.²²⁸ In the first step of the encapsulation process, the oil is emulsified within an aqueous solution. The solution contains two oppositely charged components which are

initially held above the isoelectric point of one of them, causing it to be neutral. Upon a change in pH, the component above the isoelectric point becomes charged and the molecules associate within the solution to form a particle. As more particles are formed within the system, the polymer colloids deposit on the surface of the emulsified oil droplets. To ensure the particles remain as a barrier for the oil, a cross-linking agent is added to harden the shell material.

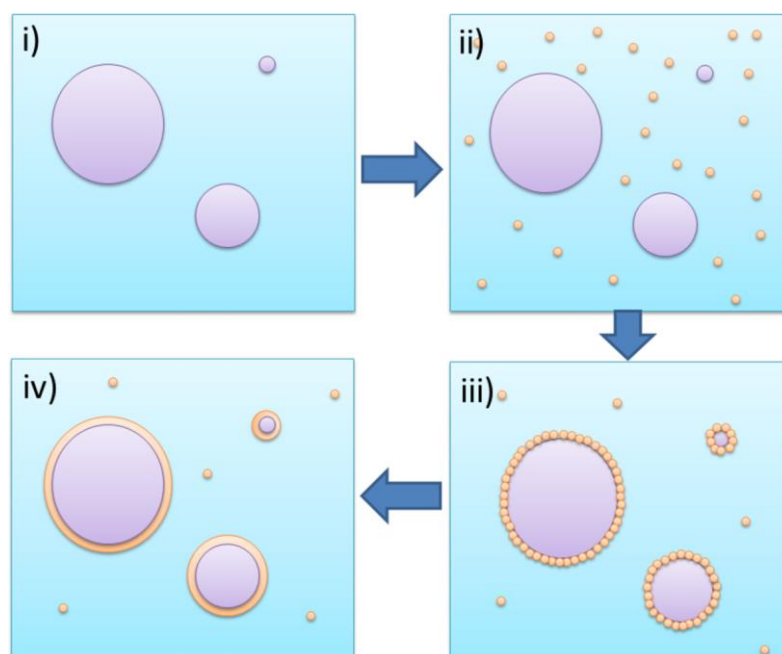


Figure 1-12. Example of coacervation forming particles within an aqueous solution involving i) oil emulsification within the solution, ii) polymer coacervation formed upon changes in pH, iii) deposition of particles onto the surface of the oil, and iv) hardening of the wall to form a barrier. ● is the oil, ● is the polymer coacervate, and ● the aqueous phase.

Coacervation can be broken into two main groups: simple and complex. A system is termed as “simple” when the polymer is salted out by the action of

a small electrolyte molecule, the addition of a non-solvent, or changes in temperature. Conversely, a system is described as complex when two oppositely charged polyelectrolytes are used. A preference towards complex coacervation is seen due to the large number of functional groups that can become charged leading to simultaneous formation of polyelectrolyte complexes forming.²³⁴ The most common polyelectrolyte used gelatin due to its ability to gel at low temperatures, holding the structure before crosslinking²³⁵ although use of synthetic polyelectrolytes such as poly(vinyl alcohol)^{236,237} and poly(styrene-co-maleic anhydride)^{238,239} have also been reported. Gelatin is often used alongside counter-ions such as gum arabic,^{232,233} sodium alginate,²⁴⁰ chitosan,²²⁸ and carboxymethyl cellulose²⁴¹ due to ready availability as naturally occurring products.

Our aim was to synthesise an oil which optically shows when a system was cooled below a certain temperature. Ideally this oil could be used both in its pure state, within strips similar to TLC thermometers, or encapsulated *via* coacervation to be dispersed within a polymeric binder. The temperatures we were interested in were 0 °C and lower to use as an indication for ice formation in roads as well optimal temperatures for applying paints and cold temperature warnings. Herein we report the synthesis of a variety of polymers, characterise the phase change using a new method, and encapsulate the oils and exhibit its use within film coatings.

1.3 Results and Discussion

Diethyl phthalate (DOP) is a commonly used plasticiser within the polymer industry (**Figure 1-13**).²⁴² DOP is prominently used to increase the flexibility of poly(vinyl chloride) though readily dissolves a wide range of polymers.²⁴³ With a melting point of $-50\text{ }^{\circ}\text{C}$, it opens a wide range of temperatures at which phase separation can occur without solvent restriction.

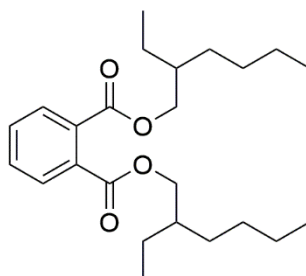


Figure 1-13. Chemical structure of diethyl phthalate.

Ver Strate and co-workers and Rangel-Nafaile *et al.* independently demonstrated the phase separation of PS in DOP.^{196,225} Initial PS in DOP solutions were made by dissolving pellets of PS in DOP overnight. Temperatures of $110\text{ }^{\circ}\text{C}$ had to be reached to fully mix the polymer into the system. Thermal decomposition of DOP into phthalic acid and 2-ethylhexane is known to occur in excess of $300\text{ }^{\circ}\text{C}$.²⁴⁴ However, DOP in the presence of PVC has shown to decrease the thermal decomposition temperature down to $< 150\text{ }^{\circ}\text{C}$.²⁴² If thermal decomposition occurs, it would lead to the presence of additional species within the system that could have a profound effect on both

the phase transition and the encapsulation process. To counter this possibility, PS was precipitated to ensure a larger surface area and this increase allowed for fully homogeneous solutions at 60 °C, well below known decomposition temperatures.

1.3.1 Measuring the Phase Change

Multiple ways have been reported to record the phase change of LCST/UCST capable solutions. Originally, optical determination was used to determine the point at which the solution appeared white.^{132,245,246} More recently melting point apparatus,^{247,248} dynamic light scattering,^{151,249} and UV/Vis spectrometers^{150,250} fitted with heating stages have been used. The combination of high wt% of polymer dissolved within the solution and high viscosity of the solution, UV/Vis was employed initially to determine phase change. Following this, a new photographic method was used to determine the phase change.

1.3.1.1 UV/Vis

Before the full phase change curve of 10 wt% PS in DOP could be recorded, an equilibration time was needed. In order to determine this, a 3.5 cm³ cuvette filled with 10 wt% PS in DOP was placed into a UV-Vis spectrometer with a heating/cooling unit. The sample was left at 10 °C for an hour. After the allotted time, no change in the solution's spectrum was observed (350 nm – 800 nm). The cooling unit was set to 1 °C and a spectrum was recorded every 5 minutes.

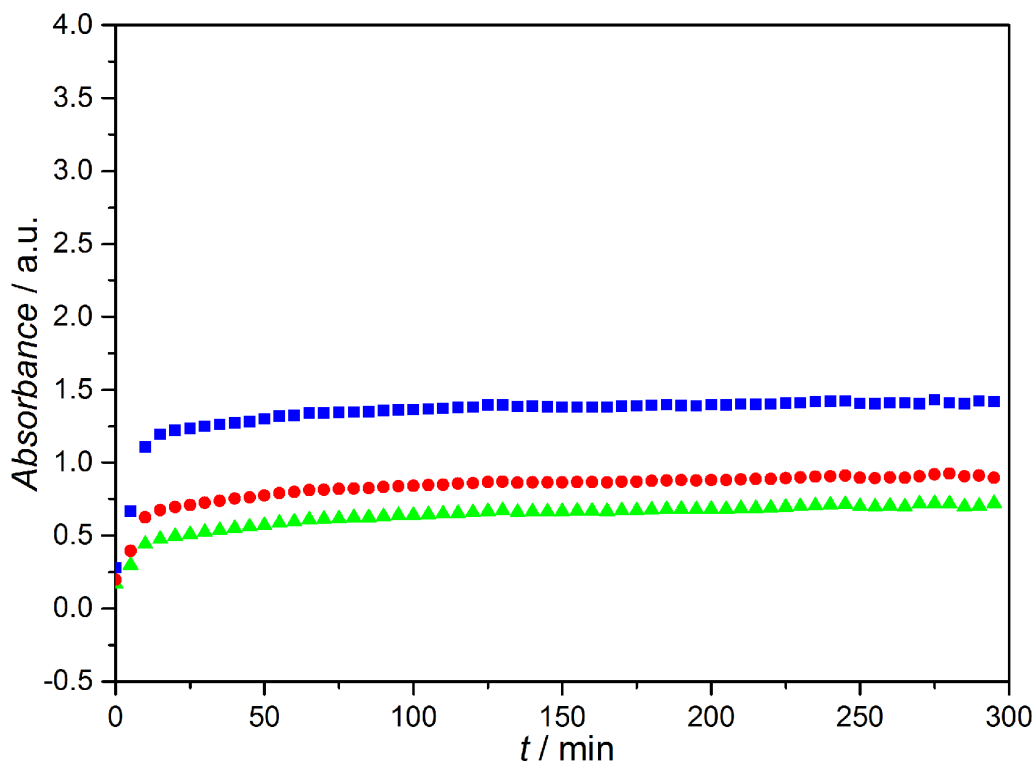


Figure 1-14. UV/Vis spectra of light absorbed by a 3.5 cm³ sample of 10 wt% PS in DOP cooled from 10 °C to 1 °C and held at that temperature. Symbols represent wavelengths of ▲ - 400 nm ● - 500 nm ■ - 600 nm. Measurements were taken every 5 minutes.

Figure 1-14 shows the absorbance of the sample over time increasing uniformly with each wavelength. The sample does not absorb the light but scatters it. Scattering occurs due to the formation of PS colloids within the DOP when going through a UCST like transition upon cooling. This results in centres of RI difference, similar to that of opacifiers in paints. The solution is white in colour as the visible light is scattered across all wavelengths. After 60 minutes, the full transition has occurred due to the plateau in absorbance recorded. There is a slight difference between the absorbance values after 60

minutes. This is caused by condensation of water onto the exterior of the cuvette, not further phase separation of the PS chains.

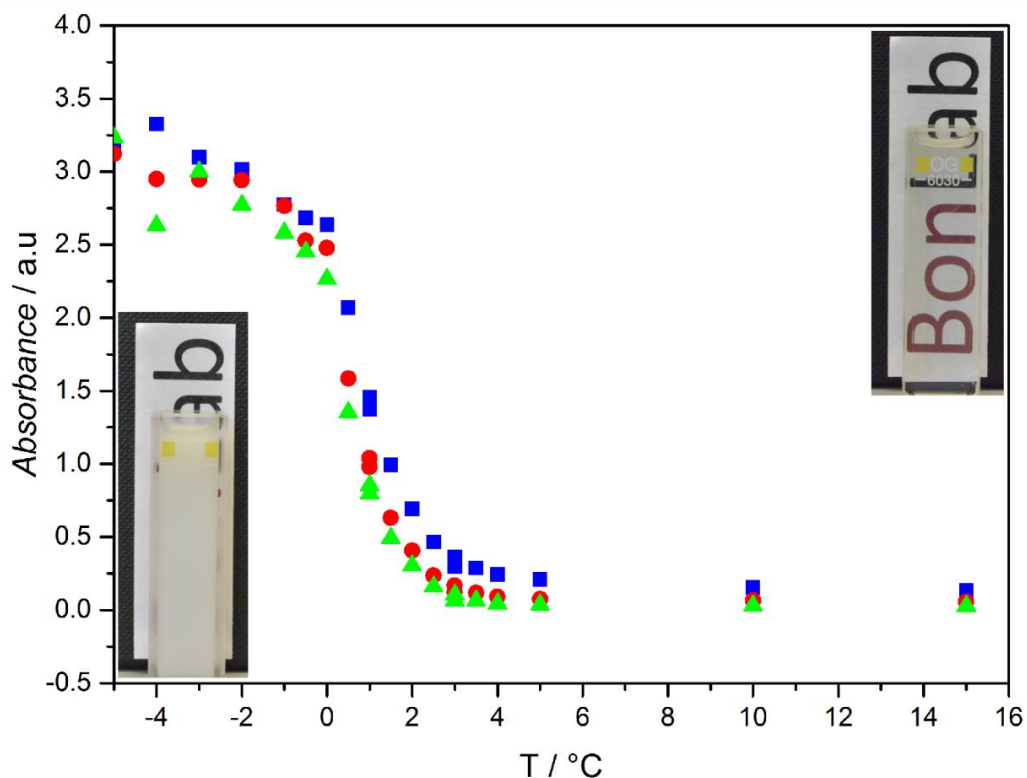


Figure 1-15. Phase transition curve of 10 wt% PS in DOP recorded *via* UV/Vis spectrometry. ▲ - 400 nm, ● - 500 nm, and ■ - 600 nm wavelength absorbance values. The samples were left 60 minutes before each spectra was recorded. Insets are the cuvette filled with 10 wt% PS in DOP (left) immediately after it was cooled to $-5\text{ }^{\circ}\text{C}$ and (right) after it was left at ambient conditions for 5 minutes.

Figure 1-15 shows the phase change of the system over the temperature range. The image insets also showed a strong change in opacity between the heterogeneous and homogenous states. There is a very distinct difference in opacity and transparency between the two states due to the high

volume of PS dissolve in the DOP. There was no great difference in absorption over the recorded ultra violet and visible spectrum, indicating that the sample fully absorbed or scattered the light waves. T_{onset} measured for 10 wt% PS in DOP was recorded to be 2.9 °C.

An issue arose when using the UV-Vis method due to how UV-Vis spectrometers record absorbance and the Beer-Lambert law (**Equation 1-28**).

$$\log_{10} \frac{I_0}{I} = A = \epsilon \cdot l \cdot c \quad \mathbf{1-28}$$

Where A is the absorbance, ϵ is the molar absorptivity, l is the path length, c is the concentration, I_0 is the incident intensity, and I is the transmitted intensity.

Using the Beer-Lambert law, an absorbance of 1 means that 10 % of the light was transmitted through the system. Therefore an absorbance of 2 means 1 % of light is transmitted and an absorbance of 3 means 0.1 % of the light was transmitted. An issue for most, if not all, UV-Vis spectrometers arises when an absorbance of >2 is recorded due to very little light is being transmitted (<1 %) through the system. When this happens, the machines start to become non-linear, meaning they fail to follow the Beer-Lambert law and because of this, the values on **Figure 1-15** become unreliable. It should also be noted as the system is not absorbing the UV/Vis light but scattering, it is possible for all the light to become fully scattered before the full phase transition has occurred within the system

Another issue is the UV/Vis run time. Each sample loaded needed to be kept at each temperature for 1 hour leading to long down times between each measurement and only single samples running at a time. This led to a run time of 19 hours per sample. Coupling this with the issues with the Beer-Lambert law and limited temperature range leads this method to be relatively restrictive. A new method was required to allow for a higher throughput of samples over a larger temperature range.

1.3.1.2 Photographic Phase Change Measuring

Herein we describe the setup of our new technique for measuring the phase transition of solutions. An aluminium plate was used as the basis for the cooling plate. Into this 36 flat bottom holes were drilled into it to act as the wells for the solution to reside (**Appendix II Figure II - 1**). An additional hole was required for the insertion of a Pt 100 immersion thermometer. Into the base of each well a piece of non-leaching black card was added for a black background for each sample. This was to reduce error of light being reflected off the aluminium base.

For a typical setup, the PS in DOP solution was added in warm ($\sim 40\text{ }^{\circ}\text{C}$) into the wells. The plate was then also warmed to $40\text{ }^{\circ}\text{C}$ by mounting onto a Kruss TC40 heating/cooling stage in order to control the temperature. The stage is fitted with a Peltier cooler with a separate liquid cooling system to ensure it does not burn out. To combat condensation build up on the samples, a glass plate was placed onto the system. This allowed for easy removal of any ice forming without disturbing the samples being measured. In order to

reduce ambient light effecting the measurements taken, the whole system was placed inside an enclosed box. A camera was mounted 450 mm above the plate. Two 160° light sources were also inside the box to allow for even illumination over the entire plate. The temperature of the heat exchange plate was controlled by an external unit using a digital controller and recorded using the Pt 100 immersion thermometer.

Using the mounted camera above the plate, images were taken. The same settings were applied for all occasion to remove any lighting bias. Following the recording of the solutions at temperatures, the images were processed. Each image needed to be converted from raw to grey scale using ImageJ. Following this, an average grey value for the aluminium plate was recorded. This value was scaled up/ down to 200 using a conversion factor. Once the conversion factor had been obtained, the average grey value of each well was then converted to a standard grey value by multiplying by the conversion factor. This allowed for comparison between temperatures and separate system measurements.

Using the UV/Vis method, an equilibration time of 1 hour was recorded (**Figure 1-14**). This large time period is due to three variables: volume of solution measured, thermal conductivity of surrounding material, and surface area in contact with heating/cooling surface. The UV/Vis method used a cuvette of filled with 3.5 cm³ of solution. In contrast, the aluminium wells decreased the volume of solution measured to 0.19 cm³. Aluminium has high thermal conductivity in comparison to quartz (237 W/cm·K to

1.3 W/cm·K).²²⁴ This allows for higher temperature flow through the material. The total surface area of PS in DOP within the cuvette is 16 cm². The cooling plates act fully on two sides and partially on the other two. Only 12 cm² of surface area is in contact with the plates (75 %). The total surface area of the aluminium wells is 1.87 cm² with 1.49 cm² (79.6 %) in contact with the cooling surface. The cooled surface-area-to-volume ratio of the cuvette is 3.42 cm⁻¹ whilst the well is 7.84 cm⁻¹. This higher ratio indicates that the solution within the well has a better thermal contact than that of the cuvette. Overall, the new technique should show improved heating and cooling characteristics. Using the new photographic technique, the equilibration time of a 10 wt% PS in DOP was measured (**Figure 1-16**).

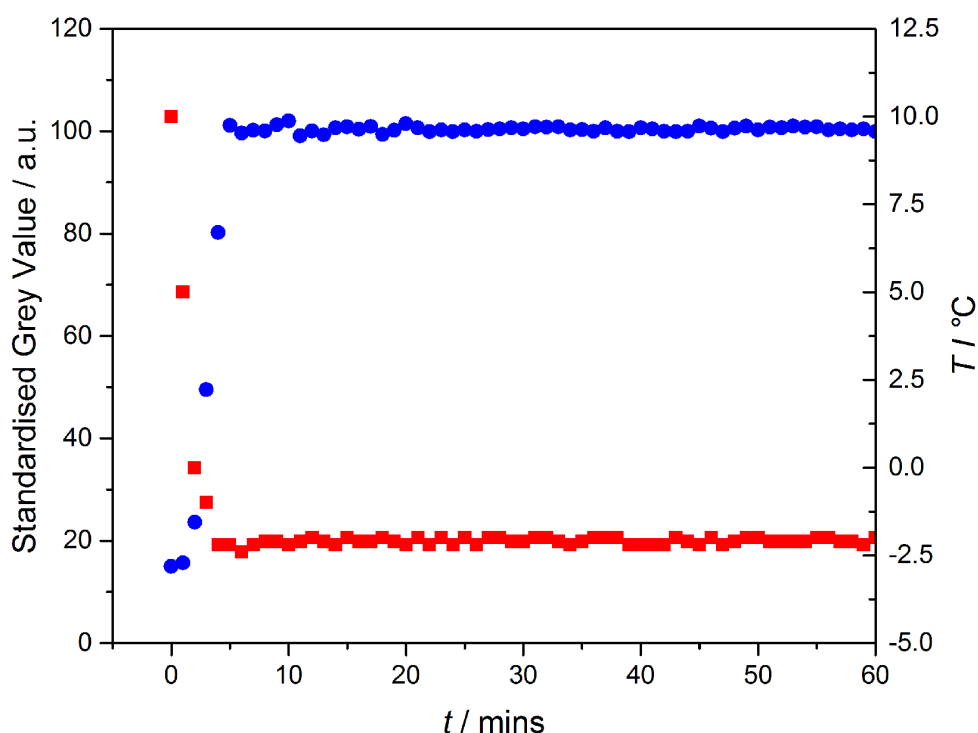


Figure 1-16. Phase curve of 10 wt% PSDOP solution held at 10 °C for 5 minutes before cooling to -2.4 °C. Recorded using the new photographic technique. Images were taken every minute before processing. ● - the grey value measured and ■ - the temperature recorded at each point.

A 0.19 cm³ sample of PS in DOP was measured to determine the equilibration time for the photographic technique (**Figure 1-16**). The plate was held at 10 °C for 5 minutes before cooling to -2.4 °C. Whilst cooling, an image was taken every minute. It can be seen that the change in temperature has a very rapid response within the solution. After 5 minutes, the system has fully equilibrated and no difference seen within the system. In comparison to the UV/Vis technique (**Figure 1-14**), this new method is far quicker. Slight fluctuations on the temperature can be seen. This is due to the ambient

conditions surrounding the measurement plate. However, these fluctuations have little impact on the measured grey scale value. Regardless, to allow for this, the time for each heating step was set to 12 minutes.

Once the equilibration time of 12 minutes was obtained, a full phase transition curve for 10 wt% PS in DOP could be recorded (**Figure 1-17**). It can be seen that there was a close concordance between both techniques. Whilst the methods are close, a variance in temperature can be observed. T_{onset} of the phase change recorded using the new photographic method is at 2.4 °C. T_{onset} of the UV/Vis method is shown to start at 2.9 °C. This discrepancy is due to how the temperature was recorded using the UV/Vis method. The cooling plate is controlled externally by a digital controller with no additional temperature recording. The temperature difference between the plates and the sample at < 5 °C was ~0.8 °C. Once cooled below - 2 °C a difference of 1.1 °C was observed. Taking this into account, both graphs would show transitions at the same temperature. It should be noted there is a lack of consistent plateau with the UV/Vis values. This is due to the large variations of the recorded absorbance values as stated earlier (**Equation 1-28**). The new photographic technique can also reach much lower temperature (- 20 °C) than that of the UV/Vis system (- 5 °C). With this, any further change in phase transition could also be recorded. It is possible using the UV/Vis method that all the light is scattered by the colloids before the full transition has occurred. This would lead to incorrect values being recorded for the end of the phase transition. The photographic technique relies on the observed colour of the

sample. If further colloids were formed within the solution, the system would appear whiter due to higher quantities of scattering colloids.

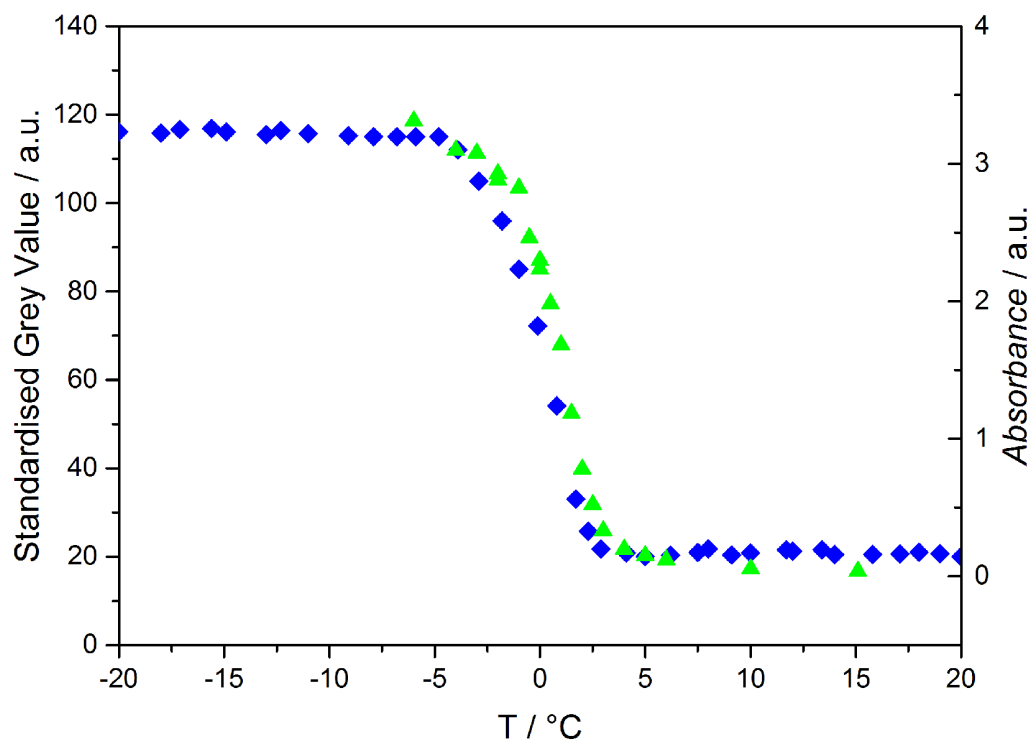


Figure 1-17. Phase change curve of 10 wt% of PS in DOP measured using ▲ – UV-Vis at 500 nm and ◆ – photographic technique.

UCST curves of polystyrene (M_w 280,000 g·mol⁻¹ \bar{M}_w 3.0) in DOP have been recorded by both Ver Strate (UCST of 7 °C) and Rangel – Nafaile (UCST of 8 °C).^{196,225} Using the new photographic technique, a UCST curve for PS in DOP is shown in **Figure 1-18**. It should be noted that both Ver Strate and Rangel - Nafaile's work investigated the effect of stress induced phase separation of PS in DOP when flowing through a capillary. The polymers used in both Rangel-Nafaile and Ver Strate's work were reported to be the same

polymer though the differences in temperature were thought to be due to innate pressure placed upon the system by trapping within a capillary.

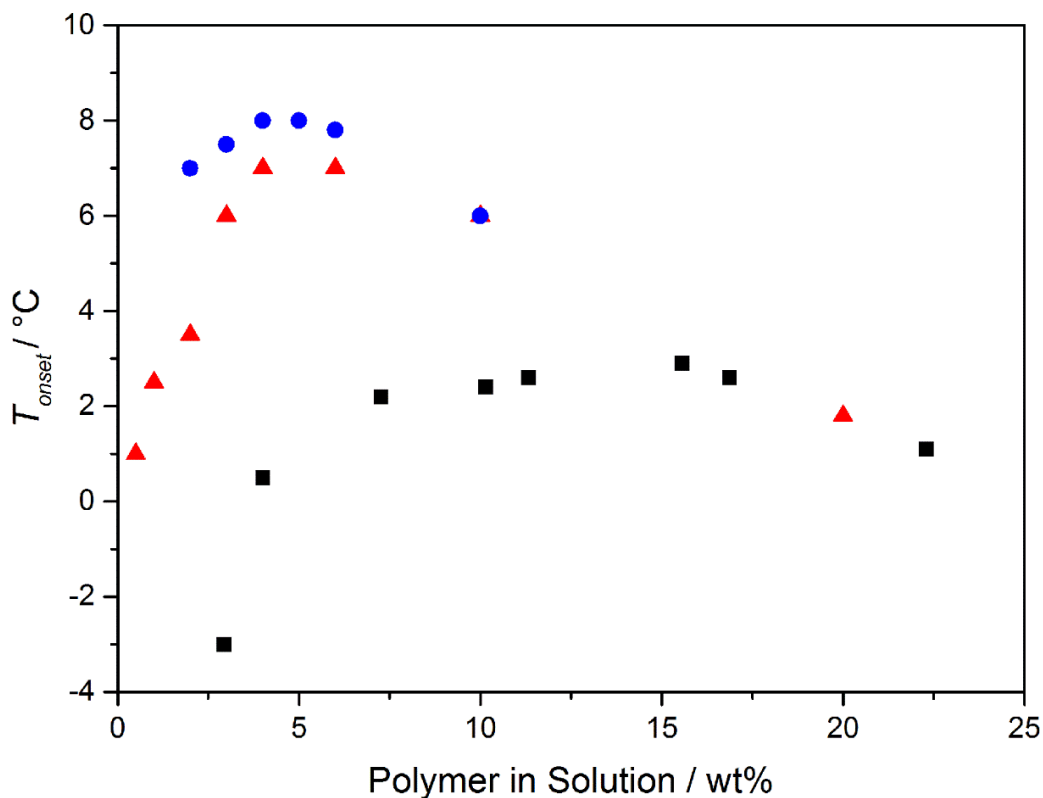


Figure 1-18. UCST curves of PS in DOP. ■ - measured using the photographic technique, ▲ - measured by Ver Strate,²²⁵ and ● - measured by Rangel – Nafaile.¹⁹⁶

1.3.2 Copolymers

Thermal self-initiation of styrene occurs at temperature of $<100\text{ }^\circ\text{C}$.²⁵¹ Both the Mayo and Flory mechanism have been proposed (**Figure 1-19**). Fundamentally, Mayo proposed the polymerisation initiates *via* a Diels-Alder dimerization of styrene. A third styrene molecule assists homolysis between the dimer and two monoradical species are made to further the

polymerisation.^{251,252} Flory proposed the formation of a 1,4-diradical species. This species would hydrogen abstract from a third styrene molecule to form two monoradical species for initiation. Computational studies by Khuong and co-workers suggest that the Mayo mechanism's Diels-Alder dimer was the key step for thermal self-initiation of styrene.²⁵³

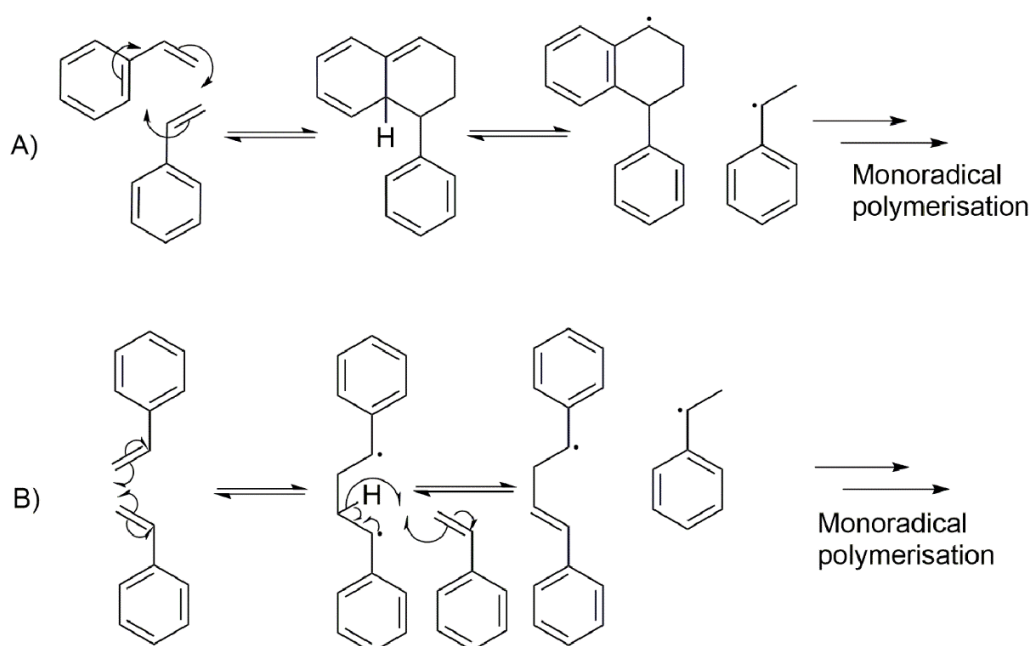


Figure 1-19. Schematic of a) Mayo and b) Flory proposed reaction mechanism for thermal self-initiation of styrene at high temperatures.²⁵³

Dow Chemical have long used thermal initiation of styrene to produce high molecular weight PS which can be controlled using sulphuric acid.²⁵⁴ Following this, thermal self-initiation of styrene was used as a source of radicals for the co-polymerisation of styrene and co monomers. A series of

bulk polymerisation were undertaken using methyl methacrylate (MMA), ethyl methacrylate (EMA), ethyl acrylate (EA), 2-ethyl hexyl acrylate (2EHA), lauryl acrylate (LA) and NIPAM as co-monomers. A typical reaction was as follows. Styrene and co-monomer (0.5, 1, 2, 2.3, 5, and 10 wt% co-monomer with respect to styrene) were charged into a crimp top vial, stirred, and sealed. The solutions were degassed with N₂ for 15 minutes. Following degassing, the vials were transferred into a 140 °C oil bath for 1 hour. Polymerisation was terminated *via* submersion into ice cold water and injection of 10 mL of air.

1.3.2.1 MMA

PMMA has been shown to exhibit UCST behaviour in methanol, water/ethanol mixtures, as well as cyclohexanol solutions and polymer blends.^{255–258} However, to our knowledge, no phase behaviour has been recorded for PMMA in DOP. PMMA is a known hydrophobic polymer which can undergo hydrolysis of the ester groups to form a hydrophilic polymer.²⁵⁹ MMA was chosen as a starting co-monomer due to both its hydrophobic nature and small molecular size relative to styrene. DSC's were run over –150 °C to +150 °C with an isotherm at 150 °C to ensure no solvent was present. The wide range chosen was to determine the T_g of the polymer as well as possible side chain crystallisation. To determine the MW and \bar{D} all samples were run through a CHCl₃ SEC. The data of the copolymerisation of MMA and styrene to give poly(styrene –*co*- methyl methacrylate) (PSMMA) is shown in **Table 1-1**. It can be seen that using thermal self-initiation of styrene

to initiate the polymerisation resulted in polymers with similar M_W and \bar{D} values. There is a slight decrease in \bar{D} from the initial PS sample used, though work mentioned earlier by Scholte indicated that this would of effected the UCST point only slightly.²¹¹ As expected, increasing the wt% of MMA present in the reaction led to an increased incorporation of MMA units within the end polymers.

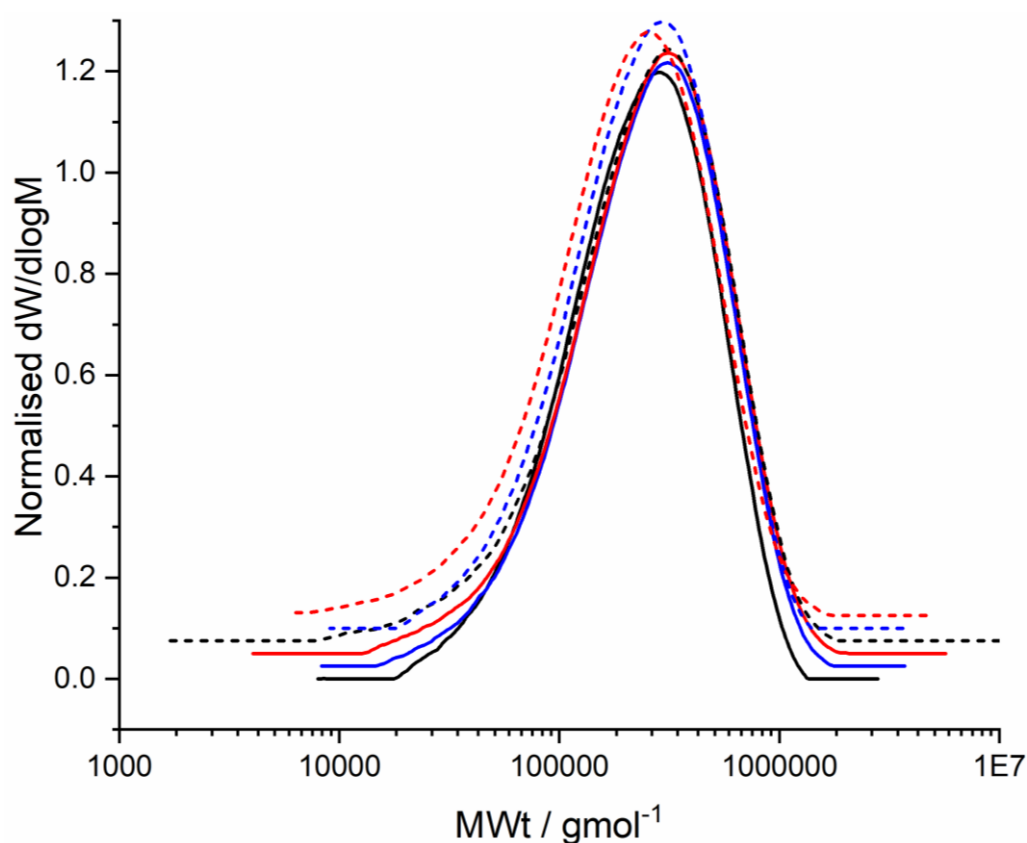


Figure 1-20. Offset SEC traces of the polymers synthesised from the polymerisation of different concentrations of styrene and MMA after 1 hour at 140 °C. The traces are — PSMMA 1, — PSMMA 2, — PSMMA 3, -- PSMMA 4, -- PSMMA 5, and -- PSMMA 6.

Upon isolation of the polymer from the reaction mixture, NMR characterisation was used to determine both the purity of the polymers and the composition of the polymers obtained. It is important to ensure no monomer remains within the polymer as the monomers will act as a solvent within the end system and affect the phase change point of the systems.

Figure 1-21 shows the NMR spectrum of the PSMMA series.

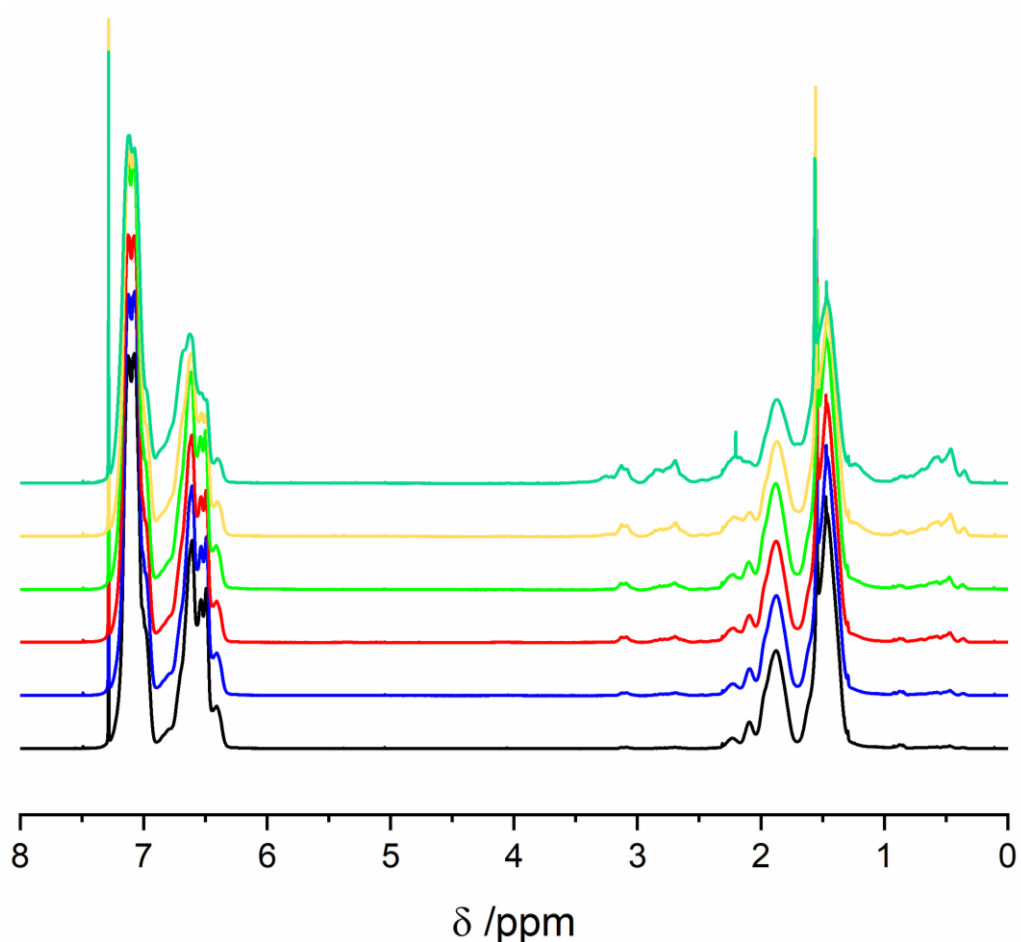


Figure 1-21. NMR spectrum of (—) PSMMA 1, (—) PSMMA 2, (—) PSMMA 3, (—) PSMMA4, (—) PSMMA 5, and (—) PSMMA 6 in CDCl₃.

Comparison between the aromatic region of the polystyrene (7.7-5.9 ppm) and the alkyl region (2.7-0.5ppm) of the polymer that contains both the polystyrene backbone and PMMA alkyl groups were analysed. From this the composition of the polymer can be determined using the following equations

$$N_{Co,Al} = \frac{N_{Al} - n_{Ar}N_{Ar}}{n_{Co,Al}} \quad \mathbf{1-29}$$

$$N_{St,Ar} = \frac{N_{Ar}}{n_{St,Ar}} \quad \mathbf{1-30}$$

Where:

$N_{x,Al}$ = integration value of the alkyl region for component x

N_{ar} = integration value of the aromatic region

n = number of protons in the environment

Co = comonomer component

Ar = Aromatic region

Al = Alkyl region

Molar percentage (mol %) of each component can then be determined using **Equation 1-31** and **1-32**.

$$St \text{ mol}\% = \frac{N_{St,Ar}}{N_{St,Ar} + N_{Co,Al}} \quad \mathbf{1-31}$$

$$Co \text{ mol}\% = \frac{N_{Co,Al}}{N_{St,Ar} + N_{Co,Al}} \quad \mathbf{1-32}$$

Using the above equation, along with the NMR Spectra of PSMMA 1 to PSMMA 6, the mol% of comonomer was calculated for the polymerisation series and report in **Table 1-1**.

Table 1-1. Tabulated data for MMA containing polymers recorded from NMR, SEC and Equation 1.33.

Sample	$M_w /$ kg·mol ⁻¹	\bar{D}	MMA Feed / mol%	Polymer MMA/ mol%	Predicted MMA / mol%	Yield/ %
PSMMA 1	335	2.09	0.52	2.43	0.99	32.00
PSMMA 2	322	1.84	1.05	3.36	1.97	28.88
PSMMA 3	372	1.90	2.09	5.02	3.83	30.96
PSMMA 4	318	2.04	2.38	5.24	4.33	30.11
PSMMA 5	300	1.76	5.2	10.4	8.91	30.00
PSMMA 6	330	1.84	10.4	14.3	16.12	33.00

All of the polymers synthesised clearly show a larger percentage of comonomer in the end polymer than in the initial feed, indicating that there is a difference between the initial feed and end result. Utilising the Mayo-Lewis equation (**Equation 1-33**), along with reactivity ratios, it is possible to determine the distribution of repeat units within the end polymer.

$$F_1 = 1 - F_2 = \frac{r_1 f_1^2 + f_1 f_2}{r_1 f_1^2 + 2 f_1 f_2 + r_2 f_2^2} \quad \mathbf{1-33}$$

Where

F = mole fraction of each monomer within the copolymer

f = mole fraction of each monomer within the reaction system

r = reactivity ratio of each monomer

The 6 main cases of reactivity ratios can be used to show an approximate composition of the polymer system.

- 1) $r_1 = r_2 \gg 1$
- 2) $r_1 = r_2 > 1$
- 3) $r_1 = r_2 \approx 1$
- 4) $r_1 = r_2 \approx 0$
- 5) $r_1 \gg 1 \gg r_2$
- 6) $r_1 < 1, r_2 < 1$

In the first case, both monomers have such a high reactivity ratios that the growing polymer chain solely reacts with the same monomer, causing homopolymers to form within the system. In the second case, homopolymerisation is still favoured within the system; however events of cross polymerisation can occur. Upon these events occurring, the polymer will preferentially grow with the other repeat unit, resulting in block like polymers. The third case shows monomers of similar reactivity ratio. In these

cases, growing polymer chains will react quickly with either monomer, resulting in the formation of a random or statistical copolymer. Systems containing monomers with r_1 and r_2 similar to that shown in case 4 result in polymers with alternating composition. This is due to the growing chain being unable to react with a similar monomer and therefore only adding on a different monomer to the chain. In the 5th case, a polymer produced will express larger amounts of monomer 1 as it is reacted in faster. As monomer 1 is consumed in the reaction, larger amounts of monomer 2 will be incorporated into the polymer. This results in a drift of composition within the polymer. In the final case, the polymer formed is the same as the monomer feed. When this system occurs, it is called an azeotropic polymerisation. This also occurs for other systems where the Mayo-Lewis plot crosses the diagonal ($f_1=F_1$).

The r_1 and r_2 values for styrene and MMA were determined by Meyer to be $r_{\text{Sty}} = 0.52$ and $r_{\text{MMA}} = 0.46$.²⁶⁰ In this case, the system tends towards the fourth system where the polymer formed is a statistical copolymer of both monomer systems. The Mayo-Lewis plot using numbers determined by Meyer show that in low feed ratios (less than 20 mol%) the end polymer will contain a higher ratio of MMA units within (**Appendix II Figure 7-2**). The polymers formed using these systems will show a higher concentration of MMA initially, with a decrease over time, resulting in a heterogeneous polymer formed. The values obtained also show a higher concentration of MMA units within the end polymer than predicted using the Mayo-Lewis equation. PSMMA 5 shows an end composition of 10.4 mol% MMA whilst the initial feed only contained 5.2

mol% and the predicted mol% is 8.91. The polymers formed initially will have some heterogeneity due to this difference in incorporation. As the systems are all roughly 30 % converted, similar to that reported by van der Goot.²⁶¹ This low conversion indicates the polymers are likely to have similar composition. However, if the reaction mixture was left to polymerise further, even greater heterogeneity would be formed with some chains containing little to no comonomer.

With the polymers synthesised, each sample was then dissolved in DOP at varying wt% (between 0.5 – 22.5 wt% with respect to overall mass) overnight at 60 °C with constant stirring to form a viscous oil. The wide range of wt% was chosen to allow for a phase diagram to be obtained in keeping with other PS in DOP systems.¹⁹⁶ Following this, the homogeneous solutions were transferred into wells on the aluminium plate to measure the grey values with respect to time. From the recorded curves, the temperature of the inflection point was obtained and the phase diagram plotted (**Figure 1-22**). Please refer to **Appendix II Figures 7-3** for the phase change curves.

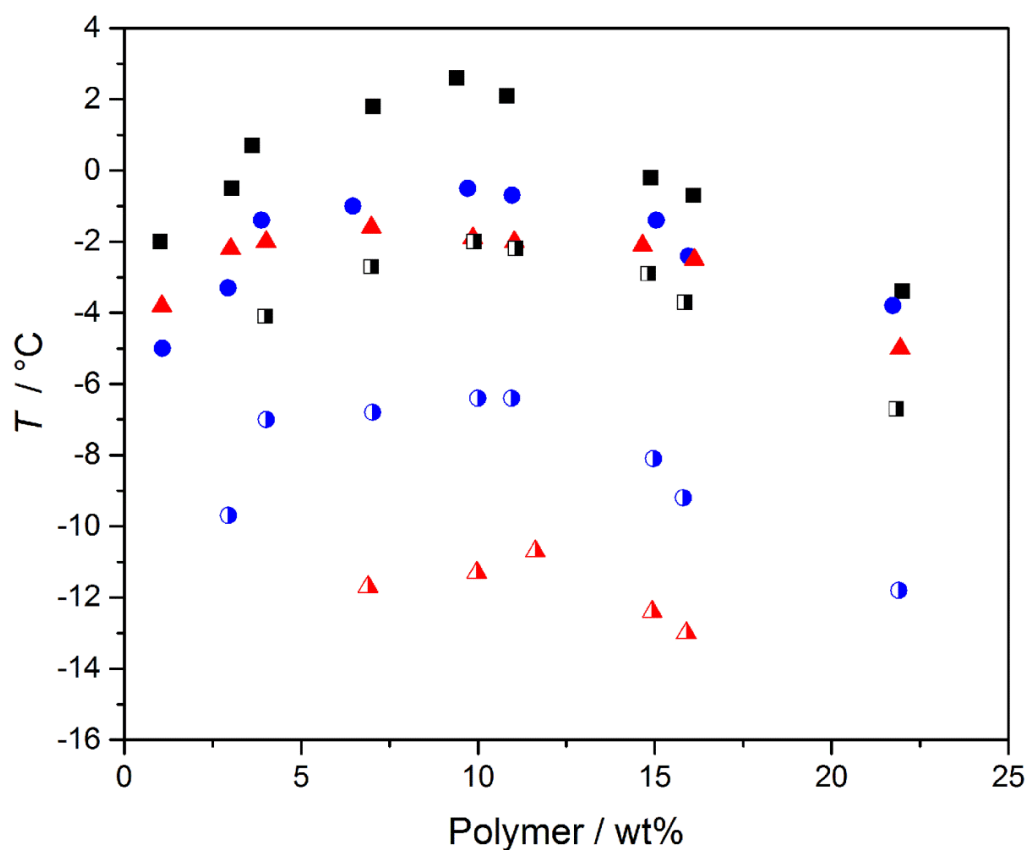


Figure 1-22. Phase diagrams of PSMMA 1 (■), PSMMA 2 (●), PSMMA 3 (▲), PSMMA 4 (◻), PSMMA 5 (◐), and PSMMA 6 (◔) in DOP.

Table 1-2. UCST point data of the PSMMA series from **Figure 1-22**

	PSMMA 1	PSMMA 2	PSMMA 3	PSMMA 4	PSMMA 5	PSMMA 6
UCST	2.5 °C	- 0.5 °C	- 1.5 °C	- 2.1 °C	- 6.3 °C	- 10.7 °C

For all samples of PSMMA 1 – 6, the similar response of low and high wt% of polymer within the solution giving a lower phase transition onset than others was observed (**Figure 1-22**), resulting in the classical shape shown in

Figure 1-9. A similar UCST was recorded for both the pure PS system and that of PSMMA 1 (2.6 °C and 2.5 °C respectively). The slight difference in temperature is due to the low amount of MMA present within the polymer (2.4 mol% with respect to polymer total), causing the styrene moieties to dictate the overall characteristics of the system. However, increasing the MMA content into the polymer causes the polymer to become more soluble, resulting in a decrease in phase transition temperatures of all the polymers. As mentioned in the introduction, UCST behaviour relies on the balance entropic mixing and enthalpic interactions between both polymer and solution. The increased addition of MMA units to the polymer system causes a more favourable enthalpic interaction between solvent and polymer to occur, leading to lower phase change temperatures arising. A close agreement in phase transition temperatures between PSMMA 3 and PSMMA 4 at high wt% of polymer in solution is observed. A similar response was expected due to the similar mol% of MMA moieties present within the polymer (5 and 5.2 mol% respectively). Between samples PSMMA 4, PSMMA 5, and PSMMA 6 there is roughly a 4 °C difference in UCST temperatures when increasing MMA present within the polymer to the point where the PSMMA 6 highest wt% (22.1 wt polymer in DOP) did not show a transition within the measureable range (lowest temperature of - 20 °C).

It is clear from **Figure 1-22** that inclusion of the small hydrophobic monomer MMA within the copolymer led to an increase in solubility of the polymer. This is indicated by the decrease in UCST and other phase change temperatures in comparison to the pure PS system even with an increased M_w

(**Figure 1-20**). Furthermore, increased MMA concentration within the polymer leads to further decrease in phase change temperatures, allowing for possible tuning of the transitional temperature by controlling the polymer composition instead of the polymer wt% in solution.

1.3.2.2 EMA

Similar to PMMA, phase transition of PEMA in DOP has not been previously reported, however both UCST and LCST behaviour in a polymer blend has been.²⁶² The chemical structure of EMA is very similar to that of MMA, with only an elongation of the pendant alkyl chain by an extra carbon. This leads the monomer to exhibit a slightly higher hydrophobic nature than that of MMA. As it was found that inclusion of MMA into the copolymer increased the solubility of the polymer, it was expected that EMA would further increase the solubility. The same conditions for copolymerisation were used as MMA and the resulting polymers data is shown in **Table 1-3**. Similar M_w and \bar{D} for the poly(styrene-co-ethyl methacrylate) (PSEMA) copolymers in comparison to each other and the PSMMA copolymers were obtained. The bell curve shape of the SEC curves (**Figure 1-23**) indicate that no chain to chain termination occurred. Presence of these chains would be should be a shoulder into the higher molecular weight range.

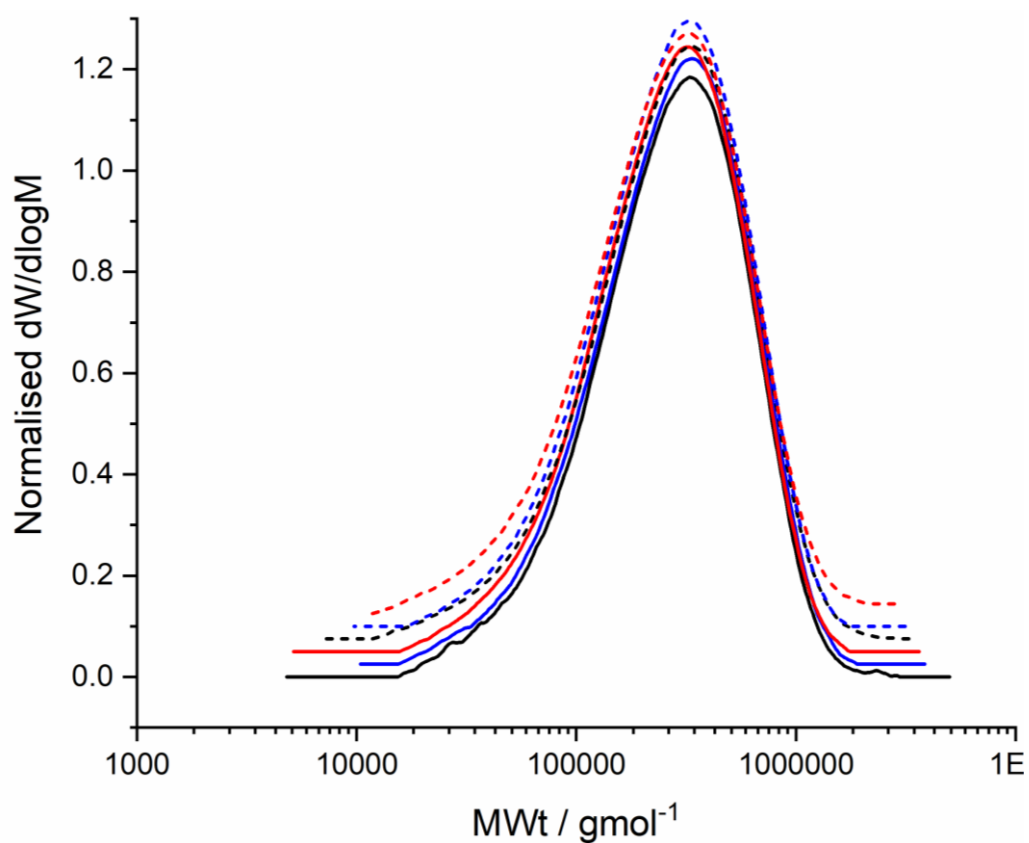


Figure 1-23. Offset SEC traces of the polymers synthesised from the polymerisation of different concentrations of styrene and EMA after 1 hour at 140 °C. The traces are — PSEMA 1, — PSEMA 2, — PSEMA 3, -- PSEMA 4, -- PSEMA 5, and -- PSEMA 6.

No shoulders are present within the PSEMA series (**Figure 1-23**), which is also shown with the \bar{D} remaining around 2 (**Table 1-3**).

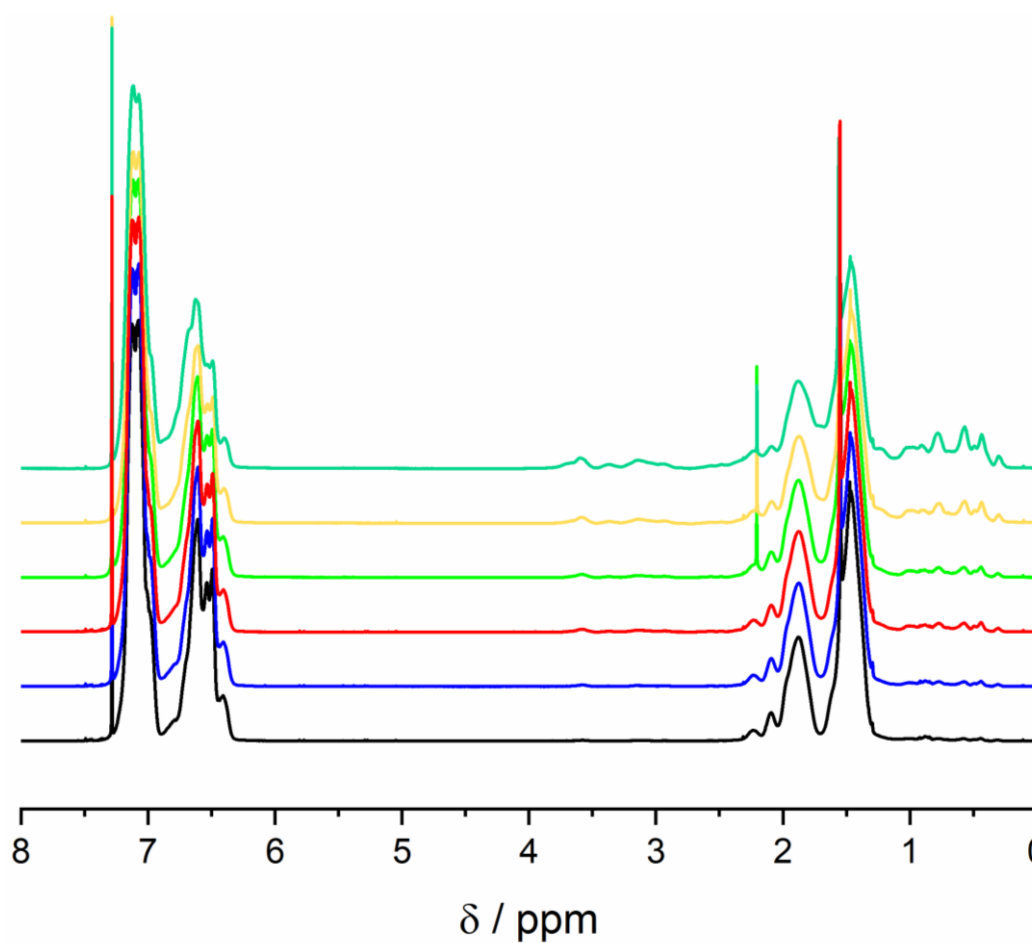


Figure 1-24. NMR spectrum of (—) PSEMA 1, (—) PSEMA 2, (—) PSEMA 3, (—) PSEMA4, (—) PSEMA 5, and (—) PSEMA 6 in CDCl_3 .

No monomer vinyl peaks can be observed in the NMR spectra of the isolated PSEMA series (**Figure 1-24**). Increasing the feed of EMA into the reaction mixture shows a clear increase in the EMA units within the end polymer similar to that of the PSMMA series. Mol% of EMA present in the polymer is shown in **Table 1-3**.

Previous reports have not shown r_1 and r_2 values for styrene and EMA in wider literature, hence values for styrene and butyl methacrylate (BMA) will be used instead. Van der Goot determined the ratios to be $r_{\text{sty}} = 0.52 \pm 0.03$ and $r_{\text{BMA}} = 0.86 \pm 0.03$.²⁶¹ Again this system tends towards the fourth system where the polymer formed is a statistical copolymer of both monomer systems. The Mayo-Lewis plot using numbers determined by Meyer show that in low feed ratios (less than 20 mol%) the end polymer will contain a higher ratio of BMA units within (**Appendix II Figure 7-2**). The predicted composition of EMA units is higher than the experimental values obtained in feeds over 0.9 mol% EMA. This discrepancy is most likely due to the r values used being measured for BMA instead of EMA. Due to polymerisation being stopped at $\sim 30\%$ in all cases, the polymers formed will most likely be heterogenous. Whilst no homopolymers were formed, the heterogeneity of the polymers would blur the UCST point if there was a large difference in r values (i.e. $r_1 \gg 1 \gg r_2$). Here the values show that some difference in UCST may be attributed slightly to the homogeneity, though the cause is stop most likely that of the comonomer incorporation. Low mol% feed of monomers show good correlation to the predicted incorporation. As the mol% increases in the feed, the end polymers show lower incorporation than predicted. The polymer chains formed show a greater homogeneity due to higher monomer concentrations still present in the reaction mixture. It should be noted that the discrepancies in values can also be attributed to the use of r values for BMA and not EMA.

Table 1-3. Tabulated data for EMA containing polymers recorded from NMR, SEC, and Equation 1.33.

Sample	$M_w /$ kg·mol ⁻¹	\bar{D}	EMA Feed / mol%	Polymer EMA / mol%	Predicted EMA / mol%	Yield / %
PSEMA 1	344	1.90	0.5	1.56	1.2	30.00
PSEMA 2	346	1.78	0.9	2.31	2.2	30.10
PSEMA 3	329	1.84	1.8	3.32	4.2	31
PSEMA 4	345	1.97	2.1	4.05	4.9	30.61
PSEMA 5	336	1.82	4.6	6.84	10	30.97
PSEMA 6	340	2.04	8.5	11.8	16.9	29.95

The resulting copolymers were then dissolved at 60 °C in DOP until a homogenous mixture was obtained. Following this, the phase change of the polymers was recorded (please refer to **Appendix II Figure 7-4** for the phase change graphs) and the inflection point of each graph noted to allow for the creation of the phase diagram (**Figure 1-25**). Upon cooling, the PSEMA 6 in DOP solution showed no phase change when cooled to – 20 °C.

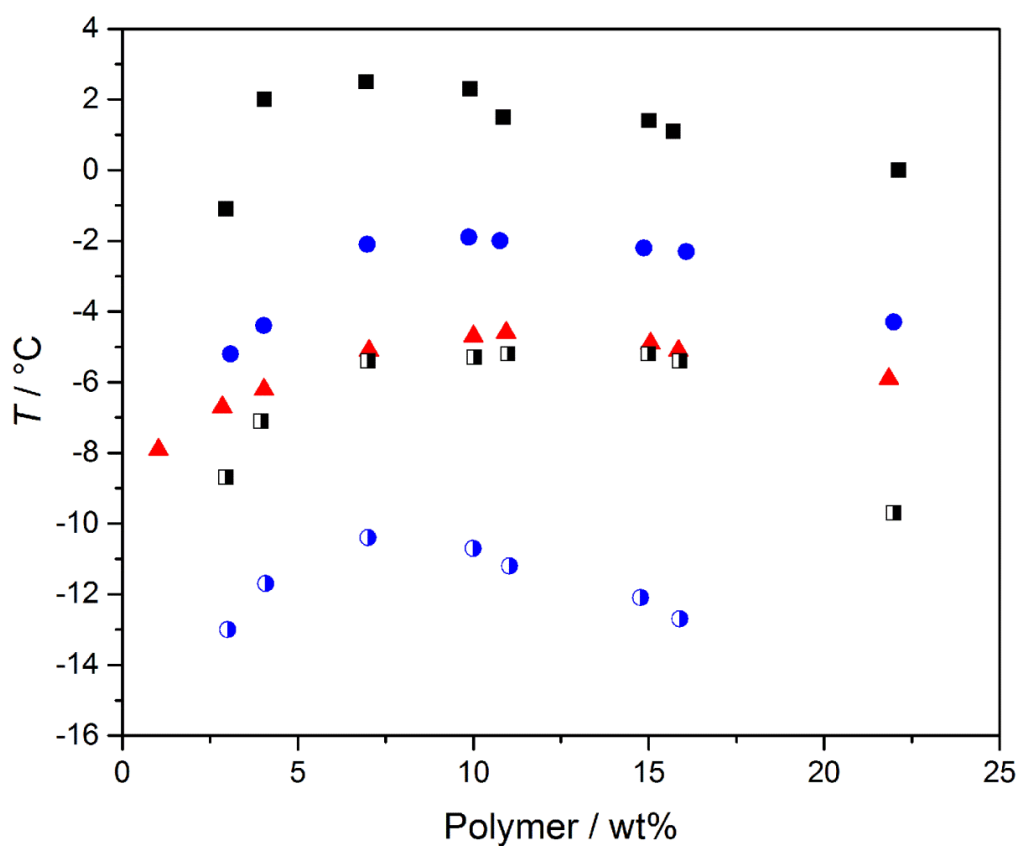


Figure 1-25. Phase diagrams of PSEMA 1 (■), PSEMA 2 (●), PSEMA 3 (▲), PSEMA 4 (◼), and PSEMA 5 (◐) in DOP.

Table 1-4. UCST data for the PSEMA series from **Figure 1-25**.

	PSEMA 1	PSEMA 2	PSEMA 3	PSEMA 4	PSEMA 5	PSEMA 6
UCST	2.5 °C	- 1.8 °C	- 4.6 °C	- 5.2 °C	- 10.3 °C	n/a

The phase diagram (**Figure 1-25**) of PSEMA 1-PSEMA 5 show a clear correlation that increasing the EMA content within the copolymer causes the polymer to become more soluble within the DOP, and thus, lowering the UCST

for each polymer. This result was mirrored with the inclusion of MMA within the polymer, however the increased length of the alkyl chain led to a more profound change. This is best represented with the comparison of PSMMA 2 and PSEMA 3, which have similar mol% of the comonomer (3.4 and 3.32 mol% respectively) and M_w . The UCST of PSMMA 2 was found to be at $-0.5\text{ }^{\circ}\text{C}$ whereas the UCST of PSEMA 3 was observed at $-4.6\text{ }^{\circ}\text{C}$ with a difference of $4.1\text{ }^{\circ}\text{C}$. This increased effect of EMA's presence upon the UCST is also exhibited with the lack of a phase transition occurring for PSEMA 6 with 11.8 mol% of EMA. PSMMA 6 contained 14.3 mol% of MMA though still exhibited a UCST at $-10.7\text{ }^{\circ}\text{C}$. Therefore, inclusion of monomers with long chains increased the solubility of the copolymer as expected, and thusly, lowered the UCST point.

1.3.2.3 EA

Increasing the alkyl pendant group from methyl to ethyl indicated an increased lowering of the UCST point for PSEMA over PSMMA. Therefore EA was used to investigate whether removing the methyl group along the backbone of the polymer would affect the UCST point at all. No previous reports upon the phase transition of pure PEA (either LCST or UCST like) have been found, though we believed the removal of the methyl group will increase the UCST from similar polymers of EMA.

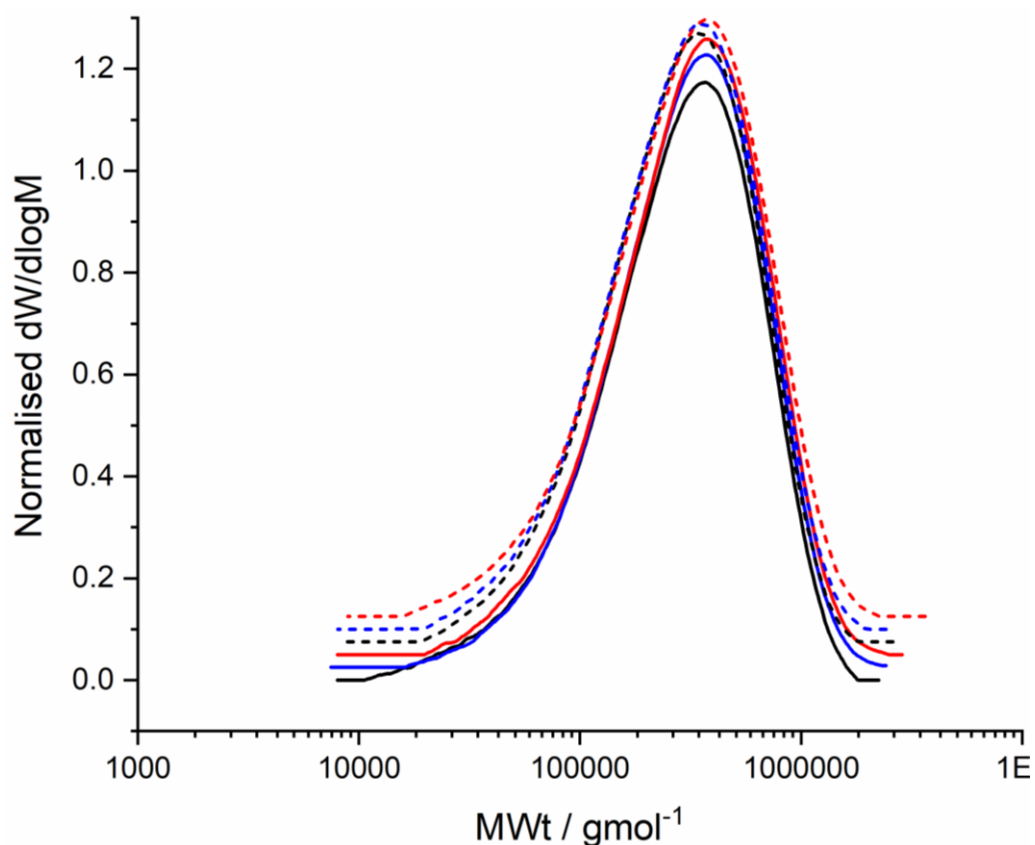


Figure 1-26. Offset SEC traces of the polymers synthesised from the polymerisation of different concentrations of styrene and EA after 1 hour at 140 °C. The traces are — PSEA 1, — PSEA 2, — PSEA 3, -- PSEA 4, -- PSEA 5, and -- PSEA 6.

Similar to both PSMMA and PSEMA, PSEA series shows no sign of either low or high molecular weight shoulders in the SEC curves (**Figure 1-26**). The copolymerisation of EA and styrene was undertaken using the same conditions as with previous polymerisations. However, as **Table 1-5** shows, the M_w of the polymers were slightly higher than that found in PSEMA (**Table 1-3**).

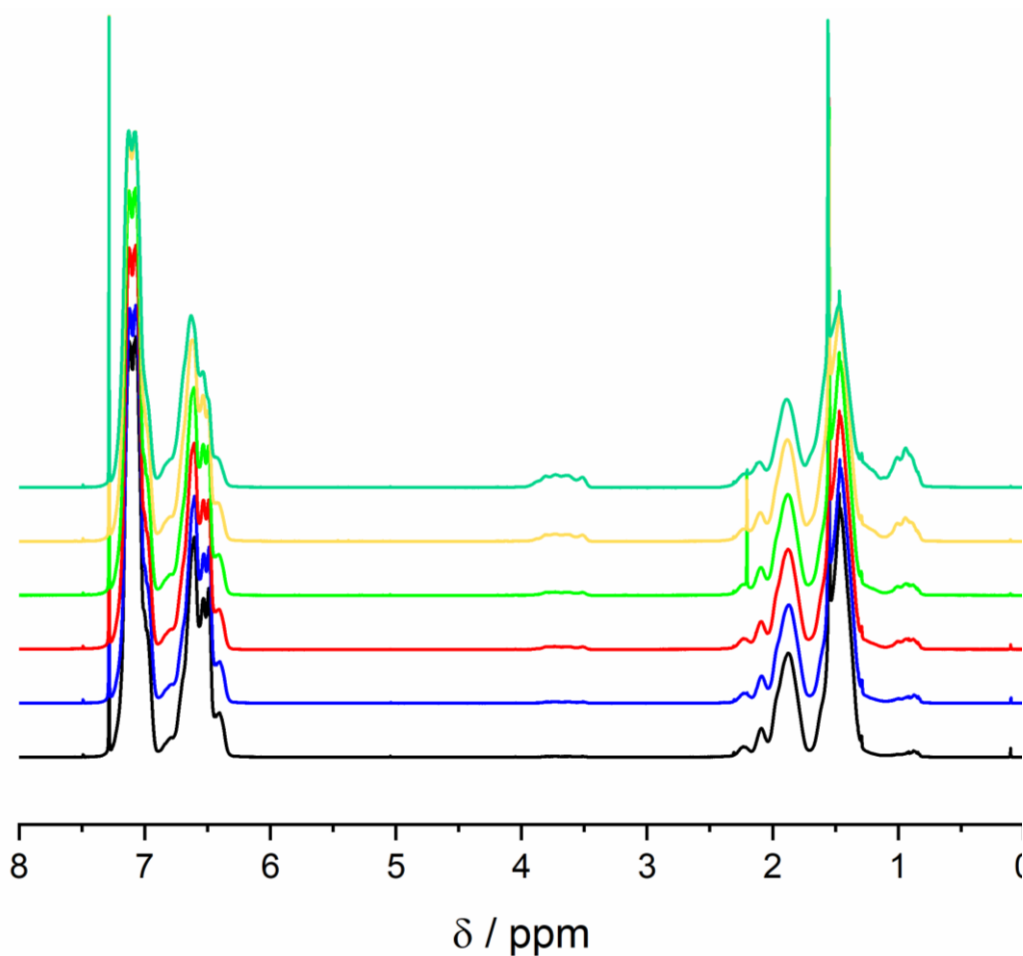


Figure 1-27. NMR spectrum of (—) PSEA 1, (—) PSEA 2, (—) PSEA 3, (—) PSEA4, (—) PSEA 5, and (—) PSEA 6 in CDCl₃.

As there are no vinyl/monomer peaks present within the polymer series (**Figure 1-27**), the composition of the polymer was calculated and reported in **Table 1-5**.

Table 1-5. Tabulated data for EA containing polymers recorded from NMR, SEC, and Equation 1.33.

Sample	$M_w /$ kg·mol ⁻¹	\bar{D}	EA Feed / mol%	Polymer EA / mol %	Predicted EA / mol%	Yield / %
PSEA 1	361	2.01	0.55	2.31	0.56	30.49
PSEA 2	382	1.84	1.05	3.33	1.1	30.97
PSEA 3	392	1.83	2.08	3.75	2.1	28.61
PSEA 4	354	1.81	2.4	4.00	2.4	29.56
PSEA 5	365	1.82	5.2	6.47	5.1	31.98
PSEA 6	383	1.92	10.4	11.1	9.8	30.97

Each copolymer was found to dissolve into DOP to form a homogeneous mixture. Upon cooling, all solutions exhibited a phase transition with the recordable range. Please refer to **Appendix II Figure 7-5** for the phase change curves. The phase diagram (**Figure 1-28**) was created from the inflection points of these phase change curves.

Penlidis *et al.* reported the ratios to be $r_{\text{Sty}} = 0.974$ and $r_{\text{EA}} = 0.222$.²⁶³ Again this system tends towards the fourth system where the polymer formed is a statistical copolymer of both monomer systems. The Mayo-Lewis plot using these ratios (**Appendix II Figure 7-2**) indicates an equal incorporation of both EA and styrene units within the polymer at low feed rates. With the

PSEA series, the polymers are likely to show a greater homogeneity than the previous polymer systems, blurring the UCST less because of this. The polymers obtain also show a higher incorporation of EA units than predicted using the instantaneous polymerisation equation. As the conversion is not at 100 %, it is likely the polymer chains formed will so a greater heterogeneity. This difference could affect the curve obtained.

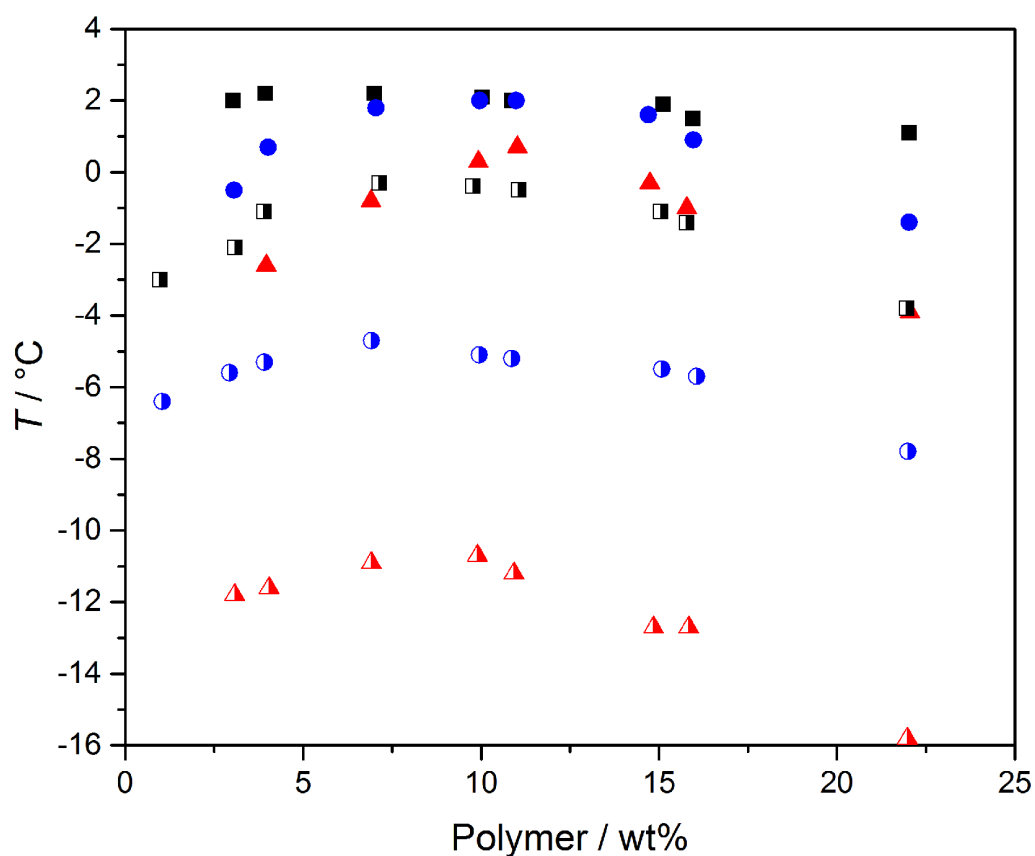


Figure 1-28. Phase diagram of PSEA 1 (■), PSEA 2 (●), PSEA 3 (▲), PSEA 4 (◻), PSEA 5 (◐), and PSEA 6 (▲) in DOP.

Table 1-6. UCST data for the PSEA series from **Figure 1-28**.

	PSEA 1	PSEA 2	PSEA 3	PSEA 4	PSEA 5	PSEA 6
UCST	2.3 °C	2.0 °C	0.7 °C	-0.3 °C	- 4.7 °C	- 10.7 °C

Similar to both the PSMMA and PSEMA series, increased incorporation of EA into the copolymer lead to a decrease in the UCST point (**Table 1-6**). However, whilst the increased inclusion of EA within the polymer, only slight changes in the UCST were observed between 2.31 – 4.06 mol% (PSEA 1-4) at 2.3 to -0.3 °C. Upon increasing the mol% of EA to 6.47 a large difference in UCST was observed at – 4.7 °C, indicating that in small quantities, EA has very little effect on the overall system. This is further shown when compared with the PSMMA series. PSMMA 2 and PSEA 2 have similar mol% of comonomer present in the end polymer (3.36 and 3.33 mol% respectively). The polymers both show a decrease in UCST from the pure PS system though PSMMA 2 UCST was found to be -0.5 °C whilst PSEA 2 only exhibited a UCST at 2.0 °C. Whilst M_w of PSEA 2 is higher than that of PSMMA 2, the phase change should not be altered by 2.5 °C by small difference in M_w alone. The polymers are likely to exhibit a greater heterogeneity due to the larger incorporation of EA units than predicted. However, the curves obtained (**Appendix II Figure 7-5**) exhibit no initial phase change at temperatures seen with the pure PS.

PSEA also demonstrated the effect of no methyl group presence along the polymeric backbone. Comparing similar mol% of EA and EMA presence

within the copolymer shows a drastic difference in UCST. PSEMA 2 and PSEA 1 contain the same mol% of comonomer within them (2.31 mol%). However, the difference in UCST between these systems is 4.1 °C. This large difference is further shown between PSEMA 4 (4.05 mol% EMA) and PSEA 4 (4.00 mol% EA) where the UCSTs are -5.2 °C and -0.3 °C respectively. It is finally shown between both PSEMA 6 (11.8 mol% EMA) and PSEA 6 (11.1 mol% EA). PSEMA 6 exhibited no phase transition at all due to the high solubility within DOP whereas PSEA 6 exhibited a UCST at -10.7 °C. It is clear from the comparison of the PSEA and PSEMA series that the presence of the methyl group along the polymeric back bone has a substantial effect on the overall phase transition temperatures of the system. It was hypothesised that this was due to the methyl group adding some steric hindrance along the backbone where the DOP molecules could interact. When the polymer possess no groups along that chain, it becomes harder for the DOP to solubilise the polymer until large quantities of the EA comonomer were present.

1.3.2.4 2EHA

2EHA has a similar molecular structure to that of the side chain moieties of DOP, suggesting that it would possess a high affinity to solubilise within the solvent. Presence of 2EHA within the copolymer should therefore reduce the phase transition temperature to a higher degree than the previous monomer with a smaller presence within the polymer itself.

Copolymer data of poly(styrene-*co*-2-ethyl hexyl acrylate) (PS2EHA) is shown in **Table 1-7**. The data shows that very high molecular weight

polymers and high \bar{D} polymers were obtained. The cause of these high molecular weights is due to the chain transfer to polymer during the polymerisation which can be observed.^{264,265} Due to the large molecular weights caused by chain transfer to polymer, the solutions of DOP containing 2EHA exhibited a more gel-like consistency. The larger M_w were observed upon increasing the 2EHA presence within the polymerisation mixture (Figure 1-29).

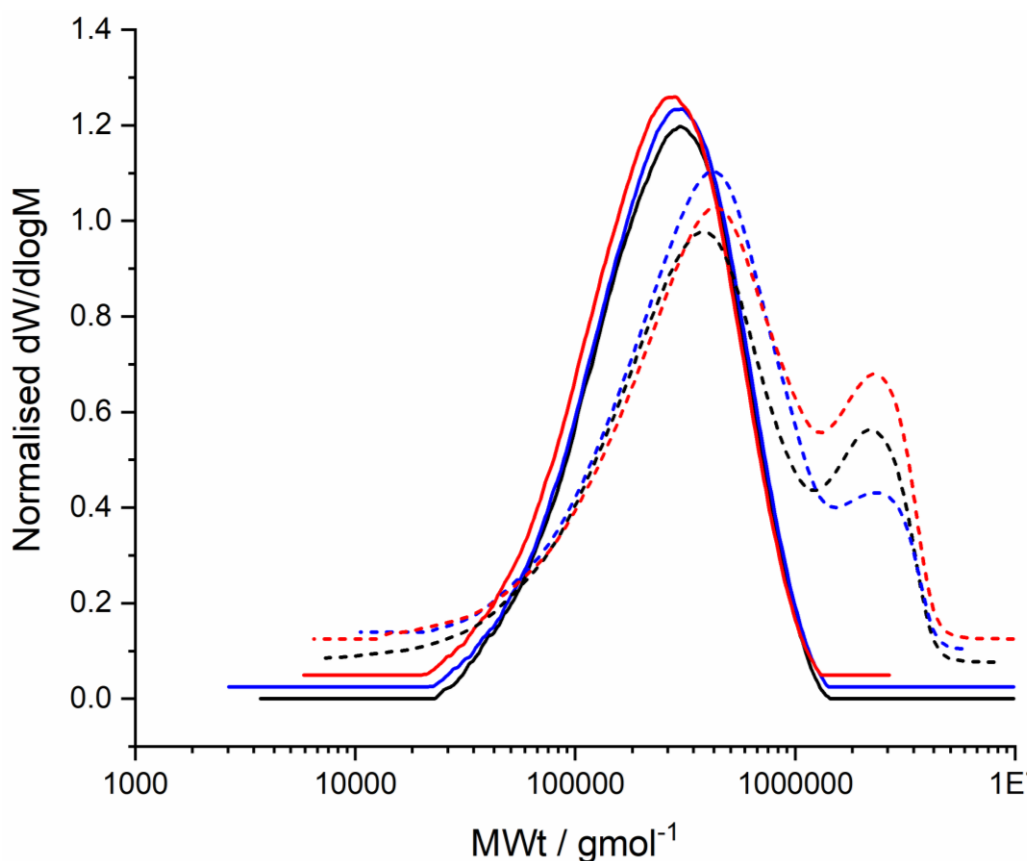


Figure 1-29. Offset SEC traces of the polymers synthesised from the polymerisation of different concentrations of styrene and 2-EHA after 1 hour at 140 °C. The traces are — PS2EHA 1, — PS2EHA 2, — PS2EHA 3, -- PS2EHA 4, -- PS2EHA 5, and -- PS2EHA 6.

SEC traces of the PS2EHA 4-6 all show a high molecular weight shoulder (**Figure 1-29**). This is indicative of chain-chain termination/coupling where polymer chains effectively double in molecular weight by 2 growing chains joining.

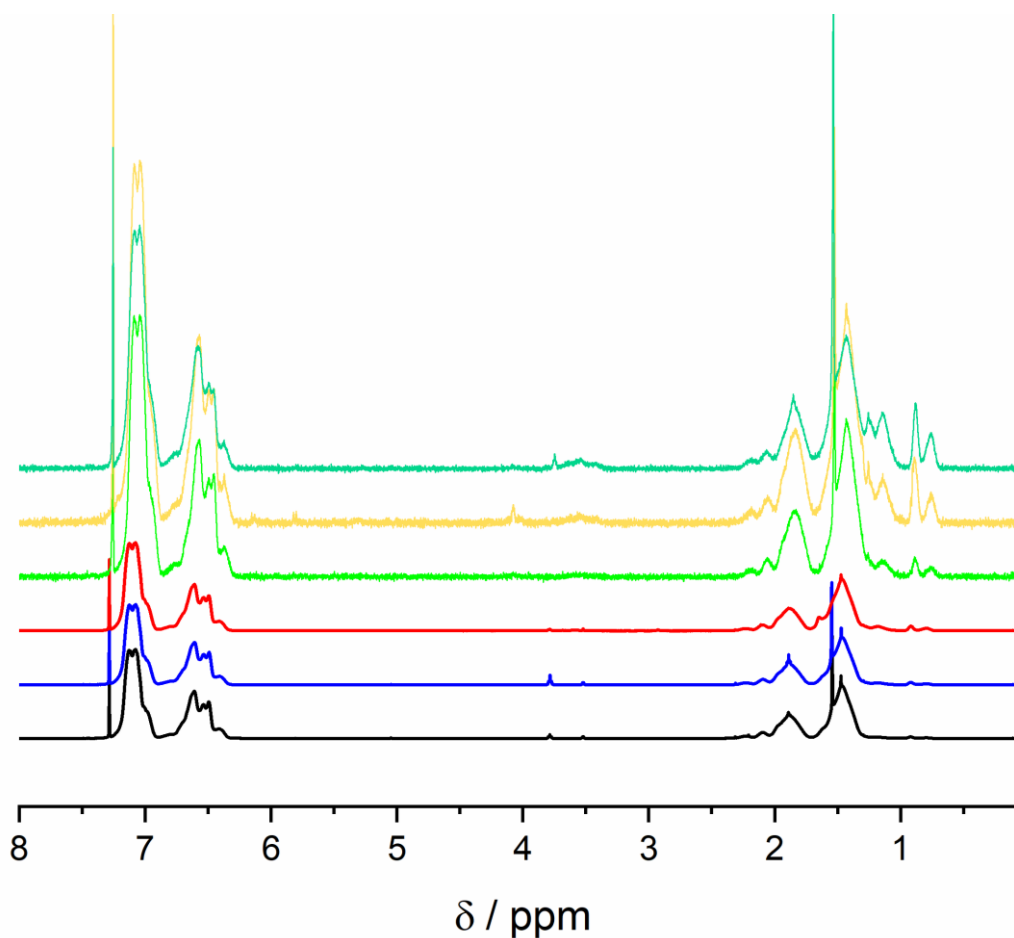


Figure 1-30. NMR spectrum of (—) PS2EHA 1, (—) PS2EHA 2, (—) PS2EHA 3, (—) PS2EHA 4, (—) PS2EHA 5, and (—) PS2EHA 6 in CDCl_3 .

The NMR spectra of the PS2EHA series (**Figure 1-30**) indicate no monomer groups present within the isolated polymer. Monomer composition is tabulated in **Table 1-7**.

Penlidis *et al.* reported the ratios to be $r_{\text{Sty}} = 0.979$ and $r_{\text{2EHA}} = 0.292$.²⁶⁶ It should be noted that whilst the paper did investigate the bulk polymerisation of styrene and 2EHA, it was undertaken at 80 °C instead of

140 °C. Therefore the r values may differ. With similar r values as seen with EA, the polymers formed in this system will be a random copolymer. The Mayo-Lewis plot using these ratios (**Appendix II Figure 7-2**) indicates a similar incorporation of both 2EHA and styrene units within the polymer at low feed rates. Coupled with the conversion reaching only ~30 % in all cases, the end polymers will show a higher degree of homogeneity. All the polymers, including the system that don't show coupling, exhibited a higher inclusion of 2EHA units than the predicted mol%. Whilst the r values obtained do refer to an 80 °C bulk reaction, the values should not differ largely. The large difference between values is a clear indicator that more heterogeneous polymers have been formed. Further evidence of heterogeneous polymer chains forming is the presence of the high molecular weight shoulder caused by polymer chain-chain coupling.

Table 1-7. Tabulated data for 2EHA containing polymers recorded from NMR, SEC, and Equation 1.33.

Sample	$M_w /$ $\text{kg}\cdot\text{mol}^{-1}$	\bar{D}	2EHA Feed / mol%	Polymer 2EHA / mol %	Predicted 2EHA / mol%	Yield / %
PS2EHA 1	309	1.75	0.29	0.8	0.3	30.01
PS2EHA 2	308	1.72	0.57	1.4	0.6	30.00
PS2EHA 3	520	3.93	1.15	1.7	1.2	34.00
PS2EHA 4	760	3.76	1.31	2.3	1.3	30.11
PS2EHA 5	683	2.88	2.89	4.3	2.89	30.24
PS2EHA 6	859	3.22	5.91	8.3	5.8	31.23

Upon dissolving the copolymers within DOP, highly viscous homogeneous oils were made. As each solution was cooled at different wt%, only 3 samples appeared to undergo a full transition (PS2EHA 1, PS2EHA 2, and PS2EHA 3). The phase diagrams shown in **Figure 1-31** was made using the phase change graphs (see **Appendix II Figure 7-6**).

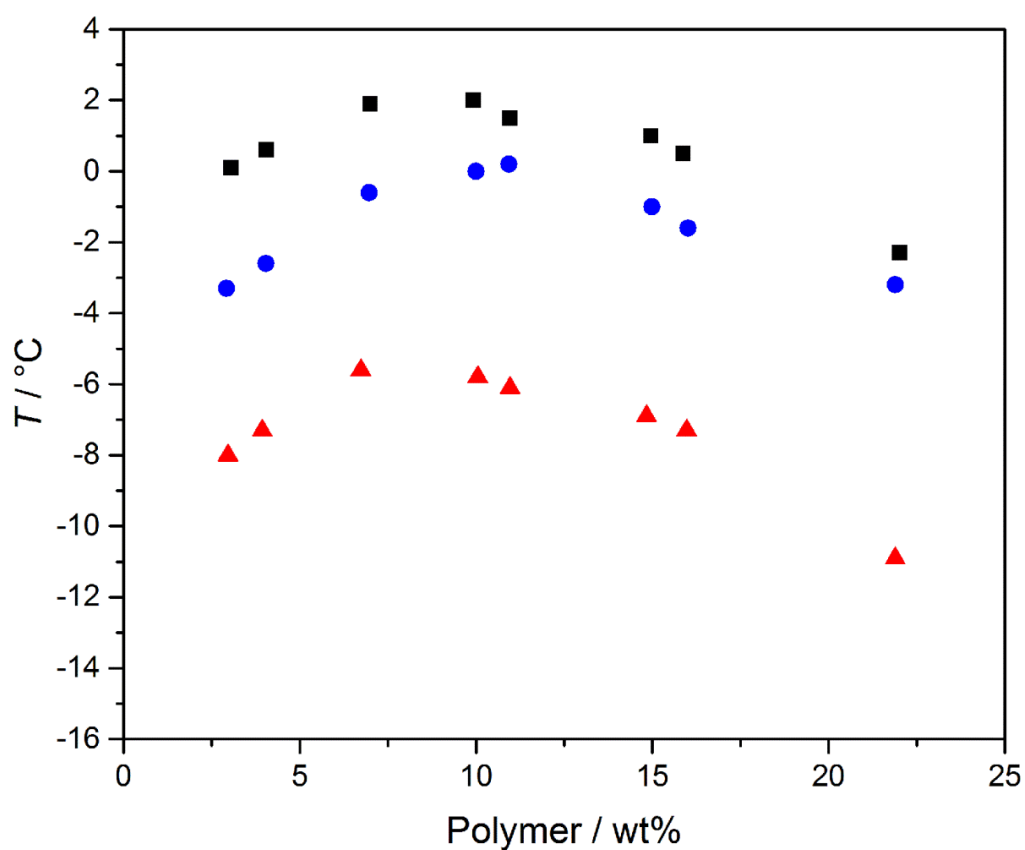


Figure 1-31. Phase diagram of PS2EHA 1 (■), PS2EHA 2 (●), and PS2EHA 3 (▲) in DOP.

Table 1-8. UCST data for the PS2EHA series from **Figure 1-31**.

	PS2EHA 1	PS2EHA 2	PS2EHA 3	PS2EHA 4	PS2EHA 5	PS2EHA 6
UCST	2.0 °C	0.2 °C	- 5.6 °C	n/a	n/a	n/a

Similar to the PSEA series, the PS2EHA polymers possess no methyl group along the polymeric backbone. However, unlike EA, 2EHA does possess

a very large ethyl hexyl pendant group with the same chemical structure of the side arms found within DOP. The phase diagram in **Figure 1-31** and data shown in **Table 1-8** clearly show that inclusion of 2EHA has a profound effect on the UCST to the point that PS2EHA 4 has a phase transition just starting at $\sim -17\text{ }^{\circ}\text{C}$ (**Appendix II Figure 7-6**) though a full curve cannot be made and, therefore, no inflection point obtained. Very low incorporation of 2EHA within the copolymer (PS2EHA 1 with 0.8 mol% 2EHA) exhibited a shift of UCST down to $2\text{ }^{\circ}\text{C}$, lower than all other systems with low incorporation (PSMMA 1, PSEMA 1, and PSEA 1). Further increase in the 2EHA content to 1.4 mol% led to a decrease in UCST to $0.2\text{ }^{\circ}\text{C}$. To obtain a similar result using EA, incorporation needed to be at 3.75 mol%. A drastic drop in UCST was observed with the increase in mol% to 1.7 (PS2EHA 3) from 1.4 (PS2EHA 2). The UCST for PS2EHA 3 was found to be at $-5.6\text{ }^{\circ}\text{C}$, a temperature far below similar incorporated polymers. For similar results with MMA, EMA, or EA the incorporation of comonomer is needed to be 10.4 mol%, 4.1 mol%, or 6.47 mol% respectively indicating that the bulky alkyl group has a very large effect on solubility. Surprisingly, PS2EHA 3 also exhibited a very high M_w ($520\text{ kg}\cdot\text{mol}^{-1}$) in comparison to other polymers. It would be expected that high molecular weight polymers would occupy a larger number of lattice sites within the system (**Equation 1-5**) which in turn would lead to a higher temperature UCST. Therefore it is reasonable to assume that a lower molecular weight PS2EHA would exhibit an even lower UCST. A possible cause for this high molecular weight seen in the polymers containing 2EHA is due to transfer to polymer as stated earlier. The result of transfer to polymer

is a polymeric chain with a branched unit where polymerisation has occurred. It has been shown in the past that branched polymers often exhibit a lower UCST point than linear due to more favourable polymer – polymer pair interactions occurring due to the close confinement.^{267,268} Incorporation of 2EHA within a polymer clearly shows a decrease in phase transitional temperatures across all wt% to the point at which no transitions can be observed for both PS2EHA 5 and 6. (4.3 mol% and 8.3 mol% respectively).

1.3.2.5 LA

LA was employed as a comonomer due to its long alkyl chain (12 carbons long) imparting large hydrophobic moieties similar to 2EHA though in a less sterically hindered state. The longer pendant chains should increase its solubility within DOP and, thus, lower the phase change temperatures of the systems containing the copolymer.

Data of the poly(styrene-*co*-lauryl acrylate) (PSLA) copolymer is shown in **Table 1-9**. The polymers obtained show a higher M_w than that seen in the previous systems, which is due to the larger molar mass of the LA monomer in comparison. Whilst the M_w of PSLA 1-6 are large, they are still within a similar range of those found for PSMMA, PSEMA, and PSEA.

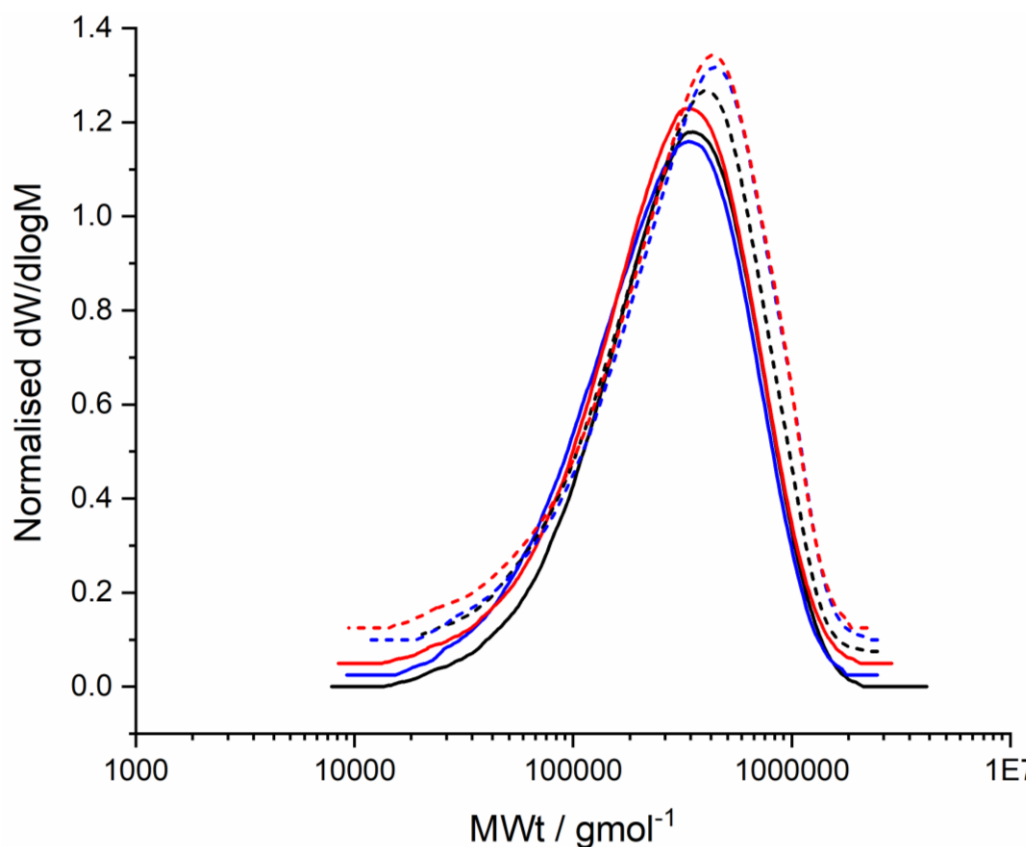


Figure 1-32. Offset SEC traces of the polymers synthesised from the polymerisation of different concentrations of styrene and LA after 1 hour at 140 °C. The traces are — PSLA 1, — PSLA 2, — PSLA 3, -- PSLA 4, -- PSLA 5, and -- PSLA 6.

The PSLA series express a higher molecular weight than those observed in the smaller molecular weight counterpart (MMA and EMA). However, unlike 2EHA, no larger molecular weight shoulders can be observed in the SEC trace (**Figure 1-32**). This is due to LA not containing the same labile H present in 2EHA.

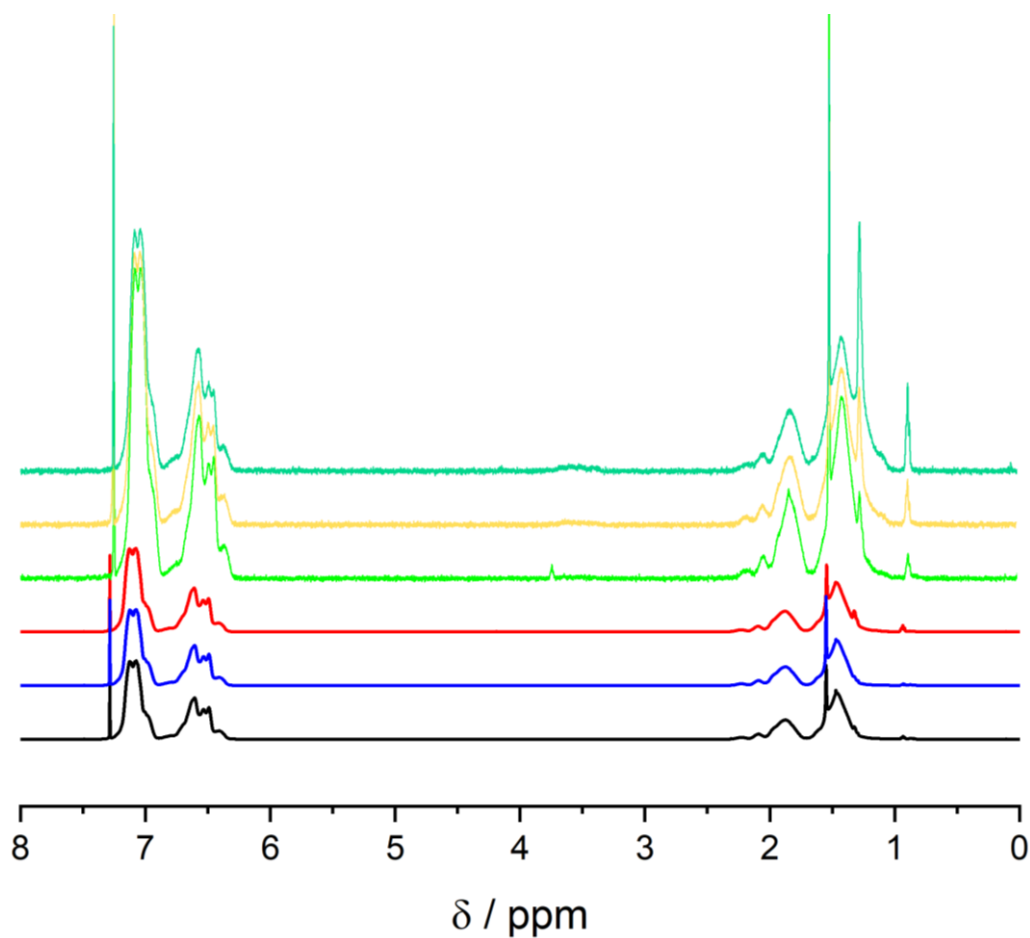


Figure 1-33. NMR spectrum of (—) PSLA 1, (—) PSLA 2, (—) PSLA 3, (—) PSLA 4, (—) PSLA 5, and (—) PSLA 6 in CDCl_3 .

The composition of the PSLA series was determined using the NMR spectra (**Figure 1-33**) and tabulated in **Table 1-9** as no monomer peaks can be observed.

Similar to ethyl methacrylate, no values for LA could be found. However, Janovi and coworkers previously reported the ratios to be $r_{\text{Sty}} = 0.52$ and $r_{\text{LMA}} = 0.42$.²⁶⁹ These values are similar to those seen with MMA, the

polymers formed in this system will be a random copolymer. The Mayo-Lewis plot using these ratios (**Appendix II Figure 7-2**) indicates a larger incorporation of the LA units over styrene within the polymer at low feed rates. PSLA 6 is an indicated that all the polymers formed with show a large homogeneity. The initial feed only contained 4.59 mol% LA units whilst the end polymer contained 6 mol% LA. The system was stopped at 30 % conversion, otherwise the polymers formed at the end of the reaction would show dramatically different UCST behaviour than those at the beginning as they would be largely styrene homopolymers. The polymers formed exhibited LA both in higher and lower amounts than that predicted using the Mayo-Lewis equation. As these values are close, it can be assumed the end polymers will exhibit some heterogeneity between the polymer chains, but overall be largely homogenous. However, if the reaction was left to go further, the polymers synthesised later would exhibit a much lower concentration of LA than the initial. This would lead to a very mixed UCST curve being formed where the temperature change would spread from pure polystyrene down to nothing as seen with PSLA 5 and PSLA 6 (**Figure 1-34**).

Table 1-9. Tabulated data for LA containing polymers recorded from NMR, SEC, and Equation 1.33.

Sample	$M_w /$ $\text{kg}\cdot\text{mol}^{-1}$	\bar{D}	Feed LA / mol%	Polymer LA / mol %	Predicted LA / mol%	Yield / %
PSLA 1	393	1.64	0.22	0.7	0.42	29.49
PSLA 2	340	1.92	0.44	0.9	0.84	31.00
PSLA 3	371	1.90	0.88	1.4	1.6	30.60
PSLA 4	384	1.94	1.01	2.6	1.9	30.00
PSLA 5	427	1.87	2.23	3.2	4.1	31.06
PSLA 6	414	1.91	4.59	6.0	7.9	30.00

The copolymers formed a homogenous system at room temperature after overnight stirring at 60 °C. However, upon cooling, phase transitions were only observed within the PSLA 1-4 systems with no phase change occurring for PSLA 5 or PSLA 6 within the recordable region due to the higher solubility imparted by the large incorporation of LA into the system. The grey value change for each solution was recorded (See **Appendix II Figure 7-7**) and the inflection points of the curves used to create the phase diagram (**Figure 1-34**).

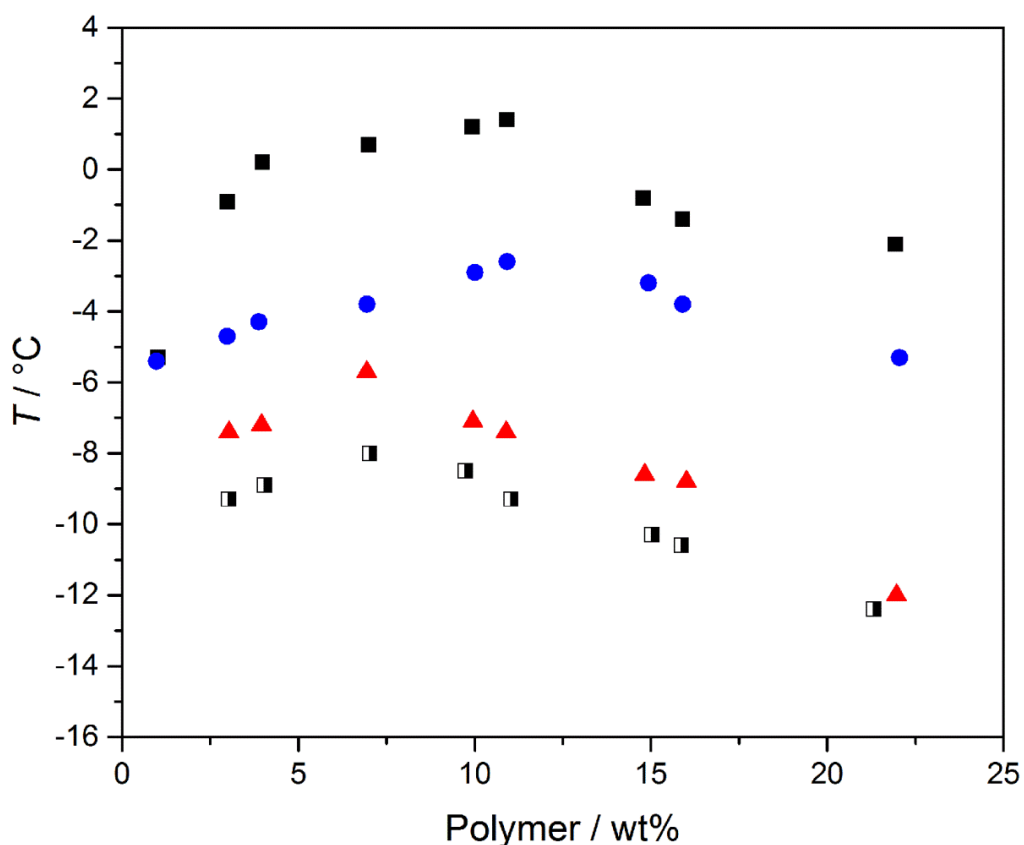


Figure 1-34. UCST curve of PSLA 1 (■), PSLA 2 (●), PSLA 3 (▲), and PSLA 4 (◼) in DOP.

Table 1-10. UCST data for the PSLA series from **Figure 1-34**.

	PSLA 1	PSLA 2	PSLA 3	PSLA 4	PSLA 5	PSLA 6
UCST	1.4 °C	- 2.6 °C	- 5.7 °C	- 8.0 °C	n/a	n/a

From both **Figure 1-34** and **Table 1-10** it is clear that the addition of large lauryl alkyl chain into the copolymer imparted a strong change in transitional temperature to the system. PSLA 1 contains 0.7 mol% LA units within the end copolymer, however the UCST point (1.4 °C) is lower than that

of PS2EHA 1 (0.8 mol% 2EHA) at 2.0 °C. This difference in UCST point is the first indicator that the lauryl alkyl chains have a greater effect on the UCST point than the 2-ethyl hexyl chains. Further evidence of LA imparting a greater change in phase change temperature is seen in PSLA 3. This copolymer contains 1.4 mol% LA within the copolymer and exhibits a UCST point at - 5.7 °C. In comparison, PS2EHA 2 also contains 1.4 mol% of 2EHA whereas the UCST point was shown to occur at 0.2 °C, 5.5 °C higher than that of PSLA 3. Increasing the LA content to 2.6 mol% further decreased the UCST point to - 8.0 °C, far lower than that observed within the PS2EHA systems. Similarly to 2EHA, increasing the comonomer content to 3.2 mol% and above led to the systems becoming fully soluble at all temperatures with no phase change occurring. The PSLA copolymer series do exhibited slightly higher M_w than the PS2EHA series, however this would only impart a very small change in phase transition temperatures. Therefore, this indicates that long alkyl chains have a greater effect on the transitional temperatures than bulky polymers.

1.3.2.6 NIPAM

As stated earlier, NIPAM is a commonly used monomer to synthesis polymers that have thermoresponsive behaviour in water.^{132,137} However, whilst many publications show the LCST behaviour of PNIPAM based polymers in water and small chain alcohols, to the best of our knowledge, none have shown thermoresponsive behaviour in oils.

Copolymerisation of NIPAM with Styrene under the same conditions resulted in polymers with slightly higher M_W and \mathcal{D} than obtained for the previous copolymers (**Table 1-11**).

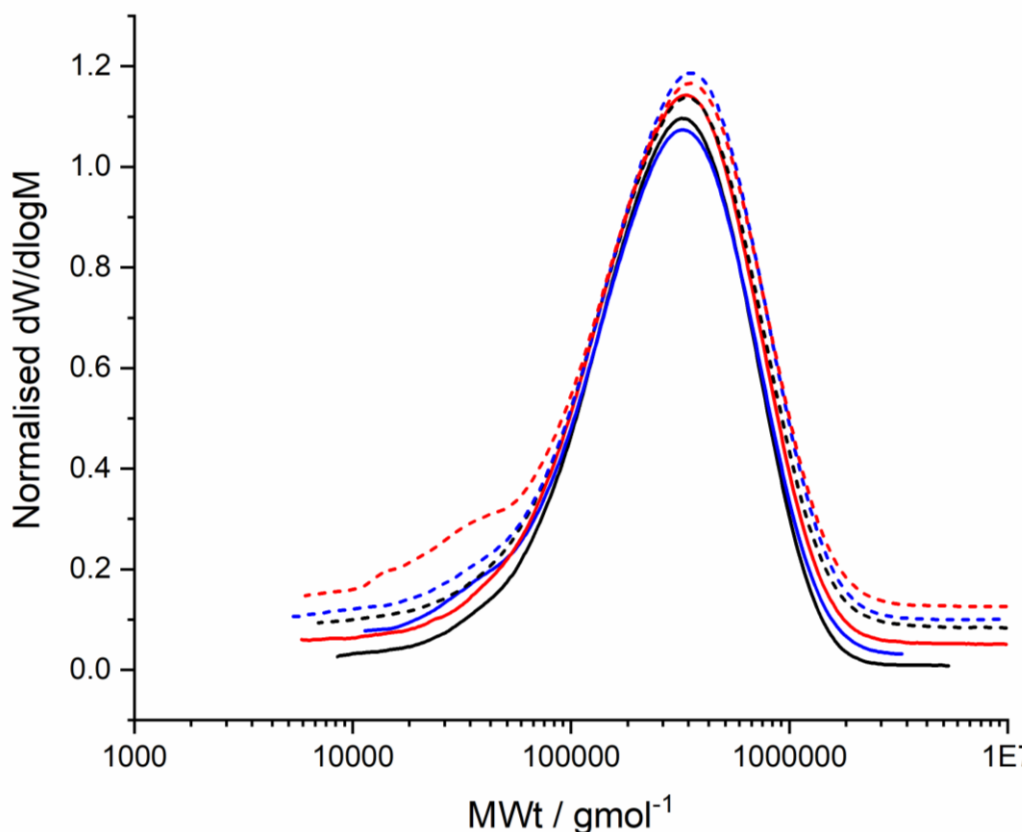


Figure 1-35. Offset SEC traces of the polymers synthesised from the polymerisation of different concentrations of styrene and NIPAM after 1 hour at 140 °C. The traces are — PSNIPAM 1, — PSNIPAM 2, — PSNIPAM 3, -- PSNIPAM 4, -- PSNIPAM 5, and -- PSNIPAM 6.

Unlike the other polymer series, PSNIPAM 6 shows a low molecular weight shoulder present in the end polymer (**Figure 1-35**). This is possibly due to homopolymerisation of the NIPAM monomer units.

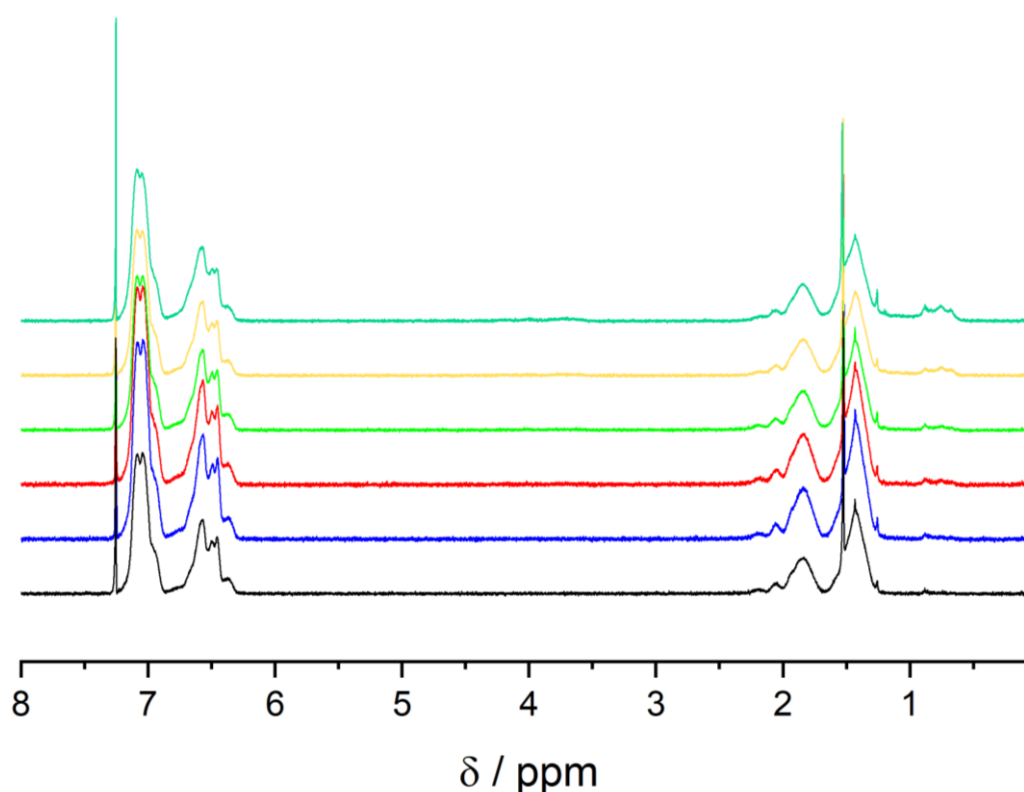


Figure 1-36. NMR spectrum of (—) PSNIPAM 1, (—)PSNIPAM 2, (—)PSNIPAM 3, (—)PSNIPAM 4, (—)PSNIPAM 5, and (—)PSNIPAM 6 in CDCl_3 .

Neither NIPAM monomer nor styrene monomer can be observed in the isolate polymer NMR spectra (**Figure 1-36**). Therefore the composition of the polymer was determined and tabulated in **Table 1-11**.

Previous reports have not shown r_1 and r_2 values for styrene and NIPAM in wider literature. Values have been reported for acrylamide ($r_{\text{AM}} = 9.14$, $r_{\text{Sty}} = 0.67$)²⁷⁰, *N,N*-dimethylacrylamide ($r_{\text{DMAA}} = 0.23$, $r_{\text{Sty}} = 1.23$)²⁷¹, and *N*-tert-amylacrylamide ($r_{\text{TAA}} = 0.62$, $r_{\text{Sty}} = 3.52$).²⁷² Values reported for TAA will be used due to the closeness in structure of the monomers reported.

Unlike the other systems reported here, this system would follow the 5 case. The polymer will contain a higher concentration of Styrene units than NIPAM units. The Mayo-Lewis plot using numbers determined by Meyer show that in low feed ratios (less than 20 mol%) the end polymer will contain a higher ratio of styrene units within (**Appendix II Figure 7-2**). The predicted composition of NIPAM units is lower than the experimental values obtained in all PSNIPAM systems (**Table 1-11**). This indicates that there is a large difference between polymer chains due to heterogeneity of the polymer. The difference is several % off of each other, though this could be due to no report r values for a pure NIPAM and styrene system. The predicted mol% of NIPAM would result in a polymer that exhibited higher concentration of styrene and therefore should show similar behaviour to that of pure polystyrene. However, incorporation of NIPAM shows a clear decrease in the UCST point, (**Figure 1-37**) indicating that the r values are lower than expected.

Table 1-11. Tabulated data for NIPAM containing polymers recorded from NMR, SEC, and Equation 1.33.

Sample	$M_w /$ $\text{kg}\cdot\text{mol}^{-1}$	\bar{D}	NIPAM feed / mol%	Polymer NIPAM / mol%	Predicted NIPAM / mol%	Yield / %
PSNIPAM 1	366	2.42	0.46	2.3	0.130	28.49
PSNIPAM 2	352	3.06	0.93	2.5	0.266	29.41
PSNIPAM 3	379	2.33	1.87	3.0	0.540	30.20
PSNIPAM 4	438	2.82	2.13	3.0	0.619	28.80
PSNIPAM 5	390	2.46	4.65	4.3	1.388	29.40
PSNIPAM 6	386	2.61	9.3	7.4	2.922	31.00

Each polymer synthesised readily dissolved into DOP to form a homogenous solution. However, upon cooling, only PSNIPAM 1-5 exhibited phase change over the range of wt% chosen. The grey values were recorded for each sample over the range of temperatures (see **Appendix II Figure 7-8**) and the inflection points of each used to create the phase change diagram (**Figure 1-37**).

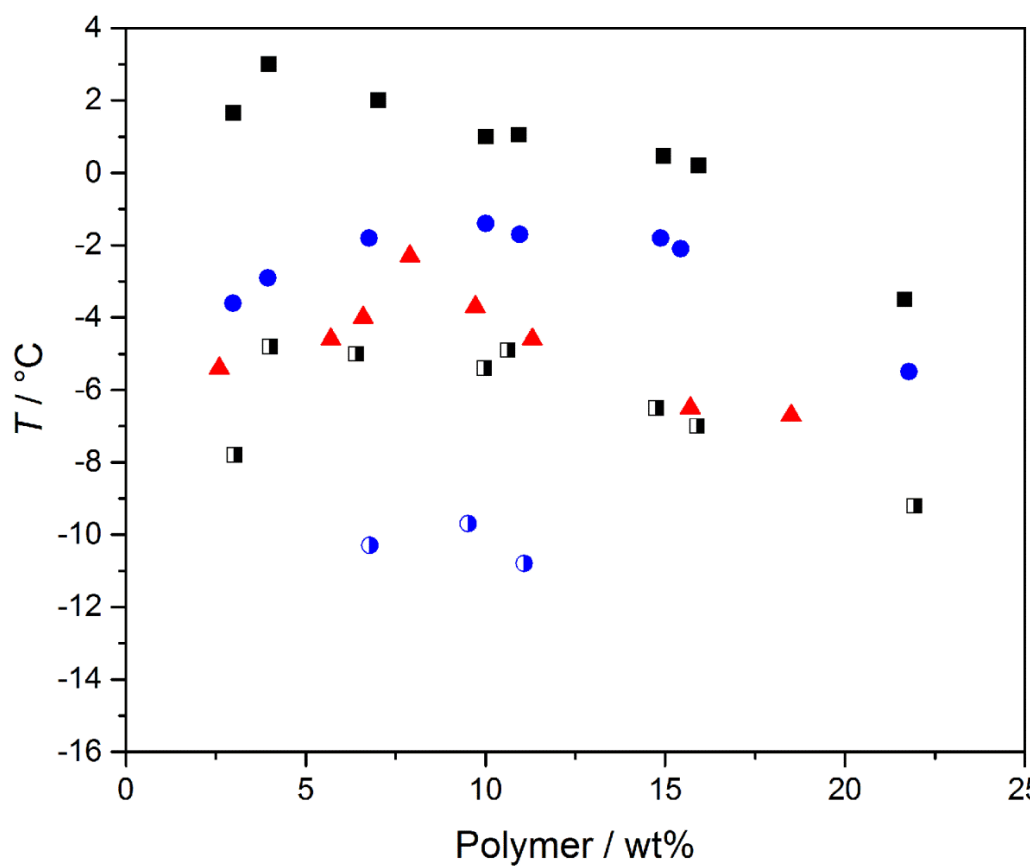


Figure 1-37. UCST curve of PSNIPAM 1 (■), PSNIPAM 2 (●), PSNIPAM 3 (▲), PSNIPAM 4 (□), PSNIPAM 5 (◐), and PSNIPAM 6 (◔) in DOP.

Table 1-12. UCST data of the PSNIPAM series obtained from **Figure 1-37**.

	PSNIPAM 1	PSNIPAM 2	PSNIPAM 3	PSNIPAM 4	PSNIPAM 5	PSNIPAM 6
UCST	3.0	- 1.3	- 2.3	- 4.9	- 9.6	n/a

Figure 1-37 and **Table 1-12** indicate that the inclusion of NIPAM within the polymeric chains proved to have an effect on the UCST as seen with previous comonomers. Unlike previous polymeric systems, inclusion of a low amount of NIPAM (2.3 mol%) in PSNIPAM 1 increased the UCST point for the polymer above that of the pure PS's value (2.6 °C). With increased inclusion of NIPAM, however, a decrease in UCST is observed. Whilst a low temperature of – 9.6 °C is observed with the polymer containing 4.3 mol% NIPAM, the effect on the UCST point is not as profound as that seen with LA. Only a 3.2 mol% incorporation of LA is required before the system becomes fully soluble at all temperature whilst over 4.3 mol% is required for the NIPAM containing systems. Increasing the NIPAM content to 7.4 mol% in PSNIPAM 6 led to a loss in all phase change events. Overall, it can be observed that the wt% of polymer in solution has a large impact on the phase transition of the systems, most notably with PSNIPAM 5 where only three wt% of polymer (6.79, 9.52, and 11.08 wt%) transitioned. This reduction stems from the side arms hydrophobic chains forming a greater entanglement with the DOP molecules whilst hydrogen bonding cannot be formed.

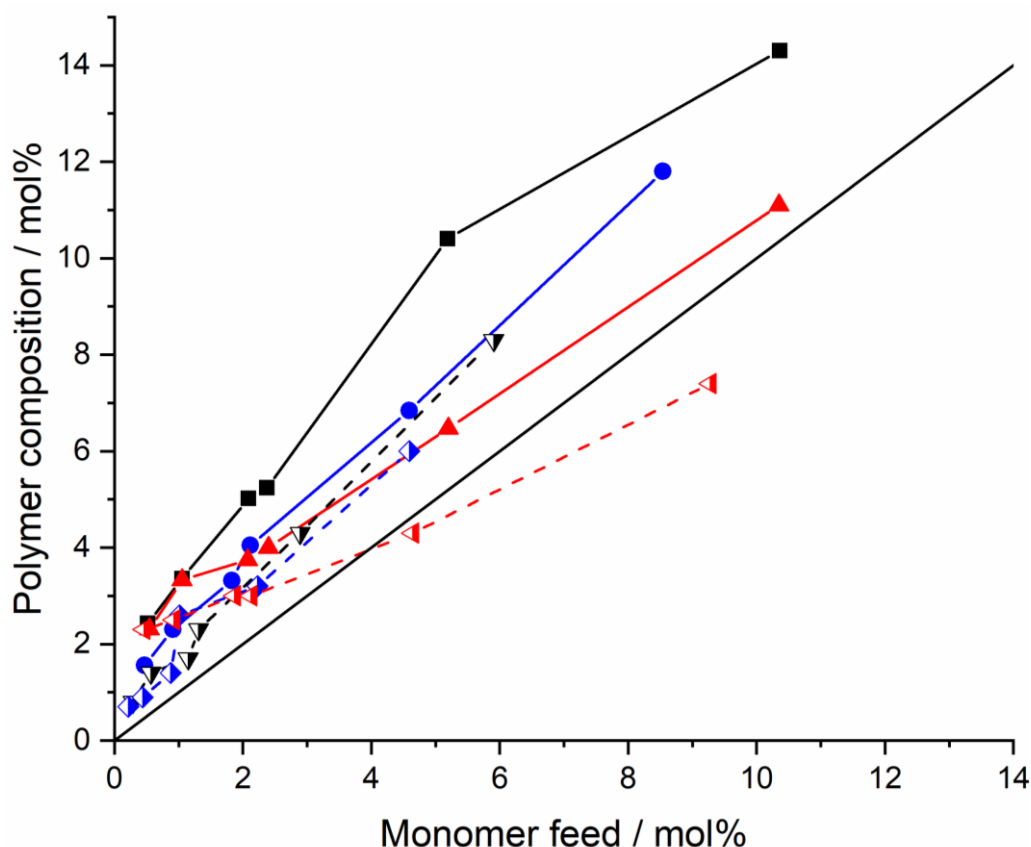


Figure 1-38. Experimental Mayo-Lewis plot of monomer feed versus end polymer composition of comonomer for the (■) PSMMA, (●) PSEMA, (▲) PSEA, (▼) PS2EHA, (◈) PS2LA, and (◄) PSNIPAM series after 1 hours at 140 °C resulting in roughly 30% conversion. The diagonal (—) indicates an azeotropic polymerisation where mol% of monomer in feed and end polymer are equal.

Figure 1-38 shows the experimental Mayo-Lewis plot of all the polymer series after 1 hour at 140°C where all the systems managed roughly 30 % conversion. As seen, only the NIPAM series crosses the azeotropic line where feed and end polymer composition are equal. All the other polymer series remain above the line, where a higher composition of monomer units is

incorporated into the end polymer than in the initial feed. This would not be the case if full polymerisation occurred as then all polymers would revert to the azeotropic line. However, this does indicate that there is likely a compositional drift in all the polymers presently studied. **Figure 1-38** also closely agrees with the Mayo-Lewis plots. An increase in incorporation at low monomer loadings is seen for all systems.

Copolymerisation of styrene with monomers of different length has shown to drastically alter the phase transitional temperature of the polymers dissolved within DOP. The most drastic changes were observed in both the LA and 2EHA systems where the copolymer moieties both exhibit large alkyl chain pendant groups. As well as chain length of the pendant groups, inclusion of methyl groups along the polymeric backbone were shown to decrease the temperature the UCST occurs at indicated by comparison between both the EMA and EA systems.

1.3.2.7 Copolymer Blend

As previously shown, copolymerisation of styrene with monomers exhibiting increasing hydrophobicity indicated a trend for lower phase change temperatures to occur. Whilst literature of polymer blends shows a great number of UCST of polymers blended together in a solid state,²⁷³⁻²⁷⁵ we have been unable to find any that show the effect of dissolving two polymers within a solvent and the effect this has on the phase transition. As the polymers of PS and PSLA 4 have strong, clear transitions where no overlap between the transitions was observed, three solutions containing the weight

ratios 75:25 PS:PSLA 4, 50:50 PS:PSLA 4, and 25:75 PS:PSLA 4 were created and the phase transition recorded (**Figure 1-39**). It was theorised that if a polymer mixture only exhibited a binary phase transition, it would be expected that a shift in temperature onset would occur. However, a system that exhibited a ternary phase change (a system where after the phase change occurred, 3 different phases of solvent rich, polymer A rich, and polymer B rich existed) would show no change in phase change temperature onset but would exhibit differing levels of transition depending on the temperature and composition.

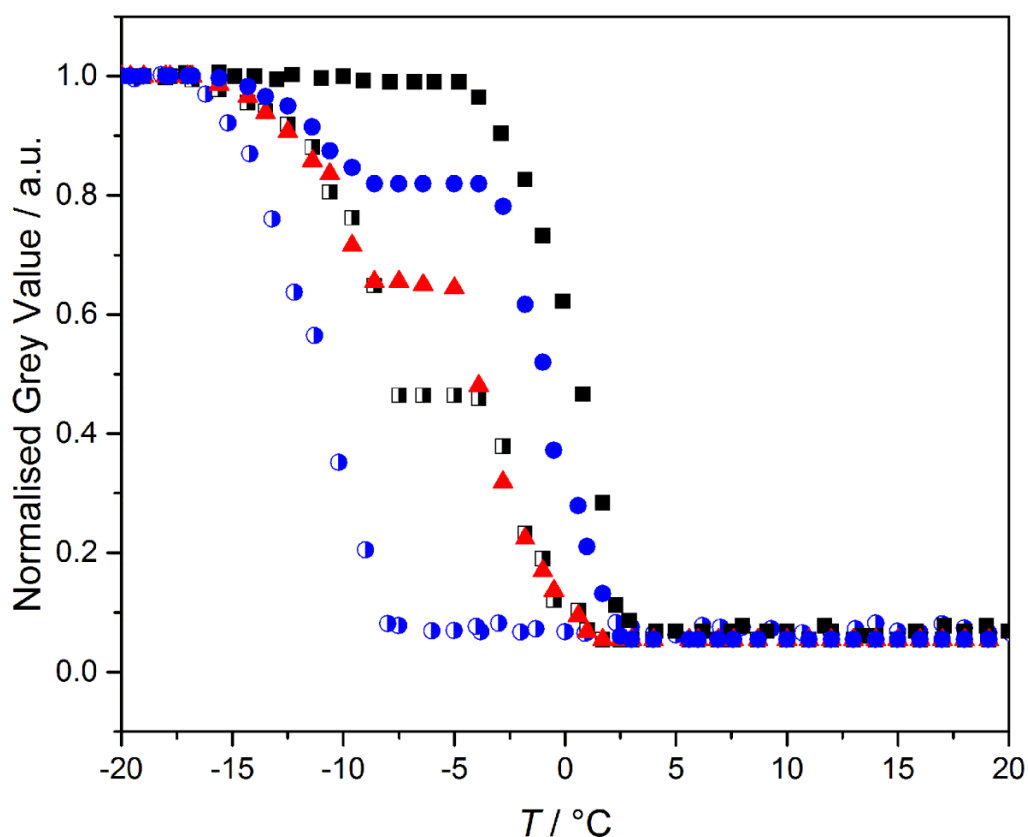


Figure 1-39. Normalised phase transition curves of 10 wt% polymer in DOP solutions of pure PS (■), 75 : 25 weight ratio of PS : PSLA 4 (●), 50 : 50 weight ratio of pure PS :PSLA 4 (▲), 25 : 75 weight ratio of PS : PSLA 4 (□), and PSLA 4 (○).

Figure 1-39 shows the clear transitions of both PS and PSLA 4 in DOP where there is a clear 5 °C region in which there is no overlap between the systems' phase change. This lack of overlap led them to be perfect choices for investigating this blending effect. Upon cooling, all the systems exhibited the phase change onset at the same temperature of the pure PS system. However, due to the mixing of polymers, varying degrees of the transitions occurred after the full temperature range for the PS system was reached. The system

composed of higher weight ratio of PS (75:25 PS:PSLA 4) exhibited a strong initial phase transition starting at the same point of the pure PS system and plateauing 82 % of the way through the overall transition. Upon cooling further to the point of where the PSLA 4 system began its transition, a further increase was observed where the maximum of the transition coincided with the end of the pure PSLA 4 system. This phenomena was also observed within the 50:50 and 25:75 PS:PSLA 4 weight ratio systems where a plateau was exhibited at 65 % and 46 % respectively. The clear plateauing and increased response seen upon further cooling indicates that separate polymer colloids of PS and PSLA 4 are forming with in the DOP solution, creating a system where three phases occur: DOP rich phase, PS rich colloids, and PSLA 4 rich colloids. This indicates that whilst other polymers were present within the solution, they imparted no impact upon the other polymers present. Therefore, it is feasible to form mixtures of multiple polymers within DOP where varying degrees of transition can indicate varying temperatures of a system.

1.3.3 Labels

Thermochromic liquid crystal thermometers are readily available. The essential components are the black backing, LC compound, and the polyester film (**Figure 1-40**). The backing is required to absorb light and not reflect any back through the crystal. The LC compound is required for the thermochromic effect. The polyester film is present to seal the system from external influence.

Using the same principles, prototype labels using PS copolymers in DOP were made. A black label was attached to the cooling plate with glass slides applied on top at the edges to act as a spacer between the bottom sheet and the top layer. Compartments were created by the addition of further rectangular glass segments to form compartments. PS in DOP solutions were added into the compartments and sealed in using a top label with transparent sections. The labels were then heated and cooled accordingly.

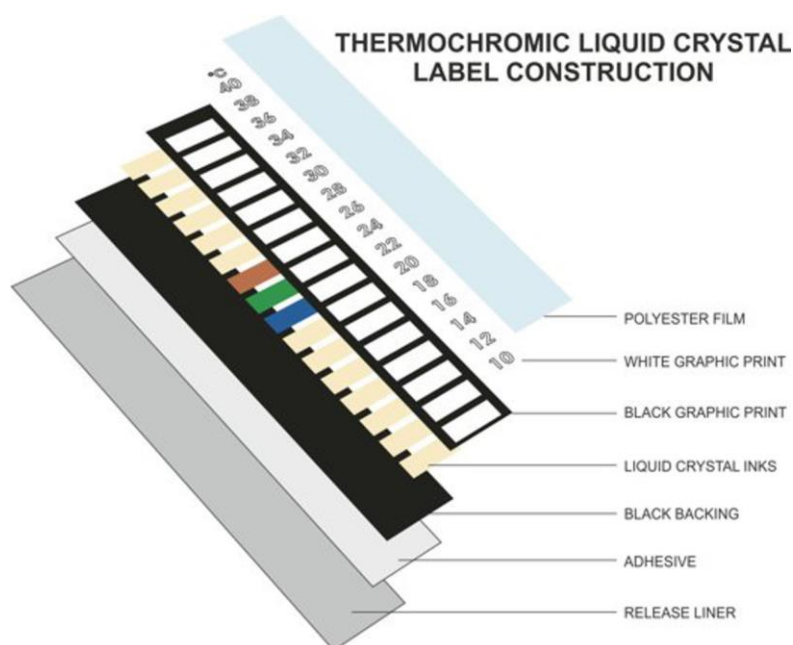


Figure 1-40. Liquid crystal thermometer schematic. Copyright Hallcrest © 2016. ³

Figure 1-41 displays one of the label prototypes. Small quantities of dyes (~10 mg) were added to a 10 wt% PS in DOP solution in order to give a coloured solution. A black background was required to absorb light and not reflect any through the system. Upon cooling below the phase transition

temperature of the solution, the PS phase separated and acted as an opacifier, reflecting light back through the system. Due to the dye residing within the system, a coloured response was seen. The darker dyes (oil blue and rose bengal) demonstrated the greatest contrast between hot and cold states. 4-phenylazophenol still exhibited a change from strongly coloured to weakly though some colour could still be observed (**Figure 1-41 b**).

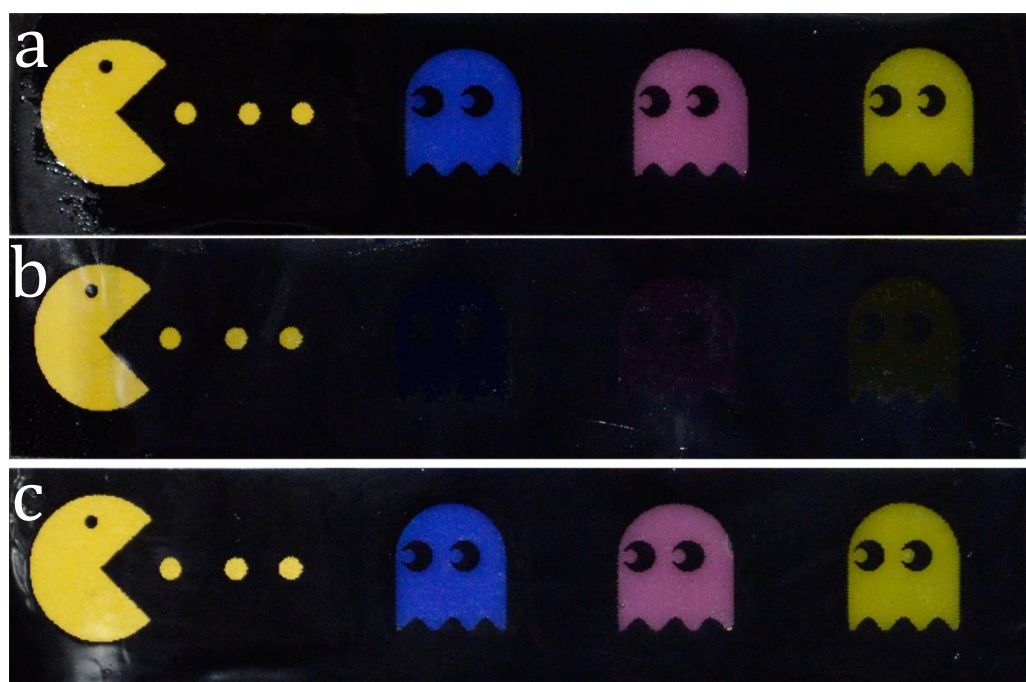


Figure 1-41. Prototype thermochromic strip using 10 wt% PS in DOP when a) cooled below phase transition point, b) warmed above phase transition point, and c) cooled below the phase transition point again. Dyes used were oil blue, rose bengal, and 4-phenylazophenol.

A second prototype, shown in **Figure 1-42**, was made using three different polymers in DOP that exhibited different phase change temperatures. The three polymers were pure PS, PSLA 2, and PSEMA 5

dissolved at 10 wt% with respect to the total solution weight. The temperatures at which a full transition has occurred for 10 wt% pure PS, PSLA 2, and PSEMA 5 in DOP are -3°C , -11°C , and -16°C respectively. These polymer solutions were chosen due to each having no overlap between phase transition temperatures.

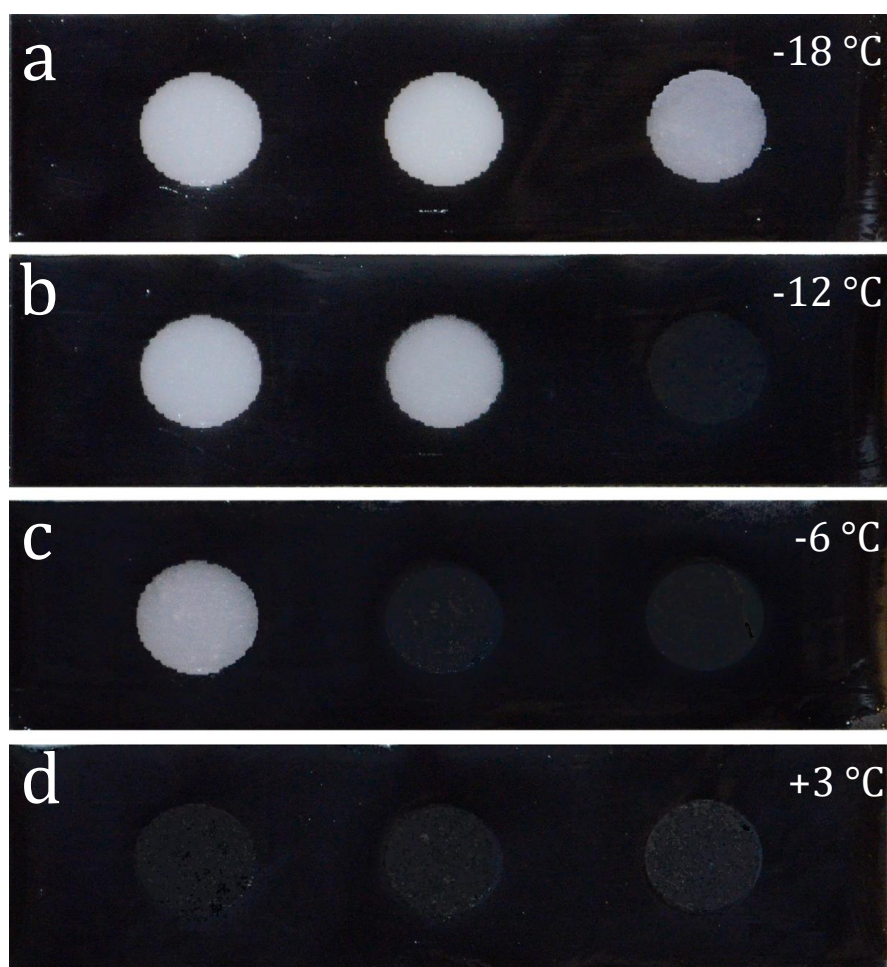


Figure 1-42. Prototype thermochromic label comprised of three different polymeric solutions: 10 wt% of PS, PSLA 2, and PSEMA 5 in DOP. The labels were held at a) -18°C , b) -12°C , c) -6°C , and d) 3°C . The temperature was held for 15 minutes before each photo was acquired.

Figure 1-42 shows the label held at 4 different temperatures where a clear transitional change can be observed upon each sample reaching the phase transition point for each solution. Upon each solution fully transitioning to a homogenous state, a slight discolouration where each of the oils resides still remains. This is due to the refractive index difference between the oil and air, causing some reflection from the oil surface to occur. However, even with this slight greying where the oils exist, a strong transition between phases is still present and, therefore, clearly indicates when the label is lowered to a temperature below each of the phase transition points. It is therefore possible to use a series of oils within a single label to indicate when a certain temperature is reached.

1.3.4 Encapsulation - Capsules

Once the prototype labels were found to be successful, we looked towards incorporation into films. To do this, the solutions must be encapsulated within a shell. The shell would hinder movement of DOP and polymer out into the film whilst also acting as a barrier towards exterior contamination. As previous stated, DOP is a common plasticiser and therefore would swell many potential encapsulation materials. Therefore we looked to use an ionic shell that is both insoluble in DOP and flexible to allow for mixing without breakage due to rigidity.

The encapsulation method proceeded as follows. The gelatin was dissolved in deionised (DI) water at 70 °C in a water jacketed reactor fitted

with overhead stirring. Once fully dissolved, the pH was raised to 8, ensuring gelatin went through its isoelectric point and became neutral. PS in DOP solution (10 wt% PS) was then transferred drop wise to the solution with stirring at 200 rpm. After the solution returned to 70 °C, further water preheated to 70 °C was added and the stirring was increased. Following 15 minutes of stirring, the counter ion (sodium hexametaphosphate solution in DI water) was added before addition of acetic acid. The acid was drop wise added ($1 \text{ drop} \cdot \text{min}^{-1}$) until the pH had reduced to 4.5 and the solution was left for 15 minutes before the heat was removed. The reduction in pH causes the gelatin within the system to revert to its positively charged state, causing an electrostatic attraction between the hexametaphosphate and the gelatin. This attraction causes coacervate colloids to occur within the solution which settle on the interface between the water and PS in DOP droplets formed by the stirring. After 2 hours, an aqueous glutaraldehyde solution was added to crosslink between the gelatin's amine groups, resulting in a gelatin-hexametaphosphate (GHMP) capsule surrounding the PS in DOP. Through laser scattering analysis (**Figure 1-43**) it is clear that large capsules have been made, though a secondary shoulder occurs at 45 μm . Filtering through a 200 mesh removed these. The resulting particles have an average diameter ($d_{0.5}$) of 478 μm .

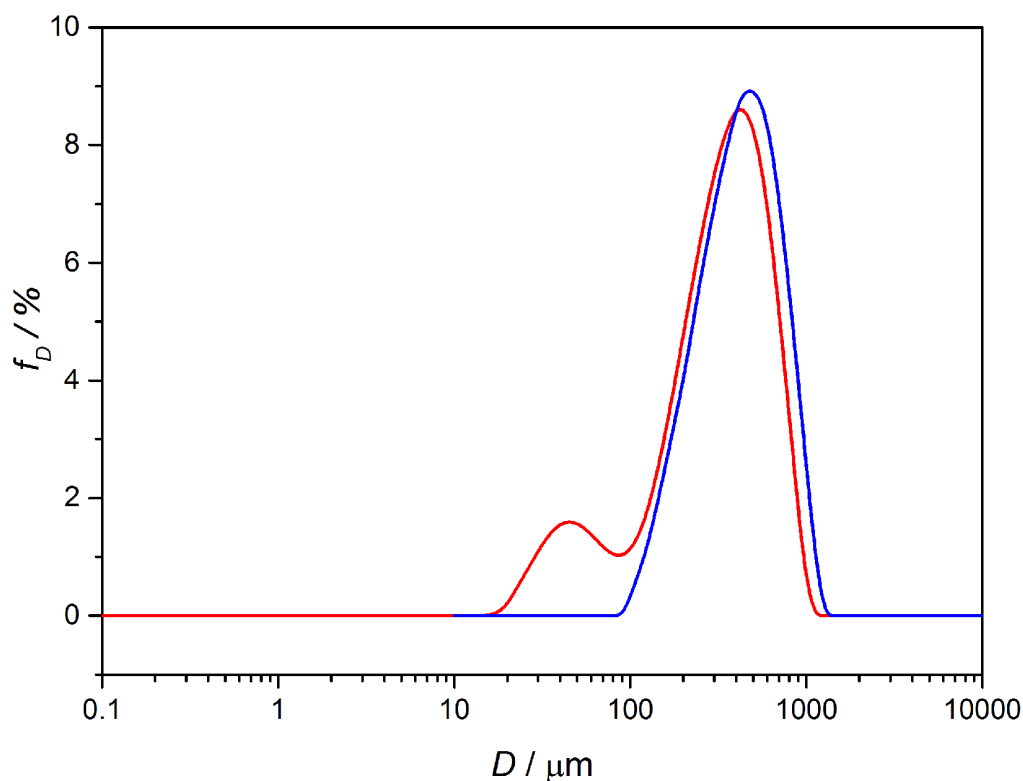


Figure 1-43. Particle size distribution of PS in DOP capsules of (—) unfiltered and (—) filtered samples.

Coacervation of gelatin and counter ions gives a peculiar geometry when forming around a viscous material with constant stirring.²³³ Upon removing the heat from the system, the gelatin goes below its gelation temperature (26.5 °C for this system).²⁷⁶ Once the gelation begins, the constant flow of the solutions deforms the spherical geometry into the lemon shaped observed (**Figure 1-44**). A sample was cycled through a -5 °C to 5 °C cycle to determine whether the phase change still occurred (**Figure 1-44 b and c**).

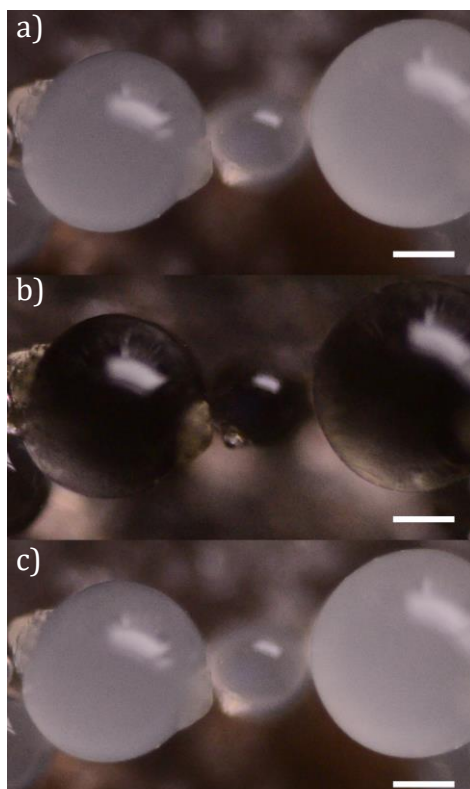


Figure 1-44. Micrograph of the lemon shaped gelatin coated PS in DOP capsules at a) -5°C , b) 5°C , and c) -5°C . Scale bar is $250\text{ }\mu\text{m}$.

Following the synthesis of the capsules (**Figure 1-44**), the particles were dispersed within a PS/BA/AA binder and introduced to a metallic mould liberally applied with a release agent to aid the removal of the mould once the latex binder had dried. The resulting binder and capsules were then cooled to -15°C in a freezer and recorded immediately upon removal from the freezer (**Figure 1-45**).

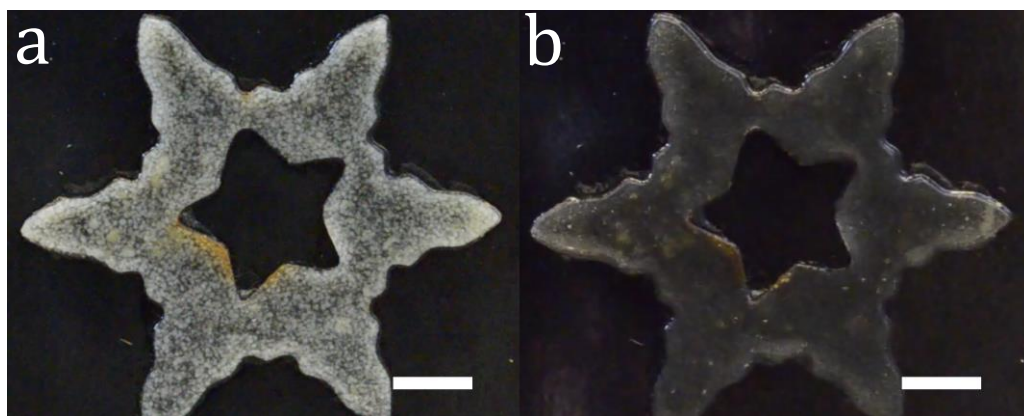


Figure 1-45. Images of a PS/BA/AA latex binder containing 25 wt% PS in DOP capsules a) immediately after cooling to - 15 °C and b) after being left at 20 °C for 2 minute. Scale bar represents 10 mm.

The GHMP capsules exhibit a strong change in colour between the heterogeneous (**Figure 1-45 a**) and homogenous states (**Figure 1-45 b**). As indicated by the thermochromic behaviour, the GHMP capsules stop the migration of the PS in DOP throughout the system and localise them within the capsules. Upon decreasing the temperature to below the phase change point, the capsules become a centre of refractive index difference within the binder and reflect the light back, giving the binder a white colour. Once the temperature is raised above the transitional temperature, the system becomes transparent once more due to the loss of the refractive index difference between capsules and binder. Similar to the labels shown in **Section 1.3.3**, a loss of the colour orange can be observed upon returning to the homogeneous state. A slight greying at the extremities of the star in **Figure 1-45 b** can be observed. This is due to slight delamination between the

binder and the substrate underneath, leading to the inclusion of some air between them leading to a refractive index difference. The samples were left for three months in ambient conditions before undergoing further cooling/heating cycles. The transition was still observed after the three months, indicating that the capsules remained stable within the binder over longer periods of time. The particles were dispersed within additional binders consisting of two epoxides, a polysiloxane, and silicone (**Appendix II Figure 7-9**). It was found that the two part epoxide systems showed visible a loss in thermochromic behaviour which is believed to be due to the addition of the curing agent solubilising some of the PS or DOP within the capsules. A difference between the cooled and warmed states was observed with the silane binder, however some turbidity remained in the system. This was due to water migration from the capsule shells forming centres of miscibility difference within the binder, leading to a difference in refractive index and a slightly turbid end binder. The polysiloxane binder was found to incorporate the particles and show similar responses as the PS/BA/AA binder. Some air was incorporated into the binder during the dispersing process of the particles which resulted in binder exhibiting slight greyness.

An important factor for the oil both encapsulated within the gelatin barrier and free oil is possible evaporation or leakage over time. Three samples of pure DOP, 10 wt% PS in DOP, and encapsulated 10 wt% PS in DOP were decanted into glass vials capped with a piece of filter paper to ensure no contaminants could enter each sample. The three samples were then left at ambient conditions for three months with the mass recorded at 1, 4, 8, and 12

weeks. The results of this are shown in **Table 1-13**. There is a slight initial mass loss of the capsules over the first 4 week period though this is believed to be due to the evaporation of water from within the capsule walls as they became more brittle to the touch. Both the PS in DOP oil and the PS in DOP capsules retained their ability to phase change after the 12 week period, indicating that both systems are stable for potential long term storage.

Table 1-13. Mass of DOP, PS in DOP, and encapsulated PS in DOP over time.

Time / weeks	Mass of DOP / g	Mass of PS in DOP / g	Mass of PS in DOP capsules/ g
0	19.2428	20.1027	13.9582
1	19.2428	20.1026	13.9576
4	19.2420	20.1014	13.9570
8	19.2421	20.1013	13.9571
12	19.2419	20.1014	13.9570

1.3.5 Encapsulation - Fibres

Another form of encapsulation is the embedding oil droplets within a fibre made using a microfluidic device (**Figure 1-46**). Microfluidic devices

have often been employed for the creation of monodisperse droplets within another media such as oil in water (O/W) or water in oil (W/O) with expansion upon these to multiple droplets within droplets forming (O/W/O and W/O/W). Simpler glass microfluidic devices, first shown by Nurumbetov *et al.*, introduced an easier method to creating devices that allowed more access to the option.^{277,278} Use of microfluidics devices to form fibres has also been reported.^{279,280} Sodium alginate is a naturally occurring anionic polysaccharide that is extracted from brown seaweed and kelp. When exposed to a calcium chloride solution, the sodium ions complexed to the carboxylic acid groups along the polymeric chains are replaced with calcium ions. Ca^{2+} ions can complex between differing alginate polymer chains, causing a crosslinked polymer to form.

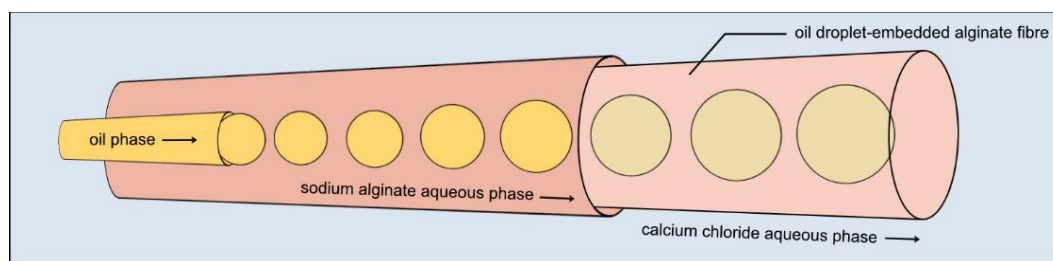


Figure 1-46. Schematic for the formation of PS in DOP oil droplets within an alginate fibre *via* microfluidic manufacturing.

A simplified schematic for the formation of PS in DOP droplets within an alginate fibre is shown in **Figure 1-46**. The typical procedure for the fibres was as follows. An inner oil phase was pumped into an outer aqueous phase

consisting of 1 wt% alginic acid sodium salt. A combination of both flow focussing and lower flow rate of the inner phase leads to uniform oils droplets with regular spacing between each being formed within the sodium alginate solution. The sodium alginate solution containing oil droplets flowed out into a $\text{CaCl}_2 \cdot 6\text{H}_2\text{O}$ solution for the crosslinking to occur and the fibres kept within this solution overnight. Stabilisation of the oil phase was not required due to both the high viscosity of the alginic acid salt solution coupled with the fast crosslinking of the system when introduced to the CaCl_2 solution. This allowed for entrapment of the oil droplets within the fibre. The high viscosity of the 10 wt% PS in DOP solution was too great for a constant flow within the device and led to blockages occurring, therefore the PS in DOP was dissolved in DCM at 50 vol% reducing the viscosity to allow it to flow through the system. The high water solubility of DCM (17.5 g / L at 25 °C)²²⁴ led to the solvent migrating into the aqueous phase, returning the PS in DOP solution to 10 wt%. The resulting fibre is shown in **Figure 1-47**.

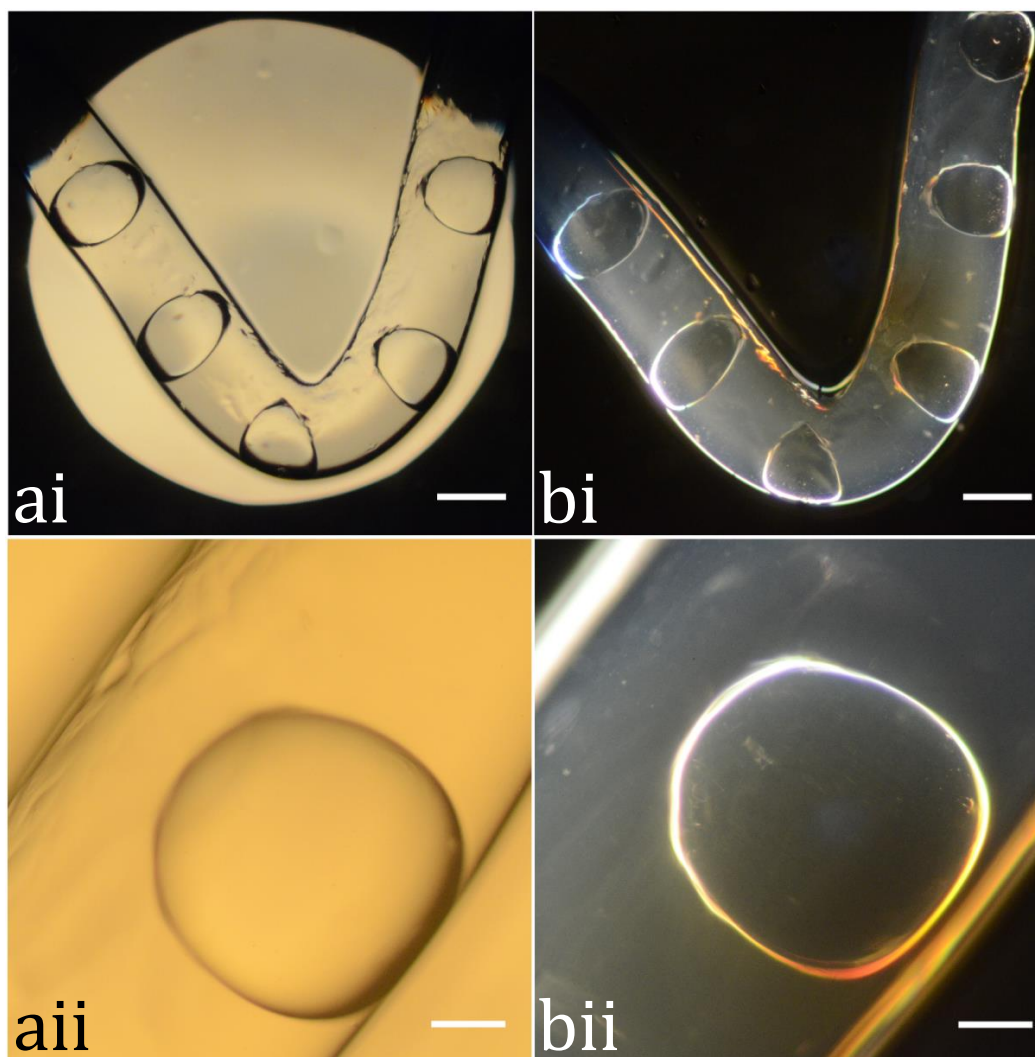


Figure 1-47. Both a) light and b) dark field micrographs of alginate fibres encapsulating PS in DOP oil droplets. Scale bars in ai and bi represent 800 μm whilst in aii and bii they represent 200 μm .

Fibres shown in **Figure 1-47** clearly exhibited that the oil droplets remain stable within the alginate without the need for further stabilisers. Flexibility of the fibre can also be observed due to the acute angle at which the fibre was contorted to within **Figure 1-47 aii - bii**. Only slight deformation of

the oil droplets occurred with no splitting and loss/migration of the oil droplets. The droplets within the fibre exhibited a diameter of 805 μm whilst the fibre's diameter is 1160 μm . It can be observed that the fibres produced using this method do not form perfectly smooth as **Figure 1-47 aii** indicates a rough surface being formed. Due to the constant flow of the outer alginate solution, the inner diameter of the exit port on the microfluidic device is the same as the diameter of the fibre made. It should be noted that the oil droplets do not remain central within the fibre due to the lower density of the DOP oil though the oil droplets do remain fully enveloped within the alginate fibre.

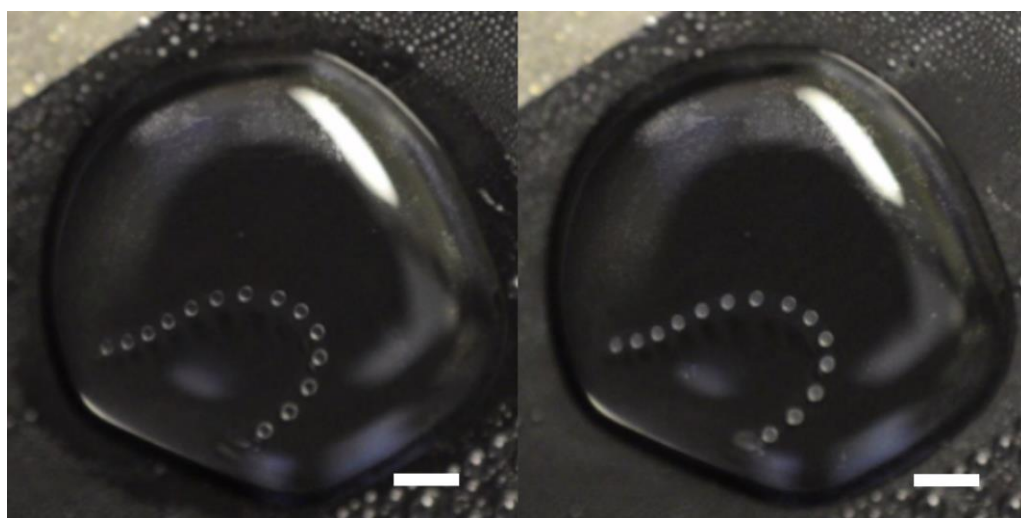


Figure 1-48. Images cross linked alginate fibre containing droplets of 10 wt% PS in DOP within a saturated salt solution at a) ambient temperature and b) $-2\text{ }^{\circ}\text{C}$ where phase change occurs. Scale bar = 3300 μm

Figure 1-48 shows the phase transitions of 10 wt% PS in DOP embedded within a crosslinked alginate polymeric matrix. The flexible fibre

was placed within a saturated salt solution to reduce refractive index between the air/fibre interfaces to allow the recording. This was also required to allow for low temperatures to be reached without the aqueous solution freezing over. As it can be observed in **Figure 1-48**, a strong difference between both the homogeneous and heterogeneous phases can be seen. Before the transition, reflection from the oil/alginate interface can be observed, however, upon phase separation within the droplet, a much stronger reflection can be observed. Due to the low temperature, some condensation does occur on the platform which begins to freeze, although this does not affect the phase transition of the saturated NaCl droplet the fibre resides within. The flexible fibres can therefore be used to observe temperature changes. It should also be noted that as the droplets are 800 μm , it is clear that even low volumes of PS in DOP oil can be used as a temperature indicators.

1.4 Conclusion

In conclusion, we demonstrated the random copolymerisation of styrene and co monomers *via* free radical polymerisation using the thermal initiation of styrene. We have shown the UCST behaviour of each polymer within DOP with a reduction in phase transitional temperature being highly dependent on the co-monomers structure, where large alkyl substituents decreased the temperature most, and the concentration of co-monomer within the polymer. We also touched upon the use of the oils within labels as a form of strip thermometer where multiple temperature changes can be visualised. Along with the label using the base oils, addition of dyes dissolved within the oils showed a strong colour change upon phase transition. Having illustrated the possibility of coloured compounds forming, we are interested in exploring the use of fluorescent dyes (Chapter 4). Further to this, we have also showed the successful encapsulation of the phase changing oils in both fibres and waterborne latex films where the phase change can still be observed. We believe our method can be used to fabricate phase change particles on a wide scale for the use as a thermochromic pigment.

1.5 Experimental

1.5.1 General Characterisation Techniques

All SEC experiments were performed on Agilent 390-LC multi-detector suites equipped with a PL-AS RT/MT autosampler, fitted with a PLgel 5 μm guard column and two PLgel 5 μm Mixed C columns (with an exclusion limit of $2.0 \times 10^6 \text{ g mol}^{-1}$). All data was collected and analysed using Agilent GPC software. Solvent used was THF with 2 % TEA and 0.01 % BHT, with a flow rate of 1 ml min^{-1} and an injection volume of $100 \mu\text{L}$. The column sets were maintained at ambient temperature. A DRI detector was used for conventional calibration. Calibrations were created using poly(styrene) EasiVial standards ($162\text{-}508,000 \text{ g mol}^{-1}$) purchased from Agilent, with a minimum of 9 points fitted with a third order calibration curve. Points with an error greater than 10 % were not included in the final calibration. Samples were prepared by dissolving 0.5 mg of dried polymer in 1.5 mL SEC solvent, allowing the solution to equilibrate for 90 minutes after which the solution was filtered.

UV/Vis phase change measurements were taken using an Agilent Cary 60 UV/Vis Spectrophotometer with a heating stage heated between -4.0°C to 10°C in 0.5°C stages and left to heat for 60 minutes at each temperature with 10°C steps up to 60°C after 10°C .

Particle sizing measurements of micron sized colloids were undertaken using a Mastersizer 2000 (Malvern Instruments, Malvern, UK).

Dilute particle suspensions in water were introduced using the Hydro 2000S dispersion unit. The laser was aligned to optimum transmission intensity and a background spectrum collected to eliminate any contaminants presenting in the final data. Dilute suspensions of 1 wt% were introduced drop wise by submerged syringe until 5% laser obscuration was reached. A 30 second sampling time across the entire measurement range from 2 nm – 2 mm was conducted three times before averaging to yield final results.

Optical micrographs (both light and dark field) were acquired using a Leica DM 2500M optical microscope accompanied with a Nikon D5100 camera.

All DSC's were acquired using Mettler Toledo STARe DSC fitted with an autosampler with each sample weighing ~10 mg within an aluminium crucible. Each sample was heated to 150 °C and held there for 10 minutes before cooling to – 150 °C. Once each sample was then heated to 25 °C, 3 cycles further cycles were run to obtained the heat flow of the polymer samples.

All ^1H spectra were recorded on a Bruker DPC-400 spectrometer within deuterated CHCl_3 with a relaxation time of 6 seconds.

1.5.2 Photographic Phase Change Technique

An aluminium plate was made following the design in **Appendix II Figure II - 1**. This plate was fitted onto the Kruss TC40 heating and cooling plate fitted with spate liquid cooling for the Peltier element. Each well was

filled with a different polystyrene dioctyl phthalate solution. After the filling, a glass plate was placed on top of the plate to reduce water condensing/freezing onto the plate. Starting at 10 °C, the stage was lowered in 1 °C steps and left to equilibrate at each temperature for 15 minutes. After equilibrations of each step, a photo was taken for production of the phase change curves. Temperature was recorded using a Pt 100 thermometer fully immersed in a DOP solution. Images were converted and processed using ImageJ.

1.5.3 Materials

Styrene, polystyrene ($280 \text{ kg}\cdot\text{mol}^{-1}$, 2.98 €), *n*-isopropylacrylamide (NIPAM), lauryl acrylate (LA), 2-ethylhexylacrylate (2EHA), ethylacrylate (EA), ethyl methacrylate (EMA), methyl methacrylate (MMA), dioctyl phthalate (DOP), gelatin, sodium hexametaphosphate (+200mesh, 96%), methanol ($\geq 99.6 \%$), alginic acid sodium salt, calcium chloride hexahydrate (98%), and glutaraldehyde (50 wt% in H_2O) were purchased from Sigma Aldrich. Sodium hydroxide (analytical grade) and acetic acid (glacial) were purchased from Fisher. Tetrahydrofuran ($\geq 99.8 \%$) and dichloromethane (DCM) were purchased from VWR. All monomers were run through a basic alumina column before reactions. Standard wall borosilicate glass capillaries (GC100-10, outer diameter (OD) 1.0 mm, inner diameter (ID) 0.58 mm and GC200-7.5, OD 2.0 mm, ID 1.16 mm) were purchased from Harvard Apparatus. Clear Tygon tubing (0.8 mm ID) was purchased from ColeParmer. Evo-Stik Two Part epoxy resin was applied to seal the capillaries where

necessary. Solutions were introduced to the microfluidic device through positive displacement syringe pumps (Harvard Apparatus PHD 2000 series). Weller Dispensing Needles and KDS1812P (GA 18, ID 0.97 mm) were used to introduce the inner phase and outer phase.

1.5.4 Polymer Synthesis

Styrene and comonomers, in accordance with **Table 1-14** to **Table 1-19**, were added to a 20 mL crimp top vial. After sealing, the systems were degassed using an N₂ purge for 15 minutes. Initiation was induced by submerging the vials into a 140 °C oil bath. After 1 hour, the reaction mixtures were removed from the oil bath, placed into ice water, and injected with 10 mL of air before the seal was removed. The resulting solution was diluted into 40 mL of THF before precipitating into ice cold methanol. The polymer was then dried in a vacuum oven before characterisation.

Table 1-14. Poly(styrene-*co*-methyl methacrylate) monomer quantities.

	PSMMA 1	PSMMA 2	PSMMA 3	PSMMA 4	PSMMA 5	PSMMA 6
Sty / g	7.961	7.918	7.850	7.816	7.606	7.200
MMA / g	0.040	0.081	0.161	0.183	0.400	0.800
Yield / g	2.560	2.319	2.483	2.401	2.400	2.640

Chapter 1: UCST of Copolymers

Table 1-15. Poly(styrene-*co*-ethyl methacrylate) monomer quantities

	PSEMA 1	PSEMA 2	PSEMA 3	PSEMA 4	PSEMA 5	PSEMA 6
Sty / g	7.960	7.920	7.840	7.818	7.606	7.815
EMA / g	0.041	0.080	0.160	0.185	0.401	0.800
Yield / g	2.400	2.408	2.480	2.441	2.482	2.583

Table 1-16. Poly(styrene-*co*-ethyl acrylate) monomer quantities

	PSEA 1	PSEA 2	PSEA 3	PSEA 4	PSEA 5	PSEA 6
Sty / g	7.961	7.927	7.844	7.832	7.604	7.208
EA / g	0.042	0.081	0.1600	0.185	0.401	0.800
Yield / g	2.440	2.482	2.291	2.370	2.561	2.481

Table 1-17. Poly(styrene-*co*-2ethylhexyl acrylate) monomer quantities

	PS2EHA 1	PS2EHA 2	PS2EHA 3	PS2EHA 4	PS2EHA 5	PS2EHA 6
Sty / g	7.960	7.927	7.842	7.990	7.799	7.686
2EHA / g	0.041	0.080	0.161	0.188	0.411	0.854
Yield / g	2.401	2.402	2.721	2.462	2.483	2.667

Table 1-18. Poly(styrene-*co*-lauryl acrylate) monomer quantities

	PSLA 1	PSLA 2	PSLA 3	PSLA 4	PSLA 5	PSLA 6
Sty / g	7.965	7.922	7.841	7.913	7.828	7.291
LA / g	0.040	0.081	0.160	0.187	0.412	0.810
Yield / g	2.361	2.481	2.448	2.430	2.559	2.430

Table 1-19. Poly(styrene-*co*-*n*-isopropyl acrylamide) monomer quantities

	PSNIPAM1	PSNIPAM 2	PSNIPAM 3	PSNIPAM 4	PSNIPAM 5	PSNIPAM 6
Sty / g	7.965	8.078	7.928	7.828	7.613	7.243
NIPAM / g	0.040	0.082	0.164	0.185	0.403	0.805
Yield / g	2.281	2.400	2.444	2.308	2.357	2.495

1.5.5 Capsule Synthesis

Gelatin (8.19 g) was dissolved in deionised water (60 g) at 70°C in a 250 mL reactor fitted with water heated jacket and overhead stirring (220 rpm). Once fully dissolved, the pH was raised to 8 using 10 Wt% NaOH and left to stir for 5 minutes. After this, PS-DOP solution (60 mL) was slowly transferred in using a glass syringe. Once the reactor returned to 70°C, preheated deionised water (82.5 g) was added and the stirring was increased (610 rpm). After 15 minutes of stirring, an aqueous solution of sodium hexametaphosphate (0.789g in 15 mL water) was added and the reaction was

left to return to 70 °C. Acetic acid (50 Wt%) was dropwise added until the pH 4.5 was reached and the reaction left to stir for 15 minutes before removing the heat. After 2 hours, an aqueous solution of glutaraldehyde (7.5 g in 37.5 g deionised water) was added to harden the particle and the reaction left stirring overnight. Particles were collected by vacuum filtration after 3 washes with deionised water (100 mL).

1.5.6 Fibre Synthesis

A glass capillary with an ID of 1.16 mm and OD of 2.0 mm formed the outer casing of the device and contains the flow of the outer phase. The outer phase consisted of an aqueous solution containing 1 Wt% alginic acid sodium salt and run at 0.15 mL/min. The inner phase was introduced to the outer phase using a needle aligned to the centre of the glass capillary and consisted of a 10 Wt% PS in DOP solution diluted to 50 Vol% in DCM and pumped at 0.05 mL/min to form droplets. The output for the device was run into a reservoir of 0.1 M $\text{CaCl}_2 \cdot 6\text{H}_2\text{O}$, in which the fibres were stored overnight, allowing the DCM to migrate into the water phase and the fibres to fully crosslink. Following the migration of DCM, the fibres were removed from the storage solution and placed into a droplet of saturated NaCl water for the phase transition video *via* cooling to -3 °C and heating to 3 °C. The sample was cycled 3 times to ensure the phase change occurred reproducibly.

1.6 References

- (1) Bamfield, P.; Hutchings, M. G. In *Chromic Phenomena*; Royal Society of Chemistry: Cambridge, 2010; pp 1–8.
- (2) Bamfield, P.; Hutchings, M. G. In *Chromic Phenomena: Technological Applications of Colour Chemistry*; 2010; pp 9–140.
- (3) Liquid Crystal Thermometers (LCs) <http://www.hallcrest.com/color-change-basics/liquid-crystal-thermometers> (accessed Aug 29, 2016).
- (4) Heilbron, I. M.; Hey, D. H.; Lowe, A. J. *Chem. Soc.* **1936**, No. 1380, 1380–1383.
- (5) Berman, E.; Fox, R. E.; Thomson, F. D. *J. Am. Chem. Soc.* **1959**, *81* (21), 5605–5608.
- (6) Patel, R. G.; Patel, M. P.; Patel, R. G. *Dye. Pigment.* **2005**, *66* (1), 7–13.
- (7) Zhu, C. F.; Wu, a. B. *Thermochim. Acta* **2005**, *425* (1–2), 7–12.
- (8) Day, J. H. *Chem. Rev.* **1963**, *63* (1), 65–80.
- (9) Vidinejevs, S.; Aniskevich, a. N.; Gregor, A.; Sjoberg, M.; Alvarez, G. J. *Intell. Mater. Syst. Struct.* **2012**, *23* (12), 1371–1377.
- (10) MacLaren, D. C.; White, M. A. *J. Mater. Sci.* **2005**, *40* (3), 669–676.
- (11) MacLaren, D. C.; White, M. A. *J. Mater. Chem.* **2003**, *13* (7), 1695–1700.
- (12) MacLaren, D. C.; White, M. A. *J. Mater. Chem.* **2003**, *13* (7), 1701–1704.
- (13) Takaoka, K.; Maeda, S.; Miura, H.; Endo, K.; Chong, D. P. *Bull. Chem. Soc. Jpn.* **1998**, *71* (4), 807–816.
- (14) Tsutsui, K.; Yamaguchi, T.; Sato, K. *Jpn. J. Appl. Phys.* **1994**, *33* (Part 1, No. 10), 5925–5928.
- (15) Tang, H.; MacLaren, D. C.; White, M. A. *Can. J. Chem.* **2010**, *88* (11), 1063–1070.
- (16) Malherbe, I.; Sanderson, R. D.; Smit, E. *Polymer (Guildf).* **2010**, *51* (22), 5037–5043.
- (17) Burkinshaw, S. M.; Gri, J.; Towns, A. D. *J. Mater. Chem.* **1998**, *8*, 2677–2683.
- (18) Bašnec, K.; Hajzeri, M.; Klanjšek Gunde, M. *J. Therm. Anal. Calorim.* **2016**.
- (19) Hotta, Y. *Imaging Soc. Japan* **2011**, *50* (2), 154–159.
- (20) Hasegawa, K.; Tanabe, Y.; Kikkawa, K.; Nakatsuka, M.; Yamaguchi, A. Thermochromic materials. US 5,281,570, 1994.
- (21) White, L. J.; Gen, T. G. Thermochromic Compositions. US4424990, 1984.

- (22) White, M. A.; Leblanc, M. *J. Chem. Educ.* **1999**, 76 (9), 1201–1205.
- (23) Azizian, F.; Field, A. J.; Heron, B. M.; Kilner, C. *Chem. Commun.* **2012**, 48 (5), 750–752.
- (24) Azizian, F.; Field, A. J.; Heron, B. M. *Dye. Pigment.* **2013**, 99 (2), 432–439.
- (25) Li, K.; Li, Y.; Tao, J.; Liu, L.; Wang, L.; Hou, H.; Tong, A. *Sci. Rep.* **2015**, 5 (August), 14467.
- (26) Allen, N. S.; Hughes, N.; Mahon, P. *J. Photochem.* **1987**, 37 (2), 379–390.
- (27) Ireland, P. T.; Jones, T. V. *J. Phys. E.* **1987**, 20 (10), 1195–1199.
- (28) Seto, H.; Ueda, M.; Segawa, H. Thermometer using liquid crystal compositions. US 3,704,625.
- (29) Santacaterina, L.; Brown, G. T.; Schuberth, W. Reusable liquid crystal thermometer. US 4,779,995, 1988.
- (30) Wolfe, W. Article of Manufacture having non-uniform thermochromic display. US 6,979,120 B1, 2005.
- (31) Wolfe, W. Article of Manufacture Having Sublimatable Time Delay Thermochromic Ink Display. US 2008/0229971 A1, 2008.
- (32) Clark, A. L. System and Method for a Novelty Mood Sensing Sharing Device. US 9,064,390 B1.
- (33) Frenger, R. K. Skin Jewelry. US 4,220,016, 1980.
- (34) Levan, M. Mood Collar for Pets. US 6,675,744 B1, 2005.
- (35) TOUCH SENSITIVE™ PRODUCT LINE
<http://www.movingcolor.net/product-lines/touch-sensitive-product-line/> (accessed Aug 18, 2016).
- (36) Enz, E.; Lagerwall, J. *J. Mater. Chem.* **2010**, 20 (33), 6866.
- (37) LCR Hallcrest. *Handbook of Thermochromatic Liquid Crystal Technology*; 2015.
- (38) Reinitzer, F. *Monatshefte für Chemie - Chem. Mon.* **1888**, 9 (1), 421–441.
- (39) Rudquist, P.; Dietrich, C. F.; Mark, A. G.; Giesselmann, F. *Langmuir* **2016**, 32 (24), 6140–6147.
- (40) Kshirsagar, P. G.; Avadhanulu, M. . *A Textbook of Engineering Physics*; 1992.
- (41) Phases, N. Phases of Liquid Crystals
<http://materials.duke.edu/XCOURSES/ME83/lcrystals2.pdf> (accessed Aug 29, 2016).
- (42) Rego, J. a.; Harvey, J. a. a.; MacKinnon, A. L.; Gatdula, E. *Liq. Cryst.* **2009**, 37 (1), 37–43.

- (43) Sage, I. *Liq. Cryst.* **2011**, 38 (11–12), 1551–1561.
- (44) Zhang, F.; Yang, D.-K. *Liq. Cryst.* **2002**, 29 (12), 1497–1501.
- (45) Lv, K.; Liu, D.; Li, W.; Tian, Q.; Zhou, X. *Dye. Pigment.* **2012**, 94 (3), 452–458.
- (46) van der Werff, L. C.; Robinson, A. J.; Kyratzis, I. L. *ACS Comb. Sci.* **2012**, 14 (11), 605–612.
- (47) Hay, J. L.; Hollingsworth, D. K. *Exp. Therm. Fluid Sci.* **1996**, 12 (1), 1–12.
- (48) Fergason, J. L. *Appl. Opt.* **1968**, 7 (9), 1729.
- (49) Ireland, P.; Jones, T. *J. Phys. E.* **1987**, 1195, 22–27.
- (50) Abdullah, N.; Abu Talib, A. R.; Jaafar, A. A.; Mohd Salleh, M. A.; Chong, W. T. *Exp. Therm. Fluid Sci.* **2010**, 34 (8), 1089–1121.
- (51) Ireland, P. T.; Jones, T. V. *Meas. Sci. Technol.* **2000**, 11, 969–986.
- (52) van der Werff, L.; Kyratzis, I. L.; Robinson, A.; Cranston, R.; Peeters, G.; O'Shea, M.; Nichols, L. *J. Mater. Sci.* **2013**, 48 (14), 5005–5011.
- (53) Kasch, N.; Dierking, I.; Turner, M. *Soft Matter* **2013**, 9 (19), 4789.
- (54) Day, J. H. *Chem. Rev.* **1968**, 68 (6), 649–657.
- (55) Gaudon, M.; Deniard, P.; Voisin, L.; Lacombe, G.; Darnat, F.; Demourgues, a.; Perillon, J.-L.; Jobic, S. *Dye. Pigment.* **2012**, 95 (2), 344–350.
- (56) Caretta, a; Miranti, R.; Arkenbout, a H.; Polyakov, a O.; Meetsma, a; Hidayat, R.; Tjia, M. O.; Palstra, T. T. M.; van Loosdrecht, P. H. M. *J. Phys. Condens. Matter* **2013**, 25 (50), 505901.
- (57) Thilo, E.; Jander, J.; Seemann, H.; Sauer, R. *Naturwissenschaften* **1950**, 37 (17), 399–399.
- (58) Goodenough, J. B. *J. Solid State Chem.* **1971**, 3 (4), 490–500.
- (59) Zhu, J.; Zhou, Y.; Wang, B.; Zheng, J.; Ji, S.; Yao, H.; Luo, H.; Jin, P. *ACS Appl. Mater. Interfaces* **2015**, 7 (50), 27796–27803.
- (60) Batista, C.; Ribeiro, R. M.; Teixeira, V. *Nanoscale Res. Lett.* **2011**, 6 (1), 301.
- (61) Rakotoniaina, J. C.; Mokrani-Tamellin, R.; Gavarri, J. R.; Vacquier, G.; Casalot, A.; Calvarin, G. *J. Solid State Chem.* **1993**, 103, 81–94.
- (62) Niklasson, G. A.; Li, S.-Y.; Granqvist, C. G. *J. Phys. Conf. Ser.* **2014**, 559 (1), 12001.
- (63) Kroeber, J.; Audiere, J.-P.; Claude, R.; Codjovi, E.; Kahn, O.; Haasnoot, J. G.; Groliere, F.; Jay, C.; Bousseksou, A. *Chem. Mater.* **1994**, 6 (8), 1404–1412.

- (64) Rotaru, A.; Varret, F.; Gindulescu, A.; Linares, J.; Stancu, A.; Létard, J. F.; Forestier, T.; Etrillard, C. *Eur. Phys. J. B* **2011**, 84 (3), 439–449.
- (65) Grosjean, A.; Daro, N.; Kauffmann, B.; Kaiba, A.; Létard, J.-F.; Guionneau, P. *Chem. Commun. (Camb)*. **2011**, 47 (45), 12382–12384.
- (66) van Koningsbruggen, P. J.; Garcia, Y.; Codjovi, E.; Lapouyade, R.; Kahn, O.; Fournès, L.; Rabardel, L. *J. Mater. Chem.* **1997**, 7 (10), 2069–2075.
- (67) Letard, J. F.; Daro, N.; Auffret, S. Spin transition material. US 2010/0178511 A1, 2010.
- (68) Kahn, O.; Jay, C.; Korber, J.; Calude, R.; Groliere, F. Spin-Transition Parent Compounds and Devies Having Meands For Writing, Storing, And Erasing, Which Comprise An Active Medium Containing At Least One Of Said Compounds. US 6,043,008, 1992.
- (69) Vallée, A.; Train, C.; Roux, C. *J. Chem. Educ.* **2013**, 90 (8), 1071–1076.
- (70) Caretta, a; Miranti, R.; Arkenbout, a H.; Polyakov, a O.; Meetsma, a; Hidayat, R.; Tjia, M. O.; Palstra, T. T. M.; van Loosdrecht, P. H. M. *J. Phys. Condens. Matter* **2013**, 25 (50), 505901.
- (71) Gupta, S.; Pandey, T.; Singh, A. K. *Inorg. Chem.* **2016**, 55 (13), 6817–6824.
- (72) Zhang, Z.; Gao, Y.; Chen, Z.; Du, J.; Cao, C.; Kang, L.; Luo, H. *Langmuir* **2010**, 26 (13), 10738–10744.
- (73) Cao, X.; Wang, N.; Law, J. Y.; Loo, S. C. J.; Magdassi, S.; Long, Y. *Langmuir* **2014**, 30 (6), 1710–1715.
- (74) Wang, H.; Zhang, K. Q. *Sensors (Basel)*. **2013**, 13 (4), 4192–4213.
- (75) Ge, J.; Yin, Y. *Angew. Chemie Int. Ed.* **2011**, 50 (7), 1492–1522.
- (76) Kang, Y.; Walish, J. J.; Gorishnyy, T.; Thomas, E. L. *Nat. Mater.* **2007**, 6 (12), 957–960.
- (77) PAQUET, C.; KUMACHEVA, E. *Mater. Today* **2008**, 11 (4), 48–56.
- (78) Sveinbjörnsson, B. R.; Weitekamp, R. a; Miyake, G. M.; Xia, Y.; Atwater, H. a; Grubbs, R. H. *Proc. Natl. Acad. Sci. U. S. A.* **2012**, 109 (36), 14332–14336.
- (79) Walish, J. J.; Fan, Y.; Centrone, A.; Thomas, E. L. *Macromol. Rapid Commun.* **2012**, 33 (18), 1504–1509.
- (80) Deng, T.; Chen, C.; Honeker, C.; Thomas, E. L. *Polymer (Guildf)*. **2003**, 44 (21), 6549–6553.
- (81) Urbas, a.; Sharp, R.; Fink, Y.; Thomas, E. L.; Xenidou, M.; Fetters, L. J. *Adv. Mater.* **2000**, 12 (11), 812–814.
- (82) Noro, A.; Tomita, Y.; Shinohara, Y.; Sageshima, Y.; Walish, J. J.;

- Matsushita, Y.; Thomas, E. L. *Macromolecules* **2014**, *47* (12), 4103–4109.
- (83) Valkama, S.; Kosonen, H.; Ruokolainen, J.; Haatainen, T.; Torkkeli, M.; Serimaa, R.; Ten Brinke, G.; Ikkala, O. *Nat. Mater.* **2004**, *3* (12), 872–876.
- (84) Kang, Y.; Walish, J.; Thomas, E. L. Broad wavelength range tunable photonic materials US2009086208. US2009086208, 2009.
- (85) Valkama, S.; Kosonen, H.; Ruokolainen, J.; Haatainen, T.; Torkkeli, M.; Serimaa, R.; Ten Brinke, G.; Ikkala, O. *Nat. Mater.* **2004**, *3* (12), 872–876.
- (86) Chiappelli, M. C.; Hayward, R. C. *Adv. Mater.* **2012**, 1–5.
- (87) Yue, Y. F.; Haque, M. A.; Kurokawa, T.; Nakajima, T.; Gong, J. P. *Adv. Mater.* **2013**, *25* (22), 3106–3110.
- (88) Wang, Z.; Zhang, J.; Xie, J.; Wang, Z.; Yin, Y.; Li, J.; Li, Y.; Liang, S.; Zhang, L.; Cui, L.; Zhang, H.; Yang, B. *J. Mater. Chem.* **2012**, *22* (16), 7887.
- (89) Alvarez-Lorenzo, C.; Concheiro, A.; Dubovik, A. S.; Grinberg, N. V.; Burova, T. V.; Grinberg, V. Y. *J. Control. Release* **2005**, *102* (3), 629–641.
- (90) Liu, K.-W.; Li, C.-L.; Li, M.-C.; Ho, R.-M. *Langmuir* **2013**, *29* (28), 9016–9023.
- (91) Osuji, C.; Chao, C. Y.; Bitá, I.; Ober, C. K.; Thomas, E. L. *Adv. Funct. Mater.* **2002**, *12* (11–12), 753–758.
- (92) Fink, Y.; Urbas, a. M.; Bawendi, M. G.; Joannopoulos, J. D.; Thomas, E. L. *J. Light. Technol.* **1999**, *17* (11), 1963–1969.
- (93) Yoon, J.; Lee, W.; Thomas, E. L. *Macromolecules* **2008**, *41* (13), 4582–4584.
- (94) Thomson, N. R.; McLachlan, M. a; Bower, C. L.; McComb, D. W. *Langmuir* **2009**, *25* (19), 11344–11350.
- (95) Zhang, Y.; Wang, J.; Huang, Y.; Song, Y.; Jiang, L. *J. Mater. Chem.* **2011**, *21* (37), 14113.
- (96) Reese, C.; Guerrero, C.; Weissman, J.; Lee, K.; Asher, S. *J. Colloid Interface Sci.* **2000**, *232* (1), 76–80.
- (97) Mosquera, M. J.; Bejarano, M.; de la Rosa-Fox, N.; Esquivias, L. *Langmuir* **2003**, *19* (3), 951–957.
- (98) Joy, M.; Muangnapoh, T.; Snyder, M. a; Gilchrist, J. F. *Soft Matter* **2015**, *11* (36), 7092–7100.
- (99) Yan, X.; Yao, J.; Lu, G.; Li, X.; Zhang, J.; Han, K.; Yang, B. *J. Am. Chem. Soc.* **2005**, *127* (21), 7688–7689.
- (100) Li, X.; Wang, T.; Zhang, J.; Yan, X.; Zhang, X.; Zhu, D.; Li, W.; Zhang, X.; Yang, B. *Langmuir* **2010**, *26* (4), 2930–2936.

- (101) Park, S. H.; Qin, D.; Xia, Y. *Adv. Mater.* **1998**, *10* (13), 1028–1032.
- (102) Gates, B.; Qin, D.; Xia, Y. *Adv. Mater.* **1999**, *11* (6), 466–469.
- (103) Park, S. H.; Xia, Y. *Langmuir* **1999**, *15* (1), 266–273.
- (104) Lee, Y.-J.; Braun, P. V. *Adv. Mater.* **2003**, *15* (78), 563–566.
- (105) Weissman, J.; Sunkara, H.; Tse, A.; Asher, S. *Science* **1996**, *274* (5289), 959–960.
- (106) Pelton, R. H.; Chibante, P. *Colloids and Surfaces* **1986**, *20* (3), 247–256.
- (107) McPhee, W.; Tam, K. C.; Pelton, R. *J. Colloid Interface Sci.* **1993**, *156*, 24–30.
- (108) Debord, J. D.; Lyon, L. A. *J. Phys. Chem. B* **2000**, *104* (27), 6327–6331.
- (109) Hu, Z.; Lu, X.; Gao, J. *Adv. Mater.* **2001**, *13* (22), 1708–1712.
- (110) Kamenetzky, E. A.; Magliocco, L. G.; Panzer, H. P. *Science (80-.)*. **1994**, *263* (5144), 207–210.
- (111) Asher, S.; Holtz, J.; Liu, L.; Zhijun, W. *J. Am. Chem. Soc.* **1994**, *116* (8), 4997–4998.
- (112) Seeboth, A.; Löttsch, D.; Ruhmann, R.; Muehling, O. *Chem. Rev.* **2014**.
- (113) Lide, D. R. *CRC Handbook of Chemistry and Physics*, 53rd ed.; 2003.
- (114) Harsh, D. C.; Gehrke, S. H. *J. Control. Release* **2001**, *17* (2), 175–185.
- (115) Aguirre, C. I.; Reguera, E.; Stein, A. *Adv. Funct. Mater.* **2010**, *20* (16), 2565–2578.
- (116) Wang, J.; Han, Y. *J. Colloid Interface Sci.* **2011**, *357* (1), 139–146.
- (117) Liu, F.; Yin, H.; Dong, B.; Qing, Y.; Zhao, L.; Meyer, S.; Liu, X.; Zi, J.; Chen, B. *Phys. Rev. E - Stat. Nonlinear, Soft Matter Phys.* **2008**, *77* (1), 1–4.
- (118) Zhao, Y.; Xie, Z.; Gu, H.; Zhu, C.; Gu, Z. *Chem. Soc. Rev.* **2012**, *41* (8), 3297–3317.
- (119) Vukusic, P.; Sambles, J. R. *Nature* **2003**, *424* (6950), 852–855.
- (120) Waterhouse, G. I. N.; Waterland, M. R. *Polyhedron* **2007**, *26* (2), 356–368.
- (121) Takeoka, Y.; Watanabe, M. *Langmuir* **2003**, *19* (22), 9104–9106.
- (122) Takeoka, Y.; Watanabe, M. *Adv. Mater.* **2003**, *15* (3), 199–201.
- (123) Kumoda, M.; Watanabe, M.; Takeoka, Y. *Langmuir* **2006**, *22* (9), 4403–4407.
- (124) Katayama, S.; Hirokawa, Y.; Tanaka, T. *Macromolecules* **1984**, *17* (12), 2641–2643.

- (125) Amiya, T.; Hirokawa, Y.; Hirose, Y.; Li, Y.; Tanaka, T. *J. Chem. Phys.* **1987**, *86* (4), 2375–2379.
- (126) Li, H.; Vienneau, G.; Jones, M.; Subramanian, B.; Robichaud, J.; Djaoued, Y. *J. Mater. Chem. C* **2014**, *2* (37), 7804.
- (127) Hatton, B.; Mishchenko, L.; Davis, S.; Sandhage, K. H.; Aizenberg, J. *Proc. Natl. Acad. Sci.* **2010**, *107* (23), 10354–10359.
- (128) Wu, G.; Jiang, Y.; Xu, D.; Tang, H.; Liang, X.; Li, G. *Langmuir* **2011**, *27* (4), 1505–1509.
- (129) Couturier, J.-P.; Wischerhoff, E.; Bernin, R.; Hettrich, C.; Koetz, J.; Sütterlin, M.; Tiersch, B.; Laschewsky, A. *Langmuir* **2016**, *32* (17), 4333–4345.
- (130) Kanai, T.; Lee, D.; Shum, H. C.; Shah, R. K.; Weitz, D. A. *Adv. Mater.* **2010**, *22* (44), 4998–5002.
- (131) Pietsch, C.; Vollrath, A.; Hoogenboom, R.; Schubert, U. S. *Sensors* **2010**, *10* (9), 7979–7990.
- (132) Boutris, C.; Chatzi, E. G.; Kiparissides, C. *Polymer (Guildf)*. **1997**, *38* (10), 2567–2570.
- (133) Schild, H. G. *Prog. Polym. Sci.* **1992**, *17* (2), 163–249.
- (134) Katsumoto, Y.; Tanaka, T.; Sato, H.; Ozaki, Y. *J. Phys. Chem. A* **2002**, *106* (14), 3429–3435.
- (135) Jiao, J.; Li, X.; Zhang, S.; Liu, J.; Di, D.; Zhang, Y.; Zhao, Q.; Wang, S. *Mater. Sci. Eng. C* **2016**, *67*, 26–33.
- (136) Yu, L.; Ren, N.; Yang, K.; Zhang, M.; Su, L. *J. Appl. Polym. Sci.* **2016**, *133* (39), 1–9.
- (137) Zhang, Y.; Furyk, S.; Bergbreiter, D. E.; Cremer, P. S. *J. Am. Chem. Soc.* **2005**, *127* (41), 14505–14510.
- (138) Du, H.; Wickramasinghe, R.; Qian, X. *J. Phys. Chem. B* **2010**, *114* (49), 16594–16604.
- (139) Sun, R.; Krishna, H.; Xie, M.; Li, Q. *Dye. Pigment.* **2016**, *132*, 336–341.
- (140) Wei, R.; Ma, J.; Zhang, H.; He, Y. *J. Appl. Polym. Sci.* **2016**, *133* (29), 34–37.
- (141) Pietsch, C.; Mansfeld, U.; Guerrero-Sanchez, C.; Hoepfner, S.; Vollrath, A.; Wagner, M.; Hoogenboom, R.; Saubern, S.; Thang, S. H.; Becer, C. R.; Chiefari, J.; Schubert, U. S. *Macromolecules* **2012**, *45* (23), 9292–9302.
- (142) Idziak, I.; Avoce, D.; Lessard, D.; Gravel, D.; Zhu, X. X. *Macromolecules* **1999**, *32* (4), 1260–1263.
- (143) Van Durme, K.; Verbrugghe, S.; Du Prez, F. E.; Van Mele, B. *Macromolecules* **2004**, *37* (3), 1054–1061.

- (144) Horne, R. A.; Almeida, J. P.; Day, A. F.; Yu, N. T. *J. Colloid Interface Sci.* **1971**, *35* (1), 77–84.
- (145) Ramos, J.; Imaz, A.; Forcada, J. *Polym. Chem.* **2012**, *3* (4), 852.
- (146) Zhang, B.; Sun, S.; Wu, P. *Soft Matter* **2013**, *9* (5), 1678.
- (147) Hou, L.; Wu, P. *Soft Matter* **2015**, *11* (35), 7059–7065.
- (148) Zhang, Q.; Hoogenboom, R. *Prog. Polym. Sci.* **2015**, *48*, 122–142.
- (149) Su, M.; Shi, S.-Y.; Wang, Q.; Liu, N.; Yin, J.; Liu, C.; Ding, Y.; Wu, Z.-Q. *Polym. Chem.* **2015**, *6* (36), 6519–6528.
- (150) Woodfield, P. A.; Zhu, Y.; Pei, Y.; Roth, P. J. *Macromolecules* **2014**, *47* (2), 750–762.
- (151) Roth, P. J.; Davis, T. P.; Lowe, A. B. *Macromolecules* **2012**, *45* (7), 3221–3230.
- (152) Barauskas, J.; Landh, T. *Langmuir* **2003**, *19* (23), 9562–9565.
- (153) Rizwan, S. B.; Assmus, D.; Boehnke, a; Hanley, T.; Boyd, B. J.; Rades, T.; Hook, S. *Eur. J. Pharm. Biopharm.* **2011**, *79* (1), 15–22.
- (154) Fong, W.-K.; Hanley, T.; Boyd, B. J. *J. Control. Release* **2009**, *135* (3), 218–226.
- (155) Boyd, B. J.; Khoo, S.-M.; Whittaker, D. V; Davey, G.; Porter, C. J. H. *Int. J. Pharm.* **2007**, *340* (1–2), 52–60.
- (156) Li, W.; Huang, L.; Ying, X.; Jian, Y.; Hong, Y.; Hu, F.; Du, Y. *Angew. Chemie Int. Ed.* **2015**, *54* (10), 3126–3131.
- (157) Liu, C.; Wang, S.; Zhou, H.; Gao, C.; Zhang, W. *J. Polym. Sci. Part A Polym. Chem.* **2016**, *54* (7), 945–954.
- (158) Deguchi, Y.; Kohno, Y.; Ohno, H. *Chem. Lett.* **2015**, *44* (3), 238–240.
- (159) Zhang, N.; Luxenhofer, R.; Jordan, R. *Macromol. Chem. Phys.* **2012**, *213* (9), 973–981.
- (160) Furyk, S.; Zhang, Y.; Ortiz-Acosta, D.; Cremer, P. S.; Bergbreiter, D. E. *J. Polym. Sci. Part A Polym. Chem.* **2006**, *44* (4), 1492–1501.
- (161) Specht, E. H.; Valley, H.; Neuman, A.; Hills, N.; Neher, H. T.; Rohm & Haas; Delaware. Preparation of Acrylamides. US 2,773,063, 1956.
- (162) Shearer Jr., N. H.; Coover Jr., H. W. Amide rodent repellent compositions. US 2,790,744, 1957.
- (163) Scarpa, J. S.; Mueller, D. D.; Klotz, I. M. *J. Am. Chem. Soc.* **1967**, *89* (24), 6024–6030.
- (164) Winnik, F. M. *Macromolecules* **1990**, *23*, 1647–1649.

- (165) Lee, E. M.; Gwon, S. Y.; Ji, B. C.; Kim, S. H. *Fibers Polym.* **2011**, *12* (1), 142–144.
- (166) Yang, Y.; Mijalis, A. J.; Fu, H.; Agosto, C.; Tan, K. J.; Batteas, J. D.; Bergbreiter, D. E. *J. Am. Chem. Soc.* **2012**, *134* (17), 7378–7383.
- (167) Talalay, P.; Fishman, W. H.; Huggins, C. J. *Biol. Chem.* **1946**, *166* (2), 757–772.
- (168) Lutz, J. F.; Hoth, A. *Macromolecules* **2006**, *39* (2), 893–896.
- (169) Li, J.; Hitchcock, A. P.; Stöver, H. D. H. *Langmuir* **2010**, *26* (23), 17926–17935.
- (170) Andrieu, J.; Rudolph, C.; Agarwal, S.; Strasse, H. **2007**, No. Table 1, 8540–8543.
- (171) Hoogenboom, R.; Thijs, H. M. L.; Jochems, M. J. H. C.; van Lankvelt, B. M.; Fijten, M. W. M.; Schubert, U. S. *Chem. Commun.* **2008**, No. 44, 5758.
- (172) Glassner, M.; Lava, K.; de la Rosa, V. R.; Hoogenboom, R. *J. Polym. Sci. Part A Polym. Chem.* **2014**, 3118–3122.
- (173) Gilcreest, V. P.; Carroll, W. M.; Rochev, Y. a; Blute, I.; Dawson, K. a; Gorelov, A. V. *Langmuir* **2004**, *20* (23), 10138–10145.
- (174) Jain, K.; Vedarajan, R.; Watanabe, M.; Ishikiriya, M.; Matsumi, N. *Polym. Chem.* **2015**, *6* (38), 6819–6825.
- (175) Zhang, N.; Salzinger, S.; Rieger, B. *Macromolecules* **2012**, *45* (24), 9751–9758.
- (176) Meiswinkel, G.; Ritter, H. *Macromol. Chem. Phys.* **2014**, *215* (7), 682–687.
- (177) Soller, B. S.; Salzinger, S.; Rieger, B. *Chem. Rev.* **2015**, *116*, 1993–2022.
- (178) Cheng, H.; Shen, L.; Wu, C. *Macromolecules* **2006**, *39* (6), 2325–2329.
- (179) Shiomi, T.; Imai, K.; Watanabe, C.; Miya, M. *J. Polym. Sci. Part B-Polymer Phys.* **1984**, *22*, 1305–1312.
- (180) Bokias, G.; Staikos, G.; Iliopoulos, I. *Polymer (Guildf)*. **2000**, *41* (20), 7399–7405.
- (181) Mori, T.; Nakashima, M.; Fukuda, Y.; Minagawa, K.; Tanaka, M.; Maeda, Y. *Langmuir* **2006**, *22* (9), 4336–4342.
- (182) Chang, Y.; Chen, W. Y.; Yandi, W.; Shih, Y. J.; Chu, W. L.; Liu, Y. L.; Chu, C. W.; Ruaan, R. C.; Higuchi, A. *Biomacromolecules* **2009**, *10* (8), 2092–2100.
- (183) Dong, Z.; Mao, J.; Wang, D.; Yang, M.; Wang, W.; Bo, S.; Ji, X. *Macromol. Chem. Phys.* **2014**, *215*, 111–120.

- (184) Zhu, Y.; Batchelor, R.; Lowe, A. B.; Roth, P. J. *Macromolecules* **2016**, 49 (2), 672–680.
- (185) Käfer, F.; Liu, F.; Stahlschmidt, U.; Jérôme, V.; Freitag, R.; Karg, M.; Agarwal, S. *Langmuir* **2015**, 31 (32), 8940–8946.
- (186) Seuring, J.; Agarwal, S. *Macromolecules* **2012**, 45 (9), 3910–3918.
- (187) Chandler, D. L. Energy savings in black and white <http://news.mit.edu/2009/madmec-roof> (accessed Aug 22, 2016).
- (188) Flory, P. J. *J. Chem. Phys.* **1941**, 9 (8), 660.
- (189) Rubinstein, M.; Colby, R. H. *Polymer physics*; 2003.
- (190) Orwoll, R. a; Arnold, P. a. *Phys. Prop. Polym. Handb.* **2007**, 50 (3), 451.
- (191) Brinke, G. Ten; Karasz, F. *Macromolecules* **1984**, 17, 815–820.
- (192) Roth, P. J. *Macromol. Chem. Phys.* **2014**, 215 (9), 825–838.
- (193) Seuring, J.; Agarwal, S. *Macromol. Rapid Commun.* **2012**, 33 (22), 1898–1920.
- (194) White, R. P.; Lipson, J. E. G.; Higgins, J. S. *Macromolecules* **2012**, 45 (2), 1076–1084.
- (195) Lipson, J. E. G.; Tambasco, M.; Willets, K. A.; Higgins, J. S. *Macromolecules* **2003**, 36 (8), 2977–2984.
- (196) Rangel-Nafaile, C.; Metzner, A. B.; Wissbrun, K. F. *Macromolecules* **1984**, 17, 1187–1195.
- (197) Zhang, H.; Guo, S.; Fan, W.; Zhao, Y. *Macromolecules* **2016**, 49 (4), 1424–1433.
- (198) Konno, S.; Saeki, S.; Kuwahara, N.; Nakata, M.; Kaneko, M. *Macromolecules* **1975**, 8 (6), 799–804.
- (199) Siow, K. S.; Delmas, G.; Patterson, D. *Macromolecules* **1972**, 5 (1), 29–34.
- (200) Seuring, J.; Agarwal, S. *Macromol. Rapid Commun.* **2012**, 33 (22), 1898–1920.
- (201) Pineda-Contreras, B. A.; Schmalz, H.; Agarwal, S. *Polym. Chem.* **2016**, 7 (10), 1979–1986.
- (202) Schulz, D. N.; Peiffer, D. G.; Agarwal, P. K.; Larabee, J.; Kaladas, J. J.; Soni, L.; Handwerker, B.; Garner, R. T. *Polymer (Guildf)*. **1986**, 27 (11), 1734–1742.
- (203) Huglin, M. B.; Radwan, M. a. *Polym. Int.* **1991**, 26 (i), 97–104.
- (204) Mary, P.; Bendejacq, D. D.; Labeau, M.-P.; Dupuis, P. J. *Phys. Chem. B* **2007**, 111 (27), 7767–7777.

- (205) Hildebrand, V.; Laschewsky, A.; Wischerhoff, E. *Polym. Chem.* **2016**, 7 (3), 731–740.
- (206) Shi, M.; Duan, X.; Liu, Z.; Liu, Z.; Jiang, J. *Chinese J. Polym. Sci.* **2016**, 34 (6), 777–784.
- (207) Saeki, S.; Konno, S.; Kuwahara, N.; Nakata, M.; Kaneko, M. *Macromolecules* **1974**, 7 (4), 521–526.
- (208) Cowie, J. M. G.; McEwen, I. J. *Br. Polym. J.* **1986**, 18 (6), 387–390.
- (209) Imre, A.; Van Hook, W. A. *Macromolecules* **2000**, 33 (14), 5308–5309.
- (210) Zeman, L.; Patterson, D. *J. Phys. Chem. B* **1972**, 76, 1214–1219.
- (211) Scholte, T. G. *J. Polym. Sci. Part C Polym. Symp.* **2007**, 39 (1), 281–291.
- (212) Koningsveld, R.; Kleintjens, L. A.; Shultz, A. R. *J. Polym. Sci. Part A-2 Polym. Phys.* **1970**, 8 (8), 1261–1278.
- (213) Saeki, S.; Kuwahara, N.; Konno, S.; Kaneko, M. *Macromolecules* **1973**, 6 (2), 246–250.
- (214) Saeki, S.; Kuwahara, N.; Konno, S.; Kaneko, M. *Macromolecules* **1973**, 6 (4), 589–593.
- (215) Imre, A.; Van Hook, W. A. *J. Polym. Sci. Part B Polym. Phys.* **1996**, 34 (4), 751–760.
- (216) Dobashi, T.; Nakata, M.; Kaneko, M. *J. Chem. Phys.* **1980**, 72 (12), 6685.
- (217) Dobashi, T.; Nakata, M.; Kaneko, M. *J. Chem. Phys.* **1980**, 72 (12), 6692.
- (218) Szydlowski, J.; Van Hook, W. A. *Macromolecules* **1991**, 24 (17), 4883–4891.
- (219) Luszczyk, M.; Rebelo, L. P. N.; Van Hook, W. A. *Macromolecules* **1995**, 28 (3), 745–767.
- (220) Casielles, A. G.; Rubio, R. G.; Monroy, F.; Ortega, F. *Phys. Rev. E* **1994**, 49 (2), 1404–1410.
- (221) Strazielle, C.; Benoit, H. *Macromolecules* **1975**, 8 (2), 203–205.
- (222) Vanhee, S.; Kiepen, F.; Brinkmann, D.; Borchard, W.; Koningsveld, R.; Berghmans, H. *Macromol. Chem. Phys.* **1994**, 195 (2), 759–780.
- (223) Howard, P. H.; Banerjee, S.; Robillard, K. H. *Environ. Toxicol. Chem.* **1985**, 4 (5), 653–661.
- (224) Lide, D. R. *CRC Handbook of Chemistry and Physics, 84th Edition, 2003-2004*; 2003; Vol. 53.
- (225) Ver Strate, G.; Philippoff, W. *J. Polym. Sci. Polym. Lett. Ed.* **1974**, 12 (5), 267–275.

- (226) Wirtz, D. *Macromolecules* **1994**, 27 (20), 5639–5642.
- (227) Wolf, B. A. *Die Makromol. Chemie, Rapid Commun.* **1980**, 234 (4), 231–234.
- (228) Bakry, A. M.; Abbas, S.; Ali, B.; Majeed, H.; Abouelwafa, M. Y.; Mousa, A.; Liang, L. *Compr. Rev. Food Sci. Food Saf.* **2016**, 15 (1), 143–182.
- (229) Mishra, M. In *Handbook of Encapsulation and Controlled Release*; CRC Press, 2015; pp 3–19.
- (230) Dardelle, G.; Beaussoubre, P.; Erni, P. Hybrid Coacervate Capsules. WO 2013/174921 A1, 2013.
- (231) Song, J. K.; Kang, H. C.; Kim, K. S.; Chin, I.-J. *Mol. Cryst. Liq. Cryst.* **2007**, 464 (1), 263–269.
- (232) Onder, E.; Sarier, N.; Cimen, E. *Thermochim. Acta* **2008**, 467 (1–2), 63–72.
- (233) Ach, D.; Briançon, S.; Broze, G.; Puel, F.; Rivoire, A.; Galvan, J.-M.; Chevalier, Y. *Can. J. Chem. Eng.* **2015**, 93 (2), 183–191.
- (234) Mayya, K.; Bhattacharyya, A.; Argillier, J.-F. *Polym. Int.* **2003**, 52 (4), 644–647.
- (235) Yu, D.; Qiao, W.; Li, Q.; Pei, G. *J. Fiber Bioeng. Informatics* **2012**, 5 (1), 67–76.
- (236) Bachtzi, A. R.; Kiparissides, C. *J. Control. Release* **1996**, 38 (1), 49–58.
- (237) Horger, G. Encapsulation Process By Simple Coacervation Using Inorganic Polymers. US 3,872,024, 1977.
- (238) Yin, X.; Stöver, H. D. H. *Macromolecules* **2003**, 36 (23), 8773–8779.
- (239) Bone, S.; Fadel, A.; Geffroy, C. Improvements in or relating to organic compounds. WO2015/150370 A1, 2014.
- (240) Devi, N.; Hazarika, D.; Deka, C.; Kakati, D. K. *J. Macromol. Sci. Part A* **2012**, 49 (11), 936–945.
- (241) Dai, R.; Wu, G.; Li, W.; Zhou, Q.; Li, X.; Chen, H. *Colloids Surfaces A Physicochem. Eng. Asp.* **2010**, 362 (1–3), 84–89.
- (242) Saido, K.; Taguchi, H.; Yada, S.; Ishihara, Y.; Kuroki, T.; Ryu, I.-J.; Chung, S.-Y. *Macromol. Res.* **2003**, 11 (3), 178–182.
- (243) Choi, S. Y.; Rodríguez, H.; Gunaratne, H. Q. N.; Puga, A. V.; Gilpin, D.; McGrath, S.; Vyle, J. S.; Tunney, M. M.; Rogers, R. D.; McNally, T. *RSC Adv.* **2014**, 4 (17), 8567.
- (244) Saido, K.; Kuroki, T.; Ikemura, T.; Kirisawa, M. *J. Anal. Appl. Pyrolysis* **1984**, 6 (2), 171–181.

- (245) Zeman, L.; Biroš, J.; Delmas, G.; Patterson, D. *J. Phys. Chem.* **1972**, 76 (8), 1206–1213.
- (246) Bae, Y. C.; Lambert, S. M.; Soane, D. S.; Prausnitz, J. M. *Macromolecules* **1991**, 24, 4403–4407.
- (247) Bergbreiter, D. E.; Fu, H. *J. Polym. Sci. Part A Polym. Chem.* **2008**, 46 (1), 186–193.
- (248) Bebis, K.; Jones, M. W.; Haddleton, D. M.; Gibson, M. I. *Polym. Chem.* **2011**, 2 (4), 975–982.
- (249) Hou, L.; Chen, Q.; An, Z.; Wu, P. *Soft Matter* **2016**, 12 (8), 2473–2480.
- (250) Min, E. H.; Ting, S. R. S.; Billon, L.; Stenzel, M. H. *J. Polym. Sci. Part A Polym. Chem.* **2010**, 48 (15), 3440–3455.
- (251) Mayo, F. R. *J. Am. Chem. Soc.* **1968**, 90 (5), 1289–1295.
- (252) Mayo, F. R. *J. Am. Chem. Soc.* **1953**, 75 (24), 6133–6141.
- (253) Khuong, K. S.; Jones, W. H.; Pryor, W. A.; Houk, K. N. *J. Am. Chem. Soc.* **2005**, 127 (4), 1265–1277.
- (254) Shero, E. J.; O'Brien, J. J.; Priddy, D. B. Free Radical Polymerisation of Styrene Monomer. US 5,145,924, 1992.
- (255) Hoogenboom, R.; Becer, C. R.; Guerrero-Sanchez, C.; Hoeppener, S.; Schubert, U. S. *Aust. J. Chem.* **2010**, 63 (8), 1173–1178.
- (256) Piccarolo, S.; Titomanlio, G. *Die Makromol. Chemie, Rapid Commun.* **1982**, 3 (6), 383–387.
- (257) Hoogenboom, R.; Rogers, S.; Can, A.; Becer, C. R.; Guerrero-Sanchez, C.; Wouters, D.; Hoeppener, S.; Schubert, U. S. *Chem. Commun. (Camb)*. **2009**, No. 37, 5582–5584.
- (258) García Sakai, V.; Higgins, J. S.; Trusler, J. P. M. *J. Chem. Eng. Data* **2006**, 51 (2), 743–748.
- (259) Doskočilová, D.; Mikeš, F.; Pecka, J.; Kříž, J. *Die Makromol. Chemie* **1992**, 193 (10), 2529–2538.
- (260) Meyer, V. E. *J. Polym. Sci. Part A-1 Polym. Chem.* **1966**, 4 (11), 2819–2830.
- (261) van der Goot, A. J. The extruder as a polymerisation reactor for styrene based polymers, University of Groningen, 2003.
- (262) Rana, D.; Bag, K.; Bhattacharyya, S. N.; Mandal, B. M. *J Polym Sci B Polym Phys* **2000**, 38, 369–375.
- (263) Sahloul, N.; Penlidis, A. *Adv. Polym. Technol.* **2004**, 23 (3), 186–195.
- (264) Plessis, C.; Arzamendi, G.; Alberdi, J. M.; Agnely, M.; Leiza, J. R.; Asua, J. M.

- Macromolecules* **2001**, 34 (17), 6138–6143.
- (265) Britton, D.; Heatley, F.; Lovell, P. a. *Macromolecules* **1998**, 31 (9), 2828–2837.
- (266) Kavousian, A.; Ziaee, F.; Nekoomanesh, M. H.; Leamen, M. J.; Penlidis, A. *J. Appl. Polym. Sci.* **2004**, 92 (5), 3368–3370.
- (267) Kleintjens, L. A.; Koningsveld, R.; Gordon, M. *Macromolecules* **1980**, 13 (2), 303–310.
- (268) Willcock, H.; Lu, A.; Hansell, C. F.; Chapman, E.; Collins, R.; Reilly, R. K. O. **2014**, 1023–1030.
- (269) Vidovi, E.; Sari, K.; Janovi, Z. *Croat. Chem. ACTA* **2002**, 75 (3), 769–782.
- (270) Minsk, L. M.; Kotlarchik, C.; Meyer, G. N. *J. Polym. Sci. Polym. Chem. Ed.* **1973**, 11 (12), 3037–3042.
- (271) North, A. M.; Scallan, A. M. *Polymer (Guildf)*. **1964**, 5, 447–455.
- (272) Vimala, P.; Devi, V. N.; Pazhanisamy, P. *Int. J. ChemTech Res.* **2010**, 2 (3), 1717–1723.
- (273) Sato, T.; Endo, M.; Shiomi, T.; Imai, K. **1996**, 37 (11), 2131–2136.
- (274) Sato, T.; Endo, M.; Shiomi, T.; Imai, K. *Polymer (Guildf)*. **1996**, 37 (11), 2131–2136.
- (275) Rahman, S. S. A.; Kawaguchi, D.; Ito, D.; Takano, A.; Matsushita, Y. *J. Polym. Sci. Part B Polym. Phys.* **2009**, 47 (22), 2272–2280.
- (276) Djabourov, M.; Leblond, J.; Papon, P. *J. Phys.* **1988**, 49, 319–332.
- (277) Nurumbetov, G.; Ballard, N.; Bon, S. a. F. *Polym. Chem.* **2012**, 3, 1043–1047.
- (278) Jaggars, R. W.; Chen, R.; Bon, S. A. F. *Mater. Horiz.* **2016**, 3 (1), 41–46.
- (279) Jeong, W.; Kim, J.; Kim, S.; Lee, S.; Mensing, G.; Beebe, D. J. *Lab Chip* **2004**, 4 (6), 576–580.
- (280) Bell, R. V.; Parkins, C. C.; Young, R. A.; Preuss, C. M.; Stevens, M. M.; Bon, S. A. F. *J. Mater. Chem. A* **2016**, 4, 813–818.

2 Chapter 2: Hollow Silica Shells for Opacity Modifiers and Ultrasound Contrast Agents.

2.1 Abstract

In this work we investigate the use of air voided particles as a potential opacifier replacement for TiO_2 within paint films. A common filler for paint materials was used as a template upon which a silica shell was synthesised using a reaction of tetraethyl orthosilicate (TEOS) and 1,8-bis(triethoxysilyl)octane (BTEOSO) to impart different hydrophobicities within a one pot reaction. We found that altering the acid addition during the etching step led to an increased number of silica shells remaining. The particles exhibited a good response to ultrasound imaging and also showed an increase in opacifying effect over the template particles.

2.2 Introduction

Materials with hollow voids are interesting for a wide range of applications such as ultra sound contrast agents, insulation (both thermal and acoustic), and opacifying pigments within paints.¹⁻⁵ **Section 2.2.1** describes the use of generic opacifiers within a paint formulation along with the need for additional component to create an effective paint. **Section 2.2.2** moves onto the use of TiO_2 and other replacements used within paints to achieve opacity and **Section 2.2.3** discusses how sacrificial templating can be used to create hollow particles with a variety of morphologies.

The principal idea in this chapter is the synthesis of a non-spherical hollow material containing an air void for use as both an ultrasound contrast agents and opacifiers within paints. The method of synthesis chosen was sacrificial templating using a ellipsoidal template, coating with silica based around tetraethyl orthosilicate (TEOS) reacted with differing amount of 1,8-bis(triethoxy silyl)octane (BTEOSO) to impart additional properties into the silica shell. Following the coating, an acid etch was employed to obtain the hollow particles.

The new materials were then employed as an ultrasound contrast to agent to indicate the intact air voids within the particles as well as an opacifier within a paint formulation, which will be discussed later in this chapter (**Section 2.3**)

2.2.1 Introduction to coatings

Coatings technology has been around since the 1700's⁶ and found to be ubiquitous to modern life. It has grown to be a multibillion pound industry for both protection and decorative uses.

A waterborne coating typically consists of a latex binder of low T_g , pigment of organic or inorganic nature, inorganic fillers to both space the pigments and increase the solids content, rheology modifiers, and additives such as biocides and antifoaming agents (**Table 2-1**).

Chapter 2: Silica Shells for Opacity

Table 2-1. Typical formulation for a white decorative coating including the mill base and let down. The mill base is the premixed system with the let down added after full dispersion of the mill base is acquired. Formulations were obtained from Hempel.

Component	Mill base component mass/ g	Let down component mass / g
Water	300	-
Bermoll (<i>rheology modifier</i>)	10.44	-
Ammonia (25 wt%) (<i>pH modifier</i>)	1.20	-
Dispelair CF515 (<i>antifoamer</i>)	2.01	2.01
Actinicide ® MBL (<i>biocide</i>)	1.50	-
Ethylan BCD (<i>dispersant</i>)	0.50	-
Snowcal 60 ® (<i>filler</i>)	4.07	-
Minex (<i>filler</i>)	1.31	-
TiO ₂ (<i>opacifier</i>)	74	-
Polymer Latex (<i>binder</i>)	-	150

The polymeric latex is used in waterborne paints as a binder between the substrate and pigment/additives. It is required to have a low T_g so that once applied, the polymer can exceed the minimum film formation

temperature (MFFT) at a temperature of 5 °C and above so to form an even film.⁷ However, if a film with a very low MFFT is used, it can lead to an increase in tack and loss of protection. Therefore some film formulations use higher T_g polymer latexes and add coalescing agents (such as a plasticisers) to reduce the MFFT of the system.⁸ The use of volatile organic components (VOC's) within paints has been placed under heavy legislation since 2010 in an effort to reduce harmful chemicals within them.

The process in which a waterborne paint forms a film is as follows a four step process. The paint must have a high enough viscosity so once it is applied to a substrate it does not run.⁹ After it has been applied water evaporation begins, leading to a concentration of the solid particulates of latex colloids, pigments, and other additives within the remaining water. As water evaporation continues, the solids within the paint are forced closer together. If the ambient temperature is above the MFFT of the latex, the spherical colloids begin to deform into a hexagonal array, trapping other solids within.¹⁰ Interdiffusion of polymer chains and coalescence of the latex particles occurs due to the higher surface area contact between the latex particles and high temperature of the system. The movement of the polymeric chains and inability of the other solids remaining in the system, a homogenous film is formed. This process is outlined in **Figure 2-1** and an excellent in-depth review on latex film formation has been given by Keddie.¹¹

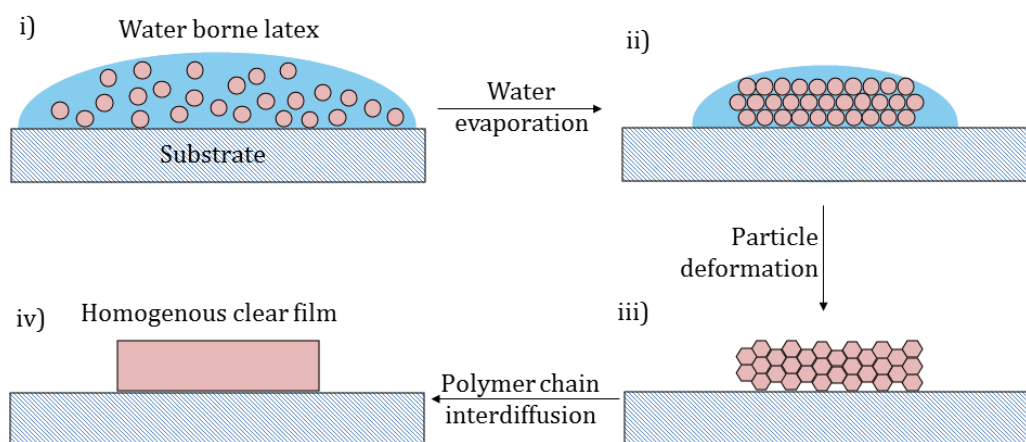


Figure 2-1. Film formation process schematic. i) application of the waterborne system, ii) concentration *via* evaporation of water, iii) hexagonal array formed by deformation of spherical latex and temperature exceeding the MFFT, iv) polymer chain interdiffusion and coalescence forming a homogenous film.

Pigments, such as TiO_2 in **Table 2-1**, are used to selectively reflect a certain portion of the visible spectrum. The most common pigment used is titanium dioxide.¹² The reason for this is the high refractive index (RI) of TiO_2 ($n = 2.5\text{--}2.7$ depending on crystal morphology) compared to the RI of the binder ($n = 1.4\text{--}1.6$ depending on polymer binder used) and TiO_2 absorbs very little and scatters evenly across the visible spectrum.^{13,14} The RI difference (>0.9) leads to a large amount of light refraction, which results in an opaque white film. This process will be expanded upon later in **Section 2.2.2**. Both organic (such as quinacridone red) and inorganic (such as Phthalocyanine Green G) pigments, also referred to as tints, are then added on top of the base TiO_2 for desired colour *via* selective light absorption.

Fillers and extenders such as SOCAL P3 ® and SNOWCAL 60 ®, which are often CaCO₃ based, though barium sulphite extenders are often used instead of CaCO₃ extenders when the paint market is based on mass of paint and not volume of paint¹⁵, are added to the paint system for two reasons: i) they act as a spacing agent between TiO₂ to reduce crowding. This is particularly important with TiO₂ as when the particles become closely packed the scattering efficiency reduces (referred to as optic crowding). This leads to more TiO₂ being added, which is often the most expensive component in a paint system, and ii) inclusion of air within the paint. Extenders are often added into a system to increase to pigment volume concentration (PVC) of a system. The PVC of a coating is the ratio of the volume of pigment to the total volume of solids within the system (**Equation 2-1**).

$$PVC = \frac{V_{pig} + V_{fill}}{V_{pig} + V_{fill} + V_{bind}} \times 100 \quad 2-1$$

Where V_{pig} is the volume of pigment in the system, V_{fill} is the volume of fillers with in paint, and V_{bind} is the non-volatile components of the binder.

If enough extender is added, the PCV can go above the critical pigment volume concentration (CPVC) which leads to an inclusion of air voids within the film (**Equation 2-2**).^{16,17} These air voids increase the opacity of a paint as the pockets of air ($n = 1.00$) within the paint which leads to a RI difference. This can lead to a reduction of TiO₂ in the system whilst retaining the hiding power. The inclusion of air within the paint also changes the paint from a gloss finish to a matte finish and lead it to become more permeable to both

liquids and gases. As matte paints have a reduction in barrier properties, they are solely used within the decorative sector.¹⁸

$$CPVC = \frac{1}{1 + (OA)(\rho)/93.5} \quad 2-2$$

Where OA is the oil absorption of linseed oil per 100 grams of pigment, ρ is the density of the pigments(s) and 93.5 is 100 times the density of linseed oil.

Rheology modifiers (such as Bermocoll in **Table 2-1**) are a vital component of the paint system. Paints are required to be shear thinning at high shear rates so the system can be evenly mixed whilst at low shear rates the system must remain viscous enough to not drip or run once painted or sediment whilst stored in the can.

Finally, additives are required for a wide variety of reasons. Dispersants (Ethylan BCD from **Table 2-1**) are added to aid the even dispersion of solids within the system. Biocide additives (Acticide MBL in **Table 2-1**) are there to reduce the risk of bacterial decomposition of CaCO_3 and other organic material within the paint. Antifoaming agents (Dispelair CF515 in **Table 2-1**) are required to reduce unwanted air inclusion within the paint. Wetting agents are used to help the polymer film fully wet around the solids upon drying and levelling agents are sometimes added to help reach a level end film once dried.

The dry film thickness (DFT) of any film can be calculated using the total volume of solids (*VS*) (%) and the wet film thickness (*WFT*) (μm) assuming only 1D drying occurs (**Equation 2-3**).

$$DFT = \frac{VS \times WFT}{100} \quad 2-3$$

An important factor affecting the DFT is the spreading rate (SR) (m²·L⁻¹) of the paint solution. This term indicates the theoretical coverage 1 L of paint will cover at a certain DFT. For example, using **Equation 2-4**, a paint with Vol% of 35% solids with a require DFT of 125 μm would have a SR of 2.8 m²·L⁻¹.¹⁹

$$SR = \frac{10}{DFT} \times VS \quad 2-4$$

2.2.2 TiO₂ and replacement opacifiers for coatings

Opacifiers work within film coatings by adding centres of refractive index differences. Scattering occurs due to the interaction of light at the interface of two materials with different refractive indexes (**Figure 2-2**). As the films contain multiple centres of differing RI, the light will interact with many interfaces before reaching the substrate. If the particles have a high enough RI or are present in a high enough volume, the light could be completely reflected resulting in an opaque film (**Figure 2-2 b**). Conversely, if the film contains pigment with a low RI or in too low a concentration, the light will be only partially scattered before coming in contact with the substrate

and the resulting film will be cloudy instead of a fully opaque (**Figure 2-2 a**). Due to the volume of pigments within the film, film thickness also plays a large role in opacity though manufacturers are aiming towards the thinnest possible film to give the best results.

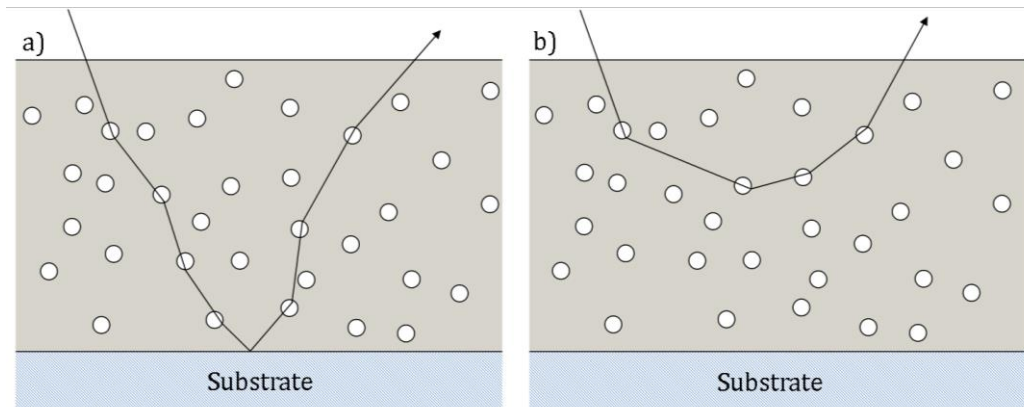


Figure 2-2. Schematic particles (circles) scattering light (arrows) within a film where a) the particles have low RI and b) the particles have high RI. Due to the light being fully scattered before contacting the substrate, (b) would be considered fully opaque and (a) only partially.

Mie theory has long been used to describe the scattering of light through the entire spectrum of UV to infrared. Mie scattering calculations use two Mie coefficients, two incident polarisations complex scattering amplitudes, an asymmetry factor, and extinction and scattering efficiencies.²⁰ This allows Mie theory to accurately describe the scattering of individual particle or very dilute systems. This makes it ideal for particle sizing though not paints due to the high concentration within the films.

Kubelka-Munk (KM) theory is a more effective way of looking at light scattering within a film.²¹ The simplified version of the KM equation (**Equation 2-5**) is used within the coatings industry to describe the scattering of films.²² Reflectance and any wavelength using this method is a function of the k/s ratio and therefore cannot be used to give absolute values but comparative ones.

$$R = \frac{(1 - R)^2}{2R} = \frac{k}{s} = \frac{Ac}{s} \quad 2-5$$

Where R is the reflectance, k is the absorption coefficient, A is the absorbance, c is the concentration of absorbing species, and s is the scattering coefficient.

The following assumptions made with the KM theory:

- i. Scattering and absorption constants do not vary in a thin film.
- ii. Films contain particles able to disperse light and are homogenous.
- iii. Film thickness is known but is infinitely long and wide to eradicate boundary effects.
- iv. Surface reflectance does not occur internally or externally.
- v. Polarisation and fluorescence are ignored.
- vi. Incident light hitting the film is diffuse and homogenous.

TiO₂ is vital for most common coatings due to its high refractive index and therefore its ability to “hide” the substrate underneath it. TiO₂ naturally occurs in four forms; anatase (TiO₂), rutile (TiO₂), ilmenite (FeTiO₃), and leucoxene (TiO₂/FeTiO₃). Of the four, only anatase and rutile are used within coatings. Whilst the chemical composition of both are equal, they vary in lattice structure, density, and refractive index (anatase $n_{avg} = 2.5$, rutile $n_{avg} = 2.7$).¹² Whilst it does have highly desirable properties, the coatings industry is looking to reduce the quantity of TiO₂ for both environmental and economic reasons.²³ TiO₂ is used for other purposes such as developing self-cleaning, anti-microbial products and dye-sensitised solar cells. However, of the six million tonnes produced yearly, 99 % is used as pigment.^{24–27} Environmentally, TiO₂ production results in the destruction and loss of habitat in South America and Africa along with the production of sulfuric acid and a carbon foot print of 5.2 tonnes of CO₂ per tonne of TiO₂.²⁸

Direct replacement of TiO₂ can be done using minerals already on the market. ZnO has long been used widely as a white pigment but also within brass production, rubber production, and medicinal uses.^{29–32} With the appearance of TiO₂, ZnO has seen a drop in use as the pigment. This is largely due to its RI being only 2.0 in comparison to TiO₂'s ~ 2.6 .³³ In addition to the unfavourable interaction within the paint between TiO₂ and ZnO. If both are present within a waterborne latex, destabilisation occurs causing a gel complex to form. The general consensus for this is that either solubilisation of Zn and chelation with dispersion occurs, aggregates form between ZnO and binder, or co-flocculation between TiO₂ and ZnO occurs.³⁴ Despite this issue,

ZnO is still widely used within marine coatings as both an opacifier and an antifouling agent.^{35,36}

Another mineral used as opacifying agent is CaCO_3 . With a RI between 1.60 – 1.68, depending on polymorph, it does not have the scattering power of TiO_2 , although using a grinding mill or precipitation method can improve its scattering efficiency.³⁷ In particular, precipitated calcium carbonate (PCC) can form unique geometries that have shown an increase in scattering efficiency and volume replacement of TiO_2 with these can have no effect on opacity.³⁷

Incorporation of stable air voids within the polymer films is a way to attain light scattering with a reduction of TiO_2 . There are 3 types of air voids:

- i. Intercoating voids – air voids occurring at the pigment-binder interface. These often occur when formulations go above the CPVC by using an extender. These aid opacity *via* acting similar to foam, causing scattering of light at the air-binder interface.
- ii. Intraparticle voids – air voids within a particle. These systems do not require concentrations above the CPVC as they formed before addition to the system. These aid opacity *via* the air void existing in a large enough volume to scatter light.
- iii. Intrabinder voids – air voids within the binder itself. These can occur when mixing the paint draws air into it. These aid opacity *via* the use of very small air voids reducing the RI of the air/binder mixture, increasing the RI difference between binder and pigments.

As type (ii) is seen as the best opacifying route without reduction of quality of the film, it will be the focus of this work. In this case the air voids need to be self-contained within the applied coating and kept below the CPVC thus retaining the barrier properties and gloss finish.³⁸ Inclusion of these air voids could also show increased thermal and acoustic insulation whilst reducing transport cost due to lower density. Several technologies exist to form air voids within a coating.

Excellent examples of air voids creating opacity are found within nature in both the Small White butterfly, *Pieris rapae*, and the brilliantly white *Cyphochilus* beetle. The scales of the *Pieris rapae* butterfly (**Figure 2-3**) exists as an ordered series of rectangular hollows of $2.3 \pm 0.1 \mu\text{m}$ by $0.95 \pm 0.15 \mu\text{m}$. Within these hollows rests nanoscale beads shown in **Figure 2-3 C**. It was found that upon the removal of these colloids, increased the reflectance of UV wavelengths though reduced the reflectance of the longer wavelengths. Even with full removal of the beads, the ordered structure of the hollows still reflected significant visible light giving the system a white colour.³⁹

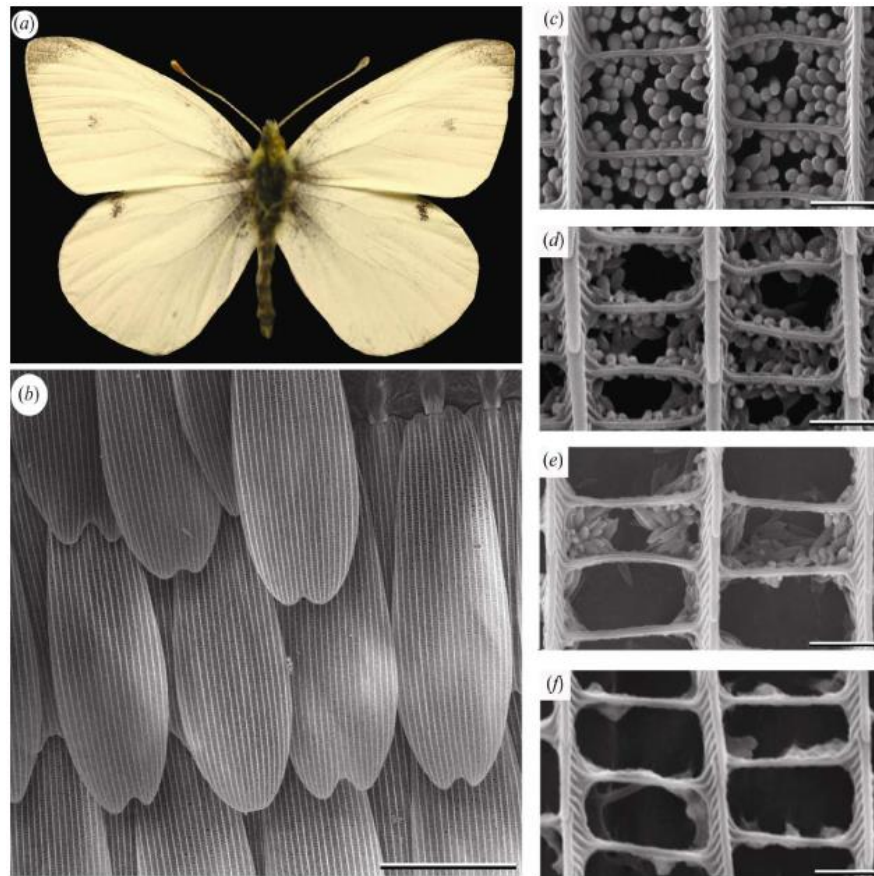


Figure 2-3. a) *Pieris rapae* butterfly, b) overlapping scales on the wings of the *P. rapae* (scalebar = 50 μm). c-f) SEM micrographs of a dorsal wing scale after immersion in a 1% ammonium hydroxide solution. c) an untreated scale, d) 10 second exposure, e) 30 second exposure, and f) 1 minute exposure. (c-f scale bars 1 μm).³⁹

Unlike the *Pieris rapae* butterfly, the air voids within the *Cyphochilus* beetle are random distributed throughout the scales and randomly sized (**Figure 2-4**).^{40,41} The scattering centres (air voids) are separated by fibres roughly 250 nm wide that are randomly connected throughout the network which aids in reducing optical crowding. The scales are a mere 5 μm in size compared to that of 40-70 μm coatings that can produce an equal whiteness.

The beetle therefore shows that neither order nor symmetry is needed to reach an effective hiding power.⁴⁰

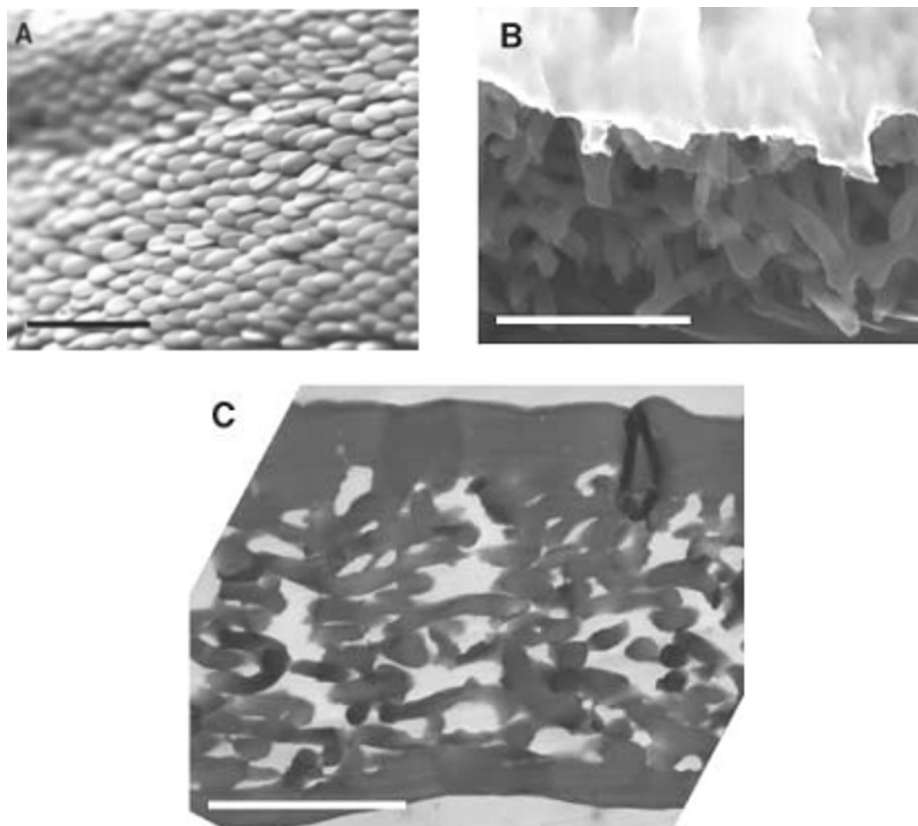


Figure 2-4. A) An optical micrograph showing the arrangement of the scales of the *Cyphochilus* beetle (scale bar 1.0 mm). B) SEM image of a fractured edge of one of the scales showing a disordered internal structure (scale bar 3.0 μm) and C) TEM images of a section of the scale (scale bar 3.0 μm).⁴¹

There are some examples of hollow particles used within the coatings industry. Hollow glass spheres are predominately used as insulators within coatings due to the central air void but also as agents to stop crack propagation.⁴² The low porosity of the glass microspheres leads to a wet and

dry opacity.⁴³ However the synthesis method of using flames to convert glass to spheres often leads to solids particles being formed as well. The solid particle would have no RI difference within so would show no difference if incorporated within the film.

The most commercially successful hollow void additive to paints is currently the ROPAQUE™ brand produced by Dow. ROPAQUE™ is a hollow polymeric particle where pores and interior voids are filled with water in the wet state. Upon application and subsequent drying, the water leaves the interior of the particle, leaving behind an air void which acts as a scattering centre (**Figure 2-5**).^{44,45} These particles, on average, have a core void of ~1 µm with a shell of 200 nm. The shell material is similar in RI to that of the binder system it is used in so any opacity the system has is purely from the scattering of the interior air core and not the shell material.

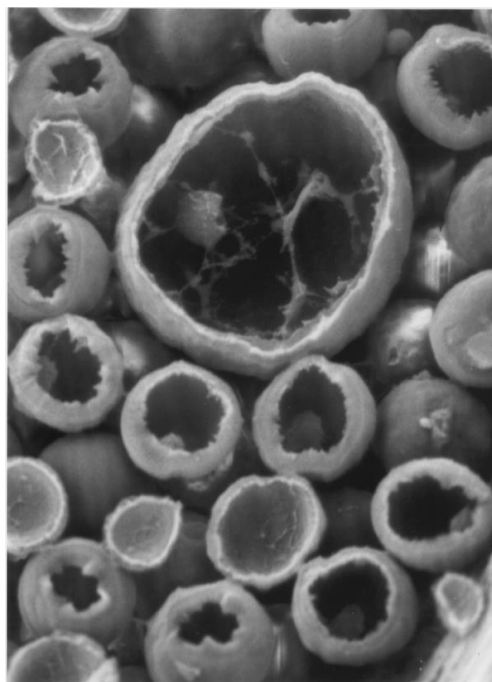


Figure 2-5. Image of hollow ROPAQUE™ freeze fractured particles. The hollow particles have an interior space of $\sim 1\ \mu\text{m}$ and a shell wall of $\sim 200\ \text{nm}$.⁴⁴

Kowalski *et al* first developed a method to produce hollow latex by using an osmotic swelling method.⁴⁵ This method used a seed particle that could be swollen depending on the pH and a shell material that has a high T_g . An initial seed of methyl methacrylate, 3-(dimethylamino)propyl methacrylate, and 1,3-butylene glycol dimethacrylate, using an active quaternary ammonium cation as the surfactant, was synthesised by emulsion polymerisation where the monomer was fed in over 1 hour. Under acidic conditions, the seed could be swollen and then shrunk again upon returning to basic conditions. A seeded emulsion polymerisation was used to form the hard shell material. At pH 9.5, 3-(methacrylamide)propyl

trimethylammonium chloride was added to the solution and isobutyl methacrylate was fed in over 1 hour. Once the core-shell particle (core@shell) latex was produced, it was heated above the T_g of poly(isobutyl methacrylate) and acidified to pH 0 using acetic acid.⁴⁵ Due to the acidic conditions and high temperature, the soft core was able to swell and force the hard shell to swell with it. After an hour, the latex was cooled down to room temperature and the pH increased to 9.5. The shell material was trapped in the swollen state whilst the core material returned to the original size. The core could then be extracted, leaving a hollow void.

Taking the success of hollow polymer particles effectively producing white paint films, hollow particles can clearly be used for opacifiers. As shown with the *Cyphochilus* beetle and *Pieris rapae* butterfly, non-spherical air voids can act as effective light scatters also and, in the case of the beetle, monodispersity is also not an issue.^{39,41} Therefore, this poses the interesting question of whether anisotropic particles can effectively scatter light with equal or greater efficiency of spherical particles. An effective and well known method of synthesising hollow materials is the use sacrificial templating.

2.2.3 Sacrificial Templating

The process of sacrificial templating, such as that used by Kowalski *et al*, is to form a nanocomposite *via* coating a core particle with shell material. Once coated, the core is then removed *via* a chemical or physical process such as dissolving, etching, or calcining.^{46–48} The shell material selected should be

resistant to the removal process so to retain the morphology of the core particle (**Figure 2-6**).

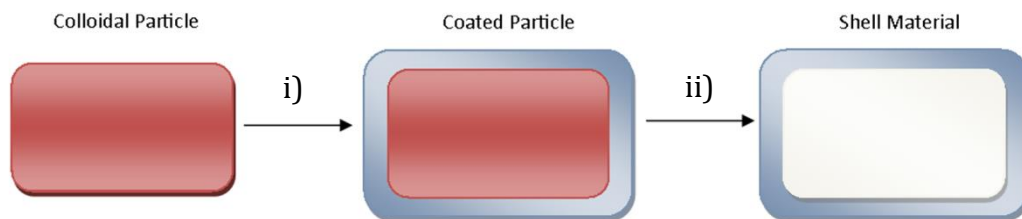


Figure 2-6. Schematic for sacrificial templating where i) the formation of the shell material by layer by layer, precipitation, or polymerisation occurs, ii) removal of core material via a selective process to obtain a hollow particle.

The end geometry is solely dependent on that of the original seed, opening up the options to the wide selection present in colloidal form. Precise, complex geometries can therefore be obtained using this powerful technique. Kuo and Huang demonstrated the synthesis of novel Cu_2O geometries (**Figure 2-7**).⁴⁹ These different nanocrystals were obtained by altering the concentration of $\text{NH}_2\text{OH}\cdot\text{HCl}$ to an aqueous solution containing 0.1 mM CuCl_2 and 30 mM sodium dodecyl sulfate. They found that with addition of increasing quantities of $\text{NH}_2\text{OH}\cdot\text{HCl}$, the crystals changed from cubic to octahedral.⁴⁹

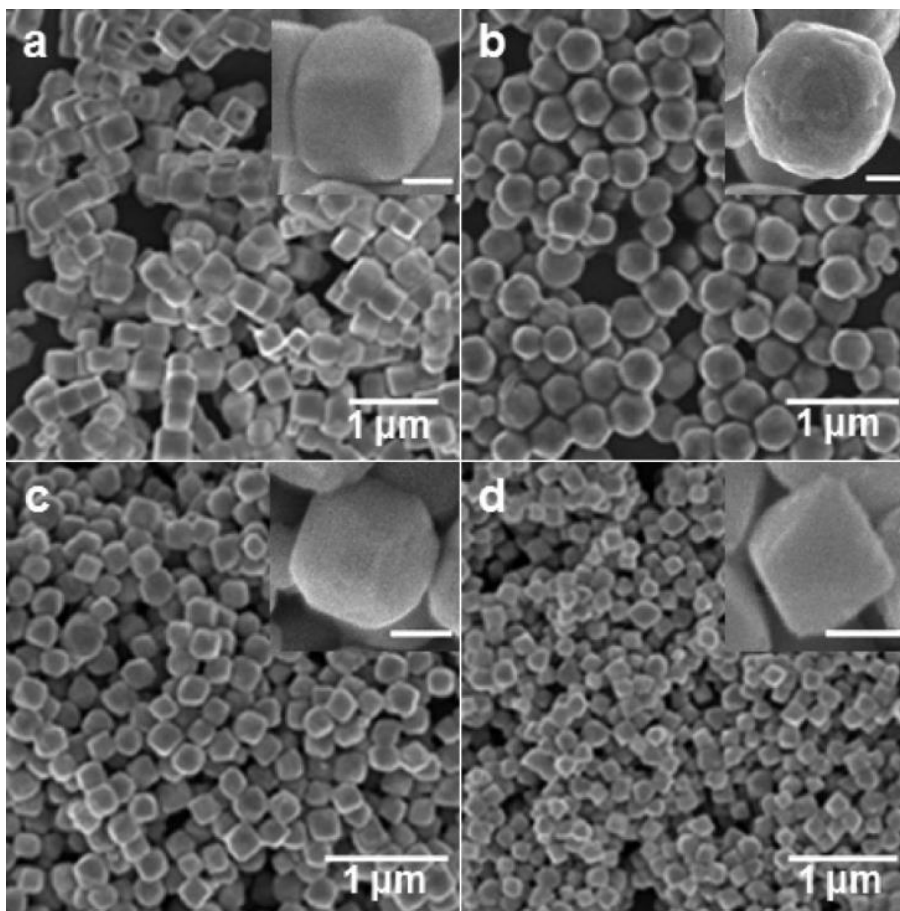


Figure 2-7. SEM images of Cu_2O nanocrystals of a) truncated cubic, b) cuboctahedral, c) truncated octahedral, and d) octahedral. Insets show an enlarged view of individual nanocrystals with a scale bar of 100 nm.⁴⁹

Taniguchi and co-workers successfully synthesised a hollow polymer latex from a polystyrene seed.⁵⁰ The seed was synthesised using a shot growth, surfactant free polymerisation. Styrene was charged into a reactor containing water and potassium persulfate. After 2 hours, 2-(2-chloropropionyloxy)ethyl methacrylate was shot added in and left to come to 100% conversion. Following this, surface modification was carried out using ARGET-ATRP of N-

[2- (4-vinylbenzenesulfoneamido)ethyl] lactobioneamide (VBSAELA) forming a shell of ~80 nm. Following this, the particles were freeze dried to remove water and then introduced to THF. Due to the high solubility of poly(styrene) and the low solubility of poly(VBSAELA) in THF, the poly(VBSAELA) was left behind.

Another method of coating with polymers was shown by Donath and co-workers.⁵¹ Here the method of coating was not polymerisation from but a layer by layer approach of oppositely charge polymers onto a melamine formaldehyde colloid. Layers of poly(sodium styrenesulfonate) (PSS) and poly(allylamine hydrochloride) (PAH) were adsorbed onto the spherical colloid before removal *via* decrease the pH to below 1.6. Whilst the original colloids were spherical, upon drying, the shells became deflated like a balloon. This was most likely due to no mechanical stability existing within the polymer layers.⁵¹

A common method for synthesising shells is to use the Stöber method.^{52–55} Typically this is undergone within an alcohol/aqueous solution using either an acidic or basic catalyst to expedite the hydrolysis of an organic precursors, e.g. tetraethyl orthosilicate (TEOS), to form SiO₂. The mechanism for is shown in **Figure 2-8**. This method forms porous silica. This is advantageous for synthesis of hollow particles as the pores can aid in the removal of the interior.

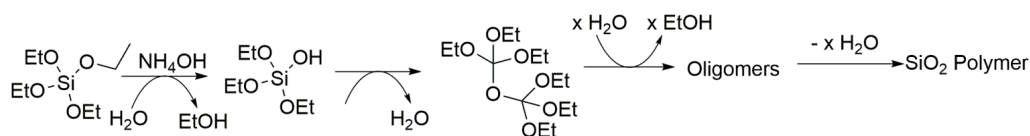


Figure 2-8. Hydrolysis and subsequent condensation of TEOS in the presence of water and ammonium hydroxide to form a silica network.

To ensure silica deposits onto the surface of the colloids, a favourable interaction needs to occur. Van Blaaderen *et al* showed an excellent example for general synthesis of silica on a wide variety of colloids *via* the adsorption of poly(vinyl pyrrolidone) before the synthesis.^{55,56} This method showed the possibility of coating multiple different materials such as gibbsite, gold, silver, and polystyrene. Also shown is the coating of a variety of different morphologies including spherical, rods, and platelets. Rossi and co-workers synthesised hollow cubic silica shells using this method.^{57,58} First, hematite cubes were synthesised *via* a condensation of ferric hydroxide gel. The cubes were then coated in PVP. This produced some steric stability when redispersed in ethanol. The solution was then sonicated and stirred with additions of a TEOS/ethanol mixture over 2 hours before being stirred overnight. The core material was then removed with addition of HCl (**Figure 2-9**).

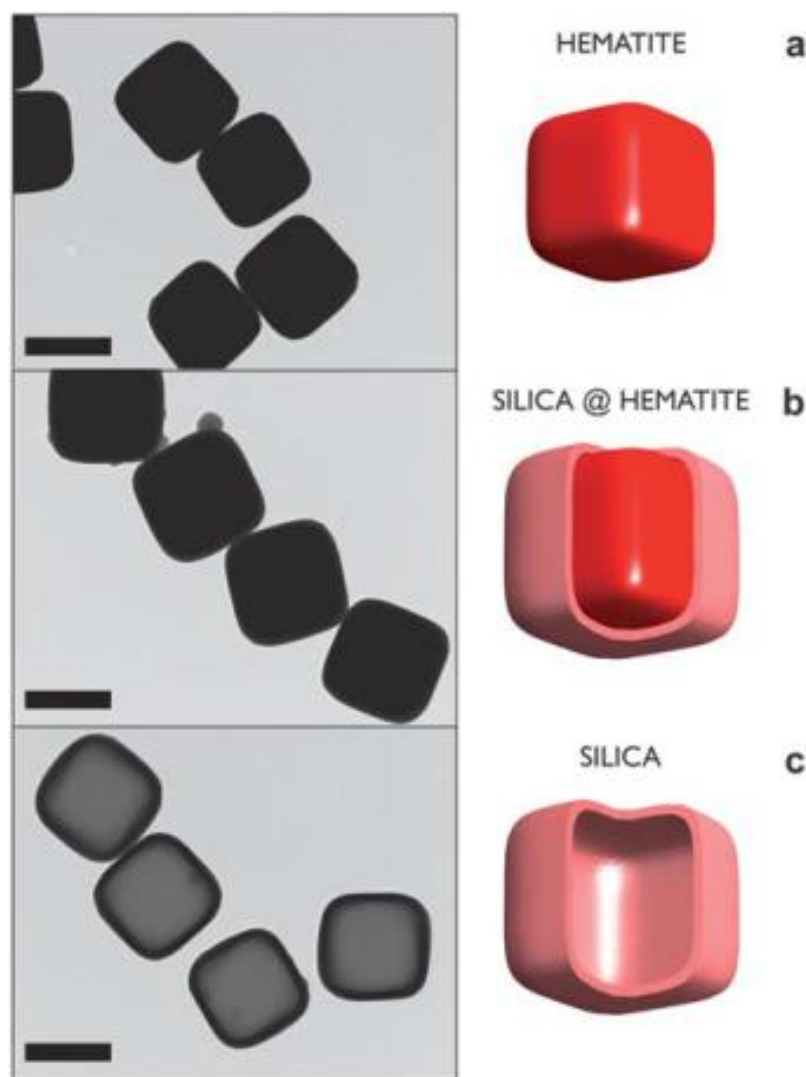


Figure 2-9. TEM images of a) hematite ($\alpha\text{-Fe}_2\text{O}_3$) cubes, b) hematite cubes coated in amorphous silica, c) silica hollow cubes after acid etching of hematite. Scale bars are 1 μm .⁵⁷

Work has been done by many groups looking into making the silica shell more mechanically robust.^{59–61} A brilliant example of this is work done by Hall and co-workers.⁶² Poly(styrene) latexes were dispersed in a 2-propanol/ammonia solution with a mixture of TEOS, bis[3-(trimethoxysilyl)propyl]amine (TSPA), and octyltriethoxysilane (OTES). After this, the

nanocomposites were subjected to a pure THF system for the removal of the poly(styrene) cores. The aim of this work was to produce large hollow silica particles (~550 nm) with a thin wall (~50 nm) without breakage occurring. Hollow silica particles have been used as contrast agents for ultrasound systems and it has been found that thinner walls produce a better response. An issue arising with thinner walls is a reduction in stability of the silica shells. Due to the copolymerisation of OTES and TSPA with the TEOS, flexible shells were obtained and worked successfully as an ultrasound contrast agent.

2.2.4 Microbubbles as Ultrasound Contrast Agents

The use of microbubbles as an effecting ultrasound contrast agent was first observed by Gramiak and Shah in 1968.⁶³ Air bubbles formed around the tip of a catheter led to an increase in the ultrasound signal being observed.⁶³ Following this initial finding, further research was undertaken to determine how microbubbles interacted with ultrasound waves to increase the contrast within water solutions. To ensure the ultrasound contrast agents can move freely within the body without causing potential blockages, particle sizes of 1 – 4 μm are deemed as safe in size.^{64,65} Submitting microbubbles to ultrasound waves causes rapid contraction and expansion of the air in response to the changes in the sound wave (**Figure 2-10**).⁶⁶ This rapid changes in volume lead to the bubbles reflecting ultrasound waves strong enough to increase the reflection of the bubble several thousand times higher

than that of normal body tissue.⁶⁷ If hollow microbubbles were replaced with solid particles of an equal diameter, the hollow particle would exhibit a response 1000 times higher.⁶⁸ It has been found that the ultrasound response obtained from hollow particles within a system is directly linked to both the size of the air void under sonication and the number of particles within the system.

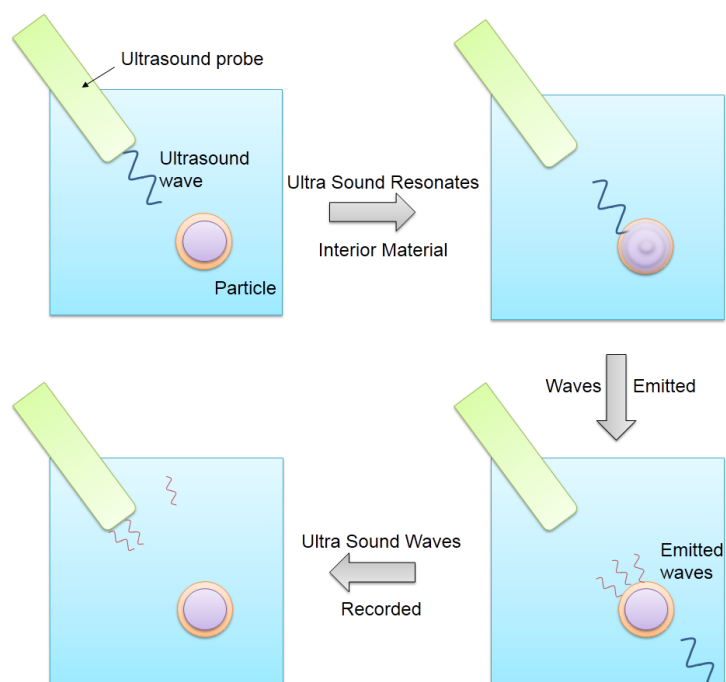


Figure 2-10. Schematic for how ultrasound contrast agents interact with ultrasound waves.

Initially, microbubbles were formed *in situ* by the stabilisation of air bubbles with the addition of a surfactant.^{69,70} Bubbles produced by this method exhibited strong ultrasound responses. However, due to the particles stability controlled solely by the surfactant present, the bubbles broke down quickly.^{64,71} As ultrasound is applied to a system, a pulse of pressure is

applied to the system. The mechanical index (MI) applied by each imaging machine is an estimate of the maximum amplitude of pressure the pulse inflicts upon the measured system.⁷² If a too high MI is used, breakdown of the ultrasound contrast agent occurs. As bubbles formed *in situ* exhibited short time lives within systems (especially when high MI's were used) synthesis of hollow particles was pursued, where an air void has an stability both in and outside of aqueous conditions. The advantage of using pre-synthesised hollow particles is that great control of the bubble size is obtained along with the concentration of the particles in the system.⁷³

A brilliant example of silica based ultrasound contrast agents is shown by Hall. Hall *et al.* synthesised hollow capsules *via* the polymerisation of organosilane around a sacrificial template to form spherical particles.⁷³ Similar to sacrificial templating by Imhof and coworkers,^{59,60,74} additional silane reagents were added during the synthesis to allow for a more mechanically robust end particle. Monodisperse polystyrene particles were dispersed within a propanol/water solution containing ammonia. Mixtures of TEOS, octyltriethoxysilane (OTES), and bis[3-(trimethoxysilyl)-propyl]amine (TSPA) were added and a silica shell formed. The resulting nanocomposites were dispersed within tetrahydrofuran to remove the inner polystyrene core. Varying degrees of flexibility was found when increasing the OTES and TSPA concentration. Upon drying, it was found that the softer silica shells would buckle and therefore needed storing in DCM to retain the shape.

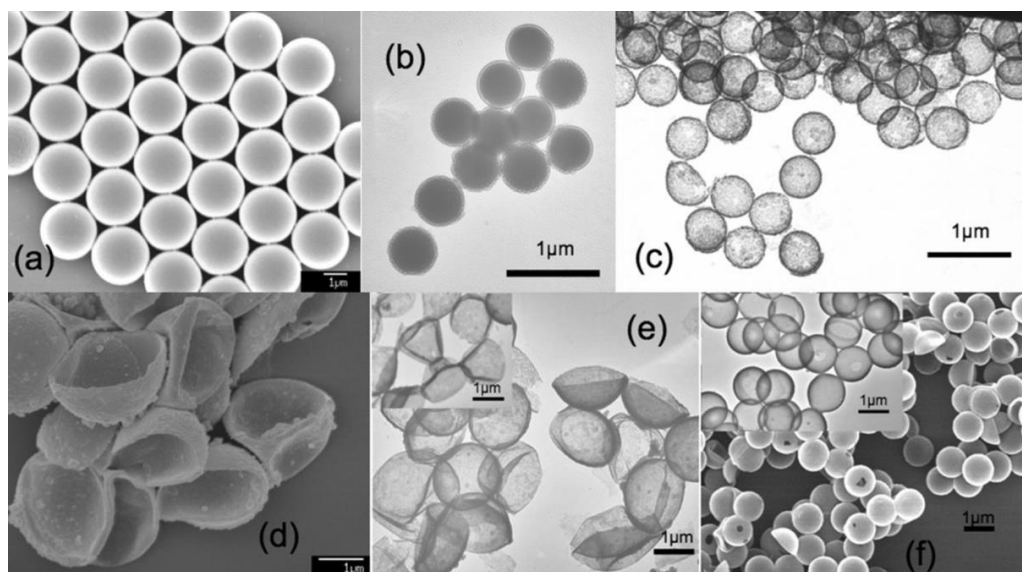


Figure 2-11. a) SEM image of 2089 ± 150 nm, b) TEM images indicating polystyrene core coated in silica, c) TEM images of etched particles with some breakages in the silica shell, d and e) SEM and TEM of OTES – TSPA - TEOS hollow silica particles collapsing under high vacuum, f) SEM (insert) and TEM images of TSPA – TEOS composite with little collapse. Scale bars are all 1 μm .⁷³

The increased flexibility found with the incorporation of both TSPA and OTES resulted in capsules that exhibited a stronger response to ultrasound imaging as well as being able to reach a higher MI. The pure TEOS capsules exhibited no response upon increase the MI above 1.5, indicating that the breakdown of the particles had occurred. In comparison, the TSPA and OTES containing capsules exhibited a strong response up to 1.5 and continued to work upon lowering the MI again, indicating that no breakdown of the particles occurred.⁷³

Hall clearly showed that the incorporation of flexible silyl groups into a silica shell increases the ultrasound response.⁷³ However, to our knowledge, only spherical particles have been studied to determine their ability as use as an ultrasound contrast agent.

Previous work within our group has shown that using SOCAL[®] P3 as a template, opacity can be obtained, though a large degree of breakage after processing was shown.⁷⁵ In this chapter we synthesised anisotropic air voided silica particles using sacrificial templating methodology. The template was a cigar shaped precipitated calcium carbonate known as SOCAL[®] P3. It was chosen due to its relative cheapness and abundance, it was amenable to coating in large quantities, and had appropriate dimensions for light scattering. Part of the process is the removal of CaCO₃, done *via* the addition of acid which causes the generation of CO₂. This in turn causes large pressures within the particle which favours rupture of the shell. It is to this end that we investigated different etching time parameters and the incorporation of a flexible siloxy cross-linking agent within the shell. Determination as to whether the hollow particles contained hollow air voids was done using ultrasound imaging before investigating what effect the different shell materials would have upon addition to a coatings formula.

2.3 Results and Discussion

2.3.1 Characterisation of calcium carbonate particles

SOCAL P3 ® (herein referred to as SOCAL) is a cheap, widely commercially available precipitated calcium carbonate that was chosen for fabrication of hollow silica particles. SOCAL was selected for the encapsulation owing to its ellipsoidal morphology and its current use as an extender in paint formulations. The elliptical “cigar” shape of the particles was confirmed *via* transmission electron microscopy (TEM) and scanning electron microscopy (SEM) (**Figure 2-12**). A maximum length of 1 µm and width of 350 nm were determined. According to TEM imaging, the calcium carbonate particles exhibit a varying electron density internally. This varying electron density is shown in imaging by rings on the sample caused by the diffraction of the electrons *via* the crystalline material. Whilst the particles are polydisperse, their shapes are equal throughout the sample. Other morphology and chemical structures are available in wide varieties, CaCO₃ with spherical morphology, Cu₂O colloids with octahedral structure and Fe₂O₃ particles with pseudocubic morphologies can also be synthesised.⁴⁹

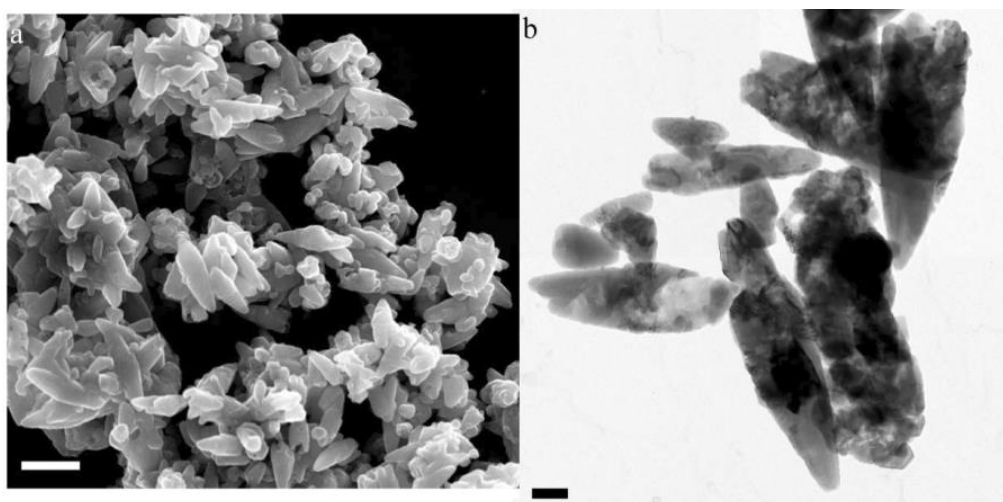


Figure 2-12. a) SEM micrographs of the SOCAL template with scale bar of 200 μm , and TEM micrograph of the SOCAL template with scale bar 200 nm.

Calcium carbonate exists as four main polymorphs; Calcite, aragonite, vaterite and amorphous in order of stability.^{76,77} Issues arise when attempting to encapsulate CaCO_3 in the vaterite polymorph due to its high instability in water leading it to dissolve and reprecipitate into calcite. Therefore using a template that exists as the calcite polymorph is favourable as the morphology will be retain during the encapsulation process.^{78,79} Energy-dispersive X-ray spectroscopy (EDX) was employed on the powder to examine whether the sample contained any other elements/compounds (**Figure 2-13 a**) along with powder x-ray diffraction (XRD) to resolve the SOCAL's polymorph (**Figure 2-13 b**).

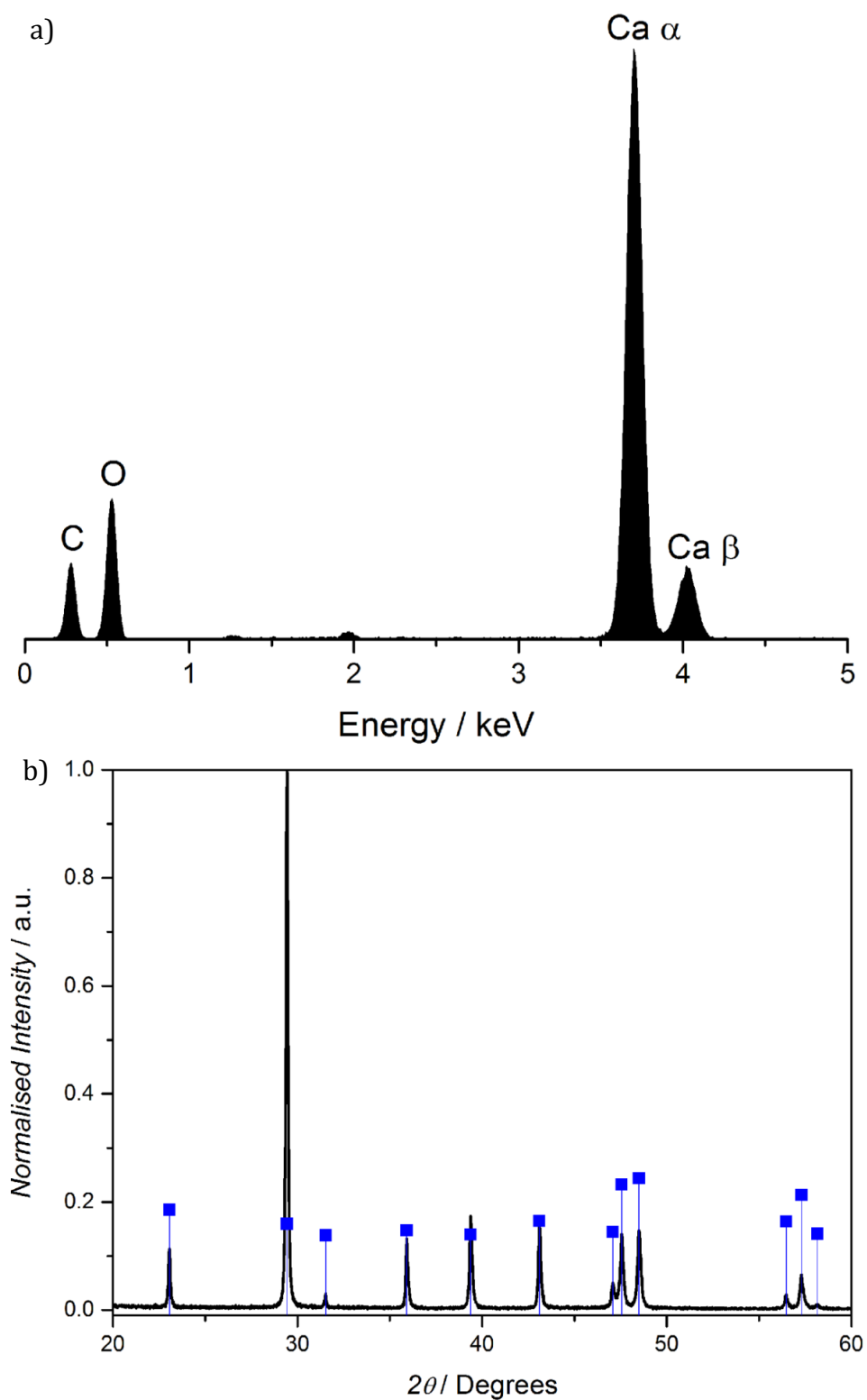


Figure 2-13. a) EDX spectrum of SOCAL indicating only the presence of Ca, O, and C and b) XRD of spectrum of SOCAL (—). (■) represent peaks corresponding to calcite, demonstrating that SOCAL is calcite.

EDX of SOCAL is shows that it contains only C, O, and Ca (**Figure 2-13 a**). The CaCO_3 sample exhibits 2 emission peaks for Ca, Ca α and Ca β . The Ca α peak corresponds with an electron from the 2p orbital filling the hole of the 1s orbital electron that has been ionised and the energy given off as an x ray emission. The Ca β peak corresponds to an electron from the 3p orbital filling the hole of a 1s orbital electron. The chance of a 3p electron filling the hole instead of a 2p electron is lower, hence a smaller response is observed. Please refer to **Chapter 6.3** for more information on EDX. A slight peak can be observed at both 1.4 keV and 1.98 keV which corresponds to both Al and P respectively. It is postulated that as the SOCAL sample was directly applied to the aluminium stub, the presence of these peaks is from x-ray given off by the sample holder. The XRD spectra of the sample (**Figure 2-13 b**) indicates the presence of calcite within the system with no additional crystal morphologies present. As the sample is calcite, it is safe to employing a coating technique that can take place in ethanol/water conditions.

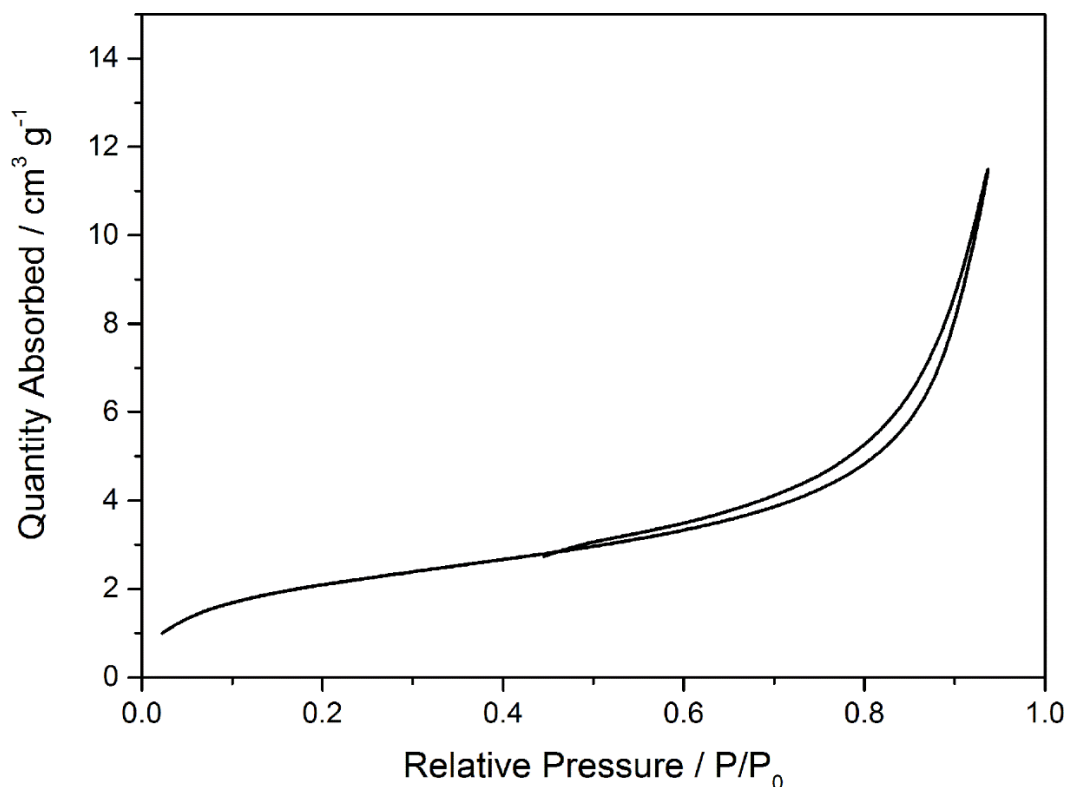


Figure 2-14. Nitrogen adsorption isotherm of SOCAL ; it has a type II isotherm, indicating that SOCAL P3 is essentially non-porous.

Porosimetry was conducted in order to determine the surface area and porosity of the particles (**Figure 2-14**). The nitrogen adsorption isotherm of volume of gas adsorbed ($\text{cm}^3 \cdot \text{g}^{-1}$) against the relative pressure, P/P_0 , indicated that the SOCAL demonstrated a Type II isotherm meaning it is essentially non-porous. The region between 0.0 – 0.5 relative pressure remained fairly flat with a gradient of 3.23, which corresponded to a monolayer of gas formation. The rapid increase in gradient to 108 at 0.9 relative pressure is indicative for gas condensation onto the surface. Furthermore the slight gradient increase between 0 - 0.2 indicated the presence of few observable micropores (<

2 nm). The slight hysteresis at high relative pressure range suggests the existence of macropores (50 – 1000 nm). This lack of pores is further corroborated by the total pore volume measurement calculated by the Barret, Joyner, and Halenda (BJH) method with a low pore volume of $0.02 \text{ cm}^3 \cdot \text{g}^{-1}$.

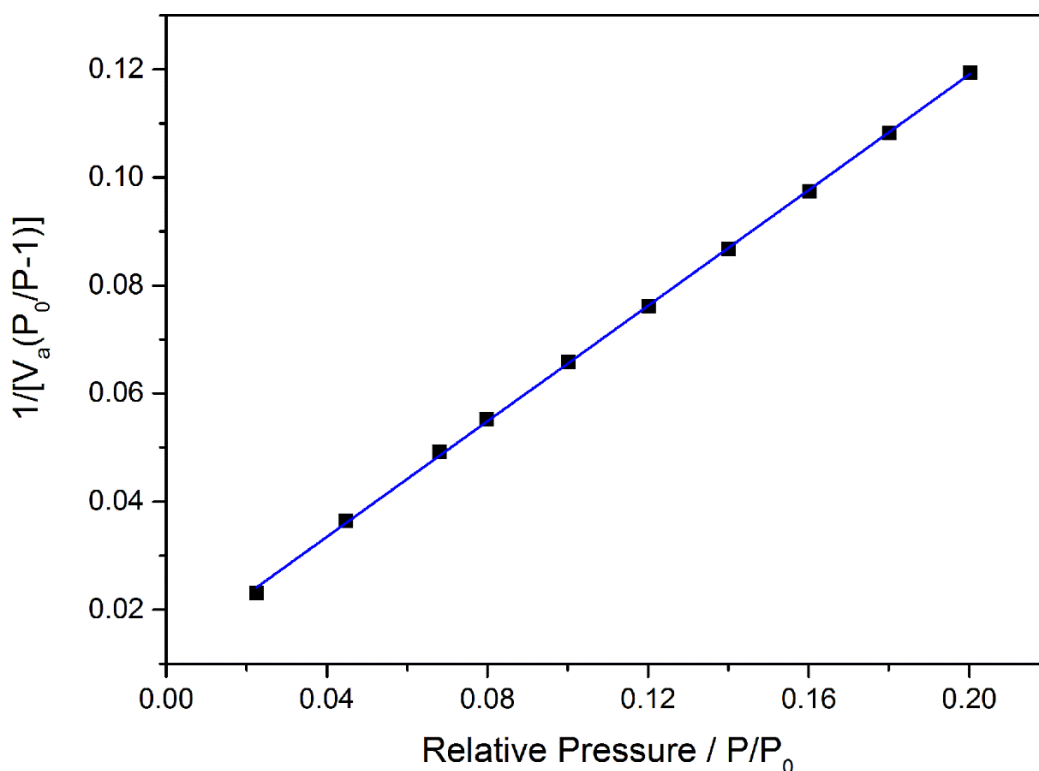


Figure 2-15. BET transform plot of SOCAL obtained by nitrogen porosimetry; quantity of gas adsorbed as a function of relative pressure. SOCAL P3 has a BET surface area of $7.96 \pm 0.05 \text{ m}^2 \text{ g}^{-1}$ and a C value of 45.

Surface area is a vital component when encapsulating particles using the Stöber synthesis. If the surface area is too low, the area for silica deposition is reduced leading to silica precipitating out into the system and homonucleating. If the surface area is too high, an uneven coating of the

template will occur potentially, leading to coagulation due to uneven charge on the particles. Brunauer-Emmett-Teller (BET) analysis was used to determine the surface area and BET constant from the BET plot (**Figure 2-15**), $1/[V_a(P_0/P-1)]$ versus P/P_0 ; where P is the absolute pressure of bulk gas above the sample, P_0 is the saturation pressure of the adsorbate (nitrogen in this case) and V_a is the volume of gas adsorbed by the sample. The intercept of the straight lines give $1/V_m C$ and the slope gives $(C-1)/V_m C$ where C is the BET constant and V_m is the volume of gas adsorbed when the entire surface is covered with a monomolecular layer. From this the surface was calculated by knowing the area one unit of gas takes up on the surface. Using this method, the surface area was calculated to be $7.96 \pm 0.05 \text{ m}^2 \text{ g}^{-1}$ (**Figure 2-15**). The BET constant for the SOCAL was determined to be 45 which indicates that the measurement was successful as the constant should exist within the range of $0 < C < 300$. If it above this range, it is likely due to presence of micropores. The surface area was considered acceptable as the BET constant was within the acceptable range and the correlation coefficient (0.9999) is suitably close to unity. As the surface area was relatively low, a relatively slow feed rate of silyl reagent was required to prevent secondary nucleation.

2.3.2 Encapsulation of SOCAL *via* Stöber method

A modified version of the Stöber seeded silica synthesis was employed for the encapsulation SOCAL in silica. As the SOCAL BET surface area is relatively low (at $7.96 \pm 0.05 \text{ m}^2 \cdot \text{g}^{-1}$) slow addition of tetraethyl orthosilicate

(TEOS) and 1,8-bis(triethoxy silyl)octane (BTEOSO) (**Figure 2-16**) was required to prevent secondary nucleation occurring.

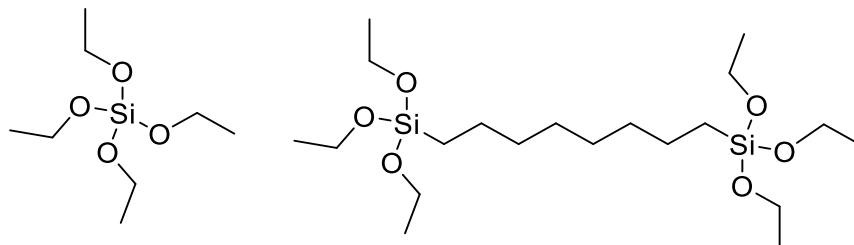


Figure 2-16. Chemical structure of TEOS (left) and BTEOSO (right).

A general synthesis procedure involves SOCAL dispersed in ethanol (7 wt%) with an addition of concentrated ammonium hydroxide (18.10 M at 9.6 wt%). A TEOS and BTEOSO (ratios in wt% 100:0, 85:15, or 70:30) mixture (silyl reagent at 2:1 wt ratio with respect to CaCO_3) was then fed in over 12 hours at room temperature. The total reaction was stirred for 24 hours before purification *via* centrifugation (refer to experimental **Section 2.5.3** more details). Once cleaned *via* centrifugation, the particles were dispersed in an ethanolic solution of polyvinylpyrrolidone (PVP) K30 (10 wt% with respect to CaCO_3) overnight. This was in order to allow the stabiliser to physisorb onto the colloids, which added further stabilisation to the particles during the etching process. Excess PVP was removed *via* centrifugation. BTEOSO was chosen to add flexibility, as well as to alter the hydrophobicity of the silica in a one pot process. Due to the presence of the BTEOSO, ethanol was required instead of water, as BTEOSO remained unreacted under aqueous conditions unless it was present in large quantities (50 wt%). The modified Stöber silica

synthesis can be catalysed under acidic or basic conditions. Basic conditions were used as; (i) under acidic condition, α,ω -bis(triethoxy silyl)alkanes can undergo intramolecular cyclisation owing to the slower condensation times whilst, under basic conditions, the rate of condensation is faster and cyclisation can be negated,⁸⁰ (ii) calcite is stable in basic environments and does not degrade, whereas acidic environments calcite dissolve into the system leaving no physical template onto which the silica could deposit.

The resulting nanocomposites were formed using 100:0, 85:15, and 70:30 wt ratio of TEOS:BTEOSO. For ease of understanding, the sample synthesised using 100:0 ratio shall be referred to as SOCAL@TBT 1, the sample from the 85:15 wt ratio shall be referred to as SOCAL@TBT 2, and the sample from 70:30 reaction will be referred to as SOCAL@TBT 3. Particle size of all the particles *via* laser diffraction is shown in **Figure 2-17**.

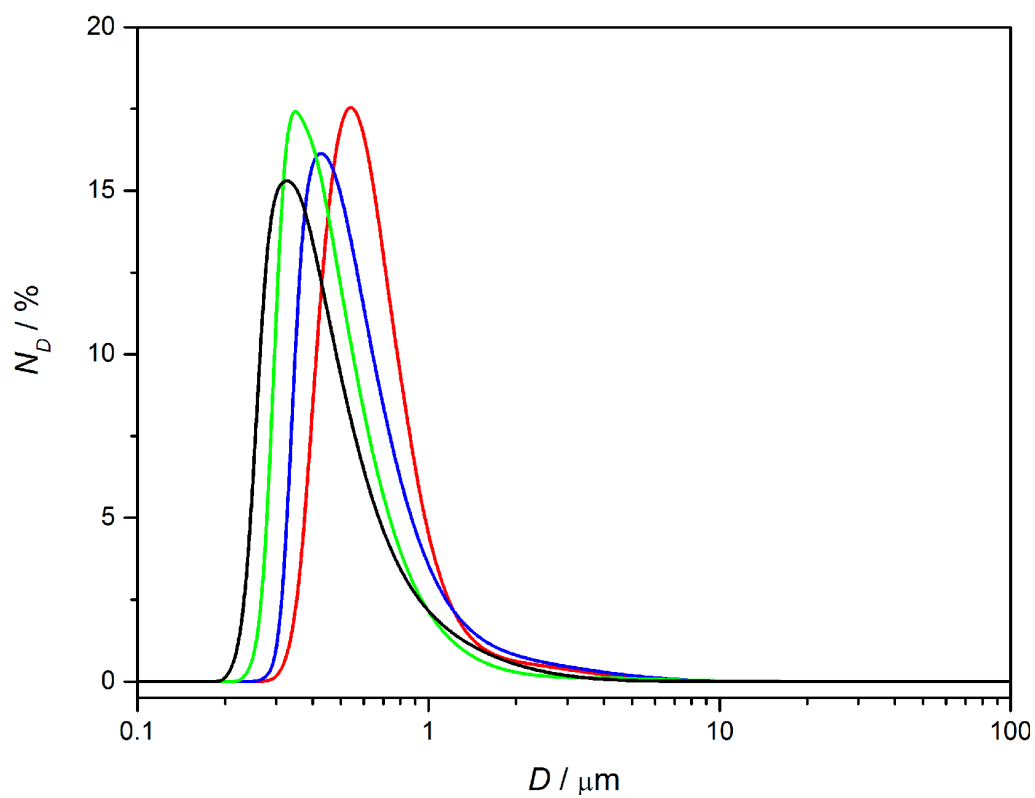


Figure 2-17. Particle size analysis by laser diffraction of CaCO_3 template (SOCAL) (—), SOCAL coated in silica (SOCAL@TBT 1) (—), SOCAL@TBT 2 (—), and SOCAL@TBT 3 (—).

Table 2-2. Tabulated statistics of laser scattering data plotted in **Figure 2-17**. The $d(0.1)$, $d(0.5)$, and $d(0.9)$ values refer to the diameter of 10, 50, and 90% of the sample.

Material	$d(0.1)$	$d(0.5)$	$d(0.9)$	Uniformity
SOCAL	0.260	0.313	0.707	0.500
SOCAL@TBT 1	0.402	0.556	0.952	0.387
SOCAL@TBT 2	0.347	0.488	1.103	0.529
SOCAL@TBT 3	0.295	0.44	0.757	0.448

Laser diffraction is a quick and effective method of determining whether the particles were coated and whether they have aggregated during their synthesis. The appearance of aggregates would have been indicated by a broad peak at a higher diameter which is not present in **Figure 2-17**. A number average approach is required for measuring *via* laser scattering due to the non-spherical nature of the material. Volume average approaches bias the system towards only large particles owing to the mathematical model being based upon a sphere and does not match the requirements for such a polydisperse sample. No aggregates were formed in these systems as the peaks displayed monomodal distributions with an increase in size with higher wt% of TEOS in the silyl mixture. This is most likely due to the higher reactivity of TEOS in comparison to BTEOSO owing to the octyl linker.⁸⁰ **Figure 2-17** and **Table 2-2** display an increase in size for all particles, indicating that each system has grown a silica shell. Furthermore the $d(0.5)$ of

SOCAL is roughly 300 nm which is close to the optimum 280 nm diameter of spherical air voids that are theorised of white light scattering.⁸¹ The uniformity of the all the particles remained similar to the initial uniformity of the template, indicating that an even coating of all the particles was formed.

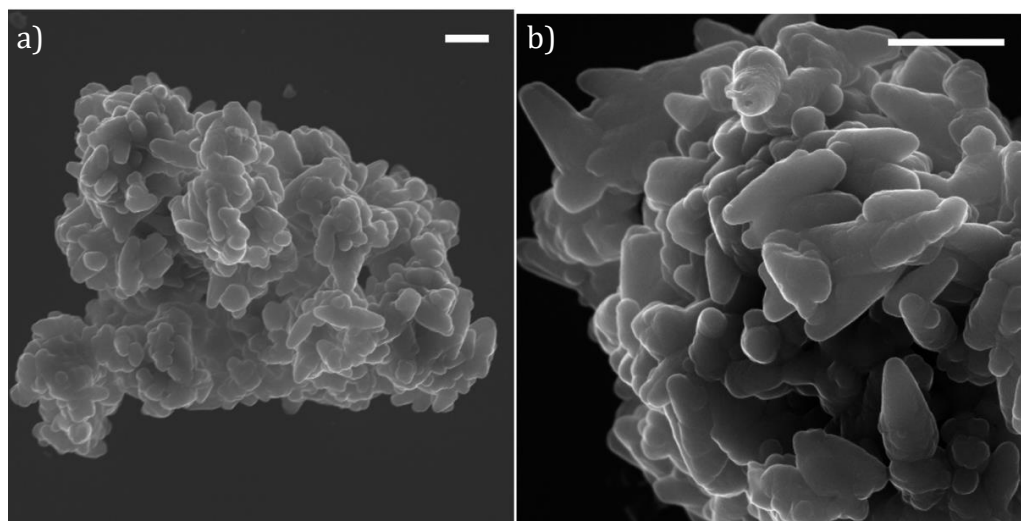


Figure 2-18. SEM micrographs of a) SOCAL@TBT 1 and b) SOCAL@TBT 3. Scale bars represent 1 μm .

SEM imaging of all systems does not show that any secondary nucleation occurred, indicating that the feed rate of the monomer was low enough to negate homonucleation. All particles exhibit a smooth, even surface resulting from a continuous coating. It should be noted that within the SEM images, all the particles can be seen to aggregate together and few can be seen to exist separately. The cause of this is the high density of the coated particles coupled with the low dielectric constant of the ethanol (25.7 at 20 °C)⁸² the

particles were dried from. The high density leads the particles to exhibiting a high Hamaker constant due to the **Equation 2-6**.

$$A = \pi^2 C \rho_1 \rho_2 \quad 2-6$$

Where A is the Hamaker constant, C is the coefficient for the particle-particle pair interaction, and ρ_1 and ρ_2 are the atoms per unit volume (density) in the two interacting bodies.

Due to the CaCO_3 template retaining a high density before the addition of the SiO_2 shell, the particles have a strong Van der Waals attraction between each other whilst drying occurs. The low dielectric constant of the ethanol also leads to a reduced electrostatic force between the particles being imparted upon one another.

A large increase in the volume of N_2 adsorbed onto the TBT 1-3 samples from the base template can be observed in **Figure 2-19**. This is an indication to both the increased surface area of the particles along with an increased internal porosity of the samples due to the silica coating. An increase in total N_2 adsorbed can be seen with all coatings. However, TBT 1 shows a higher total volume adsorbed over that of TBT 2, with TBT 3 absorbing the most. The increased volume observed with TBT 3 suggests that either a larger porosity system has been created, or a larger external surface area. As **Figure 2-17** indicates, TBT 1 has the largest growth in particle size, suggesting that TBT 2 and TBT 3 have a higher porosity within the sample, further corroborated with **Figure 2-21** and **Table 2-3**. The initial increases in

gradients present in all the nanocomposites are indicative of the capillary condensation of nitrogen in the small population of micropores.

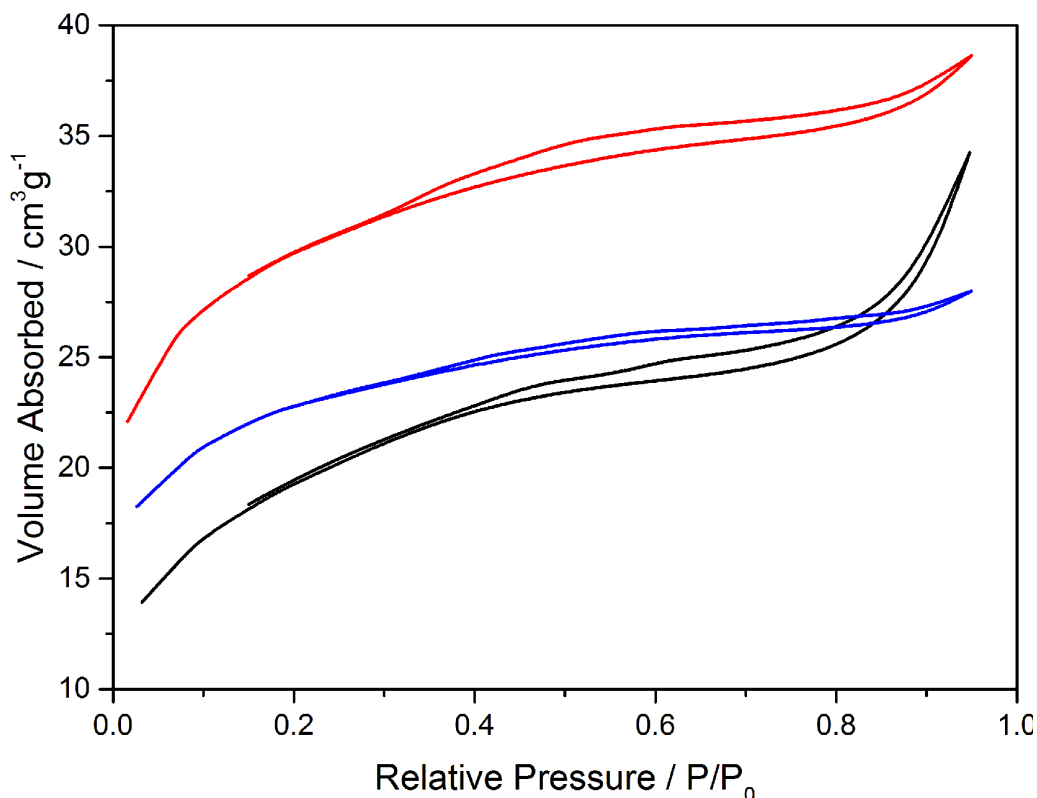


Figure 2-19. Nitrogen adsorption isotherm of nanocomposite SOCAL@TBT 1 (—), SOCAL@TBT 2 (—), and SOCAL@TBT 3 (—). The lower curve represents the adsorption portion of the isotherm, whereas the higher curve represents the desorption branch.

The BET surface area calculated for each sample shows an increase between each of the samples with increasing amounts of BTEOSO being reacted (**Figure 2-20**). The pure SOCAL exhibited a surface area of $7.96 \pm 0.05 \text{ m}^2 \text{ g}^{-1}$ with an increase to $68.86 \pm 0.05 \text{ m}^2 \text{ g}^{-1}$ with the TBT 1 coating. A further increase was observed to $80.09 \pm 0.06 \text{ m}^2 \text{ g}^{-1}$ with TBT 2 and $104.65 \pm 1.02 \text{ m}^2 \text{ g}^{-1}$ for TBT 3. As all C values were between 0-300 the values

were again considered within measureable values. An overall surface area increase is observed with the presence of BTEOSO within the reaction systems. It was postulated that this increase is due to porosity increases due to octyl linkages forming larger pores within the silica coating.

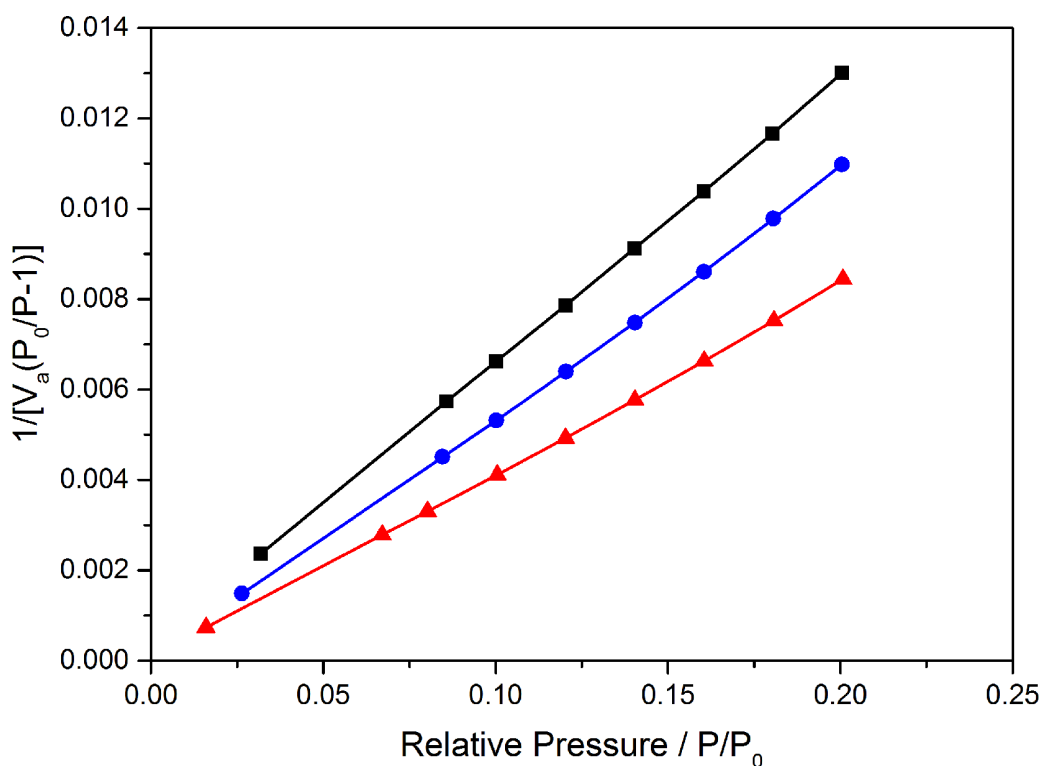


Figure 2-20. BET transform plot of TBT 1 (\blacksquare), TBT 2 (\bullet), and TBT 3 (\blacktriangle) obtained by nitrogen porosimetry; quantity of gas adsorbed as a function of relative pressure. TBT 1 has a BET surface area of $68.86 \pm 0.05 \text{ m}^2 \text{ g}^{-1}$ and a C value of 190, TBT 2 has a surface area of $80.09 \pm 0.06 \text{ m}^2 \text{ g}^{-1}$ and a C value of 108, and TBT 3 has surface area of $104.65 \pm 1.02 \text{ m}^2 \text{ g}^{-1}$ with a C value of 236.

Figure 2-21 shows the low pressure region of the adsorption branch for the coated particles which is required for the determination of the

micropore area, external surface area, and micropore volume. The pertinent data is shown in **Table 2-3**.

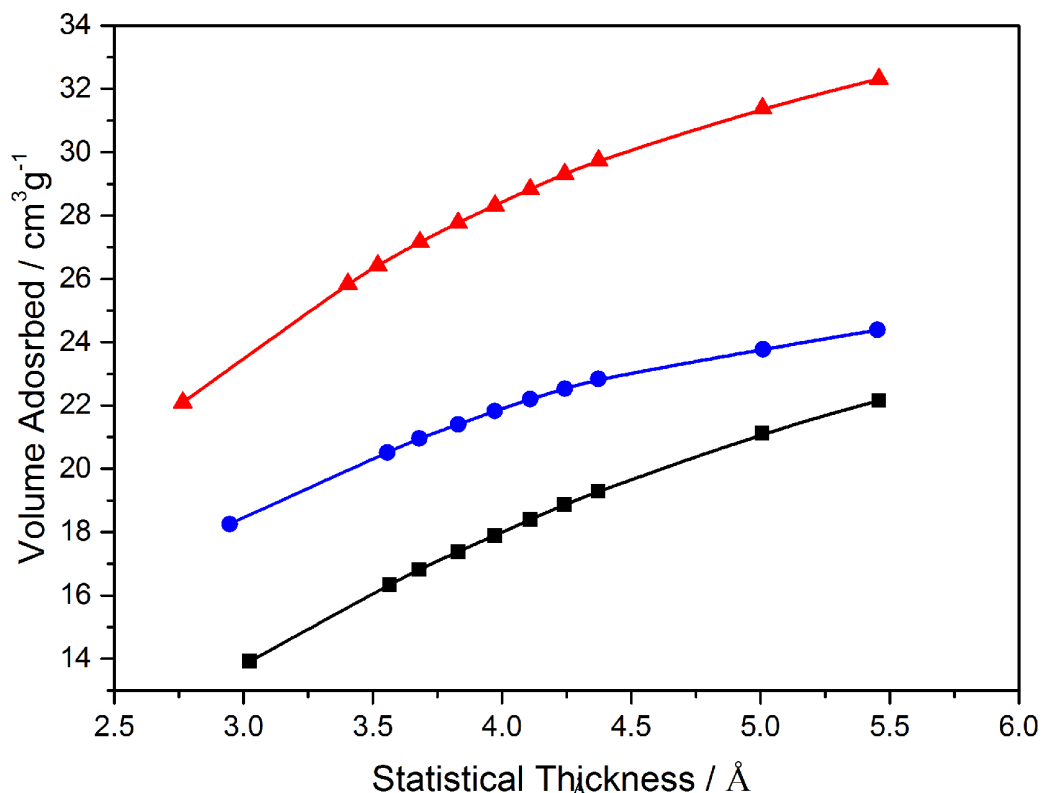


Figure 2-21. V_A - t plot for TBT 1 (■), TBT 2 (●), and TBT 3 (▲) required for the calculation of micropore area, external surface area, and micropore volume.

Figure 2-21 shows the V_A - t plot for TBT 1-3. To determine the essential data shown in **Table 2-3**, the isotherms obtained are compared to that of a standard non-porous reference with a similar BET C -constant to the materials analysed.

Table 2-3. Tabulated data obtained from the $V_A - t$ plot show in **Figure 2-21**.

Material	Micropore area / m^2g^{-1}	External Surface Area / m^2g^{-1}	Micropore volume / cm^3g^{-1}	Correlation Coefficient
SOCAL@TBT 1	12.57	56.30	5.285×10^{-3}	0.9999
SOCAL@TBT 2	36.21	43.88	1.62×10^{-2}	0.9999
SOCAL@TBT 3	44.84	59.82	2.00×10^{-2}	0.9999

The results shown in **Table 2-3** show a clear substantial increase in micropore volume with the addition of BTEOS, as expected. As no micropore volume was measured for the SOCAL template, any micropore volume measured in the nanocomposites can be attributed to the silica shells. Presence of pores in all three systems is vital for the etching process as the migration of acid through the shell is required for the removal of the CaCO_3 core.

Chapter 2: Silica Shells for Opacity

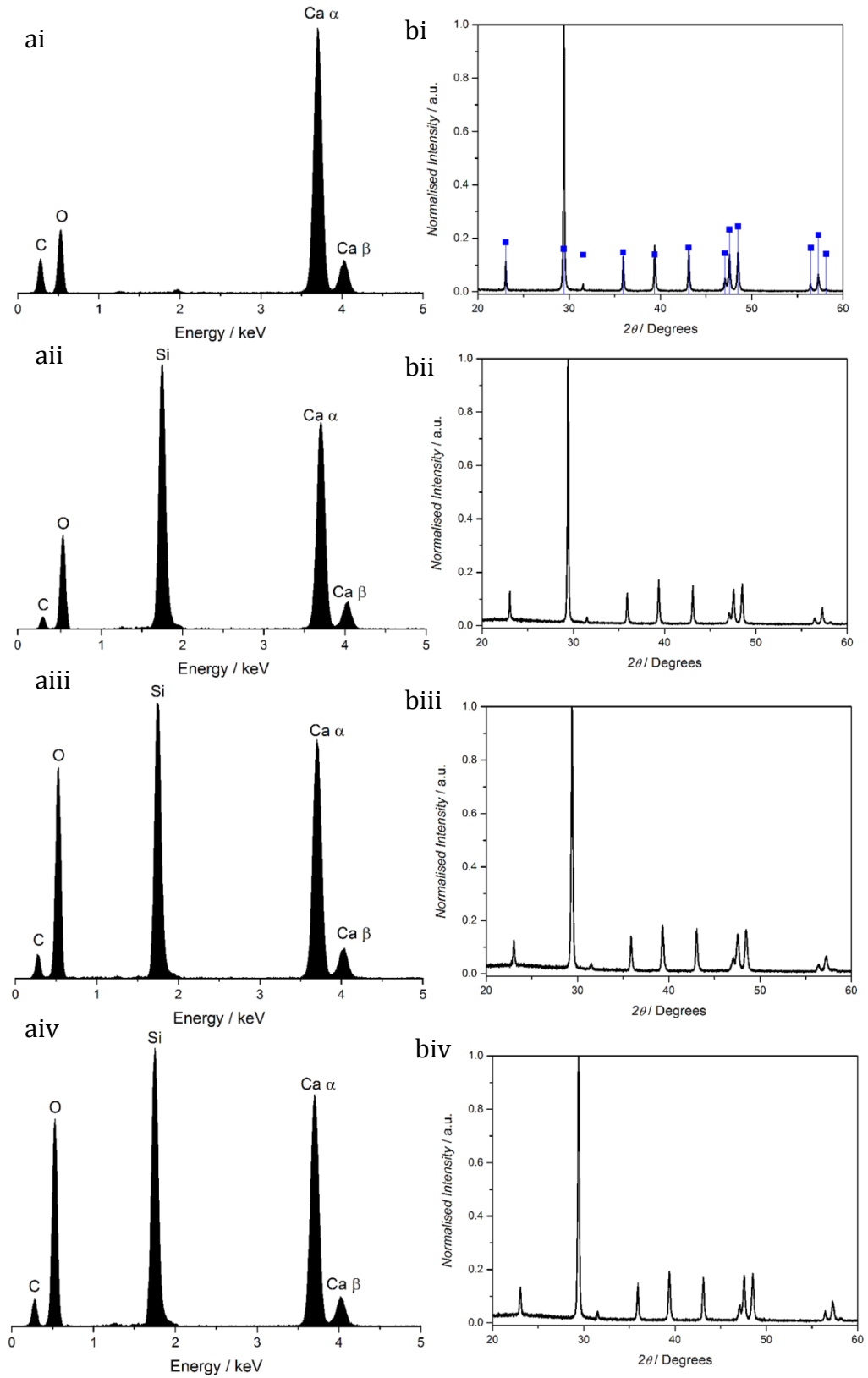


Figure 2-22. a) EDX spectra and b) XRD spectra of i) SOCAL and nanocomposites ii) SOCAL@TBT 1, iii) SOCAL@TBT 2, and iv) SOCAL@TBT 3. The ■ indicators in (bi) represent the standard crystal pattern expected for a calcite crystal.

Following the coating of SOCAL with silica, EDX and XRD analysis was used to determine whether the silica coating was successful and whether a crystal structure was generated within the SiO_2 or lost from the CaCO_3 template. EDX measurements were conducted for each sample at an accelerating voltage of 20 kV for an appropriate penetration depth and a detector at an angle of 35° with respect to the sample. It was shown that the CaCO_3 template (**Figure 2-22 ai**) contained no silica as shown earlier (**Figure 2-13 a**). All three of the coated samples (**Figure 2-22 aii – aiv**) exhibited the silicon peak, indicating that the coating process was a success even with the inclusion of the BTEOSO linker. An increase in the carbon peak can be observed with increasing BTEOSO content; however this is not evidence of the carbon content in the sample. This is due to EDX being able to record a qualitative analysis of a sample whilst exact elemental proportions are not given due to rough nature of the surface and issues involved with the electron scattering tear drop effect (**Figure 2-23**). The tear drop effect results in large internal areas releasing X-rays whilst the surface is represented in a much small portion. Therefore, due to the shape and size of the samples, a quantitative analysis cannot be recorded using EDX.

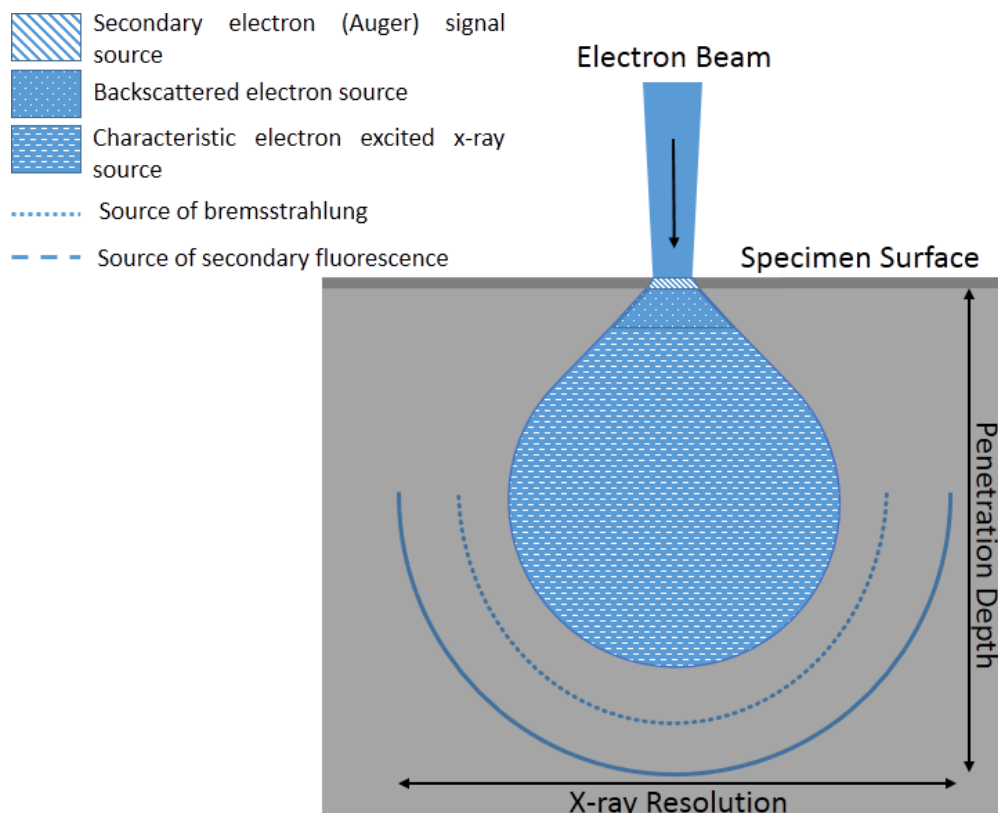


Figure 2-23. Schematic of electron microscopy showing that the electron excited x-rays used in EDX are generated within the sample in a tear drop shape, leading to a large internal area investigated.

Figure 2-22 bi represent the SOCAL template used during the coating process with the required peaks for a calcite crystal. The results from XRD of all the coated samples (**Figure 2-22 bii-biv**) indicate that the calcite crystal is retained within the template and has not undergone any transformation. An increased noise in **Figure 2-22 bi-biv** can also be observed. The cause of this noise is due to the generation of amorphous crystal within the sample. The appearance of the silicon peak within the EDX spectras coupled with the lack of new peaks arising within the XRD spectra of all the coated samples indicate

that amorphous crystal present is that of the silica formed during the coating reaction. This was expected as the Stöber silica synthesis technique leads to the generation of non-crystalline silica.

In order to quantify the presence of silica per gram of nanocomposite, thermogravimetric analysis (TGA) was conducted. CaCO_3 thermally decomposes under N_2 between 600 – 800 °C into CO_2 and CaO (**Equation 2-7**)⁸³ whereas silica is stable up to temperatures of 1000 °C.



With $\text{Ca} = 40.08$ amu, $\text{C} = 12.01$ amu, and $\text{O} = 16.00$ amu the theoretical remaining mass of CaO was determined to be 56.1% after thermal release of CO_2 . The difference between the remaining mass of CaO and the mass of the coated samples gives the mass of silica per nanocomposite (**Figure 2-24 and Table 2-4**).

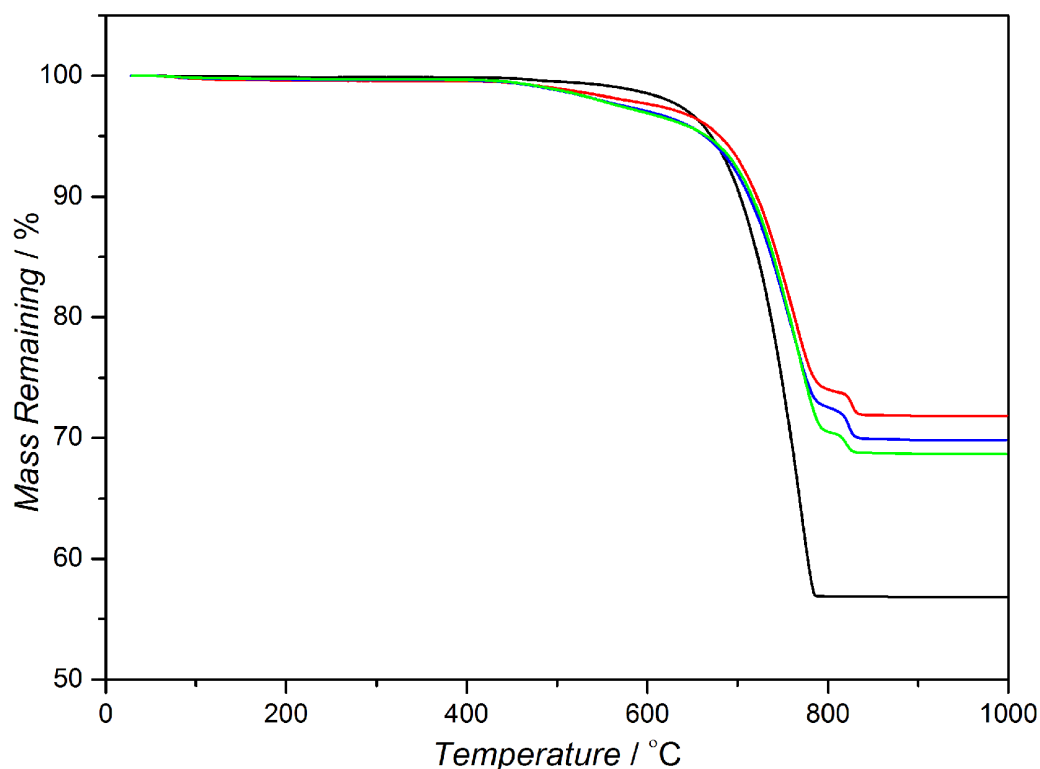


Figure 2-24. TGA of SOCAL (—), SOCAL@TBT 1 (—), SOCAL@TBT 2 (—), and SOCAL@TBT 3 (—) nanocomposites from 25 – 1000 °C. A heating rate of 10 °C min⁻¹ was used under a N₂ atmosphere.

All samples were held at a 200 °C isotherm for 1 hour to reduce the water content remaining within the pores of the nanocomposites before running the TGA. A slight loss can be observed beginning at 450 °C in **Figure 2-24**. This is indicative of small solvent molecules still residing within the silica network evaporating off. The small plateaus present at around 790-840 °C originate from the remaining ethoxy groups attached to the silica network and not from combustion of octyl groups present within BTEOSO.

This is indicated due to the plateau's presence within the SOCAL@TBT 1 sample which contained no BTEOSO linkage within it.

Table 2-4. Tabulated data extracted from TGA analysis (**Figure 2-24**).

Nanocomposite	Mass Remaining / %	Silica mass % per gram of nanocomposite / %
SOCAL	56.13 %	0.00
SOCAL@TBT 1	71.84 %	15.71
SOCAL@TBT 2	69.84 %	13.71
SOCAL@TBT 3	68.68 %	12.55

The mass of SOCAL following heating to 1000 °C is 56.13% (**Table 2-4**) which is in good agreement to the calculation of 56.1%. By using this result and the end masses of the other nanocomposites, it is possible to calculate the mass of silica per gram of nanocomposite, which will be used to determine the effective particle density of the silica shells once they have been etched in the next step.

Table 2-5. Conversion data of silica coating

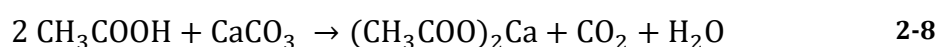
Nanocomposite	Theoretical wt % of SiO ₂ *	Actual SiO ₂ wt %	Conversion / %
SOCAL	0.00	0.00	-
SOCAL@TBT 1	36.58	21.26	58.11
SOCAL@TBT 2	39.26	20.83	53.06
SOCAL@TBT 3	41.73	18.20	43.61

*at 100% conversion

2.3.3 Etching interior core and characterisation of nanoparticles

Once the CaCO₃@SiO₂ nanocomposites were synthesised, we intended to remove the core template easily without destruction to the shell material. An acid etching approach was selected owing to the chemical resistance of silica shell, with respect to acids (except from sulfuric), and the porosity of the shell material allowed movement into and out of the particles. Different rates of acid addition were also investigated to determine whether this had any effect on the particles. Calcination was also considered as a possible approach due to CaCO₃'s thermal decomposition (**Equation 2-7**). However, an issue that arising using calcination with silica coated nanoparticles is the fusing of pendant silanol on the surface of the silica shells with other silanol groups on other particles which would lead to aggregates.⁸⁴ Acid etching in water can

overcome this issue as the nanomaterial is dispersed throughout the aqueous phase, which made aggregates less likely to form. The further addition of PVP to act as a stabiliser before the etching process increased the stability of the SOCAL@TBT 2 and SOCAL@TBT 3 samples within an aqueous environment as well as reduced the possibility of aggregation during the etching process (**Equation 2-8**).



Acetic acid ($\text{p}K_{\text{a}} = 4.6$) was selected owing to its weaker acidity compared to other acids such as hydrochloric ($\text{p}K_{\text{a}} = -8.0$). As a result lower etching rates can be achieved, which helped to mitigate potential internal pressure that the system may undergo due to a slower generation of CO_2 (**Equation 2-8**).

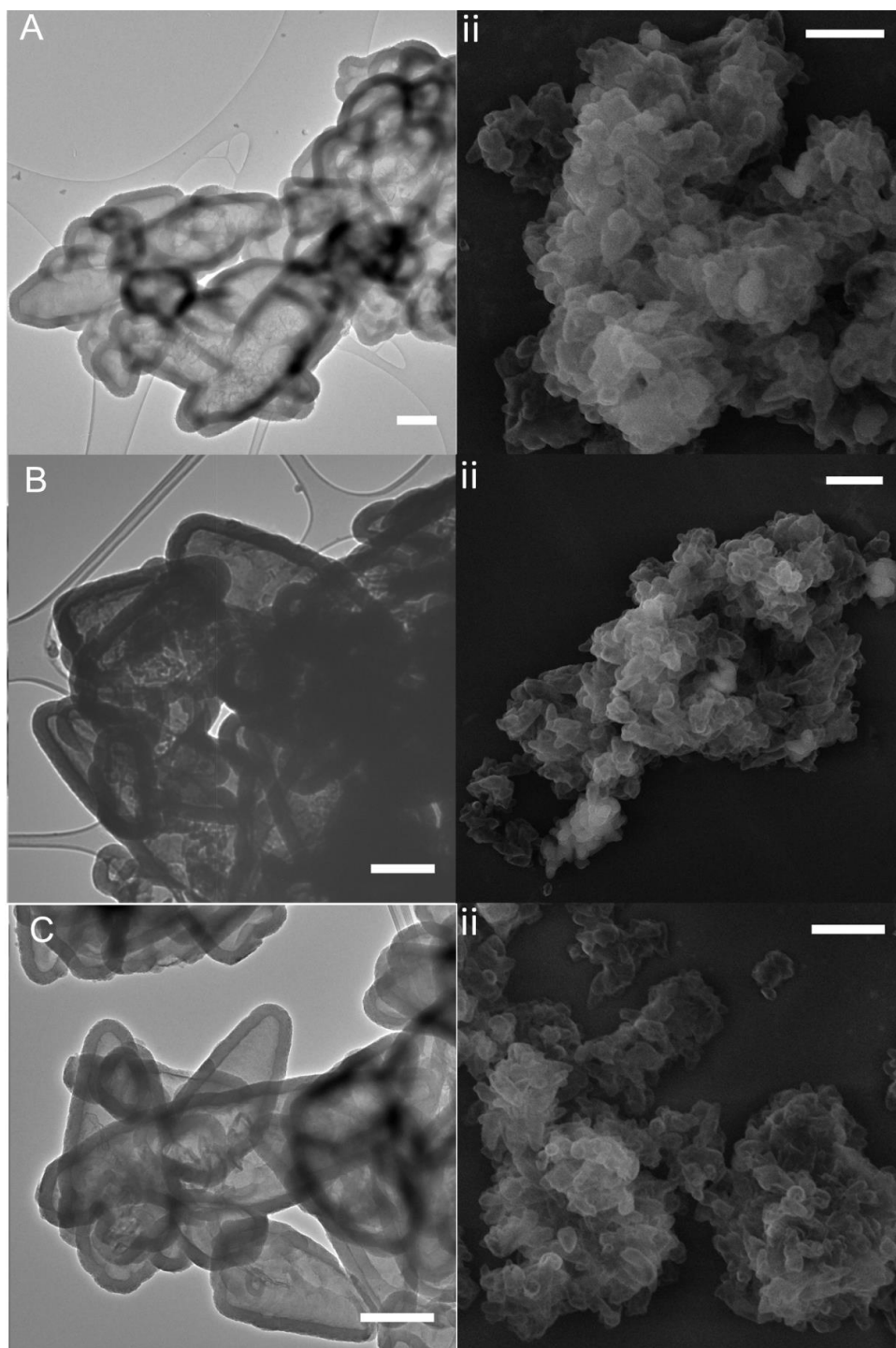


Figure 2-25. TEM micrographs of etched silica shells A) TBT 1, B) TBT 2, and c) TBT 3. Scale bars are 250 nm. SEM micrographs of etched silica shells ii) TBT 1 and ii) TBT 2, and iii) TBT 3 silica shells after interior core was acid etched.

SEM images of the etched nanocomposite showed the particles aggregated upon drop drying (**Figure 2-25 i and ii**) due to their high Hamaker constant, similar to the pre-etched samples (**Figure 2-18**). However, the TEM images (**Figure 2-25 A - C**) indicate that individual shells were formed during the synthesis and not a coating of a large group of CaCO_3 particles *in situ*. A decrease in wt% of TEOS and an increase in BTEOSO in the silyl reagent feed led to a decrease in shell thickness. The shell thicknesses for each shell were determined to be 65 nm (SOCAL@TBT 1), 50 nm (SOCAL@TBT 2), and 47 nm (SOCAL@TBT3).

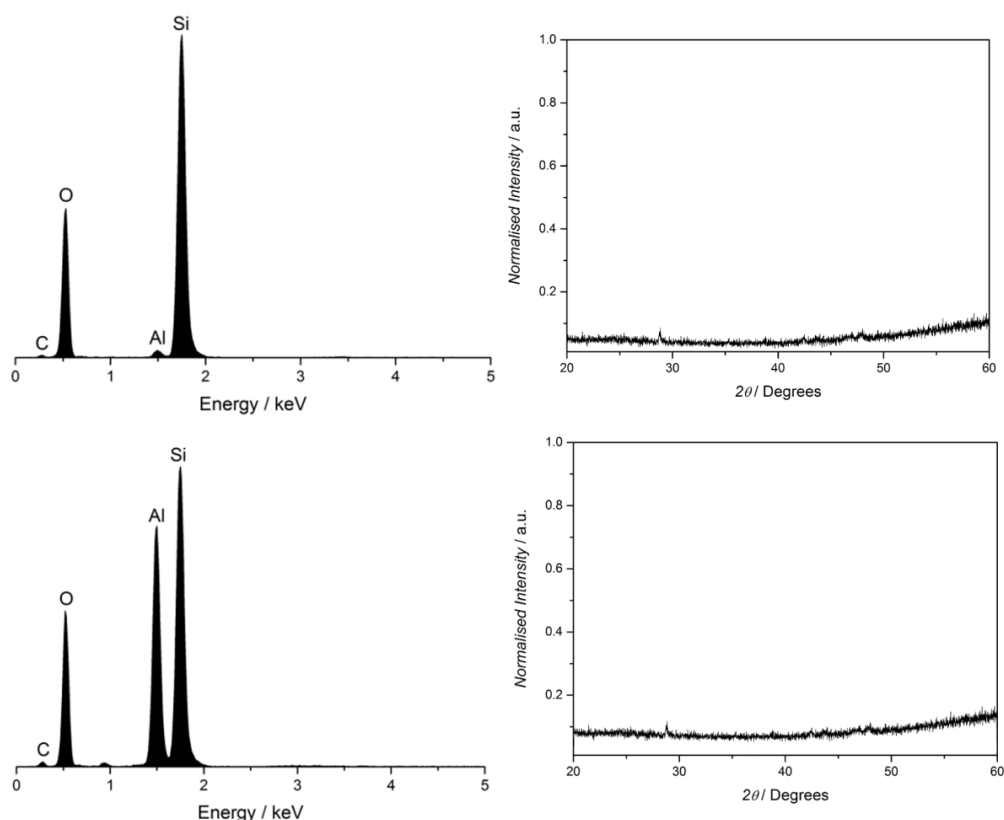


Figure 2-26. a) EDX spectra and b) XRD spectra of silica shells remaining after etching out the CaCO_3 leaving the shell of i) TBT 1 and ii) TBT 3 showing a loss of both the Ca α and Ca β in the EDX and the crystalline peaks in the XRD.

EDX and XRD were conducted in order to determine whether the calcium carbonate was fully removed. The lack of calcium peaks in **Figure 2-26 ai - aii** suggests that all internal calcium has been removed leaving a hollow void of air behind. This was further corroborated with the XRD scans (**Figure 2-26 bi - bii**) where all calcite peaks have been lost. The noisy signal remaining indicates that there is an amorphous crystal still present.

Due to the hollow nature of the particles, doing tests with respect to the volume of particles instead of the mass of particles were performed as more relevant data can be achieved in order to compare these to other particles. For this purpose, the effective particle density of the samples was then calculated. However, as there are many different types of densities, it is crucial to define them;

- *Effective particle density* is the density of hollow material where the overall volume of the sample is taken into account along with the density of the shell. Very important in the coatings industry.

- *Bulk density* (also referred to as envelope density) is the average density of a large volume of powdered material where all pores and voids within the material are measured.
- *Tap density* (occasionally referred to as bulk density also) is the density measured of a sample in a filled container after agitation in attempts to reach optimum packing. Interparticle voids are always taken into account with this measurement so the density acquired is always lower than the bulk density.
- *Skeletal density* (additionally termed as absolute, true, real, or apparent) is the density that is obtained when the volume measured excludes the pores as well as the void spaces between samples. Commonly measured using liquid or gas pycnometry.⁸⁵

It is believed that during the etching of the interior calcium carbonate, the exterior silica shell can undergo some breakage due to osmotic shock.^{75,86} Osmotic shock occurs in the event of a sudden change in concentration around the particles causing a rapid movement of water across a membrane (in this case the porous silica shell). To test whether our system was susceptible to breakage *via* osmotic shock we etched an equal volume of SOCAL@SiO₂ (100:0) particles with different etch rates. Thereafter, the silica colloids were dispersed within a poly(styrene-*co*-butyl acrylate-*co*-methacrylic acid) binder along with Acrysol SCT (a rheology modifier used to thicken up the solution) and films were cast.

The skeletal densities of each sample were measured *via* helium pycnometry. Skeletal density was used as a measure as the silica formed during the Stöber synthesis is porous and for the effective particle calculation we need the density of just the silica is required. If any particles did break upon etching and drying, it would not affect the skeletal density as the measurement was only for the silica material. The skeletal density of SOCAL was determined to be $2.602 \text{ g}\cdot\text{cm}^{-3}$ and so there is $(1/2.602) = 0.384 \text{ cm}^3 \text{ g}^{-1}$. If we added the pore volume to this calculation, we could quote this as the effective particle density. However, we did not know which pores are positioned at the surface and which were not. Thus, if we wished to easily compare the samples we had to calculate the effective particle density using **Equation 2-9**.

$$d_{eff \text{ SiO}_2} = \left(\frac{m_{\text{SiO}_2}}{\left(\frac{m_{\text{SOCAL}}}{d_{\text{SOCAL}}} \right) + \left(\frac{m_{\text{SiO}_2}}{d_{\text{SiO}_2}} \right)} \right) \quad 2-9$$

Where m_{SiO_2} is the mass of $\text{SiO}_2 \text{ g}^{-1}$ nanocomposite, m_{SOCAL} is the mass of SOCAL g^{-1} nanocomposite, d_{SOCAL} is the skeletal density of SOCAL, and d_{SiO_2} is the skeletal density of SiO_2 .

Using the TGA data collected earlier (**Figure 2-24** and **Table 2-4**) we know that 1 g of SOCAL@STBT 1 contains 0.1571 g of silica. By knowing this information and along with **Equation 2-9**, we can calculate the effective

particle density to be 0.4004 g cm⁻³. Therefore we were able to disperse an equal volume of each silicate sample into the binder.

To determine the number of intact voids, films of each sample were cast and the specific gravity of each film was measured *via* hydrostatic weighing in decamethylcyclopentasiloxane (DMCPS) employing **Equation 2-10**. The films were cast onto a polypropylene mould for the ease of release, and left to dry at ambient conditions overnight. The films mass were then recorded in both air and DMCPS. DMCPS was employed due to its large molecular structure reducing chances of penetration into the films which would alter the results by filling the air voids with DMCPS, changing the overall mass. DMCPS also had a density of 0.958 g·cm⁻³ which was lower than the expected theoretical density expected of the films samples of 1.085 g·cm⁻³. For the method to work, the film is required to sink into the submersion liquid.

$$SG_{film} = \frac{weight\ in\ air \times d_{DMCPS}}{weight\ in\ air - weight\ in\ DMCPS} \quad 2-10$$

Where SG_{film} is the specific gravity of the film and d_{DMCPS} is the density of the DMCPS

With the SG of each film measured, each of these values was then compared to the theoretical density of all the systems if all the shells had been compromised (skeletal density used in **Equation 2-11**) and all the shells remained intact (effective particle density used in **Equation 2-11**).

$$d_{theo} = \left(\frac{m_{solids}}{\left(\frac{m_{pig}}{d_{pig}} \right) + \left(\frac{m_{solids} - m_{pig}}{d_{binder}} \right)} \right) \quad 2-11$$

Where m_{solids} is the mass of solids g^{-1} of coating, m_{pig} is the mass of pigment g^{-1} of coating, d_{pig} is the density of pigment, and d_{binder} is the density of the binder.

Data shown in **Table 2-6** indicates the theoretical and experimental density of films with silica shells following the etching of the $CaCO_3$ template using 0.5 M acetic acid fed in over different time periods. The silica remaining after the etching was then dispersed within a film formulation (see **Section 2.5.6**) and films casts from the resulting formulation. The general formulation consisted of a 50 wt% PS/BA/AA binder diluted by dispersing in water. Equal amounts of silica were then dispersed within the binder dispersion at 200 RPM. Every 30 minutes, 0.5 ml Acrysol SCT-275 was added to the solution and the RPM of the dispermat increased (400, 600, 800, 1200 RPM respectively) before leaving to mix at 1200 RPM for 1 hour.

Table 2-6. Calculated density of films with both intact and compromised air voids using **Equation 2-11** along with the measured specific gravity by hydrostatic weighing.

Etch Time	d_{theo} Intact / g cm ⁻³	d_{theo} compromised / g cm ⁻³	$d_{\text{experimental}}$ / g cm ⁻³	Percentage intact / %
Instant	1.0847	1.2097	1.1141	76.5
2 Hour	1.0846	1.2075	1.1031	84.9
4 Hours	1.0846	1.2083	1.0891	96.4
12 Hours	1.0846	1.2075	1.0883	96.9

Use of high shear disperemat could cause some silica particles to undergo breakage from interacting with the blade, however, all samples underwent the same dispersing procedure. Therefore **Table 2-6** clearly shows that addition of acetic acid to the system at once causes are larger amount of breakage within the silica shells with only 76.5 % intact following the film formation. However, upon increasing the feed time of the acetic acid, an increase in percentage remaining intact can be seen for 2 – 12 hours, with little difference occurring between 4 and 12 hours.

Table 2-7. Skeletal density determined by helium pycnometry for the CaCO_3 template, $\text{CaCO}_3@\text{SiO}_2$ nanocomposites and the SiO_2 shells.

Material	Mass / g	Volume Displaced / cm^3	Skeletal Density / g cm^{-3}
SOCAL	0.3235	0.1251	2.602
SOCAL@TBT 1	0.2640	0.1109	2.815
SOCAL@TBT 2	0.3814	0.1596	2.392
SOCAL@TBT 3	0.3461	0.1527	2.385
SiO_2 Shell TBT 1	0.311	0.141	2.21
SiO_2 Shell TBT 2	0.298	0.136	2.185
SiO_2 Shell TBT 3	0.363	0.178	2.040

Using **Equation 2-9** along with the skeletal densities shown in **Table 2-7** the d_{eff} of TBT 1, TBT 2, and TBT 3 were determined to be 0.408, 0.361, and $0.332 \text{ g}\cdot\text{cm}^3$ respectively.

Cross polarised ^{29}Si solid state NMR (SSNMR) was implemented to determine whether the silica capsules of TBT 2 and TBT 3 did in fact incorporate the BTEOSO reagent into the shell or whether only TEOS formed them (**Figure 2-27**). Due to the high volume but low mass of the shells, initial tests using the one-pulse method did not show any Si bonded to C atoms which is expected at ~ -60 ppm. One-pulse experiments are known to be less

sensitive than others methods but do produce quantitative results. Cross polarised ^{29}Si SSNMR works by using nearby H atoms to help enhance the signal:noise from Si but thereby removes the possibility of quantitative analysis due to the Si bonded to H or C-H now have a greater signal. **Figure 2-27** shows the NMR's of all three samples. The TBT 1 sample only contains Q3 and Q4 Si atoms, indicating that the Si atoms are bonded to 3 or 4 Si through an O bond. Both the TBT 2 and TBT 3 also exhibit the Q3 and Q4 linkages as expected, however the spectra's also show a peak at - 65 ppm corresponding to a Si bonded to a carbon. These peaks indicate the presence of Si-CH_n species within the shells which can only arise from the BTEOSO linker. Any unreacted ethoxy groups would arise as Q3 Si.

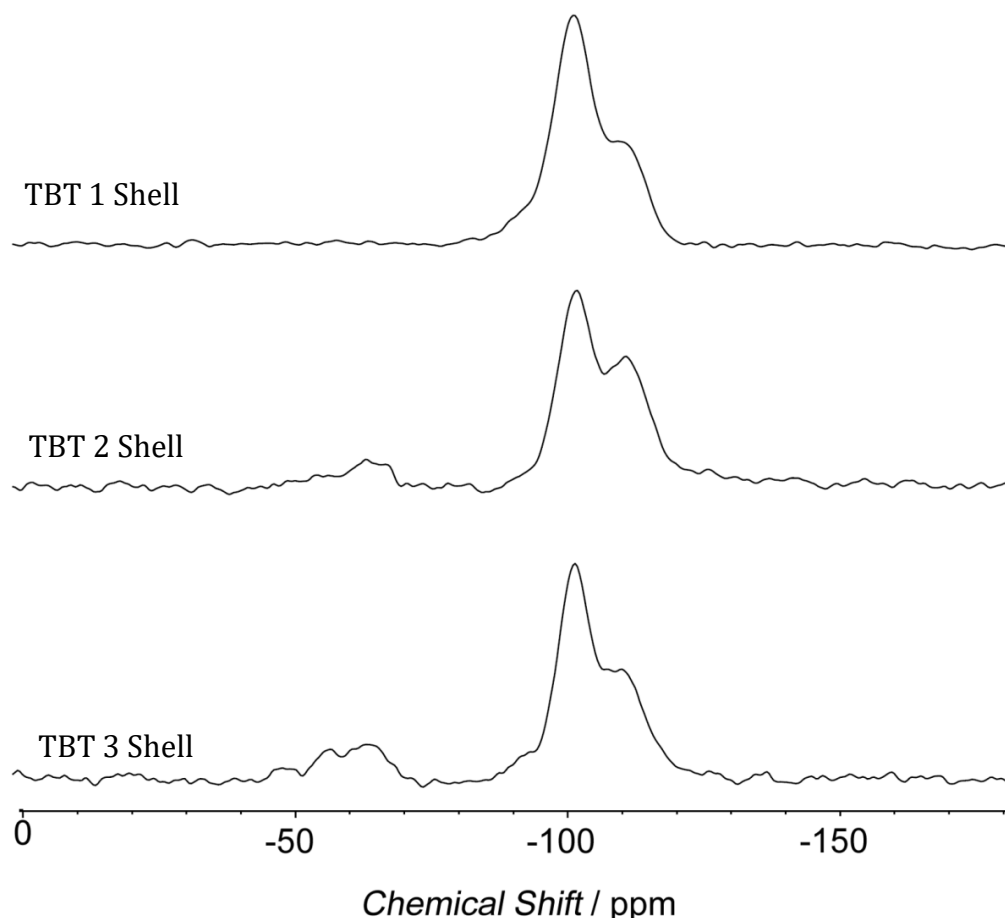


Figure 2-27. Cross polarised ^{29}Si Solid state NMR (SSNMR) of silica shells post etching. TBT 1, TBT 2, and TBT 3 correspond to the etched SOCAL@TBT 1, SOCAL@TBT 2, and SOCAL@TBT 3 nanocomposites respectively.

2.3.4 Dynamic Vapour Sorption

Each of the samples were easily dispersed in ethanol whereas attempts to disperse these in water only worked for the 100:0 sample. Both the 85:15 and 70:30 sample formed aggregates in the system. It was deduced that the inclusion of the BTEOSO octyl linker had modified the surface of the particles to become hydrophobic. To investigate this further, we conducted dynamic

vapour sorption (DVS) using two different solvent systems, namely octane (**Figure 2-28**) and water (**Figure 2-29**) to determine the mass of each liquid adsorbed. DVS is a gravimetric technique which measures how quickly and by how much a sample will absorb and desorb a solvent *via* changes in the vapour solvent concentration surrounding the sample. Each measurement was standardised to show the mass change of the particles per 10 μL to ensure easy comparison between samples.

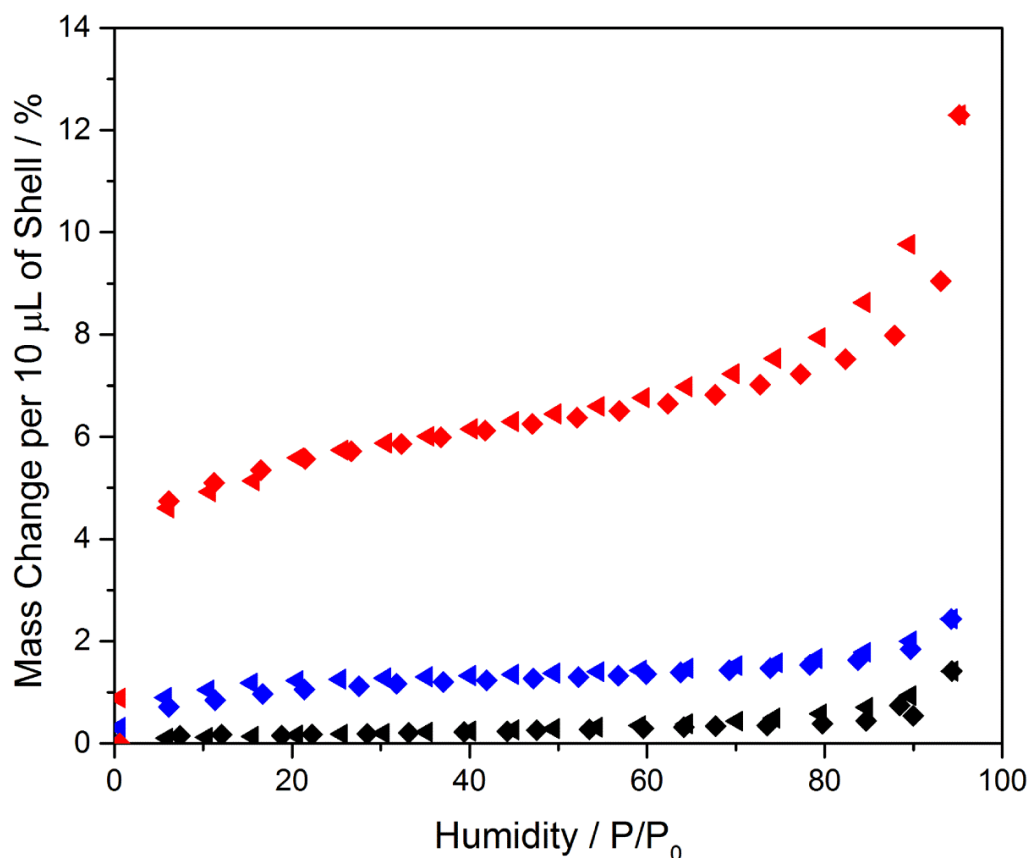


Figure 2-28. DVS isotherms of silica shells TBT 1 (◆), TBT 2 (◆), and TBT 3 (◆) in octane. Absorption curve (◆) and desorption curve (◄). The data was standardised to a constant volume to ensure an equal comparison between all samples.

From the results shown in **Figure 2-28**, we can clearly see at 95% relative humidity (RH) the particles synthesised using BTEOSO take up a larger amount of octane than the sample containing synthesised purely of TEOS which was as expected. The drastic increase in octane uptake seen in the TBT 3 sample (12.3 %) compared to the TBT 2 sample (2.4 %) is interesting. We postulate that due to the higher concentration of BTEOSO in the system, the pores have a higher chance to contain high quantities of surface octyl leading to a more hydrophobic pore that can uptake higher masses of octane. After the initial uptake of octane, all the systems remain relatively linear in uptake until 70% RH for the TBT 3 and 90% RH for the other two. These linear regions are as predicted by the Brunauer-Emmett-Teller (BET) model although liquid is being adsorbed instead of the traditional gas. The higher regions can also be accounted for in the BET theory and the systems as a whole show a Type II adsorption isotherm. The systems also show little hysteresis, though it is more pronounced with the inclusion of higher wt % of BTEOSO, suggesting they could not be used as long term carriers for oils. However, they could be used short term for release over time. Comparing the uptake of 12.3 % with the TBT 3 sample against that of 1.4 % of the system containing no octyl linker indicates that inclusion of BTEOSO alters the material to be more hydrophobic.

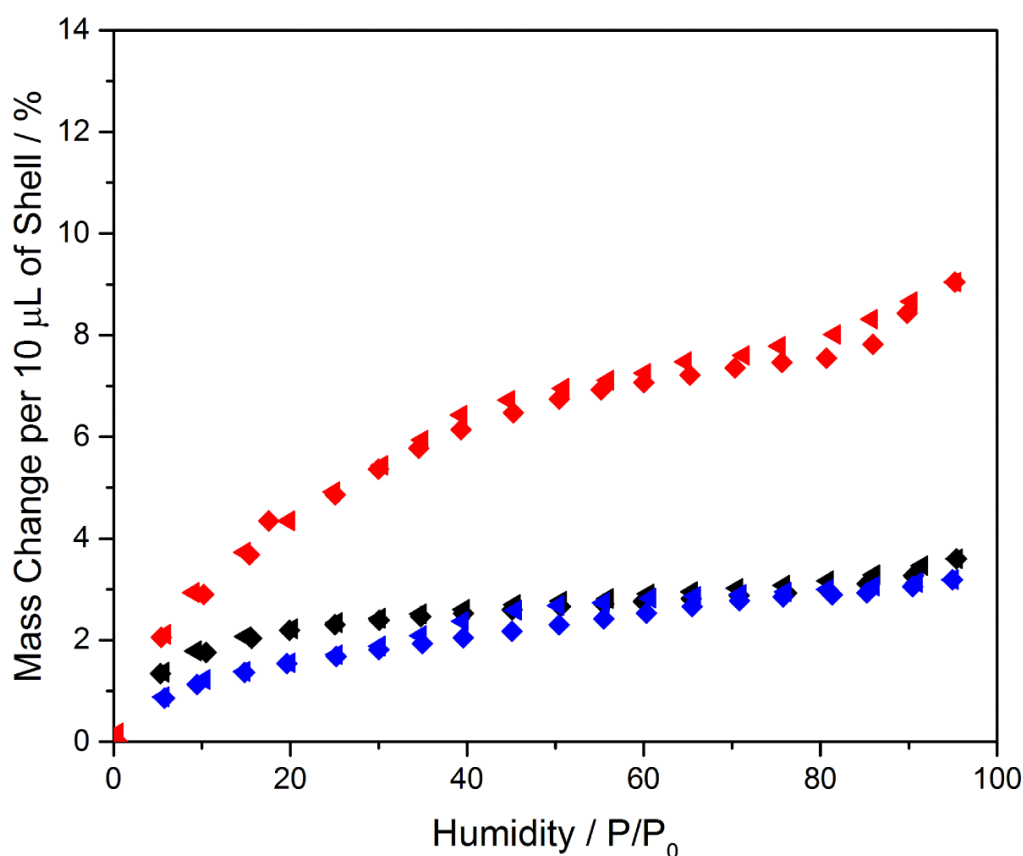


Figure 2-29. DVS isotherms of silica shells TBT 1(—), TBT 2(—), and TBT 3 (—) in water. Absorption curve (◆) and desorption curve (◀).

After investigating the particulate behaviour in octane, we then wanted to examine their behaviour in aqueous conditions (**Figure 2-29**). The systems seem to show a Type II adsorption isotherm as well. Whilst it already was expected that the TBT 1 sample would uptake more water than that of the TBT 2 (3.59 % and 3.19 %), it was not expected that the two values would be so close to one each other. In addition, the higher uptake of water into the more hydrophobic system (TBT 3) compared to the supposed hydrophilic system (TBT 1). The mass increase for the TBT 3 system was determined to

be 9.04 % versus 3.59 % for the TBT 1 system under aqueous conditions. This large difference could be attributed to porosity difference detected between the two systems as TBT 1 has a lower micropore volume than TBT 3 (**Table 2-3**). Thus, the TBT 3 sample, which is still more hydrophobic, has more pores to uptake water even against the hydrophobic nature. This data further suggests that the TBT 3 shell is more hydrophobic upon comparison of the maximum uptake of both solvents. In the octane system, maximum uptake is 12.3 % against the 9.04 % of the water system. Taking into account that the density of water at 25 °C is $0.9970 \text{ g}\cdot\text{cm}^{-3}$ and the density of octane is only $0.703 \text{ g}\cdot\text{cm}^{-3}$. Then we can clearly see that a larger volume of octane is taken up into the particles than the volume of water, which further indicates that the sample possess rather a stronger hydrophobic than hydrophilic properties.

2.3.5 Ultrasound Contrast Agent

In order to measure the ultrasound response of the silica particles, equal volumes were dispersed within water using an ultrasonic bath to break up agglomerates. To reduce erroneous results caused by air bubbles present within water, each solution was sonicated overnight. Ultrasound images of the microbubbles under harmonic mode imaging were analysed for pixel intensity and the frequency spectra of their response (**Figure 2-30**). The ultrasound intensity was characterised in terms of the mechanical index (MI), determined as the ratio between peak negative pressure of the ultrasound

and the square root of the centre frequency. Once the silica shells are dispersed in water, ultrasound was applied to the system and the response was imaged using a medical ultrasound unit. With the video response to ultrasound imaging obtained, the response was quantitatively measured by determining the contrast difference seen in the pure water system and systems containing hollow silica particles. The samples in low concentrations are shown in **Figure 2-30**.

Chapter 2: Silica Shells for Opacity

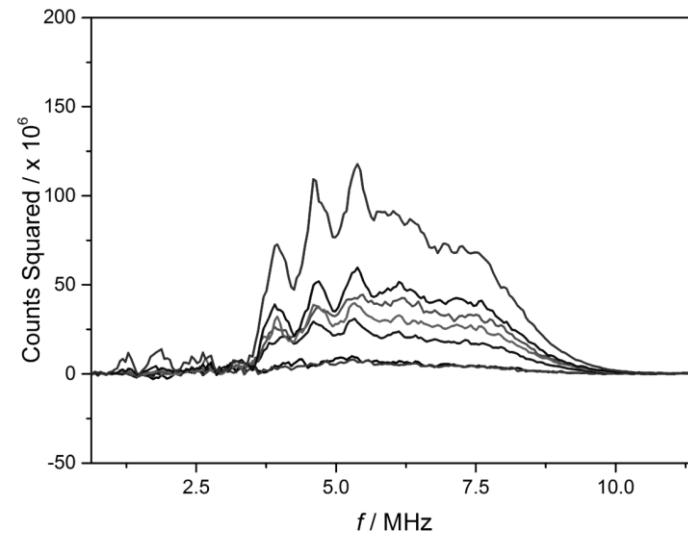
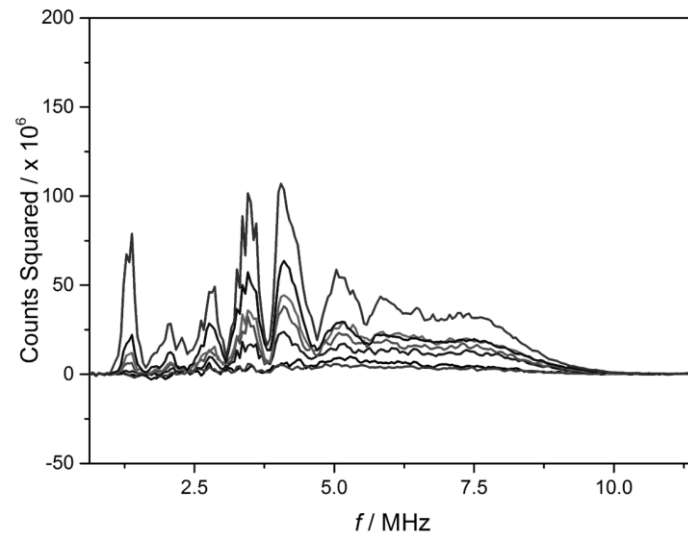
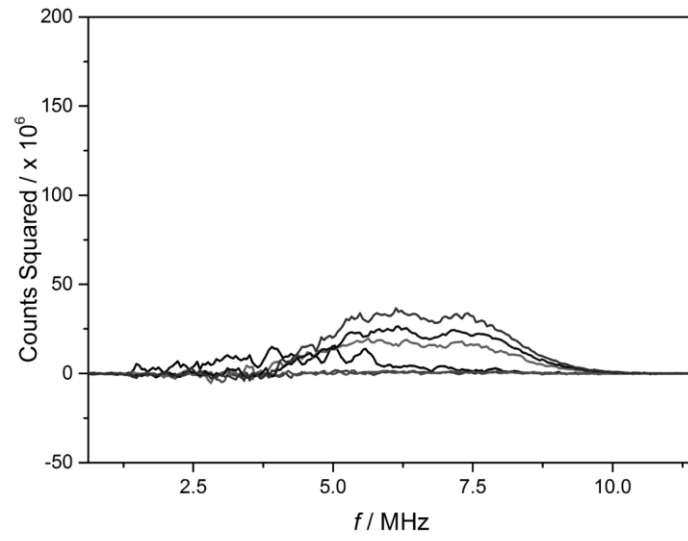


Figure 2-30. Ultrasound measurements at low concentration ($0.025 \text{ cm}^3\cdot\text{L}^{-1}$) of a) TBT 1, b) TBT 2, and c) TBT 3 silica shells at differing mechanical indexes (Top to bottom MI= 0.66 – 0.43).

Figure 2-30 represents the quantitative response of the hollow silica particles dispersed in an aqueous system after stimulation with ultrasound using a medical ultrasound unit. Videos of each sample (TBT 1 - 3) dispersed within deionised water and stimulated with ultrasonic waves at a different mechanical indexes (0.43-0.66) were taken over 30 seconds. Each video was processed using Stradwind by reducing down to 1 frame per second and the greyscale values used to determine the response given after sonication. As seen in **Figure 2-31**, brighter spots in the video indicate a stronger response from the ultrasound agent after stimulation. This is due to a stronger harmonic vibration from the particle causing an increase in the wave returned to the medical recording device. Increasing the MI corresponds to an increase in back pressure in the system, therefore stronger waves are sent out. Thus a stronger response is seen as the initial waves contain higher energy.

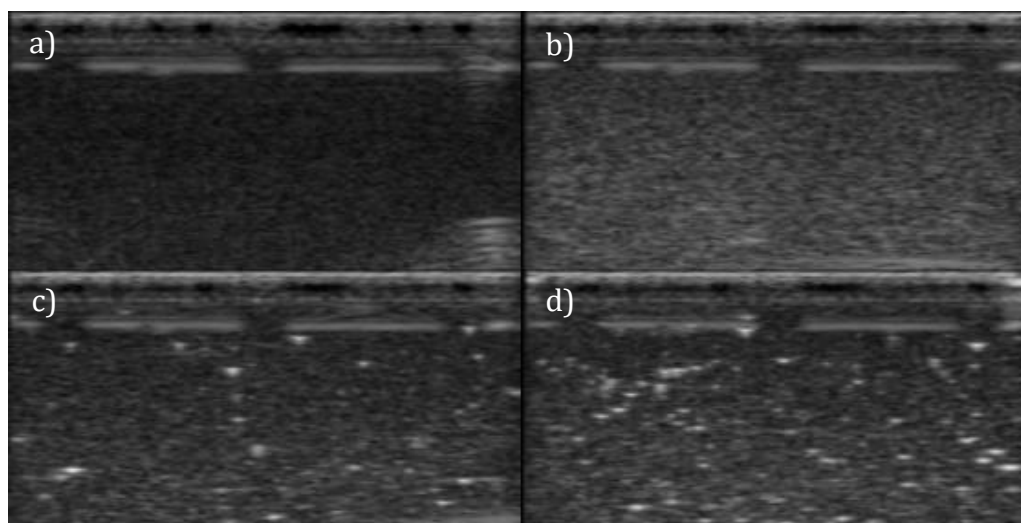


Figure 2-31. Greyscale snapshots of video from ultrasonic imaging of a) pure water and pure water containing b) TBT 1, c) TBT 2, and d) TBT 3 at $0.025 \text{ cm}^3 \cdot \text{L}^{-1}$ measured at MI 0.66. Lighter grey sections seen in b-d are indicative of low level ultrasound response whilst the white spots seen in c and d indicate a strong response to ultrasound imaging.

The silica samples containing the highest concentration of BTEOSO exhibit the strongest ultrasound response and, therefore, can be regarded as the best contrast agent. The highest responses of each sample were 117, 107, and 53 for TBT 3, TBT 2, and TBT 1 respectively. This behaviour is assumed to originate from (i) high number of octyl linkers being present in the system leading to a shell that was able flex to a higher degree to increase the harmonic resonance and (ii) higher hydrophobicity due to the octyl linkers, which leads to less water penetrating into the interior core, retaining a larger volume of air, which can oscillate with the ultrasound waves.

Chapter 2: Silica Shells for Opacity

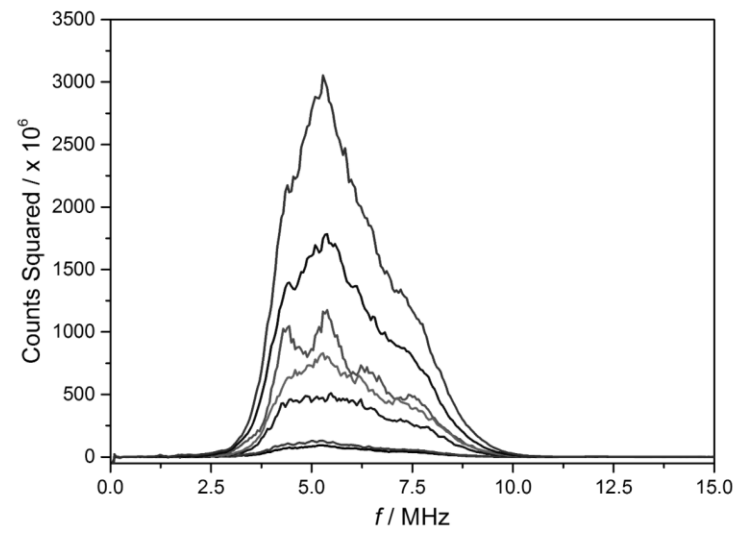
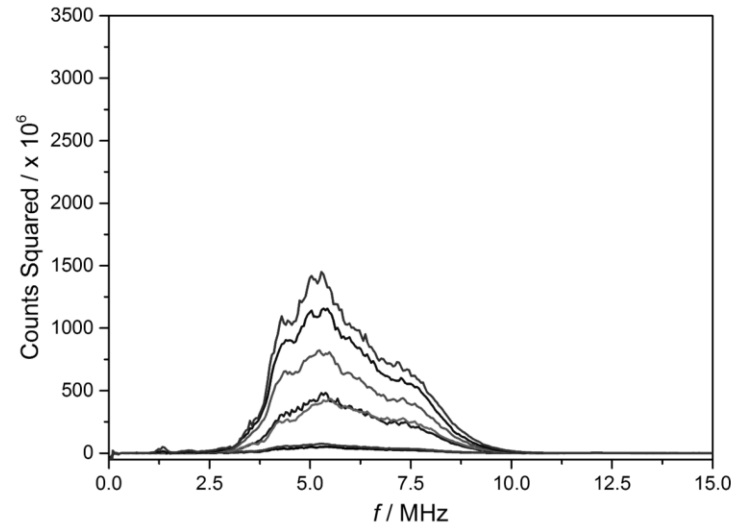
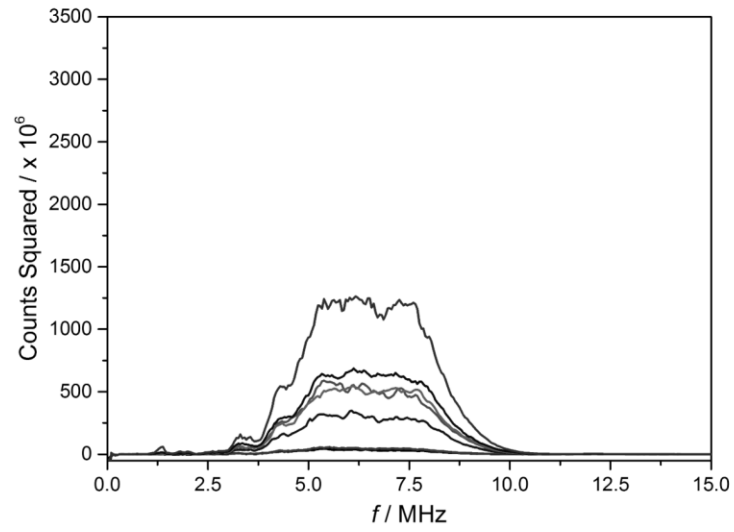


Figure 2-32. Ultra sound measurements at high concentration ($0.25 \text{ cm}^3\cdot\text{L}^{-1}$) of TBT 1, b) TBT 2, and c) TBT 3 silica shells at differing mechanical indexes (Top to bottom MI = 0.66 – 0.43).

Similar to the low concentration of silica particles, the high concentration of particles (**Figure 2-32**) show a similar response of higher BTEOSO concentration leading to a higher response. Increasing the concentration of particles by 10 times the amount increased the response measured by 26.1, 13.6, and 23.8 times for TBT 3, TBT 2, and TBT 1. Samples TBT 2 and TBT 1 response differs only slightly in both low and high concentration. This is most likely owing to the low incorporation of BTEOSO into the silica shell. Thus, the hydrophobicity of the shells may have a higher impact on the contrast agent ultrasound than on the flexibility.

2.3.6 Light Scattering

In order to investigate the use of the silica shells as an opacifier within paints, three binder formulations were made using TBT 1, TBT 2, and TBT 3 and compared to a binder formulation containing CaCO_3 as the opacifier and containing no pigment. The formulations were 25 % PVC with 19 vol.% solids within the dispersion assuming all the particles remained intact (for further experimental refer to **Section 2.5.7**). Following the successful dispersion of silica within the formulations, a film was drawn down onto a piece of Melinex[®] and left to dry. Three films per sample were drawn down at different wet

film thicknesses (WFT) to allow for a dry film thickness (DFT) of 25 μm (**Equation 2-3**). To determine the gloss values of the dry films, each of the samples were placed on a black tile and the gloss value recorded using a gloss meter. A black tile was required to absorb light passing through the sample and to ensure no light was reflected back into the gloss meter, skewing the results. The recorded data is shown in **Table 2-8**.

Table 2-8. Average multi angle gloss readings for dry films containing CaCO_3 , TBT 1-3, or no pigmentation.

Pigment in film	Gloss value at 20 ° / GU	Gloss value at 60 ° / GU	Gloss value at 85 ° / GU
No Pigment	49.3	109.4	27.3
CaCO_3	6	33.2	44
TBT 1	3.2	16.0	16.0
TBT 2	2.1	11.0	12.9
TBT 3	6.4	26.4	29.6

Gloss (also referred to as sheen) is an attribute surfaces have that causes shiny, metallic or matte appearances. The gloss of a surface is measured by exposing the surface with a ray of light with a series of detectors at 20 °, 60 °, and 85 ° from the incident light. A sample with high gloss should

show a gloss unit value (GU) above 70 at 60 ° and show a value between 10 - 70 GU at a low angle to the incidence (20 °). If a value lower than 10 is recorded at both 20° and 60° the sample is determined to be matte where little light is reflected by the sample.

Silicate materials are often used within coating formulations as an extender that introduces a matting effect to the end film.^{87,88} Silica cause a paint binder to become matte by causing an uneven surface upon film formation. Within a drying coating, silica particles are found to migrate to the surface. As the water evaporates and the latex binder undergoes particle deformation and polymer chain interdiffusion (**Figure 2-1**), the silicates on the surface become coated and cause a rough surface. Due to the matting effect of silicates, it is possible to use the gloss values as an indicator for the incorporation of silica into the binder systems. The pure binder system exhibited a very high gloss value at 60° with a value of 49.3 GU at 20 °, indicating that the binder on its own has a high gloss finish. With the incorporation of CaCO₃ into the system, a loss in gloss is seen. However, this loss is not as drastic as those recorded for the system containing the silicates (TBT 1-3). As an equal volume of each silica was used, the gloss value can give a very rough idea to how the silica was dispersed within the system. TBT 1 and TBT 2 show very similar low GU values at all angles. However, TBT 3 exhibits a higher gloss value than the previous two. This indicates that the sample has not been as well incorporated into the binder as TBT 1 and TBT 2. This reduced incorporated is likely due to the increased hydrophobicity of the sample.

The CIE L*a*b* colour space model is employed to determine both the white/black value (L*) of a sample along with the degree of green/red (a*) and blue/yellow (b*).⁸⁹ Each of the values can be obtained using **Equation 2-12 - 2-14** using the X, Y, and Z values measured *via* spectrophotometry.

$$L^* = 116 \sqrt[3]{\frac{Y}{Y_n}} - 16 \quad 2-12$$

$$a^* = 500 \left(\sqrt[3]{\frac{X}{X_n}} - \sqrt[3]{\frac{Y}{Y_n}} \right) \quad 2-13$$

$$b^* = 200 \left(\sqrt[3]{\frac{Y}{Y_n}} - \sqrt[3]{\frac{Z}{Z_n}} \right) \quad 2-14$$

Where X_n , Y_n , and Z_n are standard values dependant on instrument used.⁸⁹

Table 2-9. LAB colour space recording for films containing differing pigments.

Pigment in film	L*	a*	b*
No Pigment	27.35	- 0.06	- 1.54
CaCO ₃	40.98	- 0.71	- 3.63
TBT 1	50.58	- 0.94	- 4.37
TBT 2	46.02	- 0.95	- 4.47
TBT 3	32.36	- 0.41	- 3.22

As it can be seen in **Table 2-9**, incorporation of pigments into the binder formulation increases the white value of the end dried film. TBT 1 and TBT 2 induces a greater whiteness to a binder. A lower white value was obtained for TBT 3 than using pure CaCO_3 due to the lower incorporation of the silica sample into the binder. The use of all pigments lead to an increase in tint of the film in both the green (negative a^* value) and blue region (negative b^* value) over the base binder.

Following the gloss measurements, the reflectance of each sample was recorded over both black and white tiles to allow for calculation of the hiding power, scattering coefficient, and adsorption coefficient.

Table 2-10. Tabulated average hiding power, scattering coefficient, and absorption coefficient calculated using Kubelka – Munk theory (**Equation 2-5**).

Pigment in film	Average hiding power */ x 10 ⁻² a.u.	Scatter Coefficient* / x 10 ⁻² m ² ·g ⁻¹	Absorption coefficient* / x 10 ⁻³ m ² ·g ⁻¹
No Pigment	-8.49	-2.64	2.84
CaCO ₃	1.19	3.63	1.45
TBT 1	8.61	8.32	1.72
TBT 2	8.32	7.11	2.15
TBT 3	1.71	0.86	1.10

*Determined for the pigment within the binder

Hiding power (HP), often referred to as contrast ratio, is determined for a sample *via* the comparison of the reflected light of a sample over both black and white tiles (**Equation 2-15**). HP is often used to for quick comparison between samples measured using the same equipment as it is not film thickness dependent. However, comparison between additional systems measured at different times cannot be undertaken. This is due to the need for a constant value for both the black and white tile being the same. Difference in values for both the tiles can alter the hiding power recorded for a sample.⁹⁰

$$\text{Hiding power (Y)} = \frac{Y_{\text{black backing}}}{Y_{\text{white backing}}} \times 100 \quad \text{2-15}$$

Where $Y_{black\ backing}$ and $Y_{white\ backing}$ are the reflected values recorded using a spectrophotometer.

From the data shown in **Table 2-10**, it is clear that when no pigmentation is present, the films formed show no opacity with a hiding power of -8.49. With CaCO_3 dispersed within the system, some opacity is observed, indicated by the increase to 1.19. The refractive index of the binder used is 1.47, therefore the addition of CaCO_3 particles with a refractive index of 1.65 is expected to increase in opacity. Inclusion of TBT 1 and TBT 2 also show an increase in hiding power with similar values. However, TBT 3 exhibited a hiding power similar to that of the pure CaCO_3 sample. This large reduction from the previous TBT samples is indicative of a reduction in the silica's incorporation within the binder system, further corroboration results seen with the gloss values.

Comparison of scattering coefficient allows for comparison of pigments between systems. TBT 1 and TBT 2 show a clear increase in scattering ability over that of the basic CaCO_3 filler (**Table 2-10**). However, the use of TBT 3 as a pigment shows a diminished scattering ability to that of basic fillers. The effect shell thickness show very little difference between TBT 1 and TBT 2. This arises from the refractive index of silica being 1.45-1.49 whereas the refractive index of the binder used is 1.47. Therefore, increasing the silica thickness from 50 nm (TBT 2) to 65 nm (TBT 1) will have little effect on the end scattering ability. The scatter coefficient of rutile TiO_2 (commonly used opacifier) is $0.265 \text{ m}^2\cdot\text{g}^{-1}$ in vinyl acrylate binders. Therefore,

both TBT 1, and TBT 2 show a reduced scattering ability to that of pure TiO_2 . This is due to the high refractive index of TiO_2 (~ 2.5) in comparison to the refractive index of air (1). These results indicate that whilst the new silica particles do not exhibit an opacifying effect as strong as TiO_2 , the particles can be used as a filler to separate TiO_2 particles as well as increase the opacity of the paint system.

2.4 Conclusion

The aim of this work was to synthesise hollow colloidal particles with ellipsoidal geometry. By using SOCAL P3, we were able to synthesise large portions of silica shells reproducibly. Increasing the acid addition during the etch time increased the shell survival from 76 % of instant addition to 96 % at addition over 4 hours. The three silica shells were investigated as opacity modifiers and found to be effective in this use with the TBT 2 sample exhibiting the best opacity. Each of the samples also showed an ultrasound imaging response, with the most hydrophobic, TBT 3, exhibiting the strongest response at both high and low concentrations. Both TBT 1, and TBT 2 exhibit a similar response at high concentration, however at low concentration, the presence of the octyl linkages in TBT 2 led to a higher response being recorded.

2.5 Experimental

2.5.1 Materials

Tetraethyl orthosilicate (98 %) (TEOS), polyvinylpyrrolidone (M_n 40,000 g·mol⁻¹), and ethanol (≥99.89 %) were purchased from Sigma Aldrich. 1,8-bis(triethoxy silyl)octane (BTEOSO) was purchased from Fluorochem. Glacial acetic acid was purchased from VWR international and diluted down appropriately. Ammonium hydroxide (35 %) was purchased from Fisher Scientific. Calcium carbonate (SOCAL P3) was kindly donated by Crown Paints. Polystyrene/butyl acrylate/methacrylic acid binder was kindly donated by Akzo Nobel. All chemicals were used as purchased.

2.5.2 Characterisation Techniques

Transmission electron microscopy (TEM) was performed on a JEOL 2000FX fitted with a Gatan Ultrascan 4000 camera: Samples were prepared by applying a drop of diluted material to a suspended lacy carbon grid, wicking off excess liquid with a filter paper and left to dry.

Scanning electron microscopy (SEM) was performed on a Zeiss Supra 55-VP FEGSEM at 10 kV fitted with an EDAX Genesis analytical system: Samples were prepared by adding a drop of diluted suspension to a silicon wafer and drying at room temperature for 12 hours, the samples were subsequently carbon coated with a carbon evaporator for 4 seconds.

Thermogravimetric analysis (TGA) measurements of SOCAL P3 and SOCAL P3@SiO₂ nanocomposites were carried out in a 70 μ L alumina pan on a Mettler Toledo DSC1-Star. Samples were dried in a vacuum oven at 60 °C for 3 days prior to measuring. Sample mass was kept around 20 mg and weighed out using a 5 d.p. balance. The temperature was ramped up to 400 °C isotherm for 1 hour at a rate of 10 °C min⁻¹, followed by cooling to 25 °C at a rate of -10 °C min⁻¹. After the isotherm, the temperature was ramped up to 1000 °C at a rate of 10 °C min⁻¹. All work within the TGA was done under a flow of N₂ at 50 mL min⁻¹.

A Micrometrics AccuPyc 1330 helium pycnometer was used to measure the skeletal densities. A calibration was first run on a reference standard of known volume. A fused SiO₂ glass standard rod was then run before each sample to ensure the calibration factor was correct ($\rho = 2.20 \text{ g cm}^{-3}$). Masses of both the sample chamber and sample added were recorded with a 4 d.p. balance before the sample was inserted into analysis chamber. Before running the measurement, a steady purge of helium through the system was carried out for 30 minutes to remove moisture from the sample. Displaced volume within the sample chamber was then measured over a maximum of 50 runs until 5 concordant measurements within 0.05 % were recorded. Skeletal density was then calculated based on the sample mass, displaced volume, and calibration factor.

Dynamic vapour sorption measurements were performed in a DVSA-STD Dynamic Vapour Sorption Advantage from Surface Measurement

Systems. The machine was equipped with an active control of the relative humidity (RH) and organic vapour (containing two solution reservoirs of octane and water), sample pre-heating and a Cahn – D200 ultra-microbalance which allows gravimetric analysis up to 0.05 µg. The device's temperature ranged from 5 to 60 °C. The samples were measured within two suspended pans inside two close chambers independently connected to the microbalance.

Ultrasound imaging of the microbubbles was conducted using an Ultrasonix Sonix RP Ultrasound (Analogic Corporation, Peabody, MA)

²⁹Si Cross-polarisation solid state NMR was undertaken on a 300 MHz Varian InfinityPlus at a sample spinning frequency of 12 kHz in a 4 mm rotor.

Reflectance measurements were recorded on a Spectroflash SF600 X with a specular reflectance range over $\lambda = 400 - 700$ nm, recording each sample over both a black and white tile with each formulation measured three times.

2.5.3 Typical synthesis of hollow SiO₂ particles *via* templating onto

SOCAL P3

SOCAL P3 (10 g, 9.99 mmol, 1 eq.) was dispersed in ethanol (180 mL, 308.3 mmol, 30.8 eq.) *via* stirring at 600 RPM. Ammonium hydroxide (35 wt% ammonia) (20 mL, 36.2 mmol ammonia, 3.6 eq.) was added to the suspension and then sealed. Silyl monomer (20 g) was then fed in using a Harvard Instrument PHD 200 Infusion Syringe pump over 12 hours and left 24 hours

to react. The reaction was then washed *via* centrifugation in ethanol ($\times 3$) and in water ($\times 1$).

Calcium carbonate centres were removed by addition of acetic acid (0.5 M) in a 2 molar excess with respect to the calcium carbonate core over 4 hours. The resulting particles were then cleaned *via* centrifugation into deionised water ($\times 3$).

2.5.4 Typical DVS Method

10 mg of silica was weighed into the DVS and heated to 25 °C with dry air blown over each sample until the mass equilibrated. Following this, a mixture of air and the solvent (water or octane) was pumped through the system between 0-95 % humidity. Each recording was made when the samples equilibrated to the same mass for 15 minutes.

2.5.5 Typical Ultrasound Measurement

Typically ~ 100 mg of silica particles were dispersed within 1 mL water. A 0.1 mL sample was then taken and added to 400 mL of water in which the ultrasound imaging took place. A linear 14-5 MHz, 38 mm transducer was used. Harmonic mode was used for imaging the microbubbles, at a centre frequency of 5 MHz. The ultrasound response was collected using Stradwin ultrasound acquisition program (Department of Engineering, University of Cambridge) Both images and radio frequency intensity were analysed using MATLAB.

2.5.6 Typical Formulations for the etch tests

Table 2-11. Typical formulation used in etch test study.

Material	Mass / g	Solid Fraction	Solid in film / g	Solids Density / g·cm ⁻³	Volume solids / cm ³
Binder	12.5015	0.5	6.25075	1.08	5.7877
Silica	0.3968	1	0.3968	0.4106	0.9663
Acrysol SCT 275	2.418	0.175	0.4343	0.9	0.4826

2.5.7 Opacifier Test Formulations

Table 2-12. Opacifier test formulation for TBT 1.

Material	Mass / g	Solids / %	Solid mass / g	Density / g·cm ⁻³	Vol solids / cm ³
Binder	28.29	0.57	16.12	1.14	14.14
TBT 1	2.00	1	2.00	0.4082	4.90
Acrysol RM8W	1.99	0.22	0.43	1.23	0.35
Water	66.56	0	0	0	0
Pluronic	0.21	1	0.21	1.05	0.20

Chapter 2: Silica Shells for Opacity

Table 2-13. Opacifier test formulation for TBT 2.

Material	Mass / g	Solids / %	Solid mass / g	Density / g·cm ⁻³	Vol solids / cm ³
Binder	28.29	0.57	16.12	1.14	14.14
TBT 2	1.77	1	1.77	0.361	4.90
Acrysol RM8W	1.99	0.22	0.43	1.23	0.35
Water	66.56	0	0	0	0
Pluronic	0.21	1	0.21	1.05	0.20

Table 2-14. Opacifier test formulation for TBT 3.

Material	Mass / g	Solids / %	Solid mass / g	Density / g·cm ⁻³	Vol solids / cm ³
Binder	28.29	0.57	16.12	1.14	14.14
TBT 3	1.62	1	1.62	0.331	4.90
Acrysol RM8W	1.99	0.22	0.43	1.23	0.35
Water	66.56	0	0	0	0
Pluronic	0.21	1	0.21	1.05	0.20

2.6 References

- (1) Jada, S. S. *J. Mater. Sci. Lett.* **1990**, 9 (5), 565–568.
- (2) Sparrow, E. M.; Cur, N. *J. Heat Transfer* **1976**, 98 (2), 232.
- (3) Narayan, P.; Wheatley, M. A. *Polym. Eng. Sci.* **1999**, 39 (11), 2242–2255.
- (4) Zha, Z.; Wang, J.; Qu, E.; Zhang, S.; Jin, Y.; Wang, S.; Dai, Z. *Sci. Rep.* **2013**, 3, 2360.
- (5) Caruso, F.; Spasova, M.; Sussha, A.; Giersig, M.; Caruso, R. A. *Chem. Mater.* **2001**, 13 (1), 109–116.
- (6) Association, A. C. History of Paint <http://www.paint.org/about-our-industry/history-of-paint/>.
- (7) Protzman, T. F.; Brown, G. L. *J. Appl. Polym. Sci.* **1960**, 4 (10), 81–85.
- (8) Zohrehvand, S.; te Nijenhuis, K. *J. Colloid Interface Sci.* **2005**, 288 (1), 75–82.
- (9) Patton, T. C. *Paint Flow and Pigment Dispersion*; 1966; Vol. 68.
- (10) Keddie, J. L.; Meredith, P.; Jones, R. a. L.; Donald, A. M. *Langmuir* **1996**, 12 (16), 3793–3801.
- (11) KEDDIE, J. *Mater. Sci. Eng. R Reports* **1997**, 21 (3), 101–170.
- (12) Braun, J. H.; Baidins, A.; Marganski, R. E. *Prog. Org. Coatings* **1992**, 20 (2), 105–138.
- (13) Ross, W. D. *Ind. Eng. Chem. Prod. Res. Dev.* **1974**, 13 (1), 45–49.
- (14) Cabrera, M. I.; Alfano, O. M.; Cassano, A. E. *J. Phys. Chem.* **1996**, 100 (51), 20043–20050.
- (15) Grum, F.; Luckey, G. W. *Appl. Opt.* **1968**, 7 (11), 2289.
- (16) Karakaş, F.; Vaziri Hassas, B.; Çelik, M. S. *Prog. Org. Coatings* **2015**, 83, 64–70.
- (17) Adkins, A. S. Spacer/extender for titanium dioxide in pigment systems for coatings US 5171631 A. US 5171631 A, 1992.
- (18) Learner, T. *Modern paints uncovered: proceedings from the modern paints uncovered symposium*; Intergovernmental Panel on Climate Change, Ed.; Cambridge University Press: Cambridge, 2007.
- (19) Dulux. *Volume Solids and Spreading Rate*; 2011.
- (20) Latour, G.; Elias, M.; Frigerio, J.-M. *Appl. Spectrosc.* **2009**, 63 (6), 604–610.
- (21) Torrent, J.; Barrón, V. *Methods Soil Anal. Part* **2008**, No. 5, 367–385.

- (22) Kubelka, P.; Munk, F. Z. *Tech. Phys* **1931**, 12 (1930), 593–601.
- (23) Akiwumi, F.; Butler, D. *Environ. Monit. Assess.* **2008**, 142 (1–3), 309–318.
- (24) Park, N.-G.; van de Lagemaat, J.; Frank, a J. *J. Phys. Chem. B* **2000**, 104 (38), 8989–8994.
- (25) Bach, U.; Lupo, D.; Comte, P.; Moser, J. E.; Weissörtel, F.; Salbeck, J.; Spreitzer, H.; Grätzel, M. *Nature* **1998**, 395 (6702), 583–585.
- (26) Ashkarran, A. A.; Hamidinezhad, H.; Haddadi, H.; Mahmoudi, M. *Appl. Surf. Sci.* **2014**, 301, 338–345.
- (27) Fu, G.; Vary, P. S.; Lin, C.-T. *J. Phys. Chem. B* **2005**, 109 (18), 8889–8898.
- (28) Kroll, W. *Trans. Electrochem. Soc.* **1940**, 78 (1), 35.
- (29) Lewicka, Z. A.; Benedetto, A. F.; Benoit, D. N.; Yu, W. W.; Fortner, J. D.; Colvin, V. L. *J. Nanoparticle Res.* **2011**, 13 (9), 3607–3617.
- (30) Rasouli, S.; Moeen, S. J.; Arabi, A. M. *Prog. Color. Color. coatings* **2009**, 2, 45–51.
- (31) McDermott, B. T.; Koch, C. C. *Scr. Metall.* **1986**, 20 (5), 669–672.
- (32) Buckingham, K. W. Methods for the treatment and prophylaxis of diaper rash and diaper dermatitis US4556560 A. US4556560 A, 1985.
- (33) Park, Y. S.; Schneider, J. R. *J. Appl. Phys.* **1968**, 39 (7), 3049–3052.
- (34) Princen, L. .; Devena-Peplinski, M. *J. Colloid Sci.* **1964**, 19 (9), 786–797.
- (35) Yebra, D. M.; Kiil, S.; Weinell, C. E.; Dam-Johansen, K. *Prog. Org. Coatings* **2006**, 56 (4), 327–337.
- (36) Liang, S.; Xiao, K.; Mo, Y.; Huang, X. *J. Memb. Sci.* **2012**, 394–395, 184–192.
- (37) Bauman, H. D. Use of ground limestone as a filler in paper US4026762 A. US4026762 A, 1977.
- (38) Wang, X.; Feng, J.; Bai, Y.; Zhang, Q.; Yin, Y. *Chem. Rev.* **2016**, 116 (18), 10983–11060.
- (39) Luke, S. M.; Vukusic, P.; Hallam, B. *Opt. Express* **2009**, 17 (17), 14729.
- (40) Hallam, B. T.; Hiorns, A. G.; Vukusic, P. *Appl. Opt.* **2009**, 48 (17), 3243–3249.
- (41) Vukusic, P.; Hallam, B.; Noyes, J. *Science (80-.)*. **2007**, 315 (5810), 348–348.
- (42) Mallick, P. K.; Broutman, L. J. *Mater. Sci. Eng.* **1975**, 18, 63–73.
- (43) Delmonico, J. A. Insulating paint for interior and exterior of buildings

and method of making same U4,623,390. US 4,623,390, 1986.

- (44) McDonald, C. J.; Devon, M. J. *Adv. Colloid Interface Sci.* **2002**, 99 (3), 181–213.
- (45) Kowalski, A.; Vogel, M. Sequential heteropolymer dispersion and a particulate material obtainable therefrom, useful in coating compositions as an opacifying agent US 4,469,825. US 4,469,825, 1984.
- (46) Wu, C.; Yu, S.-H.; Chen, S.; Liu, G.; Liu, B. *J. Mater. Chem.* **2006**, 16 (32), 3326.
- (47) Cui, X.; Yu, S. H.; Li, L.; Li, K.; Yu, B. *Adv. Mater.* **2004**, 16 (13), 1109–1112.
- (48) Zhou, Y. X.; Yao, H. Bin; Yao, W. T.; Zhu, Z.; Yu, S. H. *Chem. - A Eur. J.* **2012**, 18 (16), 5073–5079.
- (49) Kuo, C.; Huang, M. H. *J. Phys. Chem. C* **2008**, 112 (47), 18355–18360.
- (50) Taniguchi, T.; Kunisada, Y.; Shinohara, M.; Kasuya, M.; Ogawa, T.; Kohri, M.; Nakahira, T. *Colloids Surfaces A Physicochem. Eng. Asp.* **2010**, 369 (1–3), 240–245.
- (51) Donath, E.; Sukhorukov, G. B.; Caruso, F.; Davis, S. a; Möhwald, H. *Angew. Chemie Int. Ed.* **1998**, 37 (16), 2201–2205.
- (52) Stöber, W.; Fink, A.; Bohn, E. *J. Colloid Interface Sci.* **1968**, 26 (1), 62–69.
- (53) Nguyen, A.-T.; Park, C. W.; Kim, S. H. *Bull. Korean Chem. Soc.* **2014**, 35 (1), 173–176.
- (54) Lu, Y.; McLellan, J.; Xia, Y. *Langmuir* **2004**, 20 (8), 3464–3470.
- (55) Zhang, L.; D’Acunzi, M.; Kappl, M.; Auernhammer, G. K.; Vollmer, D.; van Kats, C. M.; van Blaaderen, A. *Langmuir* **2009**, 25 (5), 2711–2717.
- (56) Zhang, L.; D’Acunzi, M.; Kappl, M.; Auernhammer, G. K.; Vollmer, D.; van Kats, C. M.; van Blaaderen, A. *Langmuir* **2009**, 25 (5), 2711–2717.
- (57) Rossi, L.; Sacanna, S.; Irvine, W. T. M.; Chaikin, P. M.; Pine, D. J.; Philipse, A. P. *Soft Matter* **2011**, 7 (9), 4139–4142.
- (58) Sacanna, S.; Pine, D. J. *Curr. Opin. Colloid Interface Sci.* **2011**, 16 (2), 96–105.
- (59) Zoldesi, C. I.; Imhof, A. *Adv. Mater.* **2005**, 17 (7), 924–928.
- (60) Zoldesi, C. I.; van Walree, C. A.; Imhof, A. *Langmuir* **2006**, 22 (9), 4343–4352.
- (61) Zoldesi, C.; Ivanovska, I.; Quilliet, C.; Wuite, G.; Imhof, a. *Phys. Rev. E* **2008**, 78 (5), 51401.
- (62) Lin, P.-L.; Eckersley, R. J.; Hall, E. A. H. *Adv. Mater.* **2009**, 21, 3949–3952.

- (63) Gramiak, R.; Shah, P. M. *Invest. Radiol.* **1968**, 3 (5).
- (64) Ferrara, K.; Pollard, R.; Borden, M. *Annu. Rev. Biomed. Eng* **2007**, 9, 415–447.
- (65) Schutt, E. G.; Klein, D. H.; Mattrey, R. M.; Riess, J. G. *Angew. Chemie - Int. Ed.* **2003**, 42 (28), 3218–3235.
- (66) Blomley, M. J. K.; Cooke, J. C.; Unger, E. C.; Monaghan, M. J.; Cosgrove, D. O. *Bmj* **2001**, 322 (7296), 1222–1225.
- (67) Blomley, M. J. K.; Cooke, J. C.; Unger, E. C.; Monaghan, M. J.; Cosgrove, D. O. *Bmj* **2001**, 322 (7296), 1222–1225.
- (68) Nanda, N. C.; Schlieff, R.; Goldberg, B. B. *Advances in Echo Imaging Using Contrast Enhancement*; Nanda, N. C., Schlieff, R., Goldberg, B. B., Eds.; Springer Netherlands: Dordrecht, 1997.
- (69) Ten Cate, F. J.; Feinstein, S.; Zwehl, W.; Meerbaum, S.; Fishbein, M.; Shah, P. M.; Corday, E. *J. Am. Coll. Cardiol.* **1984**, 3 (1), 21–27.
- (70) Feinstein, S. B.; Ten Cate, F. J.; Zwehl, W.; Ong, K.; Maurer, G.; Tei, C.; Shah, P. M.; Meerbaum, S.; Corday, E. *J. Am. Coll. Cardiol.* **1984**, 3 (1), 14–20.
- (71) Huang, S.; Hamilton, A. J.; Tiukinhoy, S. D.; Nagaraj, A.; Kane, B. J.; Klegerman, M.; McPherson, D. D.; MacDonald, R. C. *Cell. Mol. Biol. Lett.* **2002**, 7 (2), 233–235.
- (72) Correias, J. M.; Bridal, L.; Lesavre, A.; Méjean, A.; Claudon, M.; Hélénon, O. *Eur. Radiol.* **2001**, 11 (8), 1316–1328.
- (73) Lin, P.-L.; Eckersley, R. J.; Hall, E. a. H. *Adv. Mater.* **2009**, 21, 3949–3952.
- (74) Zoldesi, C. I.; Steegstra, P.; Imhof, a. *J. Colloid Interface Sci.* **2007**, 308 (1), 121–129.
- (75) Morgan, A. R. *Synthesis , applications and phenomena of anisotropic inorganic colloids*, 2013.
- (76) Plummer, L. N.; Busenberg, E. *Geochim. Cosmochim. Acta* **1982**, 46 (6), 1011–1040.
- (77) Spanos, N.; Koutsoukos, P. G. *J. Cryst. Growth* **1998**, 191 (4), 783–790.
- (78) Sawada, K. *Pure Appl. Chem.* **1997**, 69 (5), 921–928.
- (79) Ogino, T.; Suzuki, T.; Sawada, K. *J. Cryst. Growth* **1990**, 100, 159–167.
- (80) Loy, D. A.; Carpenter, J. P.; Alam, T. M.; Shaltout, R.; Dorhout, P. K.; Greaves, J.; Small, J. H.; Shea, K. J. *J. Am. Chem. Soc.* **1999**, 121 (23), 5413–5425.
- (81) Park, J. M.; Hong, S. M. *J. Ind. Eng. Chem.* **2001**, 7 (1), 23–29.

- (82) Wyman, J. *J. Am. Chem. Soc.* **1931**, 53 (9), 3292–3301.
- (83) Elder, J.; Ready, V. J. *Therm. Anal.* **1986**, 31 (2), 395–405.
- (84) Sahin, Y. *Metallography* **2003**, 24 (8), 671–679.
- (85) Micromeritics. *Density Analysis Brochure*; 2015.
- (86) Bai, Z.; Zhao, B.; Lodge, T. P. *J. Phys. Chem. B* **2012**, 116 (28), 8282–8289.
- (87) Technologies, G. M. 2016.
- (88) Evonik. *Acematt® Ts 100 [Brochure]*; 2012.
- (89) HunterLab. *CIE L* a* b* Color Scale*; 2008; Vol. 8.
- (90) Sawyer, R. H. *Ind. Eng. Chem. Anal. Ed.* **1934**, 6 (2), 113–116.

3 Chapter 3: Effect of Hollow Silica Particles on PMMA's Mechanical Properties

3.1 Abstract

In this work we investigate the effect on ellipsoidal hollow silica shells upon the properties of PMMA. Thermal stability is added to the system with the addition of hollow silica particles due to air voids within the composites. The UTS of the PMMA was marginally improved with 5 wt% addition of TBT 1, whilst the elongation length for the PMMA was improved with the addition of TBT 3.

3.2 Introduction

The principle idea for the nanocomposite materials presented within this chapter was to investigate the effect of hollow, non-spherical silica particles on mechanical properties of poly(methyl methacrylate) (PMMA). The basic silica particles used within this chapter are the same as those synthesised in **Chapter 2**.

3.2.1 Polymeric Composites

Polymeric systems have been widely used due to their designed flexibility, light weight, processability, and low cost.^{1,2} However, whilst polymers exhibit these advantages, the mechanical properties (such as strength and elastic modulus) are often lower than that of metallic and ceramic systems, making them less attractive. In order to improve the physical properties of polymeric systems, whilst still maintaining their desirable properties, inclusion of inorganic filler particles is required.³ Addition of micron sized inorganic filler particles as reinforcement has been a standard practice within the composite industry for decades.^{4,5} To achieve the optimal mechanical properties, maximising the interaction between both the polymer and inorganic particulate is required.^{6,7} This often achieved using smaller inorganics (1 – 5 microns) to increase the surface area for interactions between the matrix and particles to occur.⁸ In recent years, organic / inorganic nanocomposite materials have had increased attention from both academic and industrial research due to the potential diversification and application of traditional polymeric materials.⁹ Hybrid

materials synthesised in this manner often exhibit new properties, such as increased stiffness, dimensional stability, lower water uptake, and increased rigidity and strength which neither of the individual compounds possess on their own.¹⁰

Composite materials are defined as material formed by the combination of two or more materials together.¹¹ If one or more of the materials within the composite have lengths within the micron range, the material is referred to as a microcomposite.¹² Likewise, if any material used exhibits lengths in the nanometre range, the resulting material is referred to as a nanocomposite. The first three main types of nanocomposites exist: i) isodimensional nanoparticles where all three dimensions are in the nanometer range. ii) elongated nanoparticles where two of the dimensions are within the nanometer range. iii) polymer-layered crystal nanocomposites where only one dimension is within the nanometer range often presented as sheets.¹³ Increased research in the synthesis of inorganic nanoparticles has allowed for greater types of nanocomposites to be created.^{14–18} Nanocomposite possess high surface area to volume ratios, allowing for greater interactions between both components.¹⁹ This increase in surface area to volume ratio (also referred to as aspect ratio) of nanoparticles is seen to provide a high reinforcing efficiency. Significant differences in composite properties can be obtained depending on components and method of preparation used. **Figure 3-1** represents three of the main types of composites that can be made upon formed.¹³

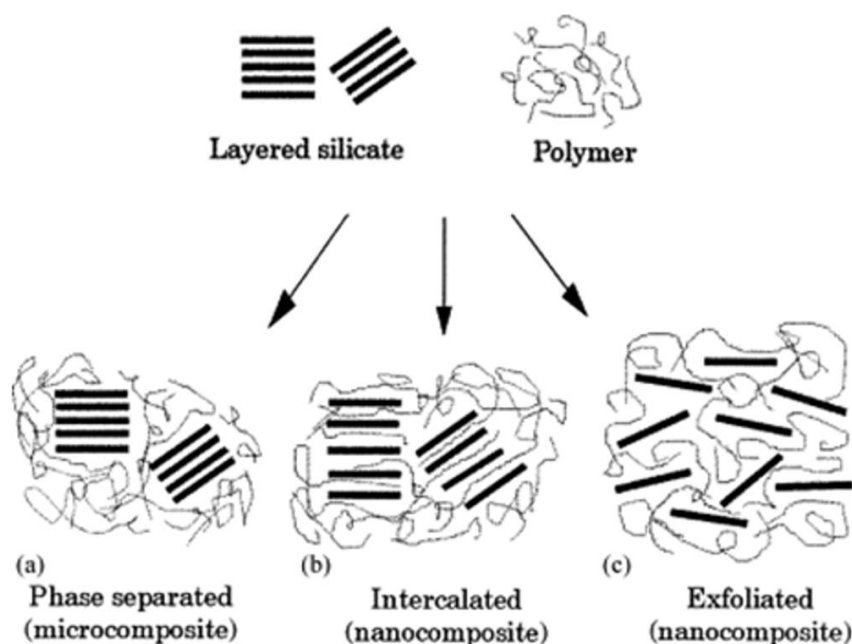


Figure 3-1. Schematic of three main types of layered composite arising from interaction between sheets and polymer chains. a) phase separated microcomposite, b) intercalated nanocomposite, and c) exfoliated nanocomposite.¹³

If the polymeric chains are unable to penetrate between the nanoparticles at all, a phase separated microcomposite is formed (**Figure 3-1 – a**).¹³ In this case, due to the aggregation of nanoparticles together, the nanoparticles now effectively act as a microparticle and the properties of the system remains within the range of the traditional microcomposites.²⁰ If penetration of the polymer between particles can occur, a well-ordered multi-layered nanocomposite can be formed, resulting in an alternating inorganic / polymer mixture.²⁰ If the nanoparticles can be fully exfoliated (separated) within the polymeric matrix, a uniformly dispersed

nanocomposite is formed.²⁰ If the nanoparticles are not well dispersed within the system (i.e. case (a)) the nanoparticle may lead to degradation of the mechanical properties of the system as opposed to increasing them. Nanocomposites have been shown to increase gas-barrier properties, electrostatic dissipation, flame retardancy, and mechanical strength enhancement.^{8,21-24}

3.2.2 Carbon based Nanocomposite

Interest in carbon based nanocomposites has shown to have increased in recent years due to the increased availability of both graphene (singular sheets of graphite) and Carbon nanotubes (CNT).^{25,26} The use of carbon, in the form of carbon black (CB), within tyres has long been conducted with ~65 % of the yearly production of CB directly used for tyre manufacturing.⁵ Inclusion of CB into rubber shows an increase in stiffness, abrasion, tensile strength, and durability over rubber tyres without any filler.^{27,28} CB is also known to change the conductive properties of polymer composites. CB was dispersed within a Polytetramethylene glycol ether based polyurethane (Pellethane® 2103-70A) at a variety of wt%.²⁹ An increase in the elastic modulus from 0.74 MPa at 0% CB to 3.75 MPa at 9.47 vol% CB. Furthermore, once CB reached above 6 vol%, an increase in conductivity from 1.88×10^{-7} S/cm (6.02 vol%) to 1.07×10^{-2} S/cm was observed.²⁹ Similar work by Knite *et al.* investigated the effect of elongation on the resistivity of a polyisoprene-CB nanocomposite.³⁰ It was found that below 8 wt% CB and above 15 wt% CB within the composite, no change in conductivity was observed upon

elongation. However, both 9 and 10 wt% CB in polyisoprene showed a distinctive increase in resistance upon stretching the nanocomposite over 10 %.³⁰ This is thought to be due to the separation of the conductive particles within the nanocomposite.

Composites containing graphene are currently the only commercialised use for graphene within industry.³¹ Graphene has garnered great interest due to 2D material exhibiting a Young's modulus of 1 TPa, high electrical and thermal conductivity, all of which should therefore help reinforce any material it is dispersed within.³²⁻³⁵ The flat structure of graphene, with the thickness of a carbon, leads to the sheets having extraordinarily high surface to volume ratios and therefore high interactions between both the polymer matrix and the graphene sheets can occur.³⁶ Incorporation of graphene within systems currently seems to divide many researchers with some indicating incorporation of graphene increase the mechanical properties up to 108 % tensile strength and tensile modulus to 103 % into epoxy systems.^{37,38} However, others have reported that incorporation of graphene into epoxide systems causes a reduction in the mechanical properties (from 52 MPa to 20 MPa) though it is theorised this is due to the aggregation of the graphene within the composite.^{21,39} Tripathi and co-workers investigated the effect of incorporation of graphene oxide nanoparticles at two loadings (1 and 2 wt%) within a PMMA matrix.⁴⁰ Three different methods for the synthesis of the composites were used: i) polymerisation of MMA in the presence of GO, ii) polymerisation of MMA in the presence of both GO and PMMA beads, and iii) polymerisation of MMA in the presence of GO followed by sheet casting. It was

found that incorporation of 1 wt% GO using the bead method and 1 and 2 wt% GO using the sheet casting method resulted in higher tensile strengths (26, 28.4, and 26.6 MPa respectively up from the pure PMMA of 24.2 MPa) and Young's modulus' (775, 963, and 1054 MPa respectively up from the pure PMMA of 750 MPa),

Similarly to graphene, CNT have received a large amount of interest due to the inherently high modulus and electrical/thermal conductivity since their discovery in 1991 by Iijima.⁴¹ Addition of CNT into polymer composites has shown an increase in strength and conductivity of the composite similar to that of CB.⁴²⁻⁴⁴ Successful dispersion of CNT into a various polymer matrices has been accomplished using screw extrusion, electrospinning, and solvent mixing.^{43,45-49} During the compounding process of the CNT into the polymer matrix, the orientation of the CNT can become either aligned or random. Both random and aligned nanotubes within polystyrene were studied by Thostenson.^{50,51} An increase in elastic modulus was observed in the unaligned system from 2.2 MPa of the base poly(styrene) system to 2.6 MPa with 5 wt% CNT dispersed within.⁵¹ However, upon aligned the CNT along the axis of tensile loading *via* drawing from extrusion, an increase to 3.5 MPa was obtained.⁵⁰ The alignment of nanotubes allowed for more efficient load transfer between the poly(styrene) matrix and the nanotube. An increase in tensile strength *via* alignment of CNT has also been shown in polyethylene and polyepoxide systems.⁵²⁻⁵⁵

Both graphene and CNT nanoparticles show great potential in increasing many properties of polymeric systems. However, whilst advances on synthesis of both graphene and CNT has advanced greatly, there is still a need for low cost / high throughput production of both carbon forms before replacement of CB occurs.⁵⁶

3.2.3 Inorganic Based Nanocomposites

Similar to carbon based nanocomposites, inorganic based composites have shown to increase mechanical properties of polymeric materials.⁵⁷⁻⁵⁹ One such composite that has gained interest are polymer systems containing TiO_2 due to the photocatalytic effect and potential as an antimicrobial agent.^{14,15,60} CaCO_3 nanoparticles have also been employed as a filler within polymeric materials to increase the ductility of the composites.^{18,61,62}

One of the most common inorganic nanoparticles used within nanocomposites is silica clays due to the low cost, high abundance, and ease of exfoliation.^{8,19} Clay minerals belong to the larger class of materials known as layered materials, defined as “crystalline material wherein the atoms in the layers are cross-linked by chemical bonds, while adjacent atoms interact by physical forces”. The width of the clay particles are within the nanometre range, along with the distances between the layers and most naturally occurring clay materials are alumina-silicate based. Due to the plate-like structure of clays, nanocomposites containing them often occur in the three different situations shown in **Figure 3-1**.⁶³

Along with clay platelets, spherical silica particles have also been investigated for their effect on mechanical properties.^{64–66} Lu *et al.* reinforced poly((3-trimethoxysilyl)propyl methacrylate) with mesoporous silica particles.⁶⁵ The methoxysilyl group along the polymeric main chain enabled linkages between the silica particles and the polymeric chains were formed with 89 % condensation of the polymer side chains being achieved. Two wt% of silica loadings were employed within their study; 28.5 wt% and 16.8 wt% SiO₂ nanoparticles. Increased loading of silica particles exhibited an increase in the thermal stability of the systems with an onset of the pure polymer starting at 250 °C, whilst an increase in temperature onset to 260 °C and 300 °C was observed with 16.8 and 28.5 wt% respectively. Low loadings of silica lead to an increase in tensile strength of 70 kPa with a Young's modulus increase of 148 kPa. Increasing to 28.5 wt% loading resulted in a an increase to 993 kPa in tensile strength along with an increase of 2605 kPa in Young's modulus. However, the overall elongation of the system was reduced to 42% with the low loadings whilst both pure and 16.8 wt% loading achieved 113 and 127 % respectively. Work by Pinnavaia and co-workers also found the incorporation of silica into a PMMA matrix increased the thermal stability of the systems with four differently sized silica particles dispersed at 5 wt%.⁶⁷ It is believed that due to the size of the particles, larger particles with higher pore sizes increase the thermomechanical properties as they induce increased polymer confinement. This leads to a higher stability and stiffness.

Hollow spherical silica nanoparticles dispersed within polymeric systems have also shown improvements in water retention, dielectric

insulation and thermal insulation over pure polymeric systems.^{24,68,69} Thermal insulation improvement arises from the inclusion of stable air pockets within the polymer matrix. However, whilst stable systems containing hollow silica spheres are obtained, a reduction in both Young's modulus and tensile strength is often found. Li *et al.* dispersed silica spheres with polystyrene sulfonate hairs grafted from them within a sulfonate poly(ether ether ketone) (SPEEK).⁶⁹ An increased water retention was observed upon dispersion of higher loadings. However, a reduction in tensile strength from 50.1 MPa of the pure system to 37.7 MPa was observed with a 5 wt% presence of hollow silica particles coupled with a reduction from 1.6 GPa to 1.3 GPa in Young's modulus. Strangely, the presence on hollow particles also led to a reduction in elongation length. It is expected that hollow particles increase elongation due to repression of crack propagation through a polymer system.⁷⁰

In this chapter, a PMMA/SiO₂ system was chosen as a model for the preparation of inorganic / polymer nanocomposites. The preparation of the SiO₂ particles (TBT 1, TBT 2, and TBT 3) is shown in **Chapter 2**. The silica particles were compounded with PMMA in an extruder to form a homogeneous nanocomposite. The optical, mechanical, and thermal properties of the materials were studied to determine the effect the hollow ellipsoidal silica particles had upon the PMMA nanocomposite. Analysis confirmed a dispersion of aggregates was obtained along with a good dispersion of the more hydrophobic SiO₂ particles within the PMMA matrix and a change in physical properties arose from this.

3.3 Results and Discussion

PMMA is an optically transparent thermoplastic commonly used within industry under the trade names of Perspex, Plexiglass, and Acrylite among others.⁷¹ Due to the inherent transparency of PMMA, it is often used as a lightweight / shatter resistant alternative to glass.⁷² The amorphous polymer has low water absorption, good electrical resistivity, remains rigid, with good relative tensile strength (72 MPa).⁷³

In order to determine the effect of hollow silica particles, TBT 1 – TBT 3 from **Chapter 2**, have upon a PMMA system, composites at varying wt% were created. Large M_w PMMA is sold in pellet form, which upon mixing with small powdered material, separates out into layers of large and small. This separation of additive and matrix is not conducive in the formation of a composite. Cryogenic grinding (also known as cryomilling and freezer grinding) was employed to reduce the size of the PMMA pellets to a fine powder. Cryogenic grinding is used for powdering thermoplastics as conventional grinding at ambient conditions is time consuming and often doesn't result in small particle size. Cooling polymers to liquid N₂ levels results in “embrittlement” of the material, facilitating crack propagation and reducing the energy required for milling.^{74,75} It has been reported that mechanical manipulation of polymers can cause breakages within the polymeric chain.⁷⁶ To ensure no change in polymer chain length occurred during the milling process, SEC was run on a pure PMMA pellet and the cryomilled powder (**Table 3-1**).

Table 3-1. SEC data from both the pure and milled PMMA.

Sample	$M_N / \text{g}\cdot\text{mol}^{-1}$	$M_W / \text{g}\cdot\text{mol}^{-1}$	\bar{D}
PMMA Pellet	157,000	345,000	2.2
Cryomilled	166,000	342,000	2.1

No change in the polymers molar mass distribution was observed (**Table 3-1**), indicating that the milling process did not fracture any chains within the polymer. The values obtained are also in close agreement to that of the manufacturer.

Once the PMMA was milled to a fine powder, mixtures of silica shells and PMMA were made. Typically, mixtures of PMMA and 5, 2, and 1 wt% of TBT 1 – 3 silica shells were made and premixed by tumbling overnight on a roller. The premixing step was found to help evenly distribute the silica within the powder before the processing steps. Following the premixing, extrusion of the composite was undertaken using a twin screw extruder. Typically, the extrusion was undertaken at 210 °C to ensure full melting of the PMMA matrix occurred with a screw speed of 20 RPM. Each sample had a residence time within the extruder of 210 seconds before cooling upon exiting the extruder. Each sample was run through the extrusion process twice to increase the chances of an even dispersion to occur. The composite was then

injection moulded into dogbones for tensile testing following ASTM D638 V standard sizes (**Figure 3-2**).

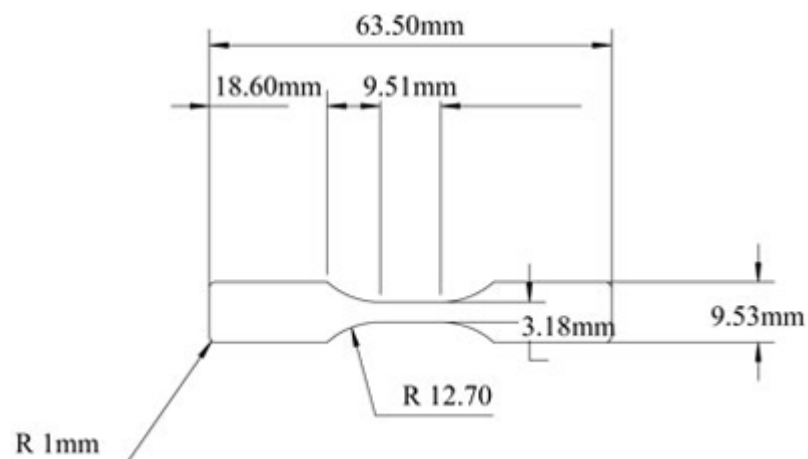


Figure 3-2. Schematic for ASTM D638 V dogbones.

Injection moulding was undertaken at a higher temperature than the extrusion (220 °C instead of 210 °C). It was found that at this higher temperature, the PMMA samples did not form bubbles within the polymer composite and were easier to remove from the mould without deformation of the specimen. Each injection moulded specimen exhibited great retention of shape and size with average length of 63.4 ± 0.2 mm, width of 3.2 ± 0.1 mm, and thickness of 3.2 ± 0.1 mm in close cooperation with the sizes of the mould.

3.3.1 Thermal Properties

As reported by Wang and co-workers, silicate nanocomposites can improve the thermal stability of PMMA systems by increasing the point at

which degradation occurs.⁷⁷ To determine both the exact wt% of silica present within the composites and the thermal properties of the nanocomposite, TGA was run on all samples. Each sample was heated from 30 °C to 1000 °C at a rate of 10 °C·min⁻¹ under N₂ to ensure full decomposition occurs. **Figure 3-3** shows both the TGA curves (solid lines) and differential thermogravimetric (DTG) curves (dashed lines) of the TBT 1 series of nanocomposites along with the base PMMA system. DTG curves are employed in this case to more clearly see the inflection points of the curve to ascertain further information on the degradation occurring.

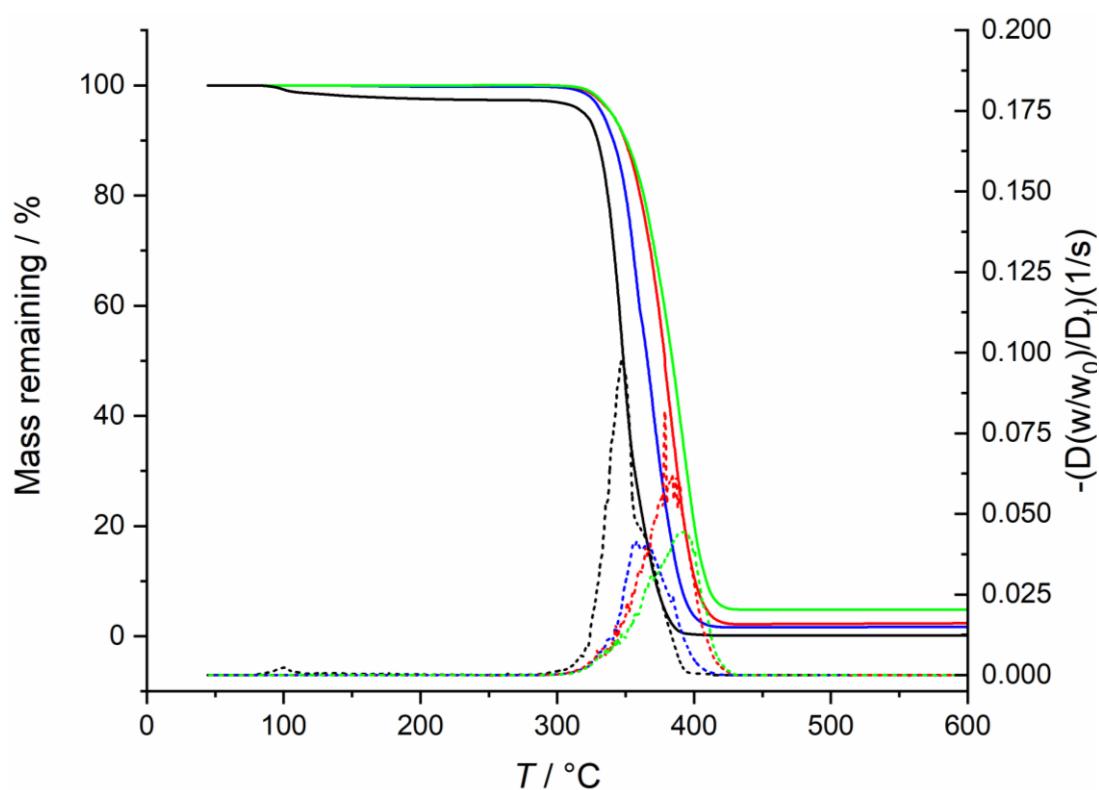


Figure 3-3. TGA (—) and DTG (---) curves of pure PMMA (—), nanocomposite of PMMA/TBT 1-1 (—), PMMA/TBT 1-2 (—), and PMMA/TBT 1-3 (—).

In **Figure 3-3**, the pure PMMA pellet sample indicates a mass loss of 3 % between 100 - 200 °C. This is indicative PMMA reaching its ceiling temperature of certain chain types (alkene terminated) and leading to the polymer chains decomposing. This has been shown previously by Haddleton *et al.* where the decomposition of PMMA produced by CCTP, free radical, and anionic polymerisation was investigated. Chains formed by CCTP are end terminated with alkene chains, leading to a lower ceiling temperature and faster degradation. Pure polymers with no unwanted termination such as those obtained through anionic polymerisation showed only a single point of degradation at a higher temperature. Polymers formed by free radical contain many different termination methods, leading to a large number of different polymer chain species being present in the end product. In these systems, only the pure PMMA product indicated any loss of mass below 300 °C. This is due to the processing of the nanocomposite where it was subjected to 210 °C heat during the extrusion process.

Table 3-2. Tabulated TGA data from **Figure 3-3**.

Sample	Mass Remaining / %	Loss Onset / °C	Inflection point / °C
PMMA	0.00	326	347
PMMA/TBT 1 – 1 wt%	1.60	332	356
PMMA/TBT 1 – 2 wt%	2.20	343	382
PMMA/TBT 1 – 5 wt%	4.83	349	392

After 410 °C, the PMMA sample indicates a mass loss of 100 % indicating the samples contained no fillers. Therefore, the mass remaining for the nanocomposite samples after each plateau is indicative of the wt% of silica within the systems. Using **Equation 3-1**, the volume % (V_1) of the silica in the composite can be calculated.

$$V_1 = \frac{1}{1 + \left(\frac{\rho_1}{\rho_2} \times \left[\frac{1}{W_{f1}} - 1 \right] \right)} \quad \mathbf{3-1}$$

Where ρ_1 is the density of the silica, ρ_2 is the density of the polymer matrix, and W_{f1} is the weight fraction of silica within the polymer matrix.

All TBT sample synthesised in **Chapter 2** are hollow in nature, therefore two vol% can be calculated for these composite systems: i) where the particles are hollow voids with air pockets within the polymer matrix, and ii) where the particles become interpenetrated by the polymer chains. In the

case of (i) the effective particle density must be used, whilst for (ii) the skeletal density of the silica must be used. Using the effective particle density for TBT 1 is $0.408 \text{ g}\cdot\text{cm}^{-3}$ results in a 12.8 vol% whereas using the skeletal density of $2.571 \text{ g}\cdot\text{cm}^{-3}$ results in a 2.28 vol% for composite TBT 1 - 1. For TBT 1 - 2, (i) is determined to be 6.11 vol% with (ii) being 1.02 vol%. Finally, for composite TBT 1 - 3 (i) is and 4.49 vol% (ii) determined to be 0.74 vol%. Determination of the correct vol% is discussed later (**Section 3.3.3**).

Both **Figure 3-3** and **Table 3-2** show a clear increase in the onset temperature at which the mass loss begins between the nanocomposites and the pure PMMA system. The onset of mass loss in pure PMMA system can be seen to occur at 326°C , however incorporation of TBT 1 into the matrix increases the onset to 332°C , 343°C , and 349°C depending on the mass percent of silica in the system (1.6, 2.20, and 4.83, wt% respectively). As stated earlier, none of the nanocomposite systems DTG curves indicate any thermal decomposition at lower temperatures as seen in the pure PMMA sample. An increase in the inflection point is also shown on the DTG curves where the pure PMMA occurs at 347°C whilst inclusion of TBT 1 increases this to 356°C , 382°C , and 392°C respectively. It is clear that presence of and inflection point of the thermal degradation where increasing the loadings of the nanocomposites increases the degree of stability. Silica nanocomposites have a high surface area, enabling an increase in interactions between silica and PMMA. This allows the thermal load to be transferred to the silica more readily and thus increasing stability.

It was theorised that the system containing the more hydrophobic silica particles (both TBT 2 and TBT 3) should interact more favourably with the PMMA chains, inducing an increase in thermal stability. **Figure 3-4** shows the TGA and DTG results for the TBT 2 composites.

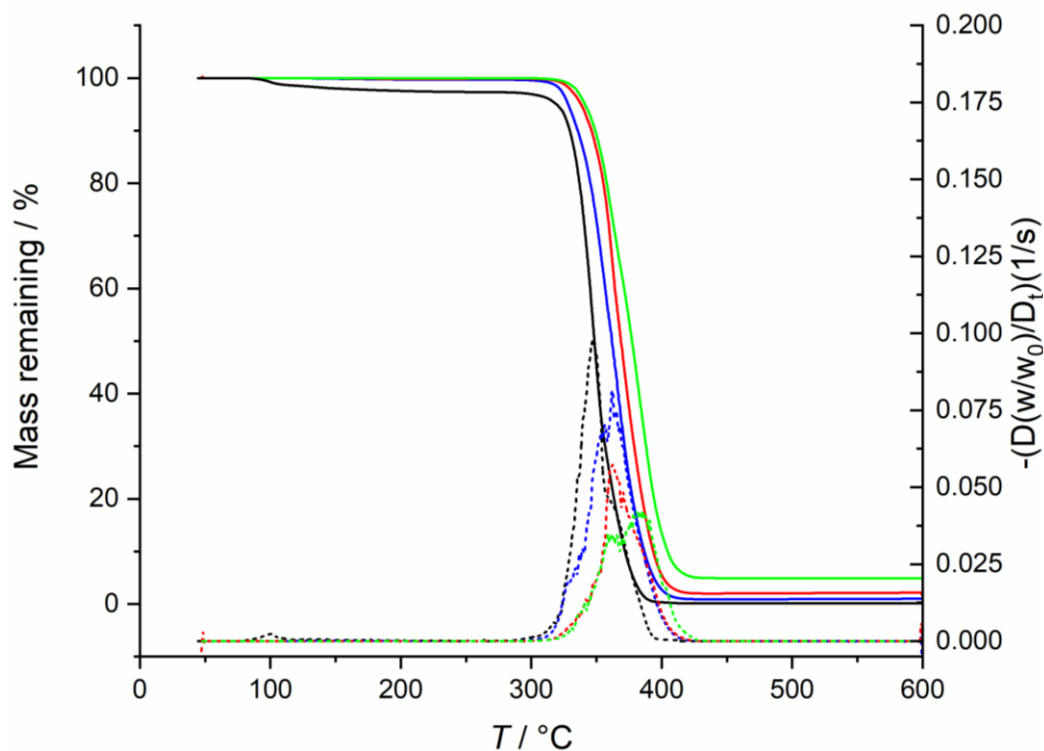


Figure 3-4. TGA (—) and DTG (--) of PMMA/TBT 2 - 1 (—), PMMA/TBT 2 - 2 (—), and PMMA/TBT 2 - 3 (—).

Similar to the TBT 1 series, no initial mass change was observed with the TBT 2 series between 100 – 200 °C (**Figure 3-4**). Tabulated data can be found in **Table 3-3**.

Table 3-3. Tabulated TGA data from **Figure 3-4**.

Sample	Mass Remaining / %	Loss Onset / °C	Inflection point / °C
PMMA/TBT 2 – 1 wt%	0.90	323	360
PMMA/TBT 2 – 2 wt%	2.00	338	364
PMMA/TBT 2 – 5 wt%	4.85	340	382

Using **Equation 3-1**, the vol% of silica can be calculated for each nanocomposite. The effective particle density of TBT 2 was determined to be $0.357 \text{ g}\cdot\text{cm}^{-3}$ whilst the skeletal density of the silica is $2.185 \text{ g}\cdot\text{cm}^{-3}$. PMMA/TBT 2 – 1 exhibits a vol% of silica at (i) 14.4 vol% or (ii) 2.68 vol%. For PMMA/TBT 2 – 2, the vol% is calculated to be (i) 6.32 vol% or (ii) 1.09 vol%. The vol% of silica within PMMA/TBT 2 – 3 was determined to be either (i) 2.92 vol% or (ii) 0.49 vol%.

Unlike the TBT 1 series, 0.90 wt% TBT 2 decreased the onset of thermal degradation by 2 °C although both 2 wt% and 4.85 wt% increased the point of degradation. The inflection point of the degradation is increased with all samples over the base PMMA system. Notably, 2 and 4.85 wt% loadings gave a lower inflection point of degradation than similar loadings of TBT 1 whilst low loading (0.9 wt% TBT 2) had a higher inflection point than seen with 1.6 wt% loading of TBT1.

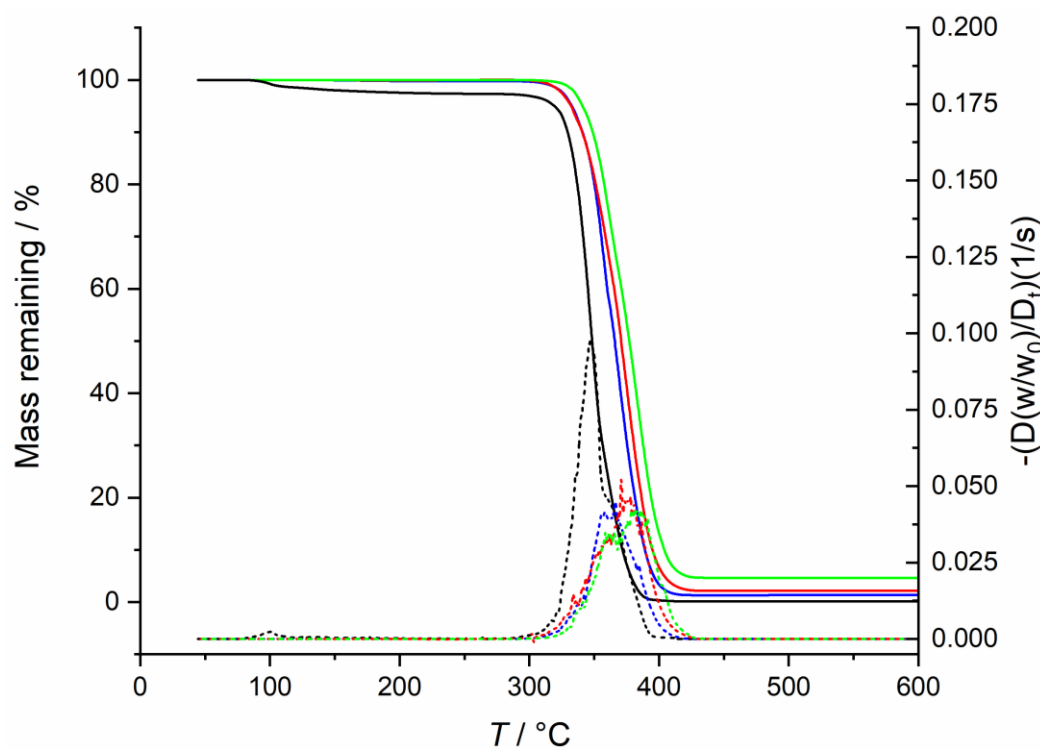


Figure 3-5. TGA (—) and DTG (--) of PMMA/TBT 3 - 1 (—), PMMA/TBT 3 - 2 (—), and PMMA/TBT 3 - 3 (—).

Table 3-4. Tabulated TGA data from **Figure 3-5**.

Sample	Mass Remaining / %	Loss Onset / °C	Inflection point / °C
PMMA/TBT 3 - 1 wt%	1.30	329	366
PMMA/TBT 3 - 2 wt%	2.20	329	374
PMMA/TBT 3 - 5 wt%	4.60	341	384

Using **Equation 3-1** and the data shown in **Table 3-4**, the vol% of silica can be calculated for each nanocomposite. The effective particle density of TBT 3 was determined to be $0.325 \text{ g}\cdot\text{cm}^{-3}$ whilst the skeletal density of the silica is $2.040 \text{ g}\cdot\text{cm}^{-3}$. PMMA/TBT 3 – 1 exhibits a vol% of silica at (i) 14.9 vol% or (ii) 2.71 vol%. For PMMA/TBT 3 – 2, the vol% is calculated to be (i) 7.54 vol% or (ii) 1.28 vol%. The vol% of silica within PMMA/TBT 3 – 3 was determined to be either (i) 4.56 vol% or (ii) 0.76 vol%.

It is clear from both **Figure 3-5** and **Table 3-4** that incorporating TBT 3 silica particles into the composite lead to an improved thermal stability. An increase both the onset and inflection point for all samples over pure PMMA can be observed. Increases between TBT 2 and TBT 3 can also be observed, indicating that whilst TBT 1 systems showed the greater impact in onset and inflection over the loading range, TBT 3 showed an increase over the TBT 2 samples. PMMA containing TBT 2 at 2 wt% exhibited an inflection point at 364°C whilst TBT 3 at 2.2 wt% exhibited it at 374°C .

Inclusion of TBT 1, TBT 2, and TBT 3 show an increase in the thermal stability of the systems with the increased loadings of silica wt% / vol% within the composites increasing the stability the most. There was a slight decrease between TBT 1 and both TBT 2 and TBT 3 systems, indicating that inclusion of TBT 1 increases the thermal stability the most.

3.3.2 Optical Properties

Due to the optical clarity of PMMA, it is often used as a replacement for glass where shattering may occur. Therefore it is often important to obtain

this optical properties upon the formation of PMMA composites. To investigate the optical properties, UV/Vis spectroscopy was employed (**Figure 3-6**). The UV/Vis absorption spectra of most polymer/inorganic composites are broadband and contain one or more maxima depending on the electron transitions.

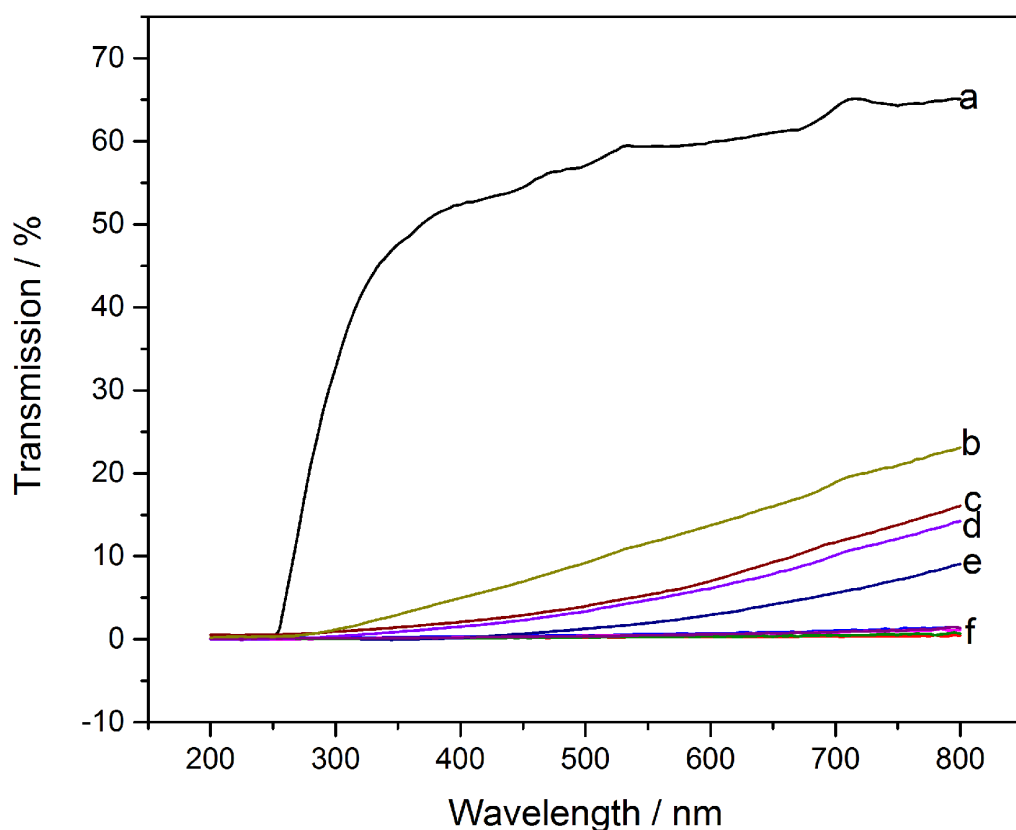


Figure 3-6. Transmission of UV and visible light recorded using a UV/Vis Spectrometer of a) PMMA dogbone, b) PMMA/TBT 3 1.3 wt% dogbone, c) PMMA/TBT 3 2.2 wt% dogbone, d) PMMA/TBT 2 0.9 wt% dogbone, e) PMMA/TBT 2 2 wt% dogbone, and f) remaining PMMA/TBT composites.

Figure 3-6 displays the transmission spectra of the PMMA/TBT composites. This indicates that the samples containing low wt% of TBT 3 (spectra lines b and c) obtain a composite that is more optically clear than the high wt% composite due to a higher transmission response within the visible region. Composites PMMA/TBT 2 – 2 and PMMA/TBT 2 – 3 also show a higher transmission than the PMMA/TBT 2 – 1 system, however there is a lower overall transmission than the TBT 3 counterparts. A higher vol% of TBT 3 is incorporated in PMMA/TBT 3 – 2 and PMMA/TBT 3 – 3 (7.54 and 4.56 vol% respectively) than in the PMMA/TBT 2 – 2 and PMMA/TBT 2 – 3 composites (6.32 and 2.92 vol% respectively) indicating that the TBT 3 silica particles form a better dispersion within PMMA.

All samples displayed a large reduction in transmission from the pure PMMA system, with no transmission detected for the composites containing TBT 1. This large reduction in transmission is indicative of the silica particles retaining the hollow particles within the system, leading to a scattering of light from non-absorbing poarticles.⁷⁸ Due to this high scattering, we were unable to obtain any information upon the electron transition within the composite.

3.3.3 Tensile Testing

To determine the mechanical properties of the composites formed, uniaxial tensile testing was undertaken on each of the injection mould samples. Measurements were performed at 25 °C, at a rate of 1 mm·min⁻¹ in a 10 kN load cell. Strain (ϵ), defined as the change in length of the sample with

respect to the original length (**Equation 3-2**), is applied to the sample and the stress, unit of force per area (Pa) required to achieve the strain, is measured.

$$\varepsilon = \frac{\Delta l}{l} \quad \text{3-2}$$

Where l is the initial length and Δl is the length change.

Plots of stress vs. strain produces bell-like curves where a positive gradient describes elastic deformation and negative gradient indicates plastic deformation occurring. During the linear portion of the curves, the stress and strain of material is proportional, therefore following Hooke's law. Due to this, the Young's modulus (also known as the elastic modulus) of the material can be obtained as the gradient of the linear portion (**Equation 3-3**). A high elastic modulus indicates that a material is stiffer than one with a lower modulus. If the load is removed from the sample below the point at which the graph deviates from the linearity, the sample will return to the original state.

$$E = \frac{\sigma}{\varepsilon} \quad \text{3-3}$$

Where E is the Young's modulus, σ is the stress, and ε is the strain.

The maxima of each curve is indicative of the toughness of the material, also referred to as the ultimate tensile strength (UTS).

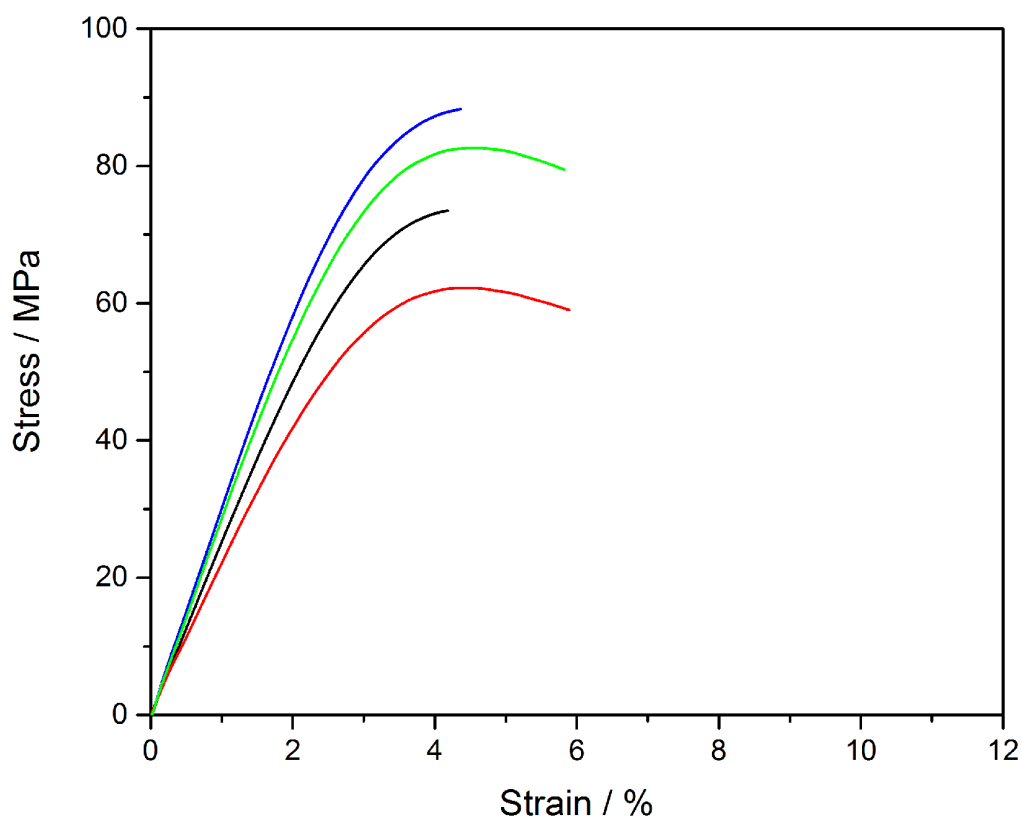


Figure 3-7. Stress – strain response curves of PMMA (—), PMMA/TBT 1 - 1 (—), PMMA/TBT 1 - 2 (—), and PMMA/TBT 1 - 3 (—) averaged over 5 runs.

Inclusion of TBT 1 at varying wt% within the PMMA matrix has a variety of effects on the mechanical properties (**Figure 3-7**). Simply looking at the curves in **Figure 3-7**, addition of both 4.83 wt% and 1.6 wt% resulted in an increase in the materials rigidity and strength. However, with the incorporation of 2.2 wt% TBT 1 within the matrix, a reduction in both UTS and elasticity can be observed in comparison to pure PMMA systems. This is due to the dispersion of the silica within PMMA/TBT 1 – 2.2 wt% (**Figure 3-8**).

Table 3-5. Tensile data of PMMA/TBT 1 composites averaged over 5 runs obtained from **Figure 3-7**. Errors are reported as 1 standard deviation from the mean.

Sample	UTS / MPa	Young's Modulus /MPa	Max Strain / %	Stress at breakage / MPa
PMMA	73.5 ± 1.9	2494 ± 10	4.19 ± 0.2	73.5
PMMA/TBT 1 4.8 wt%	88.3 ± 2.4	2995 ± 43	4.37 ± 0.2	88.3
PMMA/TBT 1 2.2 wt%	62.2 ± 1.7	2116 ± 33	5.89 ± 1	59.0
PMMA/TBT 1 1.6 wt%	82.6 ± 2.0	2822 ± 27	5.83 ± 0.5	79.5

A 20.1 % and 12.4 % increase in the UTS along with an increase of 20.1 % and 13.2 % increase in Young's modulus can be observed in TBT 1 – 4.8 wt% and TBT 1 1.6 wt% systems respectively. However, unlike the systems containing 4.83 wt% and 1.6 wt% TBT 1, PMMA/TBT 1 2.2 wt% exhibits a lower UTS and Young's modulus than the pure PMMA system (decrease of 11.3 MPa and 378 MPa respectively). This is due to the increased dispersion of the silica voids within the matrix (**Figure 3-8**). An increased dispersion leads to more centres within the matrix where hollow particle are present, reducing the PMMA chain interactions. Due to the lower loading amount, the silica particles can be dispersion within the system with less particle aggregates forming. However, it is as yet unclear as to why the

PMMA/TBT 1 2.2 wt% system exhibit a better dispersion of silica within the matrix than PMMA/TBT 1 1.6 wt%.

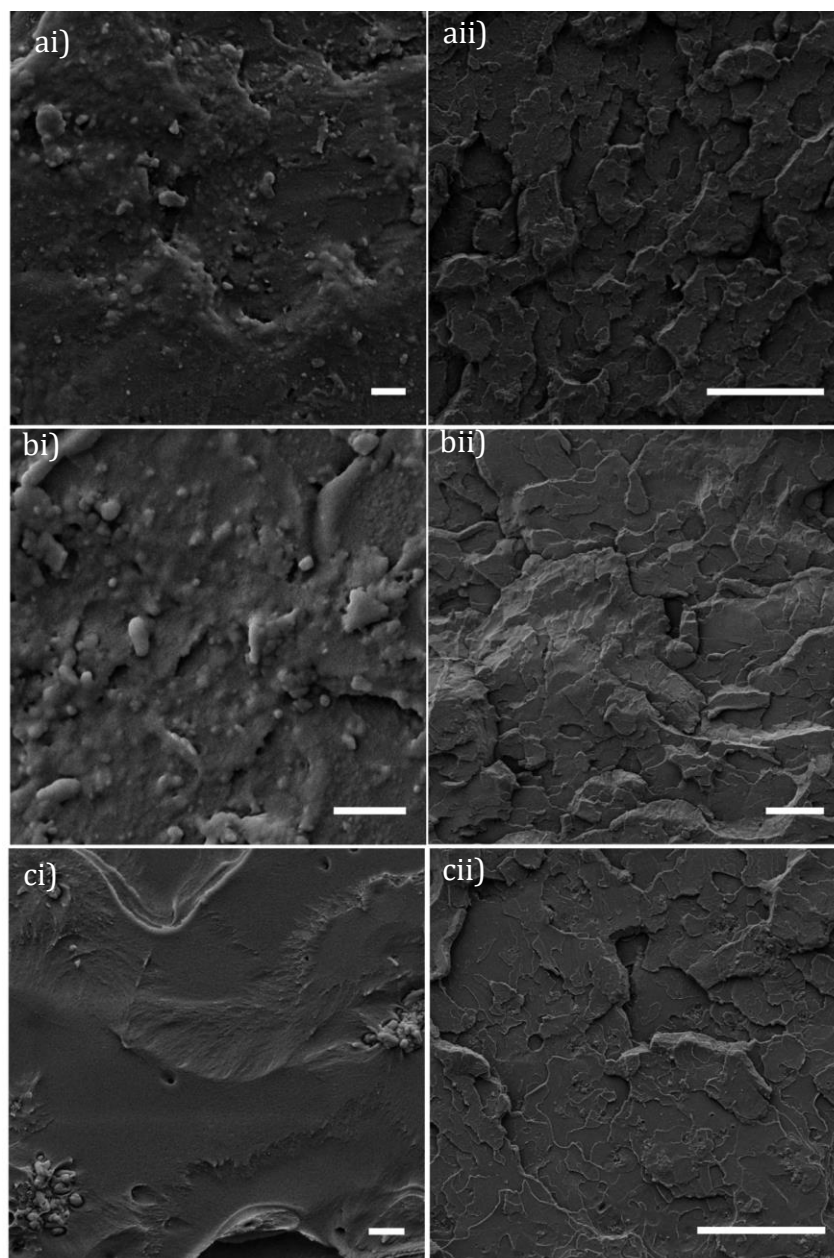


Figure 3-8. SEM images taken at the fracture points of a) PMMA/TBT 1 4.8 wt%, b) PMMA/TBT 1 2.2 wt%, and c) PMMA/TBT 1 1.6 wt% at i) high magnification and ii) low magnification. The smooth surface present in both ai and ci are indicative of pure PMMA systems with low dispersion of silica particles. Scale bars represent (i) 2 μm and (ii) 50 μm .

High magnification SEM images shown in **Figure 3-8** give great insight into the dispersion of the silica particles within the PMMA matrix at the point of breakage. No clear cracks or holes within the composite are present in the lower magnification images, indicating that there was no inherent fault within the polymeric matrix. It can be observed that both PMMA/TBT 1 4.8 wt% and PMMA/TBT 1 2.2 wt% exhibit good dispersion of the silica particles due to the low number of aggregates present. However, aggregates of the silica particles can be observed within **Figure 3-8 c** with a loading of 1.6 wt%. Due to the aggregation, the PMMA chains were unable to effectively penetrate between the particles and therefore the silica particle become less bound to the matrix. Had the particles been better dispersed within the composite, similar tensile properties for both PMMA/TBT 1 2.2 wt% and PMMA/TBT 1 1.6 wt% should have been obtained. Clear holes around the silica nanoparticles are suggestive of the lack of penetration of polymer chains within the silica particles. Therefore, the vol % of silica within the composite will be case (i) as stated earlier (12.8, 6.11, and 4.49 vol% respectively). It is therefore expected that the composites will show a greater ductility due to the ability of hollow particles to stop the propagation of cracks throughout a system.⁷⁰ This will be indicated by an increase in maximum strain.

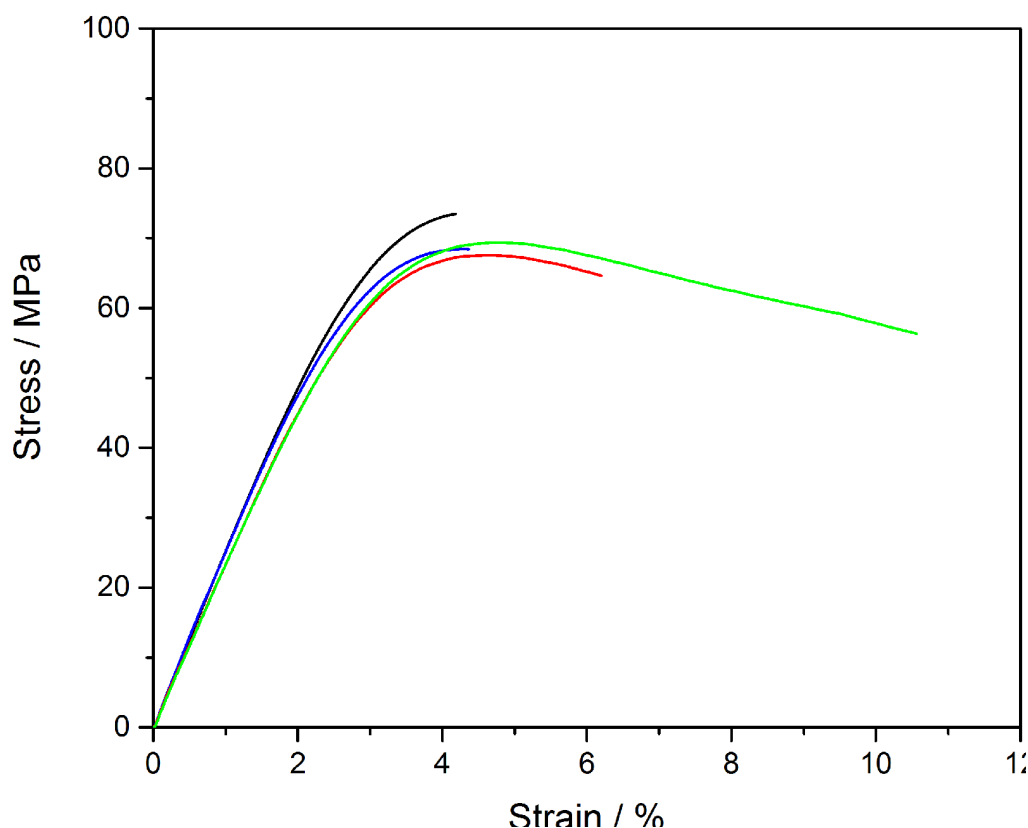


Figure 3-9 Stress – strain response curves of PMMA (—), PMMA/TBT 2 4.83 wt% (—), PMMA/TBT 2 2 wt% (—), and PMMA/TBT 2 0.9 wt% (—) averaged over 5 runs.

As observed in **Figure 3-9**, inclusion of TBT 2 within PMMA reduces the overall UTS of the system, whilst increasing the ductility (increased strain). Loadings of 4.85, 2.00, and 0.90 wt% of TBT 2 within the PMMA matrix leads to a similar UTS being obtained, whilst lower loadings exhibit an increased plastic behaviour. **Table 3-6** shows the pertinent data obtained from the tensile tests. As the samples were averaged over 5 runs, each exhibited a similar elongation without any outlying data.

Table 3-6. Tensile data of PMMA/TBT 2 composites averaged over 5 runs obtained from **Figure 3-9**. Errors are reported as 1 standard deviation from the mean.

Sample	UTS / MPa	Young's Modulus /MPa	Max Strain / %	Stress at breakage / MPa
PMMA	73.5 ± 1.9	2494 ± 10	4.19 ± 0.2	73.5
PMMA/TBT 2 4.83 wt%	68.5 ± 3	2460 ± 68	4.37 ± 0.4	68.5
PMMA/TBT 2 2 wt%	67.6 ± 1.2	2421 ± 10	6.20 ± 0.6	64.6
PMMA/TBT 2 0.9 wt%	69.4 ± 2	2296 ± 36	10.56 ± 1.5	56.3

The reduction in UTS observed in PMMA/TBT 2 systems is due to the reduced dispersion of the silica particles within the PMMA matrix (**Figure 3-10**). Agglomerates of silica particle leads to voids occurring within the matrix where PMMA cannot bind effectively, leading to a loss in tensile strength of the material. However, whilst a loss in tensile strength and Young's modulus occurs with decreasing loadings of particles, and increase in max strain can be observed. The particles increase the ductility of the material *via* suppression of craze formation within the composite material.⁷⁰ The silica particles present within the system act as fracture points within the matrix where propagation of cracks cannot continue due to the hollow nature of the silica particles. Lower loadings allow for better craze suppression as the particles are less likely to aggregate.

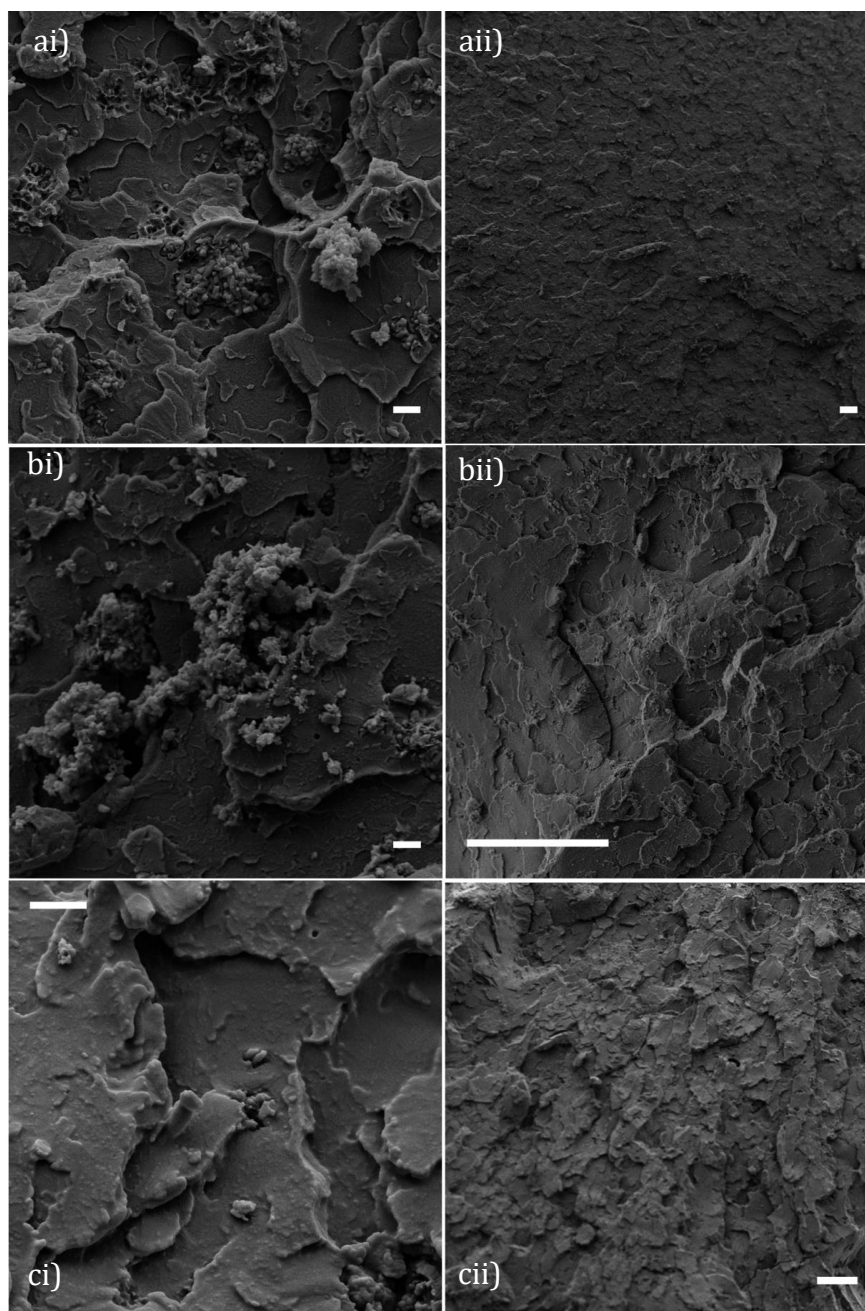


Figure 3-10. SEM images taken at the fracture points of a) PMMA/TBT 2 4.83 wt%, b) PMMA/TBT 2 2 wt%, and c) PMMA/TBT 2 0.9 wt% at i) high magnification and ii) low magnification. Scale bars represent (i) 2 μm and (ii) 50 μm .

The SEM images shown in **Figure 3-10** also show no clear cracks or holes. However, it is clear that bad dispersions are present in both the PMMA/TBT 2 4.83 wt% and PMMA/TBT 2 2 wt% composites. A greater dispersion of the particles can be observed in PMMA/TBT 2 0.9 wt% composite do to the reduction in large aggregates of silica particles being observed. However, similar to **Figure 3-8**, holes around the silica nanoparticles are again indicative of no penetration of the PMMA into the shells. Therefore the vol% of particles is 14.4, 6.32, and 2.92 vol% respectively.

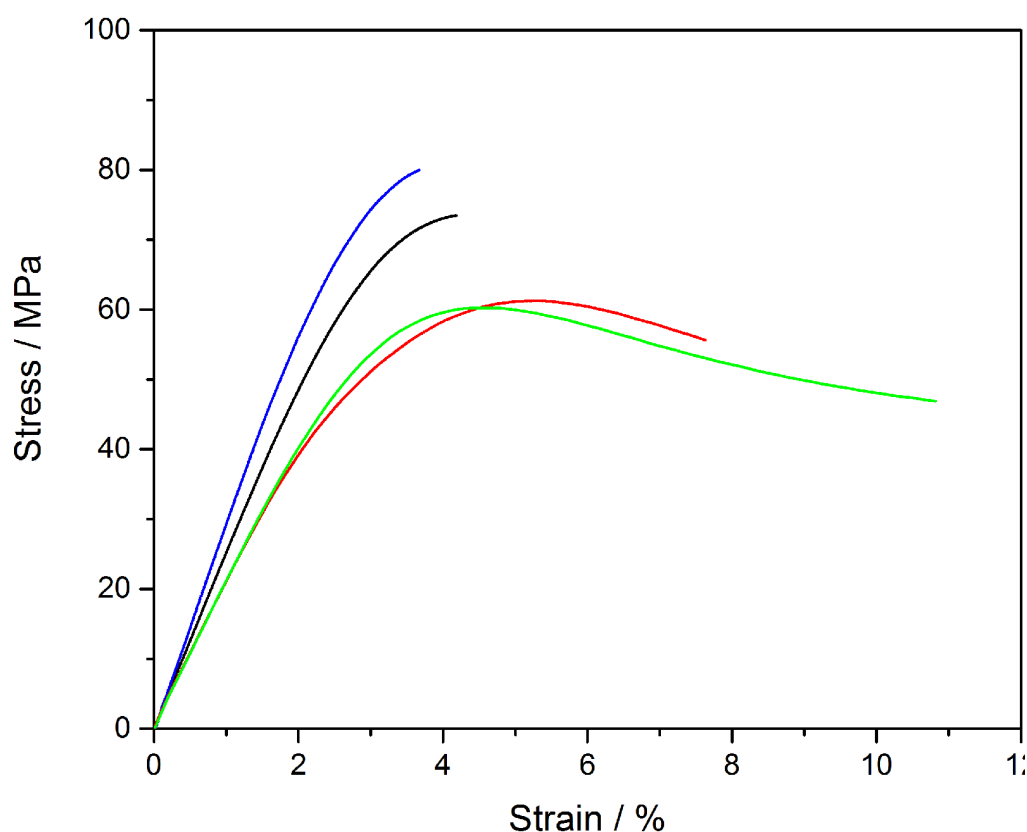


Figure 3-11. Stress – strain response curves of PMMA (—), PMMA/TBT 3 4.6 wt% (—), PMMA/TBT 3 2.2 wt% and PMMA/TBT 3 1.3 wt% (—) averaged over 5 runs.

PMMA/TBT 3 systems exhibit a similar response to that observed for PMMA/TBT 2 composites. However, extended elongation of the materials before breakage occurs can be obtained with TBT 3 systems. Loadings of 2.2 wt% TBT 3 into PMMA shows a max strain of 7.63 %, with an increase to 10.8 % with a loading of 1.3 wt%. In comparison, similar loadings in PMMA/TBT 2 2 wt% and PMMA/TBT 2 0.9 wt% only exhibit a maximum strain of 6.2 % and 10.6 % respectively.

Table 3-7. Tensile data of PMMA/TBT 3 composites averaged over 5 runs obtained from **Figure 3-11**. Errors are reported as 1 standard deviation from the mean.

Sample	UTS / MPa	Young's Modulus /MPa	Max Strain / %	Stress at breakage / MPa
PMMA	73.5 ± 1.9	2494 ± 10	4.19 ± 0.2	73.5
PMMA/TBT 3 4.6 wt%	80.0 ± 1.2	2995 ± 43	3.67 ± 0.4	80.0
PMMA/TBT 3 2.2 wt%	61.23 ± 0.5	2068 ± 69	7.63 ± 1	55.6
PMMA/TBT 3 1.3 wt%	60.22 ± 1.9	2101 ± 20.6	10.82 ± 1.2	46.9

Loadings of 4.6 wt% TBT 3 particles exhibit an increase in the tensile strength (80 MPa from 73 MPa of pure PMMA) of the composite with a reduced ductility (3.67 % elongation reduced from 4.2 % for pure PMMA) (**Table 3-7**). An increase of 20.1 % in the composites elastic modulus, equal to that of PMMA/TBT 1 – 1 can also be observed. Decreasing the loadings leads to a reduction in both UTS and Young's modulus with an increase in max strain. PMMA/TBT 3 – 2 and PMMA/TBT 3 – 3 exhibit similar ductility behaviour to that of PMMA/TBT 2 – 3 where lower loadings lead to an increase in max strain. It has been theorised that this is due to the better dispersions of TBT 3 (**Figure 3-12**) within the system, allow for a higher chance of cracks propagating through the system to interact with the hollow

particles. The more elastic nature eluded to in **Chapter 2** could also help with the increased elongation before break.

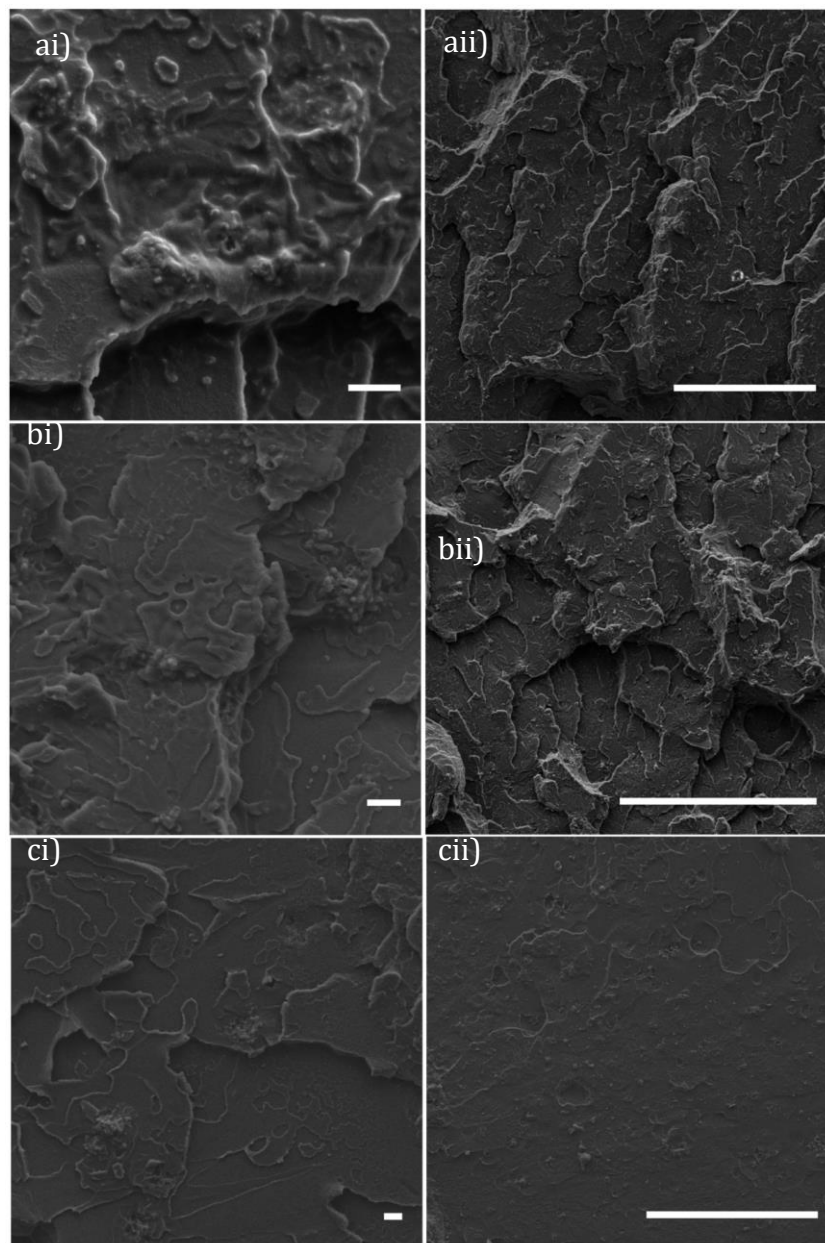


Figure 3-12. SEM images taken at the fracture points of a) PMMA/TBT 3 4.6 wt%, b) PMMA/TBT 3 2.2 wt%, and c) PMMA/TBT 3 1.3 wt% at i) high magnification and ii) low magnification. Scale bars represent (i) 2 μm and (ii) 50 μm .

No cracks within the polymer matrix can be observed in **Figure 3-12**. What is shown is a greater dispersion of silica shells can be observed for the composites containing TBT 3 silica nanoparticles (**Figure 3-12**). No large aggregates were observed during the imaging process, only small particles within the matrix. As all systems underwent the same processing conditions, the better dispersion of particles is suggestive of favourable interactions between the octyl chains present in the TBT 2 and TBT 3 systems

3.4 Conclusion

We have formulated a series of nanocomposites containing three different types of silica particles based on the particles synthesised in **Chapter 2**. Each composite showed an increase in thermal stability up to 20 °C for the burn onset and midpoint of the degradation. We have illustrated that the more hydrophobic particles are better dispersed within PMMA than the more hydrophilic counterpart. A reduction in tensile strength was observed with all samples bar the 4.8 wt% TBT 1 and 4.6 wt% TBT 3 samples. However, an increase in elongation and flexibility is shown with due to crack prevention within the matrix due to the hollow air voids.

3.5 Experimental

3.5.1 Materials

TBT 1, TBT 2, and TBT 3 silica shells were synthesised as state in **Chapter 2**. PMMA of grade IF 850 was kindly provided by the Warwick Manufacturing Group (WMG).

3.5.2 Equipment and Measurements

Cryomilling was undertaken using a SPEX Sample Prep Freezer Mill 6870. The milling chamber was filled with ~70 g of PMMA with a the large metal milling bar. Each sample was precooled in liquid N₂ for 4 minutes before undergoing 6 minutes of crushing at 15 CPS.

Compounding and extrusion of the PMMA/nanocomposites were made using a ThermoScientifife HAAKE MiniLab II compounder/extruder. Each sample was run at 210 °C to ensure full melting of the PMMA and a screw speed of 20 RPM. The residence time for the samples was three minutes from first insertion into the screw. Each sample was run through twice to allow additional time for penetration of the PMMA into the system. Following the compounding step, dog bones were injection moulded *via* the use of a ThermoScientific HAAKE MiniJet Pro into a ThermoScientific ASTM – D638 –V mould. The injection cylinder was heated to 220 °C and injected using a pressure of 650 Psi for 15 seconds into the mould held at 80 °C.

Tensile measurements were performed on a Shimadzu Autograph AGS-X using the maximum load cell of 10 kN. The measurements were run at 25 °C, at a rate of 1 mm / min⁻¹, with an average of five runs were made. The sample sizes were measured using a micrometer with average dimensions of 3 x 3 x 26 mm.

Thermogravimetric analysis (TGA) measurements of the nanocomposites were carried out in a 70 µL alumina pan on a Mettler Toledo DSC1-Star. Samples were dried in a vacuum oven at 60 °C for 3 days prior to measuring. Sample mass was kept around 20 mg and weighed out using a 5 d.p. balance. The temperature was ramped up to 1000 °C at a rate of 10 °C min⁻¹. All work within the TGA was done under a flow of N₂ at 50 mL min⁻¹.

3.6 References

- (1) Wu, C. L.; Zhang, M. Q.; Rong, M. Z.; Friedrich, K. *Compos. Sci. Technol.* **2002**, 62 (10–11), 1327–1340.
- (2) Park, J. H.; Jana, S. C. *Polymer (Guildf)*. **2003**, 44 (7), 2091–2100.
- (3) Mobarak, Y. A.; Bakry, M. *J. Eng. Sci.* **2011**, 39 (2), 377–403.
- (4) Vollenberg, P. H. T.; Heikens, D. *J. Mater. Sci.* **1990**, 25 (7), 3089–3095.
- (5) EU. *Large Volume Inorganic Chemicals -Solida and Others Industry*; 2007; Vol. BREF-LVI.
- (6) Bréchet, Y.; Cavaillé, J. Y. Y.; Chabert, E.; Chazeau, L.; Dendievel, R.; Flandin, L.; Gauthier, C. *Adv. Eng. Mater.* **2001**, 3 (8), 571–577.
- (7) Gersappe, D. *Phys. Rev. Lett.* **2002**, 89 (5), 58301.
- (8) Amir, S.; Almasi, H.; Ghanbarzadeh, B.; Akbar, A. *Carbohydr. Polym.* **2016**, 152, 253–262.
- (9) Li, W.; Li, H.; Zhang, Y. M. *J. Mater. Sci.* **2009**, 44 (11), 2977–2984.
- (10) Yang, M.; Dan, Y. *Colloid Polym. Sci.* **2005**, 284 (3), 243–250.
- (11) Royal Society of Chemistry [RSC]. *Composite Materials*; 2015.
- (12) Chao, P. hsiu G.; Sheng, S. C.; Chang, W. R. *J. Mech. Behav. Biomed. Mater.* **2014**, 38, 232–241.
- (13) Alexandre, M.; Dubois, P. *Mater. Sci. Eng. R Reports* **2000**, 28 (1–2), 1–63.
- (14) Ashkarran, A. A.; Hamidinezhad, H.; Haddadi, H.; Mahmoudi, M. *Appl. Surf. Sci.* **2014**, 301, 338–345.
- (15) Koşarsoy, G.; Şen, E. H.; Aksöz, N.; İde, S.; Aksoy, H. *Appl. Surf. Sci.* **2014**, 318, 269–274.
- (16) Park, J. J.; Yoon, K. G.; Lee, J. Y. *Trans. Electr. Electron. Mater.* **2011**, 12 (3), 98–101.
- (17) Petrovic, Z. S.; Javni, I.; Waddon, A.; Bonhegyi, G. *J. Appl. Polym. Sci.* **2000**, 76 (2), 133–151.
- (18) Lee, C. S.; Yoon, K. H.; Park, J. C.; Kim, H.; Park, Y. *Fibers Polym.* **2014**, 15 (7), 1493–1499.
- (19) Bouanani, F.; Bendedouch, D.; Hemery, P.; Bounaceur, B. *Colloids Surfaces A Physicochem. Eng. Asp.* **2008**, 317 (1–3), 751–755.
- (20) Hussain, F. *J. Compos. Mater.* **2006**, 40 (17), 1511–1575.
- (21) Wang, X.; Song, L.; Pornwannchai, W.; Hu, Y.; Kandola, B. *Compos. Part A*

Appl. Sci. Manuf. **2013**, 53, 88–96.

- (22) Yin, Z.; Chen, K.; Wang, H.; Wang, H.; Wei, Z. *J. Appl. Polym. Sci.* **2016**, 133 (39), 1–9.
- (23) Ji, X. L.; Jing, J. K.; Jiang, W.; Jiang, B. Z. *Polym. Eng. Sci.* **2002**, 42 (5), 983–993.
- (24) Ernawati, L.; Ogi, T.; Balgis, R.; Okuyama, K.; Stucki, M.; Hess, S. C.; Stark, W. J. *Langmuir* **2016**, 32 (1), 338–345.
- (25) Spitalsky, Z.; Tasis, D.; Papagelis, K.; Galiotis, C. *Prog. Polym. Sci.* **2010**, 35 (3), 357–401.
- (26) Kuilla, T.; Bhadra, S.; Yao, D.; Kim, N. H.; Bose, S.; Lee, J. H. *Prog. Polym. Sci. Vol.* **2010**, 35 (11), 1350–1375.
- (27) KRAUS, G. In *Science & Technology of Rubber*; Elsevier, 1978; pp 339–365.
- (28) Schaefer, D. W.; Rieker, T.; Agamalian, M.; Lin, J. S.; Fischer, D.; Sukumaran, S.; Chen, C.; Beaucage, G.; Herd, C.; Ivie, J. *J. Appl. Crystallogr.* **2000**, 33 (3 I), 587–591.
- (29) Hwang, J.; Muth, J.; Ghosh, T. *J. Appl. Polym. Sci.* **2007**, 104 (4), 2410–2417.
- (30) Knite, M.; Teteris, V.; Kiploka, A.; Kaupuzs, J. *Sensors Actuators, A Phys.* **2004**, 110 (1–3), 142–149.
- (31) Samorì, P.; Kinloch, I. A.; Feng, X.; Palermo, V. *2D Mater.* **2015**, 2 (3), 30205.
- (32) Lee, C.; Wei, X.; Kysar, J. W.; Hone, J. *Science (80-.)*. **2008**, 321 (5887), 385–388.
- (33) Ovid'ko, I. A. *Rev. Adv. Mater. Sci.* **2013**, 34 (1), 19–25.
- (34) Gao, Y.; Müller-Plathe, F. *J. Phys. Chem. B* **2016**, 120 (7), 1336–1346.
- (35) Khanam, P. N.; Ponnamm, D.; AL-Madeed, M. A. In *Graphene-Based Polymer Nanocomposites in Electronics*; Sadasivuni, K. K., Ponnamm, D., Kim, J., Thomas, S., Eds.; Springer International Publishing: Cham, 2015; pp 25–47.
- (36) Atif, R.; Shyha, I.; Inam, F. *Polymers (Basel)*. **2016**, 8 (12), 281.
- (37) Yang, Y.; Rigdon, W.; Huang, X.; Li, X. *Sci. Rep.* **2013**, 3, 2086.
- (38) Hsu, C. H.; Hsu, M. H.; Chang, K. C.; Lai, M. C.; Liu, P. J.; Chuang, T. L.; Yeh, J. M.; Liu, W. R. *Polym. Int.* **2014**, 63 (10), 1765–1770.
- (39) Ghaleb, Z. A.; Mariatti, M.; Ariff, Z. M. *Compos. Part A Appl. Sci. Manuf.* **2014**, 58, 77–83.

- (40) Tripathi, S. N.; Saini, P.; Gupta, D.; Choudhary, V. *J. Mater. Sci.* **2013**, *48* (18), 6223–6232.
- (41) Iijima, S. *Nature* **1991**, *354* (6348), 56–58.
- (42) Bower, C.; Rosen, R.; Jin, L.; Han, J.; Zhou, O. *Appl. Phys. Lett.* **1999**, *74* (22), 3317–3319.
- (43) Jin, Z.; Pramoda, K. P.; Xu, G.; Goh, S. H. *Chem. Phys. Lett.* **2001**, *337* (1–3), 43–47.
- (44) Lozano, K.; Barrera, E. V. *J. Appl. Polym. Sci.* **2001**, *79* (1), 125–133.
- (45) Plummer, C. J. G.; Garamszegi, L.; Leterrier, Y.; Rodlert, M.; Månson, J.-A. E. *Chem. Mater.* **2002**, *14* (2), 486–488.
- (46) Xia, H.; Wang, Q.; Qiu, G. *Chem. Mater.* **2003**, *15* (20), 3879–3886.
- (47) Jose, M. V.; Steinert, B. W.; Thomas, V.; Dean, D. R.; Abdalla, M. A.; Price, G.; Janowski, G. M. *Polymer (Guildf)*. **2007**, *48* (4), 1096–1104.
- (48) Arash, B.; Wang, Q.; Varadan, V. K. *Sci. Rep.* **2014**, *4*, 6479.
- (49) Zare, Y. *Synth. Met.* **2015**, *202*, 68–72.
- (50) Thostenson, E. T.; Chou, T.-W. *J. Phys. D: Appl. Phys.* **2003**, *36* (5), 573–582.
- (51) Thostenson, E. T.; Chou, T. *J. Phys. D: Appl. Phys.* **2002**, *35* (16), L77–L80.
- (52) Park, J. *J. Compos. Mater.* **2010**, *45* (8), 931–941.
- (53) Wang, Q.; Dai, J.; Li, W.; Wei, Z.; Jiang, J. *Compos. Sci. Technol.* **2008**, *68* (7–8), 1644–1648.
- (54) Khan, S. U.; Pothnis, J. R.; Kim, J.-K. *Compos. Part A Appl. Sci. Manuf.* **2013**, *49*, 26–34.
- (55) García, E. J.; Hart, A. J.; Wardle, B. L.; Slocum, A. H. *Adv. Mater.* **2007**, *19* (16), 2151–2156.
- (56) Pandey, G.; Thostenson, E. T. *Polym. Rev.* **2012**, *52* (3–4), 355–416.
- (57) Arif, S.; Alam, M. A.; Arif, M. R.; Ansari, A. *Int. J. Sci. Res. Publ.* **2015**, *5* (7), 0–6.
- (58) Khaled, S. M.; Sui, R.; Charpentier, P. A.; Rizkalla, A. S. *Langmuir* **2007**, *23* (7), 3988–3995.
- (59) Ribeiro, L. A.; Ito, E. N.; Senador, A.; Filho, S.; Filho, C. S.; Filho, S. *Mater. Res.* **2014**, *17* (4), 926–932.
- (60) Fu, G.; Vary, P. S.; Lin, C.-T. *J. Phys. Chem. B* **2005**, *109* (18), 8889–8898.
- (61) Xie, X.-L.; Liu, Q.-X.; Li, R. K.-Y.; Zhou, X.-P.; Zhang, Q.-X.; Yu, Z.-Z.; Mai, Y.-W. *Polymer (Guildf)*. **2004**, *45* (19), 6665–6673.

- (62) Baskaran, R.; Sarojadevi, M.; Vijayakumar, C. T. *J. Reinf. Plast. Compos.* **2011**, *30* (18), 1549–1556.
- (63) Chen, B.; Evans, J. R. G.; Greenwell, H. C.; Boulet, P.; Coveney, P. V.; Bowden, A. A.; Whiting, A. *Chem. Soc. Rev.* **2008**, *37* (3), 568–594.
- (64) Conradi, M. *Mater. Tehnol.* **2013**, *47* (3), 285–293.
- (65) Ji, X.; Hampsey, J. E.; Hu, Q.; He, J.; Yang, Z.; Lu, Y. *Chem. Mater.* **2003**, *15* (19), 3656–3662.
- (66) Khankrua, R.; Pivsa-Art, S.; Hiroyuki, H.; Suttiruengwong, S. *Energy Procedia* **2013**, *34* (3), 705–713.
- (67) Zhang, F.-A.; Lee, D.-K.; Pinnavaia, T. J. *Polym. Chem.* **2010**, *1*, 107.
- (68) Hsu, C. C.; Chang, K. C.; Huang, T. C.; Yeh, L. C.; Yeh, W. T.; Ji, W. F.; Yeh, J. M.; Tsai, T. Y. *Microporous Mesoporous Mater.* **2014**, *198*, 15–21.
- (69) Zhang, W.; Zhang, B.; He, G.; Liu, B.; Jiang, Z.; Yang, X.; Li, C. *RSC Adv.* **2015**, *5* (7), 5343–5356.
- (70) Ash, B. J.; Stone, J.; Rogers, D. F.; Schadler, L. S.; Siegel, R. W.; Benicewicz, B. C.; Apple, T. *MRS Proc.* **2000**, 661.
- (71) Plastics, P. Tradenames of Plastic Materials <http://www.professionalplastics.com/TRADENAMELIST> (accessed Sep 25, 2016).
- (72) Carraher Jr., C. E. *Introduction to Polymer Chemistry, Third Edition*; 2012.
- (73) Peters, E. N. *Handb. Mater. Sel.* **2007**, 335–355.
- (74) Ye, J.; Schoenung, J. M. *Adv. Eng. Mater.* **2004**, *6* (8), 656–664.
- (75) Loh, Z. H.; Samanta, A. K.; Sia Heng, P. W. *Asian J. Pharm. Sci.* **2014**, *10* (4), 255–274.
- (76) Caruso, M. M.; Davis, D. A.; Shen, Q.; Odom, S. A.; Sottos, N. R.; White, S. R.; Moore, J. S. *Chem. Rev.* **2009**, *109* (11), 5755–5798.
- (77) Wang, W. S.; Liang, C. K.; Chen, Y. C.; Su, Y. L.; Tsai, T. Y.; Chen-Yang, Y. W. *Polym. Adv. Technol.* **2012**, *23* (3), 625–631.
- (78) Retsch, M.; Schmelzeisen, M.; Butt, H.-J.; Thomas, E. L. *Nano Lett.* **2011**, *11* (3), 1389–1394.

4 Chapter 4: Tagging Poly(styrene) with Fluorescent Dyes

4.1 Abstract

In **Chapter 1**, a new method was developed for determination of the phase transition temperature of oils solutions along with indicating that polymerisation of additional monomers change the UCST point. Herein, we demonstrate the effect of tagging poly(styrene) chains with methacrylate modified fluorescent dyes under both visible and ultraviolet illumination.

4.2 Introduction

Forster and Kasper first discovered that increasing the concentration of pyrene within a solution of toluene weakened the fluorescence.¹ Since this first discovery, it has been found to be a common trait among many aromatic compounds.^{2,3} Self-quenching occurs due to collisional quenching between molecules (**Figure 4-1**).⁴ Collisional quenching is when excited fluorophores come into contact with atoms or molecules that can mediate non-radiative transitions to the ground state, in this case another unexcited dye molecule.

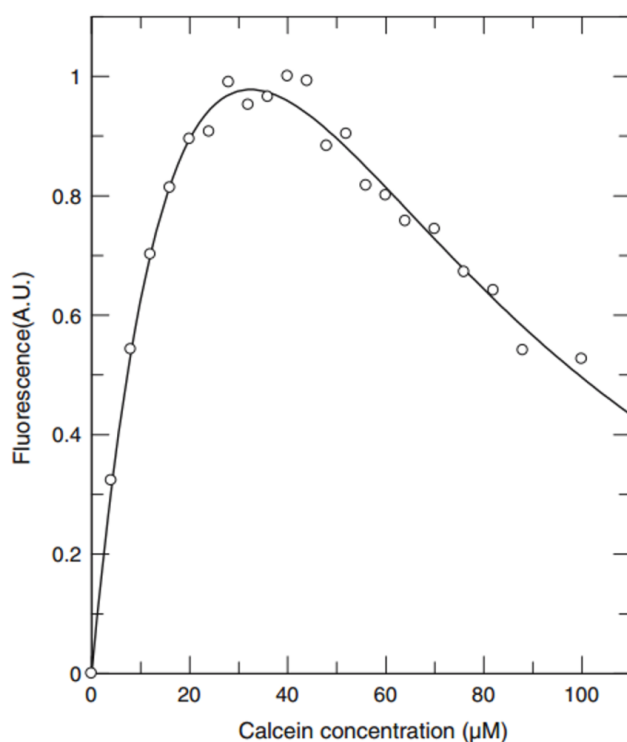


Figure 4-1. Fluorescence intensity of calcein as function of the concentration of calcein present.⁴

Andersson *et al.* clearly show that increasing the concentration of calcein above 40 μM within water leads to a loss in fluorescence (**Figure 4-1**).⁴ This loss of fluorescence leads to the utilisation of dilute solutions to reduce the self-quenching interactions. However, further issues are caused as the strength of an emission is inherently linked to the concentration of dye within a system and self-quenching can still occur. Therefore, a dye in powdered form or held within polymers will often exhibit little to no emission due to the close proximity of molecules in which non-radiative pathways can be formed.^{5,6}

In recent years, large amounts of research have been focused on the synthesis of dyes that exhibit an increase in emission upon concentration increases. Due to the nature in which aggregates of these dyes form emissive materials, they have been named aggregation induced emissive (AIE) dyes.^{7,8} AIE dyes have the direct opposite effect to the conventional dyes systems explained above (**Figure 4-2**).

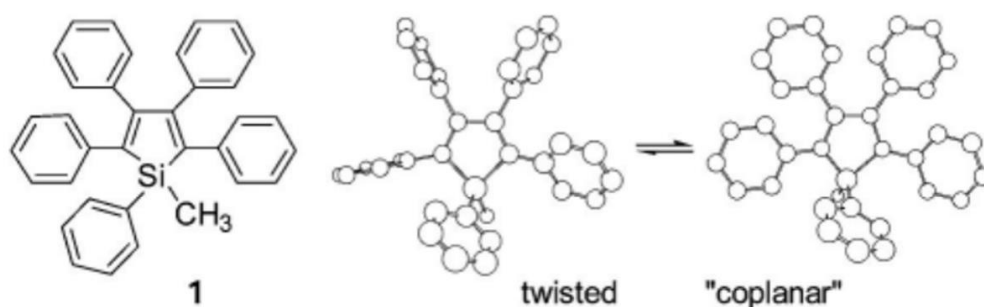


Figure 4-2. Silole based AIE dye (1,2,3,4,5-pentaphenylsilole).⁹ Reducing the free rotation of the aromatic pendant groups leads to emission.

Tang and co-workers first reported the discovery of the luminogen 1,2,3,4,5-pentaphenylsilole, where the increase in concentration led to a constructive interaction instead of destructive.^{8,9} Upon restriction of the free movement of the aromatic pendant groups, the molecule moves from the twisted state to the coplanar state.^{9,10} Once in the coplanar state, large conjugation over the whole system can occur, leading to fluorescence. Since the initial discovery of AIE based on the silole structure, additional molecules such as triphenylethene,¹¹⁻¹³ cyano-substituted diarylethene,^{14,15} distyrylanthracene,¹⁶⁻¹⁸ and 1,1,2,2-tetraphenyl ethylene (TPE)¹⁹⁻²¹ derivatives have been used as AIE dyes.²²

Wang and co-workers synthesised a series of TPE molecules with differing length PEG chains attached.²⁰ Due to temperature dependant water solvation of the PEG groups, this led to the molecule becoming thermosensitive. Once dissolved in water, the polymer phase separated (LCST-like) upon heating above the phase change point of each polymer. It was found that increasing the chain length from 3 to 5 repeat units of PEG led to an increase in phase change temperature at all concentrations. Along with the phase separation of the polymer in solution, a change in the emission from the AIE dye was observed (**Figure 4-3**).

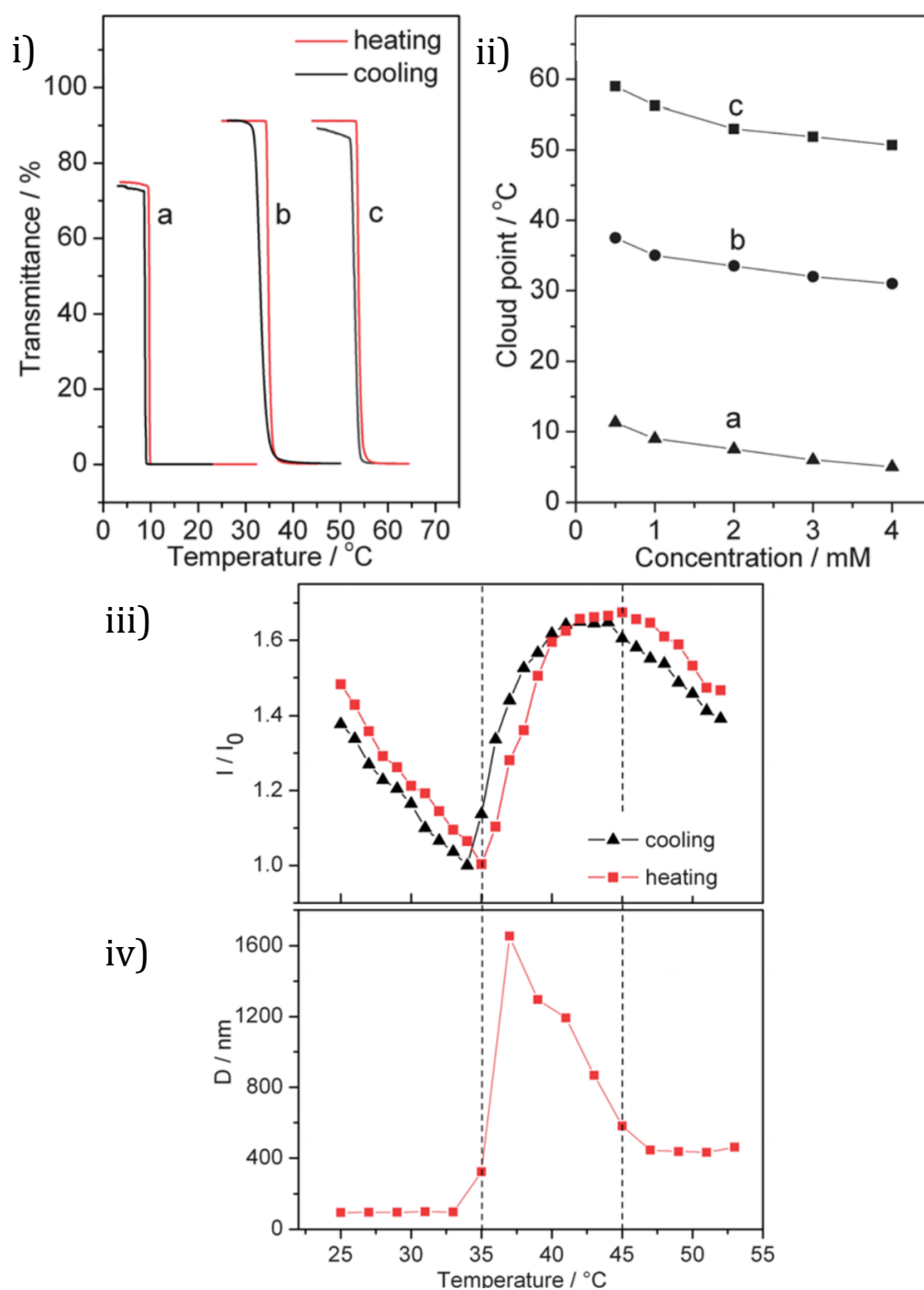


Figure 4-3. i) phase change curve of TPE with a) 3 PEO units, b) 4 PEO units, and c) 5 PEO units with ii) corresponding changes in cloud points based on concentration, iii) emission intensity of TPE with 4 PEO units dependant on temperature, and iv) particle size dependent on temperature.²⁰

Upon the point the phase change occurred, a large decrease in the emission intensity occurred (**Figure 4-3**). Upon further heating, the polymer passes further through phase change point and aggregates of TPE are formed within the particle formed. Therefore a stronger emission can be observed upon phase transition with an increase in overall emission observed in solutions with higher concentrations of the polymer.

In **Chapter 1**, we discussed the effect of copolymerisation of styrene with additional monomers to alter the phase transition temperature within dioctyl phthalate (DOP). It was also shown that addition of dyes into the system lead to colour phase changes being observed upon phase separation. In this chapter we will focus on tagging polystyrene (PS) chains with two different fluorescent dyes: hostalsol methacrylate and tetraphenyl ethylene methacrylate (TPEMA). Hostasol based dyes are known to be conventional dyes, resulting in aggregation induced quenching. However, TPE based dyes are known to be part of the aggregation induced emissive dyes.

4.3 Results and Discussion

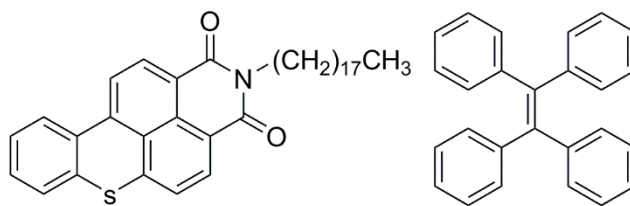


Figure 4-4. Chemical structure of (left) Hostasol, and (right) 1,1,2,2-tetraphenyl ethylene (TPE).

Yang *et al.* have shown the increased emission upon phase transition of TPMA tagged copolymers due to the restriction of the phenyl groups upon phase separation.²³ Due to the commercial availability of TPE, initial test were undertaken by dissolving TPE within 10 wt% PS in DOP solutions. However, attempts to dissolve the dye within the both DOP and DOP containing PS led to fine dispersion of the dye powder without dissolving. Therefore, both systems exhibited an emissive response at all temperatures under UV illumination.

4.3.1 Polymer Synthesis

Typical copolymerisation of styrene with the different dyes were undertaken under the same conditions as used in **Chapter 1**. Both styrene and monomeric dye were charged into a crimp top vial and degassed for 15 minutes. Following the degassing step, the vials were transferred into

140 °C oil bath for 1 hour before termination by injection of 10 mL of air and submerging within ice water.

Table 4-1. Tabulated data for dye tagged polystyrene samples.

Polymer	$M_w / \text{kg}\cdot\text{mol}^{-1}$	\bar{D}	TPEMA Feed / mol%
PSHost	396	1.94	0.1
PSTPEMA 1	275	2.38	0.1
PSTPEMA 2	354	2.70	1
PSTPEMA 3	348	2.16	0.3

Following the synthesis of PS tagged with fluorescent dyes, each polymer was dissolved at 10 wt% in DOP overnight to obtain a homogeneous solution. Therefore, attachment of TPEMA to a PS chain increases the solubility of the dye to allow dissolving within DOP system. Initial tests to determine whether phase change of the systems would indicate a change in emission were undertaken. Each sample was cooled to $-20\text{ }^{\circ}\text{C}$ and illuminated using a UV lamp then warmed to $30\text{ }^{\circ}\text{C}$ with images taken at each temperature. The resulting images are shown in **Figure 4-5**.

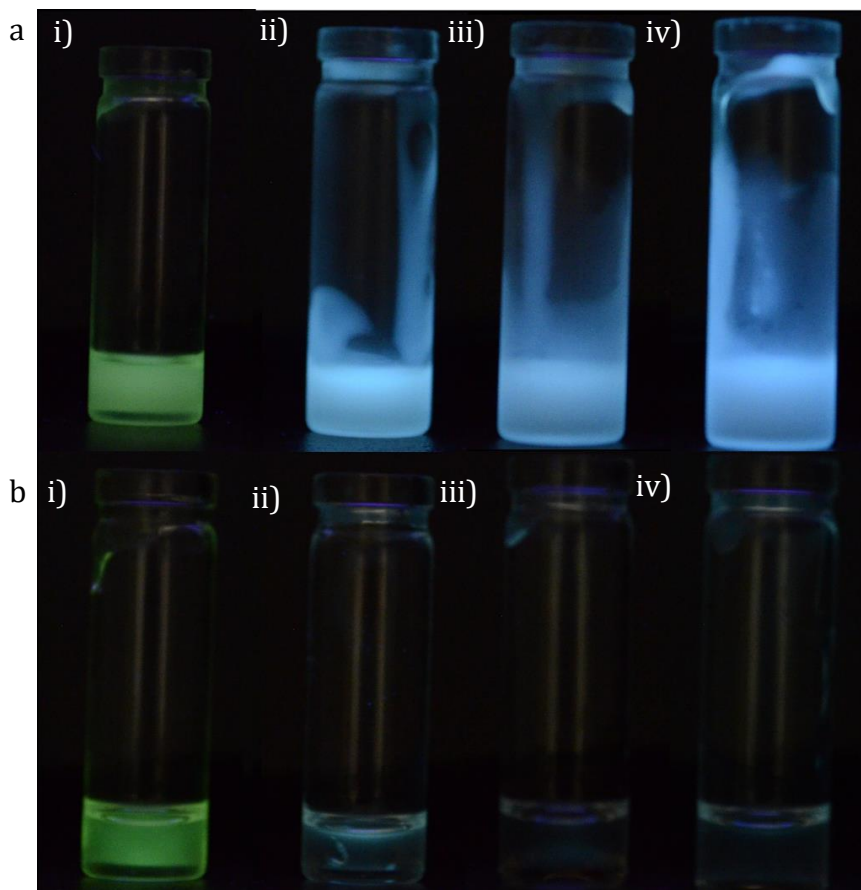


Figure 4-5. Images of DOP solutions containing i)PSHost, ii)PSTPEMA 1, iii)PSTPEMA 2, and iv)PSTPEMA 3 under UV illumination at a) – 20 °C and b) 30 °C.

It can be observed that the polymer containing Hostalsol (PSHost) exhibit little to no optical difference under UV illumination above and below the phase transition (**Figure 4-5**). However, systems containing the TPE moiety (PSTPEMA 1 – 3) all show an increase in optical emission in the cooled form. The strong emission is lost upon heating the sample to above the phase transition. In all situation below 30 °C, some emission from the PSTPEMA samples show some emission. This is due to the high viscosity of the solutions

leading to a reduction in the free movement of the TPE moieties within the solution.

4.3.2 Phase Change Response

As the PSTPEMA samples all indicated a change in emission dependant on temperature, the phase change response of each system was measured using the photographic technique described in **Chapter 1**. An initial test using visible light was used to determine at what point the phase transition of the solutions containing 10 wt% polymer occurred (**Figure 4-6**).

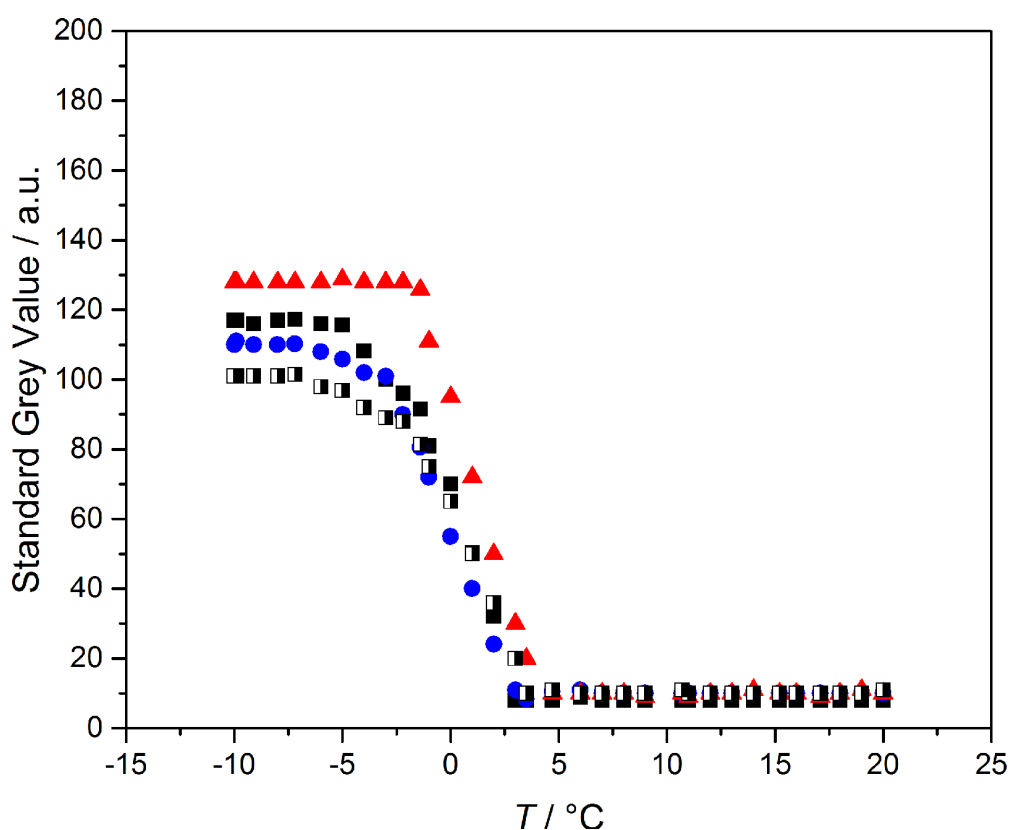


Figure 4-6. Phase change curves of PSHost (■), PSTPE 1 (●), PSTPE 2 (▲), and PSTPE 3 (□) under visible light illumination.

Figure 4-6 shows the phase transitions of each of the polymer systems in DOP when taken under visible light. The T_{onset} values for PSHost, PSTPEMA 1, PSTPEMA 2, and PSTPEMA 3 are 2.8 °C, 2.3 °C, 3.4 °C, and 2.6 °C respectively. TPE has previously been shown to be insoluble within a PS in DOP previously, therefore it is expected that the polymers containing higher content of TPEMA molecules (PSTPEMA 2) would indicated a higher temperature for phase onset. However, little overall effect can be observed with the incorporation of the different dye units and different amounts of dye within the systems. It should be noted that all systems show no visible change until the onset temperature is reached due to the black background each sample is placed upon. After cooling below – 5 °C for each sample, an opaque mixture is formed. The PSHost sample exhibited a green colour attributed to the dye whilst the PSTPEMA series showed no change in colour.

It is clear from **Figure 4-6** that the inclusion of the different dye molecule has little effect on the phase transition temperatures when recorded under visible light. However, it is theorised that due to the increase in viscosity near the phase transition points in a solution,²⁴ the temperature at which the solutions containing the AIE moieties will occur higher (**Figure 4-7**).

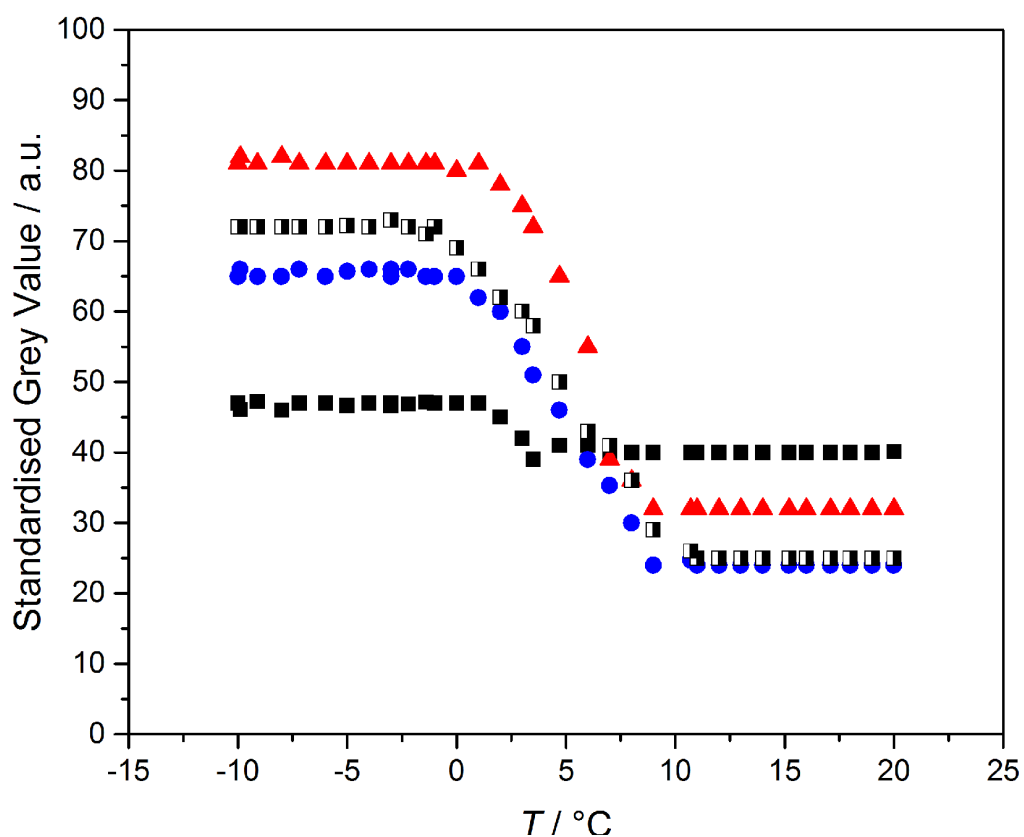


Figure 4-7. Phase change curves of PSHost (■), PSTPE 1 (●), PSTPE 2 (▲), and PSTPE 3 (□) under ultra violet light illumination.

It is clearly shown in **Figure 4-7** that the systems containing TPMEA exhibit a clear emission at a higher temperature than the phase transition occurs under visible light. The T_{onset} for PSHost, PSTPEMA 1, PSTPEMA 2, and PSTPEMA 3 under UV illumination are determined to be 3.2 °C, 8.5 °C, 8.7 °C, and 8.7 °C. The values obtained for PSHost with both visible and UV light are close enough that no overall difference in illumination can be seen (2.8 °C in visible, 3.2 °C in UV). The PSHost sample also shows very little change in grey value between the initial and end values (7 in total) when under UV

illumination. The small difference between both initial and end value for PSHost is due to the emission of the dye being present at all temperatures. The changes observed within the TPEMA systems are 42, 50, and 47 (PSTPEMA 1 – 3 respectively). As expected, a larger change is observed within the systems containing more TPEMA units. However, all three PSTPEMA systems exhibit a $T_{onset} \sim 5\text{ }^{\circ}\text{C}$ higher than observed under visible light. Due to the aggregation of TPE moieties causing emission, reducing the free movement of the dye *via* increases in viscosity has also shown to be a possible cause for emission.²⁵ As no visible changes in the solution can be made using visible light above $5\text{ }^{\circ}\text{C}$ (**Figure 4-6**), this is an indicator that the solutions viscosity has increased.

4.4 Conclusion

In conclusion, we have shown that a conventional emissive dye attached to a phase changing polymer in solution shows little difference under UV illumination both above and below the phase change temperature of the system. However, inclusion of AIE dyes into the polymeric chain allows a noticeable increase in emission. These systems also allow for a dual temperature indicator within a single system. Both standard optical phase changes can be observed with the transition to heterogeneous whilst the emission of the dyes can be observed at a higher temperature due to the increase in viscosity of the solutions.

4.5 Experimental

4.5.1 Materials

1,1,2,2-tetraphenyl ethylene (TPE), dioctyl phthalate (DOP), poly(styrene) (PS), Hi-Dry THF, Zinc powder, methacryloyl chloride, diphenyl ketone, 4-hydroxy diphenyl ketone, and styrene were all purchased from Sigma Aldrich. Hostasol methacrylate was kindly provided to our group by the Haddleton research group following synthesis previously reported.²⁶

4.5.2 General Characterisation Techniques

SEC, NMR, and the photographic technique used to determine the phase change are the same as reported in **Chapter 1**.

4.5.3 Synthesis of TPE-MA

TPE-OH was synthesised following previous reports.²⁷ Zinc powder (3.2g, 48 mmol) was charged into a three-necked flask along with 40 mL dry THF. The mixture was cooled to between -5 to 0 °C with ice water, and TiCl₄ (2.6 mL, 24 mmol) was slowly added with the temperature kept under 10 °C. Once added, the solution was left at ambient conditions for 30 mins, followed by heating at reflux for 3 hours. The mixture was again cooled to between -5 to 0 °C, charged with pyridine (1 mL, 12 mmol) and stirred for 10 min. The solution of diphenyl ketone and 4-hydroxy diphenyl ketone (1:1.2 mole ratio, 48 mmol) in 30 mL THF was added slowly and left refluxing overnight. The reaction was quenched with 10% K₂CO₃ aqueous solution and taken up with

CH₂Cl₂. The organic layer was collected. The crude product was purified on a silica gel column using ethyl acetate/petroleum ether (1:10 v/v) as eluent to give a white powder that fluorescence's under UV light with a yield of 34 % (2.60g). ¹H NMR (400 MHz, CDCl₃): δ (ppm) 4.82 (s, 1H), 6.56 (d, 2H), 6.90 (d, 2H), 6.98-7.16 (m, 15H). GC(+)MS calculated for C₂₆H₂₀O: 348.44; found 349.4.

TPE-OH (0.5 g, 1.64 mmol) was then charged into a round bottom flask with dried triethylamine (0.2 g, 1.8 mmol) and 50 mL DCM. A DCM solution containing methacryloyl chloride (0.18 g, 1.7 mmol in 20 mL DCM) was added dropwise. The reaction was quenched with water and extracted using DCM and purified *via* column chromatography using ethyl acetate:hexane 1:9 v/v to give a cream powder that fluorescence's under UV light with a yield of 44 % (0.301 g). ¹H NMR (400 MHz, CDCl₃): δ (ppm) 1.9 (s, 3H), 5.64 (d, 1H), 6.22 (d, 1H), 6.87 (d, 2H), 7-7.2 (m, 15H). GC(+)MS calculated for C₃₀H₂₄O₂: 416.51; found 418.01.

4.5.4 Hostasol Methacrylate Synthesis

Hostasol methacrylate was not synthesised in this work but synthesised previously by a member of the Haddleton group and gifted to our research group. However the synthesis route has been reported and is as follows.²⁶ 2-(8-Hydroxy-3,6-dioxaoctyl)thioxantheno[2,1,9-dej]isoquinoline-1,3-dione (10 g, 32.86 mmol) was dispersed in dry DMF under N₂. *p*-toluenesulfonic acid monohydrate (*p*TSA) (0.375g, 1.971 mmol) and 5-aminopentanol (20.34 g, 197.15 mmol) were added then heated to 130 °C. after 3 hours, additional

*p*TSA (0.375 g, 1.97 mmol) and 5-aminopentanol (1g, 9.69 mmol) were added. After 6.5 hours, the reaction mixture was cooled to 50 °C and methanol (30 mL) added. An orange powder was obtained *via* vacuum filtration. The orange powder (2g, 5.14 mmol) was added to anhydrous CHCl₃ (80 mL) along with trimethylamine (3.6 mL, 26.09 mmol) and the mixture cooled to 0 °C. Methacryloyl chloride (2.4 mL, 25.01 mmol) in dry CHCl₃ (20 mL) was dropwise added over 1 hour and the mixture left overnight. Excess methanol (10 mL) was then added to react with any unreacted methacryloyl chloride and stirred for a further hour. The mixture was washed with a brine solution, saturated NaHCO₃ solution, saturated NaCl solution and dried over MgSO₄. The solid was then purified by silica chromatography (toluene-ethyl acetate 5:1 (v:v) to give an orange solid monomer.

4.5.5 Polymer Synthesis

Styrene and co-monomers were sealed in a 20 mL crimp top vial (HostMA 0.1wt%, PSTPEMA 1 0.1 wt%, PSTPEMA 2 1 wt%, and PSTPEMA 3 0.3 wt%) and degassed for 15 minutes. Initiation was induced by submerging the vials into a 140 °C oil bath. After 1 hour, the reaction mixtures were removed from the oil bath, placed into ice water, and injected with 10 mL of air before the seal was removed. The resulting solution was diluted into 40 mL of THF before precipitating into ice cold methanol. The polymer was then dried in a vacuum oven before characterisation.

4.6 References

- (1) Förster, T.; Kasper, K. *Zeitschrift für Phys. Chemie* **1954**, *1* (5_6), 275–277.
- (2) Ma, X.; Sun, R.; Cheng, J.; Liu, J.; Gou, F.; Xiang, H.; Zhou, X. *J. Chem. Educ.* **2016**, *93* (2), 345–350.
- (3) Christophorou, L. G.; Abu-Zeid, M. M.; Carter, J. G. *J. Chem. Phys.* **1968**, *49* (9), 3775–3782.
- (4) Andersson, A.; Danielsson, J.; Gräslund, A.; Mäler, L. *Eur. Biophys. J.* **2007**, *36* (6), 621–635.
- (5) Belletête, M.; Bouchard, J.; Leclerc, M.; Durocher, G. *Macromolecules* **2005**, *38* (3), 880–887.
- (6) Thomas, S. W.; Joly, G. D.; Swager, T. M. *Chem. Rev.* **2007**, *107* (4), 1339–1386.
- (7) Lam, J. W. Y.; Tang, B. Z. *J. Polym. Sci. Part A Polym. Chem.* **2003**, *41* (17), 2607–2629.
- (8) Tang, B. Z.; Zhan, X.; Yu, G.; Sze Lee, P. P.; Liu, Y.; Zhu, D. *J. Mater. Chem.* **2001**, *11* (12), 2974–2978.
- (9) Luo, J.; Xie, Z.; Lam, J. W. Y.; Cheng, L.; Tang, B. Z.; Chen, H.; Qiu, C.; Kwok, H. S.; Zhan, X.; Liu, Y.; Zhu, D. *Chem. Commun.* **2001**, *381* (18), 1740–1741.
- (10) Levitus, M.; Schmieder, K.; Ricks, H.; Shimizu, K. D.; Bunz, U. H. F.; Garcia-Garibay, M. A. *J. Am. Chem. Soc.* **2001**, *123* (18), 4259–4265.
- (11) Shi, H.; Xin, D.; Gu, X.; Zhang, P.; Peng, H. *J. Mater. Chem. C* **2016**, *4*, 1228–1237.
- (12) Qin, W.; Yang, Z.; Jiang, Y.; Lam, J. W. Y.; Liang, G.; Kwok, H. S.; Tang, B. Z. *Chem. Mater.* **2015**, *27* (11), 3892–3901.
- (13) Li, H.; Chi, Z.; Xu, B.; Zhang, X.; Li, X.; Liu, S.; Zhang, Y.; Xu, J. *J. Mater. Chem.* **2011**, *21* (11), 3760.
- (14) Gawel, P.; Dengiz, C.; Finke, A. D.; Trapp, N.; Boudon, C.; Gisselbrecht, J. P.; Diederich, F. *Angew. Chemie - Int. Ed.* **2014**, *53* (17), 4341–4345.
- (15) Yan, Z. Q.; Yang, Z. Y.; Wang, H.; Li, A. W.; Wang, L. P.; Yang, H.; Gao, B. R. *Spectrochim. Acta - Part A Mol. Biomol. Spectrosc.* **2011**, *78* (5), 1640–1645.
- (16) Lee, S. K.; Yang, W. J.; Choi, J. J.; Kim, C. H.; Jeon, S. J.; Cho, B. R. *Org. Lett.* **2005**, *7* (2), 323–326.
- (17) Sun, B.; Yang, X.; Ma, L.; Niu, C.; Wang, F.; Na, N.; Wen, J.; Ouyang, J.

Langmuir **2013**, 29 (6), 1956–1962.

- (18) Duraimurugan, K.; Sivamani, J.; Sathiyaraj, M. *J. Fluoresc.* **2016**, 1211–1218.
- (19) Ma, H.; Qi, C.; Cheng, C.; Yang, Z.; Cao, H.; Yang, Z.; Tong, J.; Yao, X.; Lei, Z. *ACS Appl. Mater. Interfaces* **2016**, 8 (13), 8341–8348.
- (20) Yin, X.; Meng, F.; Wang, L. *J. Mater. Chem. C* **2013**, 1 (41), 6767.
- (21) Jiang, G.; Liu, X.; Wu, Y.; Wang, J.; Dong, X.; Zhang, G.; Li, Y.; Fan, X. *RSC Adv.* **2016**, 6, 59400–59404.
- (22) Becer, C. R.; Hahn, S.; Fijten, M. W. M.; Thijs, H. M. L.; Hoogenboom, R.; Schubert, U. S. *J. Polym. Sci. Part A Polym. Chem.* **2008**, 46 (21), 7138–7147.
- (23) Yang, B.; Zhang, X.; Zhang, X.; Huang, Z.; Wei, Y.; Tao, L. *Mater. Today* **2016**, 19 (5), 284–291.
- (24) Drozd-Rzoska, A. *Phys. Rev. E* **2000**, 62 (6), 8071–8075.
- (25) Chen, J.; Law, C. C. W.; Lam, J. W. Y.; Dong, Y.; Lo, S. M. F.; Williams, I. D.; Zhu, D.; Tang, B. Z. *Chem. Mater.* **2003**, 15 (7), 1535–1546.
- (26) Limer, A. J.; Rullay, A. K.; Miguel, V. S.; Peinado, C.; Keely, S.; Fitzpatrick, E.; Carrington, S. D.; Brayden, D.; Haddleton, D. M. *React. Funct. Polym.* **2006**, 66 (1), 51–64.
- (27) Zhang, L.; Hu, W.; Yu, L.; Wang, Y. *Chem. Commun.* **2015**, 51 (20), 4298–4301.

5 Conclusion and Outlook

In this thesis was have explored the implementation of nanoparticles for a wide variety of uses. In this chapter we discuss the conclusion of the work presented in this thesis and discuss future work.

Chapter 1 investigated the change in phase transition temperature of PS copolymers in DOP and the encapsulation of PS in DOP using a new photography based technique. We also touched upon the potential use within paint binders upon encapsulation. *Further investigation into creating smaller sized particle for easier incorporation into binders, such as microfluidic droplet formation for encapsulation. Further studies are needed into the potential use within additional binders.*

Chapter 2 described the synthesis of hollow silica shells from a base template. The shells indicated a possible use in both ultrasound imaging and opacifiers within paints. *Further studies into the effect on shape within ultrasound imaging is need by comparing with similar sized spherical particles of the same composition.*

Chapter 3 described the use of the hollow silica particles from Chapter 2 in nanocomposites. *Further work on more efficient dispersion of the silica particles within the PMMA matrix is required. Potential mixing within a solvent to allow full penetration of the PMMA into the particles.*

Chapter 5: Conclusion and Outlook

Chapter 4 discussed the use of an aggregation induced emission dye within UCST for emission indication on temperature. *Further work using more varied concentration of dye is needed along with a full UCST curve.*

6 Appendix I – Characterisation Techniques

Within this appendix, the theory behind some of the analytical techniques used within this thesis is covered.

6.1 Scanning electron microscopy (SEM)

Optical microscopes are limited in resolution due to the diffraction of the light source, in this case a photon source. In normal transmission mode, traditional light microscopes have a resolution of 0.5 μm , although with certain lenses and light sources a higher resolution can be obtained. In order to resolve colloidal particles on a submicron range and investigate the morphology, scanning electron microscope (SEM) is often employed. A tungsten filament is employed, along with magnetic lenses, to generate a focussed beam of accelerated electrons. The focussed beam of electrons has a much smaller wavelength than photons, resulting in a greater resolution being able to reach at 1 – 20 nm depending on the accelerating voltage (typically 1 – 20 kV). The higher the accelerating voltage, the shorter the electron wavelengths, and hence, the greater the resolution. However, increasing the accelerating voltage also increases the energy of the electron beam. This can cause damage to the sample if the energy is too high, hence

the accelerating voltage must be chosen carefully depending on the nature of the sample.

All samples must be electrically conducting and grounded to prevent electrostatic charge build up leading to artefacts within the imaging process. For non-conducting samples, a coating of gold, platinum, or carbon (among others) must be applied *via* sputtering in a vacuum. To image the smaller particles, carbon is often used as a coating as metal can form deposit clumps on the surface.

The advantage SEM has over transmission electron microscopy (TEM) is that it allows a large area of a sample to be imaged as well as analysed *via* energy dispersive x-ray spectroscopy (EDX).

6.2 Transmission electron microscopy (TEM)

Similar to SEM, transmission electron microscopy (TEM) uses an electron beam coupled with a CCD camera to image. However, an accelerating voltage in the range of 80 kV to 1 MV is used allowing a higher resolution to be obtained. TEM relies on the electron beam passing through a sample, thus only thin samples with a low enough electron density can be analysed. As the electron beams pass through the sample, internal structure, be it pores or internal voids, can be investigated giving it an advantage over SEM. However, surface morphology is difficult to obtain.

6.3 Energy Dispersive X-ray Spectroscopy (EDX)

Electron bombarded samples can have electrons knocked off from the inner shells of some atoms within a sample. An electron from a higher energy level will move to fill the vacant position, releasing an x-ray that is characteristic to both the element and the nature of the transition.

A crystal detector converts the x-ray energy into an electrical voltage, which is processed by the software. An intensity plot of certain energies is then used to determine the relative abundance of elements within a sample. However, the resolution is limited to $\sim 1\%$ of the mass of a sample and some of the lighter elements are impossible to detect. To determine the quantitative amounts of elements within a sample, the sample must be a smooth film with a suitable standard available to calibrate the machine against, which is often not possible for most synthesised samples. This leads EDX to often be used as a qualitative method over quantitative.

Both SEM and TEM can be used in conjunction with EDX, however SEM is best used to analysis over a large area of the sample, whilst TEM is better suited to spatially resolve elemental analysis.

6.4 Mie Scattering

Dispersed colloidal particles scatters light at an angle depending on its size when it passes through a laser beam. Scattering of the laser is also dependant on the cross sectional area of the particles, where a decrease in particle size leads to a decrease in scattered light intensity. Therefore large

particles scatter light at narrow angles with high intensity, whilst smaller particles scatter light over a wider angle with a lower intensity. The obtained scattering pattern generated by the sample is then compared to predictions of an appropriate model. Mie scattering is chosen over other scattering models due to its robust nature; it can process smaller or larger particles that are both transparent and opaque colloids. The general assumptions involved in Mie theory is that the particles are spherical in shape, dilute to limit multiple-scattering events, and the optical properties of both samples are known. Although the theory assumes the particles to be spherical, non-spherical particles can be measured and an equivalent spherical diameter is given **(Figure 6-1)**.^{1,2}

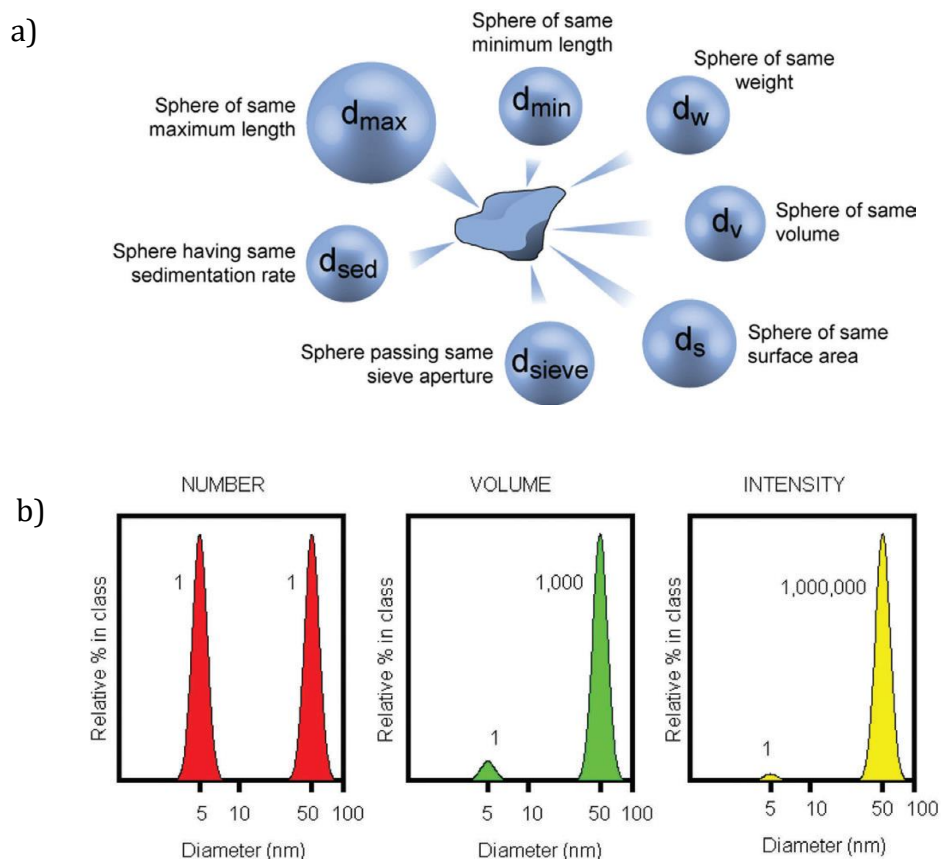


Figure 6-1. Diagram illustrating different values that can be compared between irregular samples, and b) difference seen between two differently sized samples measured using number, volume and intensity.²

Once the scattering pattern of a sample is acquired, the equivalent spherical diameter is determined *via* comparison to theoretical scattering patterns. The appropriate statistical diameter must then be reported, generally as a frequency distribution curve (similar to **Figure 6-1 b**) along with known $d(0.1)$, $d(0.5)$, and $d(0.9)$. These values are the diameters of the population in the bottom 10 % ($d(0.1)$), the bottom 50 % ($d(0.5)$), and the

bottom 90 % ($d(0.9)$). The formula for calculating weighted mean of a sample is given in **Equation 6-1**.

$$\bar{D}_{xy}^{(x-y)} = \frac{\sum D_i^x}{\sum D_i^y} \quad \mathbf{6-1}$$

Number average ($\bar{D} = 10$), volume/surface mean ($\bar{D} = 32$), and diameter/volume mean ($\bar{D} = 43$) are some of the more common weighted averages.

6.5 References

1. Kippax, P. Measuring particle size using modern laser diffraction techniques. *China Coatings J.* 30–36 (2005).
2. Levoguer, C. *Back to basics: particle characterisation. Labnews* **44**, (2012).

7 Appendix II – Supporting info for Chapter 1

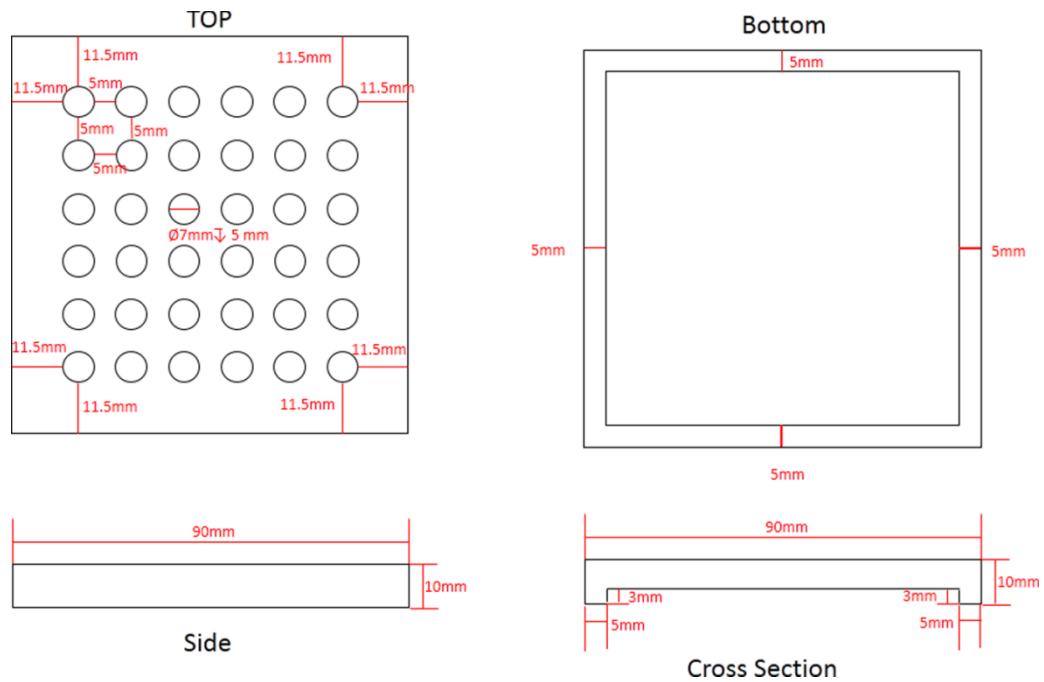


Figure 7-1 Schematic designed for aluminium block used for the photographic phase change measurement technique

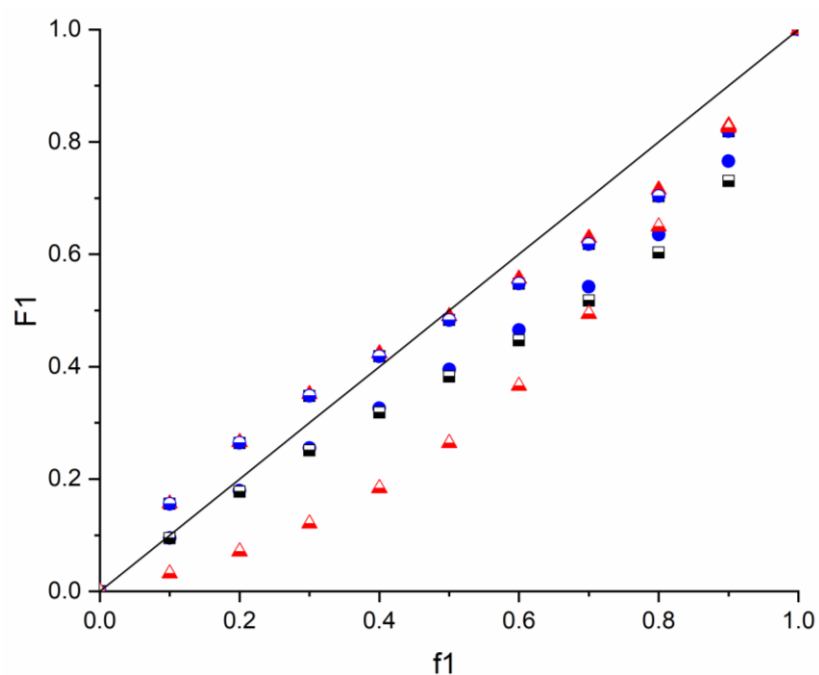


Figure 7-2. Mayo-Lewis plot of styrene and MMA (\blacktriangle), BMA (\blacksquare) (used instead of EMA), EA (\square), 2EHA (\bullet), LMA (\ominus) (used in place of LA), and TAA (\triangle) (used in place of NIPAM). Diagonal is the azeotropic line where $f_1 = F_1$.

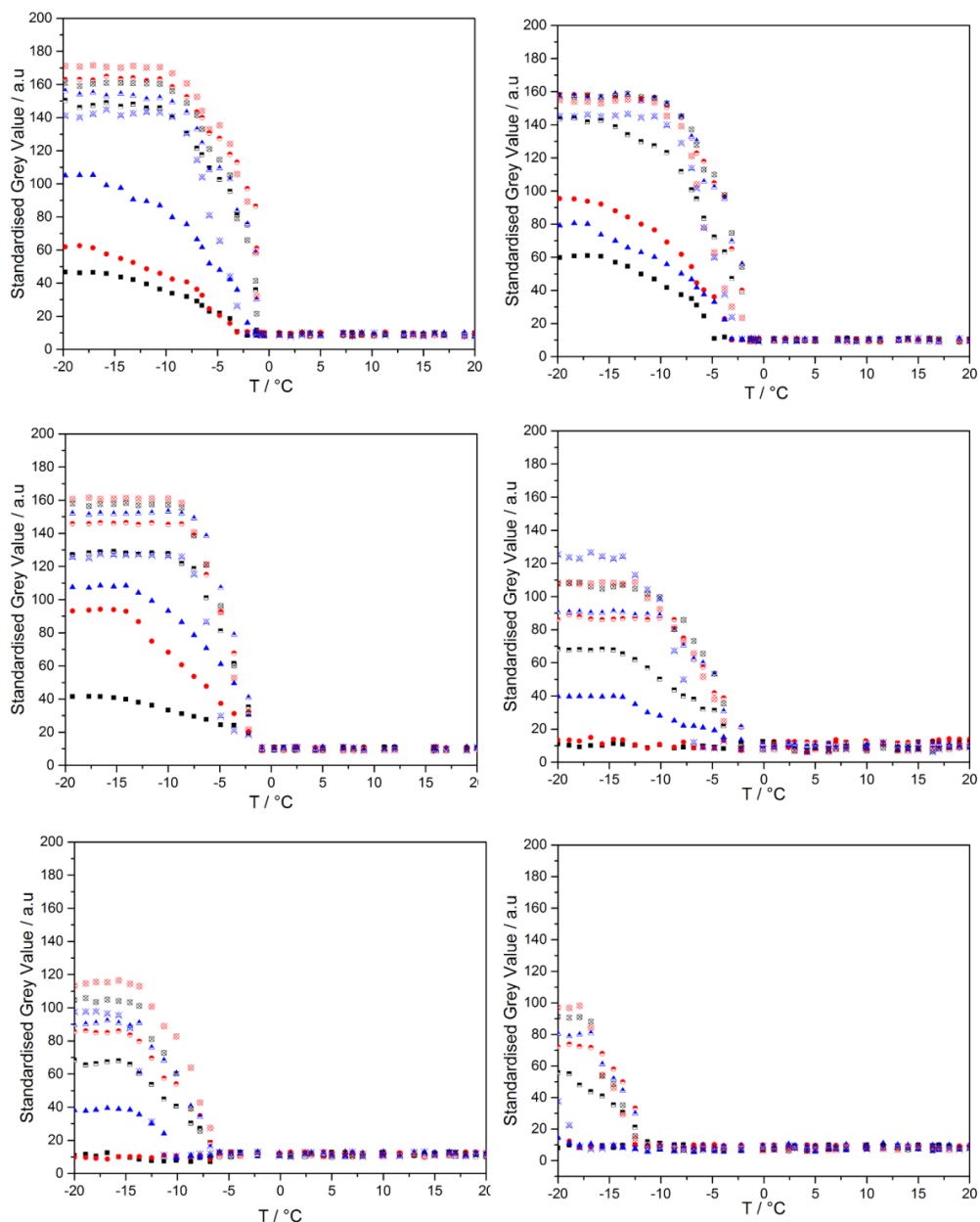


Figure 7-3. Phase change curves of a) PMMA 1, b) PMMA 2, c) PMMA 3, d) PMMA 4, e) PMMA 5, and f) PMMA 6.

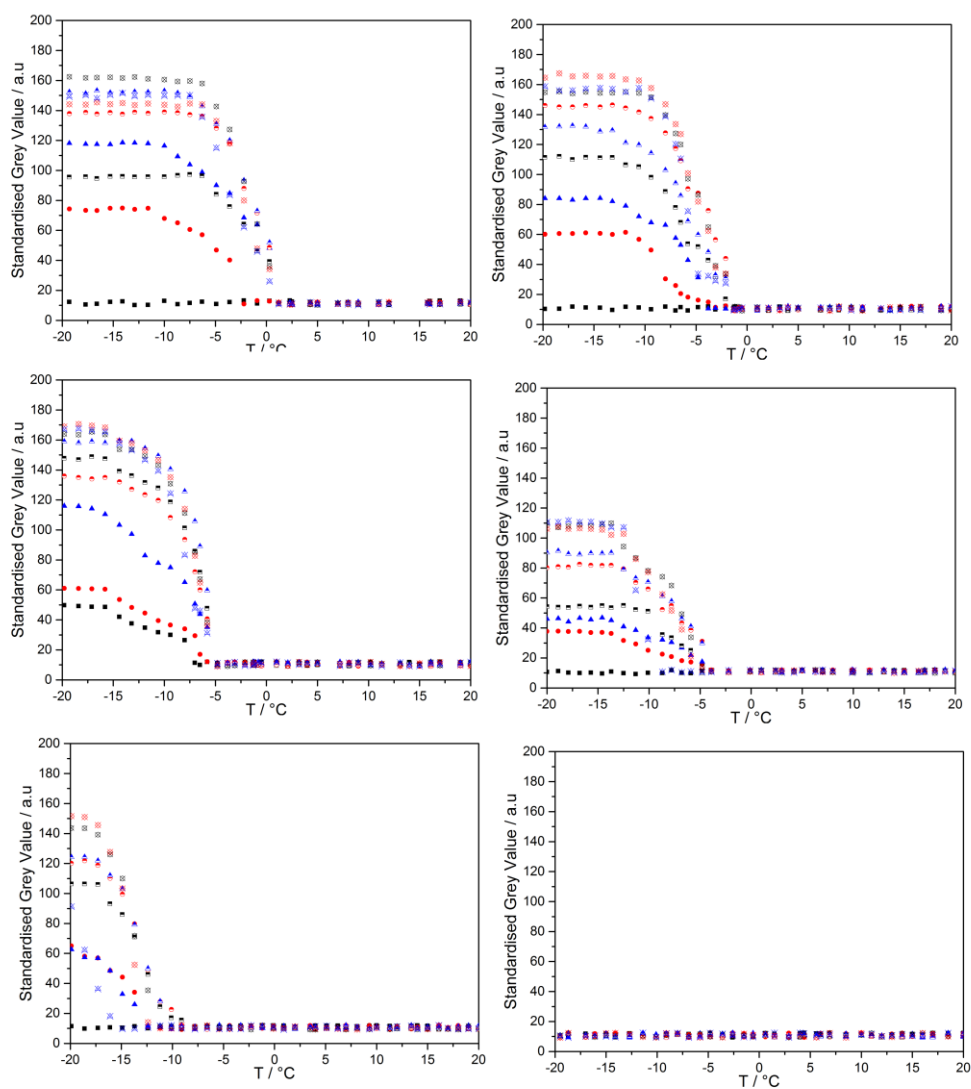


Figure 7-4. Phase change curves of a) PEMA 1, b) PEMA 2, c) PEMA 3, d) PEMA 4, e) PEMA 5, and f) PEMA 6.

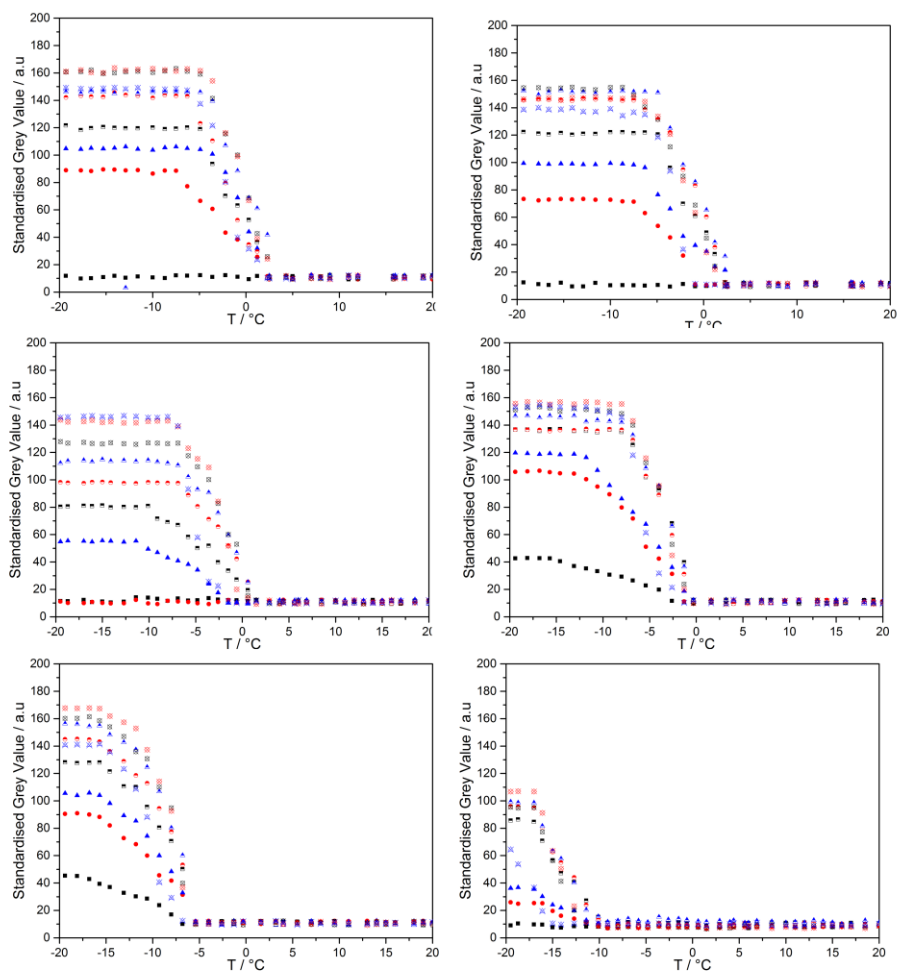


Figure 7-5. Phase change curves of a) PEA 1, b) PEA 2, c) PEA 3, d) PEA 4, e) PEA 5, and f) PEA 6.

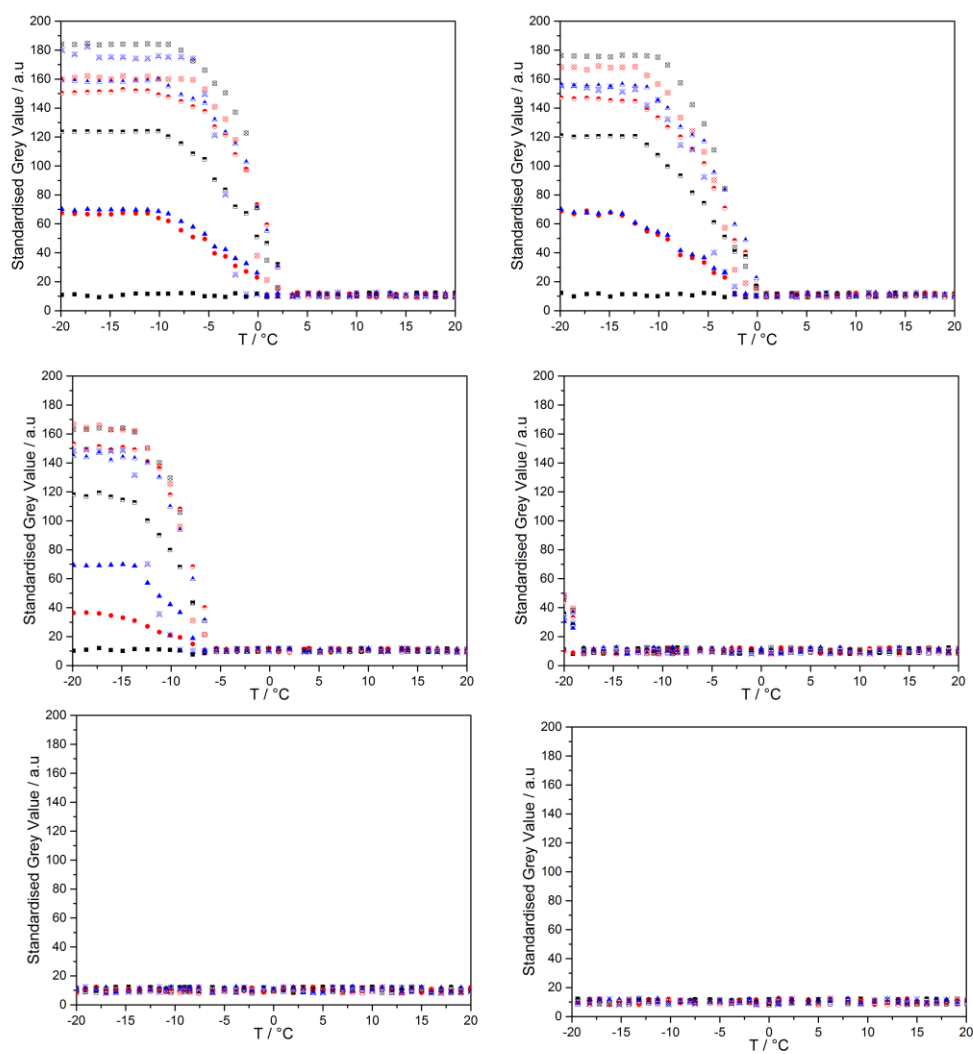


Figure 7-6 Phase change curves of a) P2EHA 1, b) P2EHA 2, c) P2EHA 3, d) P2EHA 4, e) P2EHA 5, and f) P2EHA 6.

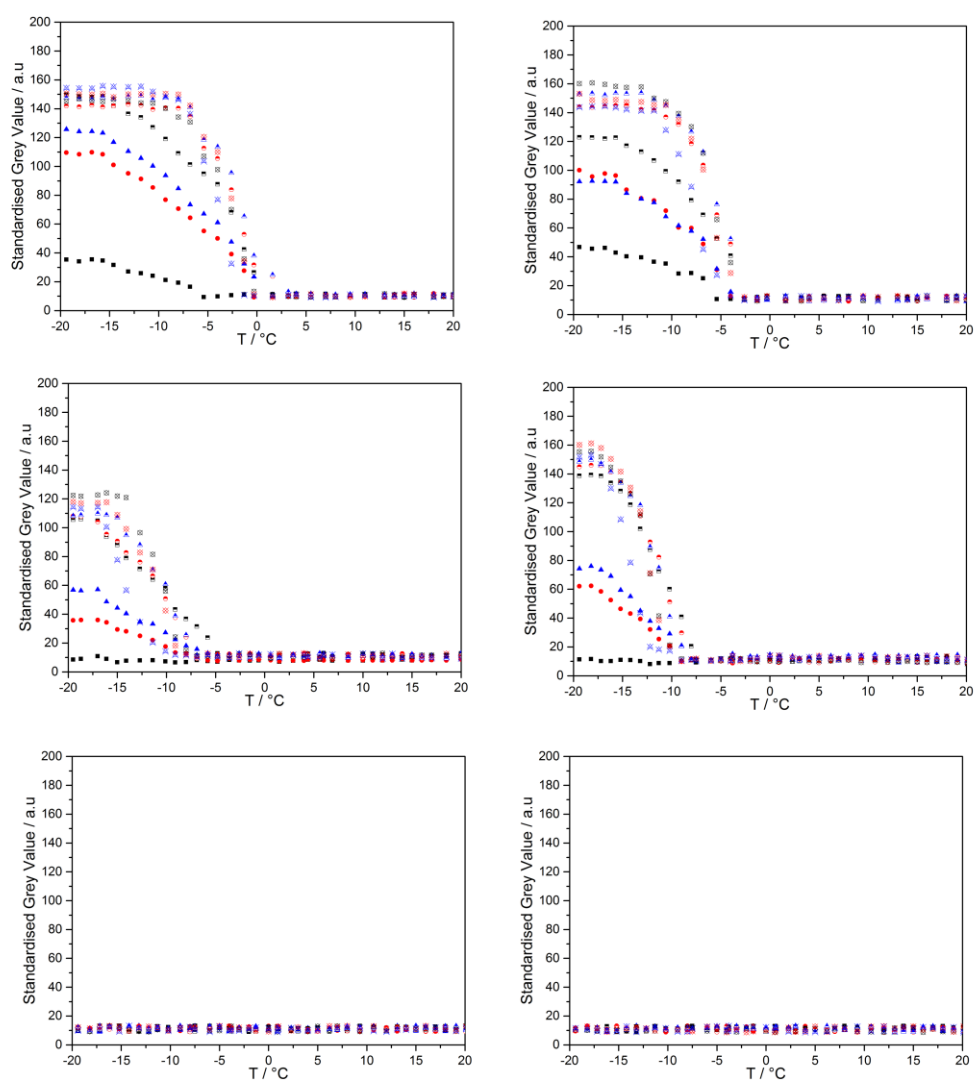


Figure 7-7. Phase change curves of a) PLA 1, b) PLA 2, c) PLA 3, d) PLA 4, e) PLA 5, and f) PLA 6.

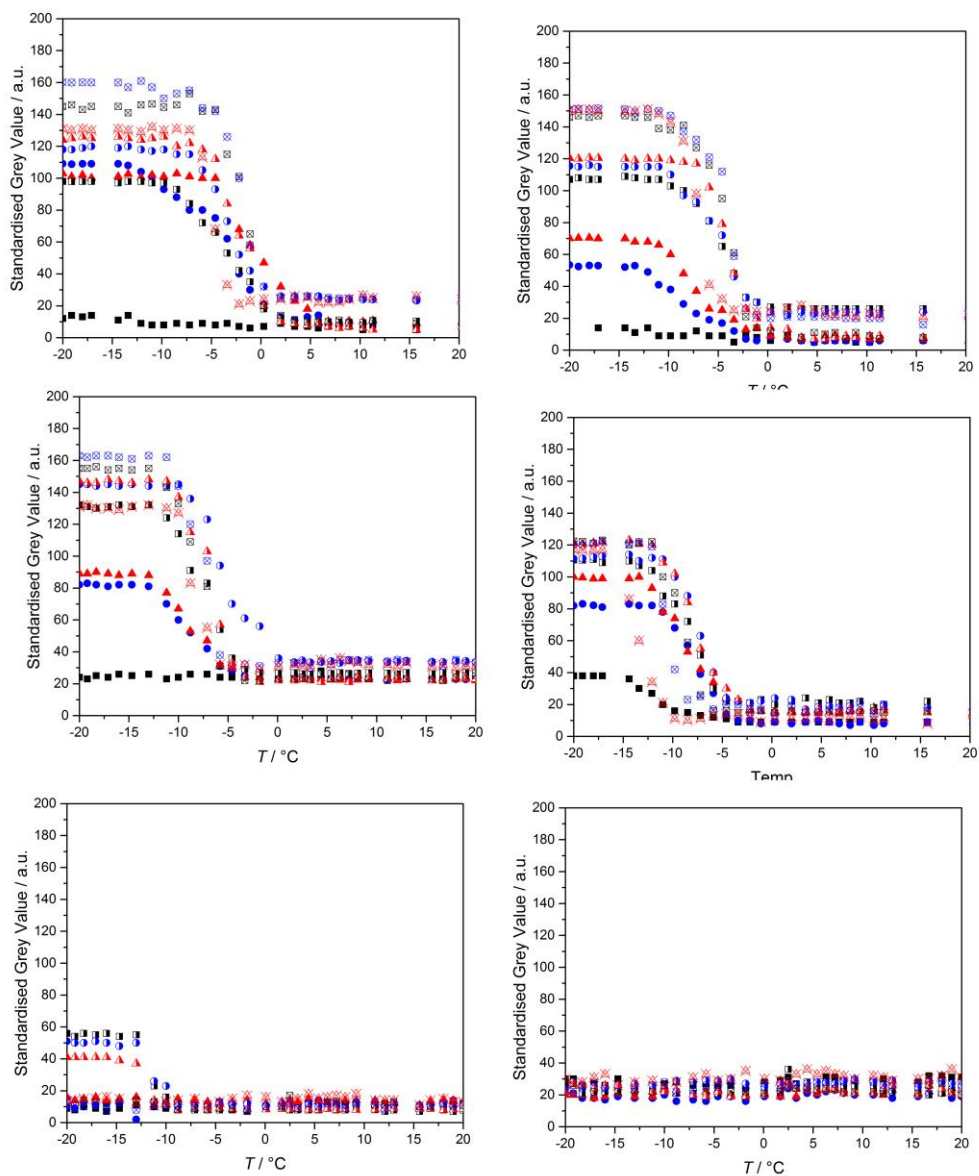


Figure 7-8. Phase change curves of a) PNIPAM 1, b) PNIPAM 2, c) PNIPAM 3, d) PNIPAM 4, e) PNIPAM 5, and f) PNIPAM 6.

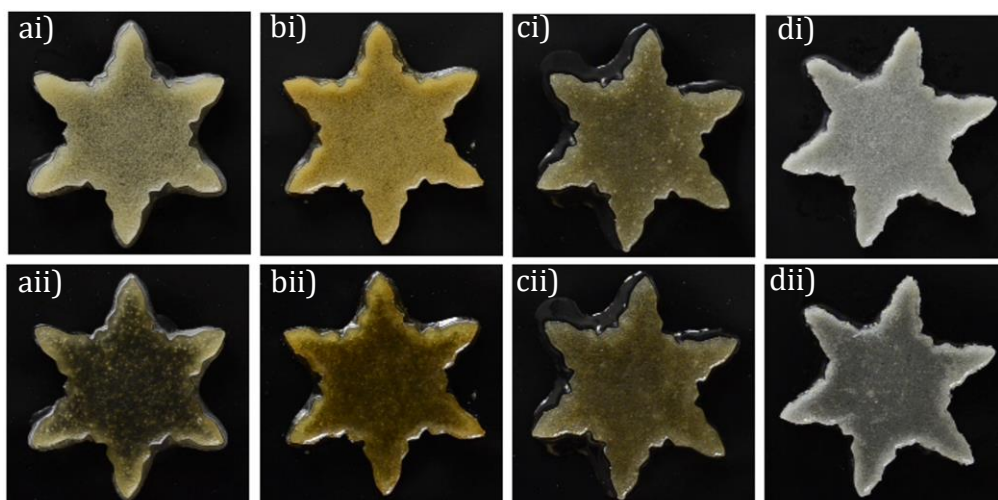


Figure 7-9. PSDOP capsules within a) polysiloxane binder, b) fast curing epoxy binder, c) slow curing epoxy binder, and d) silane binder at i) -5 °C and ii) 20 °C.